Flux-tube and global grid-based gyrokinetic simulations of plasma microturbulence and comparisons with experimental TCV measurements

THÈSE N^{O} 7065 (2016)

PRÉSENTÉE LE 1ER JUILLET 2016
À LA FACULTÉ DES SCIENCES DE BASE
SPC - THÉORIE
PROGRAMME DOCTORAL EN PHYSIQUE

ÉCOLE POLYTECHNIQUE FÉDÉRALE DE LAUSANNE

POUR L'OBTENTION DU GRADE DE DOCTEUR ÈS SCIENCES

PAR

Gabriele MERLO

acceptée sur proposition du jury:

Prof. V. Savona, président du jury
Prof. L. Villard, Dr S. Brunner, directeurs de thèse
Dr X. Garbet, rapporteur
Dr T. Görler, rapporteur
Dr S. Coda, rapporteur

ÉCOLE POLYTECHNIQUE
FÉDÉRALE DE LAUSANNE

Suisse
2016

Alla mia famiglia

Abstract

In magnetic fusion devices, the radial transport of heat and particle largely exceeds, by orders of magnitude, predictions based on collisional processes. This is widely understood as a consequence of small-scale turbulence which results from the complex nonlinear behaviour of so-called microinstabilities, driven unstable in a magnetically confined plasma by the strong pressure gradients required to reach fusion. Understanding and possibly mitigating these processes is of vital importance towards achieving controlled fusion. The complexity of such nonlinear phenomena allows one to address microturbulence only with a numerical description, carried out here within the gyrokinetic framework. This reduced kinetic model describes the evolution of the particle distribution functions and of the self-consistently generated electromagnetic fields by neglecting the fast time scale associated to the particle gyration around magnetic field lines.

In this work we extensively applied the grid-based gyrokinetic code GENE, using both its local and global versions, to model some of the experimental observations related to turbulent transport made in the Tokamak à Configuration Variable (TCV) at the Swiss Plasma Center.

Almost all simulations that will be discussed are performed considering realistic magnetic geometries, in turn provided by the MHD equilibrium solver CHEASE. In order to verify the interface of GENE with CHEASE, a series of benchmarks have been developed and successfully carried out in the linear local limit, assuming fully gyrokinetic electrons and ions. These tests have then been extended to the global version of the code, relaxing the kinetic electron response assumption mainly to reduce the overall computational cost. Linear and nonlinear simulations have been performed and compared to ORB5 results, obtaining a good agreement.

A significant part of this work deals with the electron heat confinement improvement observed when the shape of the confined plasma is modified by changing the sign of the Last Closed Flux-Surface (LCFS) triangularity δ_{LCFS} from positive to negative. In the latter case, half the heating power is required to maintain the same electron temperature and density profiles compared to the former, which was experimentally interpreted as a better energy confinement at all radial locations, even though δ has a finite radial penetration depth, becoming vanishingly small as one moves from the LCFS to the magnetic axis. A first series of local gyrokinetic simulations were carried out to investigate the dependence of profile stiffness on shaping. Local results fail at reproducing both the absolute level of heat transport as well as the observed transport ratio between positive and negative δ, while the main effect of negative δ according to the simulations appears to be in form of higher critical gradients for the onset of microturbulence. Global gradient-driven simulations have then been performed, showing a very high sensitivity of the electron heat flux with respect to the density gradient. Global runs, carried out neglecting carbon impurities in order to reduce the computational cost, are compatible with the experiments when using parameters from a recent, experimentally well diagnosed, discharge. In this case, strong global effects which lower the heat flux compared to local runs are seen. Thanks to flux-tube simulations, rotation is found not to significantly affect transport, while carbon impurities appear to further lower the heat transport level in both the ion and electron channels, and are thus expected to further improve the agreement between simulations and measurements if retained.

Local and global GENE runs have then been performed looking at axisymmetric dynamics in the frequency range of the Geodesic Acoustic Mode (GAM) in TCV conditions. Experimentally, the GAM is almost always observed as a radially coherent mode, i.e. an oscillation at constant frequency over a main fraction of the minor radius of the confined plasma. The only exception is for very large values of the edge safety factor q, where the mode looses its coherence and a dispersive GAM, with a frequency that follows the local sound speed, is measured. Among the many experimental parameter scans, a density ramp-up was first studied with local simulations, for which the mode was observed to disappear, covered by the broad-band turbulence. Flux-tube results already agree reasonably well with measurements of the heat transport as well as the GAM frequency and its amplitude.

The coherent GAM was then investigated thanks to global simulations. A series of runs, with different physical models, have been performed in order to reproduce a discharge already modeled with the gyrokinetic Particle In Cell (PIC) code ORB5. Simulation results qualitatively agree with experiments and a good agreement is recovered with the ORB5 code results when the same physical model is used. Finally, the hypothesis of a coherent-dispersive GAM regime transition related to the safety factor profile, as it was experimentally speculated was addressed. It is found that changing only q is not sufficient to induce a regime transition, which thus appears to be related to other plasma parameters, including finite machine size effects.

Key words: plasma, fusion, tokamak, turbulence, gyrokinetic simulations, plasma shaping, Zonal Flows, Geodesic Acoustic Mode

Sinossi

In plasmi confinati magneticamente, il trasporto in direzione radiale di calore e particelle è sperimentalmente osservato essere svariati ordini di grandezza superiore rispetto a stime basate su processi puramente collisionali. Questa discrepanza è universalmente intesa come causata da uno stato turbolento che si origina quale risultato di complessi processi non lineari che coinvolgono le cosiddette microinstabilità, instabilità che si sviluppano su scale microscopiche. A loro volta, queste instabilità sono alimentate dall'estremo gradiente di pressione necessario per raggiungere le condizioni richieste dalla fusione. Studiare, comprendere e mitigare questi processi è di vitale importanza per il successo della fusione nucleare controllata. L'estrema complessità di questi processi può essere tuttavia affrontata solamente con un approccio numerico. A tal scopo, nel presente lavoro viene utilizzato l'approccio girocinetico, un modello cinetico ridotto che descrive l'evoluzione della funzione di distribuzione delle varie specie che compongono il plasma, e dei campi elettromagnetici auto consistenti, trascurando la rapida scala temporale associata al moto di girazione delle particelle lungo le linee di campo.

In questa tesi, il codice girocinetico GENE, che descrive il plasma mediante un approccio Euleriano, è stato utilizzato nelle sue versioni locale e globale con l'obiettivo di riprodurre e investigare alcune delle numerose osservazioni sperimentali legate alla microturbulenza fatte sul Tokamak a Configurazione Variabile (TCV) presso lo Swiss Plasma Center.

Tutte le simulazioni sono state svolte considerando geometrie magnetiche realistiche, ottenute utilizzando il risolutore MHD CHEASE. Svariati test sono stati sviluppati e portati a termine con successo, permettendo di verificare l'interfaccia tra GENE e CHEASE nel limite lineare locale e considerando ioni ed elettroni cinetici. Questi stessi test sono poi stati estesi alla versione globale del codice, assumendo una risposta elettronica adiabatica per ridurne l'onere computazionale. Un ottimo accordo con i risultati lineari e non lineari forniti dal codice PIC ORB5 è stato ottenuto.

Una larga parte delle simulazioni svolte è dedicata allo studio del miglioramento del confinamento elettronico osservato in TCV quando la forma del plasma confinato viene modificata invertendo il segno della triangolarità δ del bordo del plasma, da positiva a negativa. Nel secondo caso è sufficiente impiegare metà potenza di riscaldamento rispetto al primo per mantenere gli stessi profili di densità e temperatura elettronica. Questo risultato viene sperimentalmente interpretato come un miglioramento uniforme del confinamento, sebbene la triangolarità abbia una lunghezza di penetrazione radiale finita, diventando rapidamente trascurabile muovendosi dal bordo verso il centro del plasma. L'ipotesi di un diverso grado di resilienza dei profili elettronici in funzione della geometria magnetica è stata studiata con una serie di simulazioni locali. Queste non sono in grado di riprodurre né i flussi di calore misurati sperimentalmente né il rapporto tra le due geometrie, ma indicano semplicemente un gradiente critico più elevato quando $\delta < 0$. Simulazioni globali a profili imposti mostrano un'elevata sensitività dei risultati rispetto a variazioni del gradiente di densità, e predicono un trasporto elettronico compatibile con i valori sperimentali solamente assumendo parametri di plasma derivati da una scarica TCV in cui le misure sperimentali sono affette da piccole barre d'errore. In questo caso appare evidente una forte stabilizzazione della turbolenza dovuta alla taglia della macchina, con una forte riduzione del trasporto rispetto a quanto ottenuto con simulazioni locali. Le simulazioni globali sono stati svolte trascurando la presenza di impurità di carbonio, mentre simulazioni locali indicano un'ulteriore forte riduzione del trasporto di calore, sia nel canale ionico che in quello elettronico, quando queste vengono considerate. Ci si attende di conseguenza un miglioramento ulteriormente dell'accordo tra simulazioni ed esperimenti qualora le simulazioni globali vengano ripetute includendo il carbonio.

Una seconda importante parte della tesi è dedicata allo studio della dinamica di modi assi-simmetrici nel range di frequenze tipiche del Modo Geodesico Acustico (GAM), investigato con simulazioni locali e globali. Il GAM viene tipicamente osservato in TCV come un modo radialmente coerente, caratterizzato cioè da una frequenza costante lungo buona parte del raggio minore del plasma. L'unica eccezione è data da scariche in cui il fattore di sicurezza al bordo q è particolarmente elevato. In questo caso il modo perde la sua coerenza e un'oscillazione con una frequenza proporzionale alla velocità sonica locale viene misurata.

Un rampa di densità per cui sperimentalmente, ad alta densità, il GAM viene osservato sparire coperto dalla turbolenza a banda larga è stata investigata mediante simulazioni locali. In questo particolare caso, l'approccio locale fornisce una buona stima sia del trasporto che della frequenza e dell'ampiezza del GAM. Le proprietà del GAM coerente sono state studiate mediante simulazioni globali dedicate, svolte assumendo diversi modelli fisici, ottenendo un buon accordo con i dati sperimentali e con i risultati ottenuti mediante ORB5 quando lo stesso modello viene utilizzato. Infine, la relazione tra la transizione da modo coerente a dispersivo e il fattore di sicurezza è stata investigata, mettendo in luce come una sola variazione di q non sia sufficiente a causare una transizione di regime. Quest'ultima viene di conseguenza legata ad altri parametri di plasma, tra cui la taglia della macchina.

Parole chiave: plasma, fusione, tokamak, turbolenza, simulazioni girocinetiche, forma del plasma, flussi zonali, Modo Geodesico Acustico

Contents

Abstract v

Sinossi vii

1 Introduction 1
- 1.1 The energy problem and nuclear fusion 1
- 1.2 Magnetic confinement 3
- 1.3 Transport in confined plasmas 6
- 1.4 Scope and outline of the thesis 10

2 Theoretical background 13
- 2.1 Tokamak plasma equilibrium 13
- 2.2 Kinetic plasma modeling and Vlasov-Maxwell system 17
- 2.3 The gyrokinetic model: the basic idea and corresponding ordering 18
- 2.4 Modern derivation of the collisionless gyrokinetic equation 20
  - 2.4.1 The unperturbed guiding center equations 23
  - 2.4.2 The gyrocenter equations 24
  - 2.4.3 The gyrokinetic equation 27
  - 2.4.4 The field equations 31
  - 2.4.5 Further simplifications 34
  - 2.4.6 The local limit 38
- 2.5 The collision operator 38
- 2.6 Microinstabilites 40
  - 2.6.1 Drift waves 41
  - 2.6.2 ITG 42
  - 2.6.3 ETG 44
  - 2.6.4 TEM 45
  - 2.6.5 Other instabilities 48
- 2.7 Zonal Flows and the Geodesic Acoustic Mode 48
- 2.8 Summary 51

3 Numerical simulation model: the GENE code 53
- 3.1 Phase space coordinate system 54
- 3.2 Numerical representations and boundary conditions of phase space directions 55

3.3 Further numerical details . . . 58
    3.3.1 Time stepping scheme and eigenvalue solver . . . 58
    3.3.2 Magnetic equilibrium . . . 59
    3.3.3 Discretization of the nonlinearity . . . 59
    3.3.4 Numerical hyperdiffusion and anti-aliasing . . . 59
    3.3.5 Gyroaveraging . . . 60
3.4 Normalizations . . . 61
3.5 Macroscopic observables . . . 62
    3.5.1 Turbulent fluxes . . . 62
    3.5.2 Spatial averages and radial conservation laws . . . 65
3.6 Other specific features of the global code . . . 66
    3.6.1 Heat and particle sources . . . 66
    3.6.2 Radial buffers . . . 68
3.7 Summary . . . 68

4 Code verification 69
4.1 Local benchmarks . . . 69
    4.1.1 Magnetic geometries and profile details . . . 69
    4.1.2 Linear k_θ-spectra . . . 73
    4.1.3 Ballooning angle scan . . . 79
    4.1.4 Rosenbluth - Hinton test . . . 83
4.2 Global benchmarks . . . 87
    4.2.1 Linear runs with adiabatic electrons . . . 89
    4.2.2 Nonlinear runs with adiabatic electrons . . . 91
    4.2.3 Linear runs with kinetic electrons . . . 94
4.3 Conclusions . . . 96

5 Local investigation of the effect of triangularity on turbulent transport 99
5.1 Overview of TCV experimental observations . . . 99
    5.1.1 Reversing LCFS triangularity in the TCV tokamak . . . 99
    5.1.2 Profile stiffness . . . 101
5.2 Simulation details . . . 102
5.3 Linear simulations . . . 103
5.4 Non-linear simulations . . . 107
    5.4.1 “Simple physics” model . . . 109
    5.4.2 “Full physics” model . . . 111
5.5 How to interpret local runs and look at stiffness? . . . 113
5.6 Conclusions . . . 116

6 Global simulations of TCV discharges with positive and negative triangularity 117
6.1 Gradient vs. flux driven global simulations . . . 117
6.2 General remarks about setting up a global simulation . . . 118

6.3 Global simulations with TCV experimental profiles 120
  6.3.1 Preliminary runs relative to core conditions 120
  6.3.2 Full-radius simulations with realistic profiles 122
6.4 Beyond the original parameter set 125
  6.4.1 Local results 127
  6.4.2 First global simulations 132
  6.4.3 Further remarks about the effects of carbon impurities and plasma rotation 133
6.5 Conclusions 138

7 Study of GAM dynamics in TCV relevant conditions 141
7.1 Analysis of an experimental TCV density ramp-up 142
  7.1.1 TCV discharge #46068 142
  7.1.2 Local linear analysis 144
  7.1.3 Local nonlinear results 151
  7.1.4 Local adiabatic electron results for ITG dominated regimes 164
7.2 Global simulations of TCV discharge #45353 with a radially coherent GAM 170
  7.2.1 Motivation 170
  7.2.2 Nonlinear simulations 172
  7.2.3 GAM frequency characterization 175
  7.2.4 GAM fluctuations 177
  7.2.5 Comparison with ORB5 results 180
7.3 Radially coherent vs. dispersive GAM regimes 183
7.4 Conclusions 187

8 Conclusions 189
8.1 Summary 189
8.2 Outlook 192

A The GKW code 195
A.1 GKW coordinate system 195
A.2 Normalization 198

B The GS2 code 199
B.1 GS2 coordinate system 199
B.2 Normalization 201

C Development of synthetic diagnostics for T-PCI and C-ECE systems 202
C.1 A Matlab post-processing graphic tool 202
C.2 Synthetic diagnostics 203

D Local simulations for the TCV discharge #45353 **206**
D.1 GAM frequency from nonlinear simulations 207
D.2 GAM density and magnetic component 208
D.3 Rosenbluth-Hinton tests investigating shaping effects 209

Bibliography **222**

Acknowledgements **223**

Curriculum Vitae **225**

1 Introduction

1.1 The energy problem and nuclear fusion

The continuous growth of world population together with the improvements in the quality of life are tightly bound to an increase of the energy demand and consumption. Industrialization and technological progress themselves are not possible without large availability of energy at low price. Today's energy production is essentially based on combustion of fossil fuels, such as oil, coal or gas. In this case, the processes involved for the production of electric energy are particularly simple to initiate and control, and the technology required is cheap and reliable. Reserves of these fuels are however depleting and will be exhausted in few decades. Moreover, all combustion processes are inevitably associated with the release of enormous amounts of CO_2, increasing the green-house effect and therefore ultimately leading to climate changes. Although there is nowadays a general growing attention to these issues and many efforts are done in order to save energy and reduce its consumption, it appears clear that a solution for mid and long term is not yet available and research is ongoing in order to improve and develop alternative energy sources.

Renewable green energies, such as wind or solar power, are often considered the ideal solution to the energy problem. Being virtually unlimited and also free from carbon emission, they appear as particularly appealing. However, sustaining the whole energy request uniquely with such sources is very difficult, mainly because of their intrinsic fluctuating nature, like the wind strength or the daily sunshine duration. The unbalance between request and availability requires a massive and efficient storage capability which is not yet available.

Exploiting nuclear reactions for energy production, appears as a particularly interesting alternative essentially because of the enormous release of energy, associated to the mass deficit between reactants and products, which is orders of magnitude larger than common chemical reactions. Two kinds of reactions, fission and fusion, can be considered. The fission process consists in breaking apart a heavy nucleus such that the products are lighter involving more tightly bound nuclei. During the process, neutrons are released as well and can be used to self sustain a chain reaction. Fission reactors are a well established and exploited technology but strongly debated, mainly because of the risk of release of radioactivity in case of severe accidents and the production of highly radioactive waste (with half-life time up to 10^3-10^4 years).

Nuclear fusion is the energy source of stars. In the process light nuclei interacting between each other fuse together resulting into heavier ones. Ever since the discovery of fusion as being the source of energy in the Sun in 1930s [1], scientists aim at harnessing nuclear fusion in a controlled way on Earth. The proton-proton chain on which the energy production in the Sun is based, involves the weak nuclear interaction in the decay of protons into neutrons [2], and therefore is too slow to be exploited on Earth. Instead, the deuterium-tritium reaction is the most promising choice for terrestrial application. The process begins with the two isotopes deuterium and tritium of hydrogen, and produces a nucleus of helium and a neutron:

$$ {}^2_1\mathrm{D} + {}^3_1\mathrm{T} \rightarrow {}^4_1\mathrm{He} + \mathrm{n} + 17.6\ \mathrm{MeV} \tag{1.1}$$

As a result of a single reaction, 17.6 MeV of energy are released and redistributed between the products according to their mass ratio ($\sim$ 14 MeV to the neutron and $\sim$ 1/5 to the helium).

The main difficulty associated to achieving such a fusion reaction is due to Coulomb repulsion: reacting nuclei have to overcome the corresponding potential barrier so as to come close enough to allow the attractive strong nuclear force to induce fusion. Hence, particles must collide between themselves at very high kinetic energy, in principle larger than the height of the Coulomb barrier. The required energies are well beyond the electron binding energy, therefore the matter is completely ionized and the state of plasma reached. Obtaining a sufficiently hot and dense plasma for a sufficiently long time, is therefore a condition necessary to be met in order to allow fusion reactions to occur. A simple energy balance allows to identify the so-called Lawson criterion [3], which states that the triple product of density n, temperature T and confinement time τ_E of the plasma must exceed a threshold in order to have a net energy production:

$$ nT\tau_E \geq 10^{21}\mathrm{keVs/m^3} \quad \text{together with} \quad \mathrm{T} \gtrsim 20\mathrm{keV}. \tag{1.2}$$

Two different strategies are currently being investigated in order to meet this constraint. The first one is exploited in the inertial confinement research, where the ultimate goal is to produce a very high density plasma, with a density of the order of $10^{30}m^{-3}$, which then needs to be confined only for a short time $\tau_E \sim 10^{-9}s$. This is achieved by compressing pellets of fuel with shock waves generated by high power lasers or ion beams.

The alternative approach, magnetic confinement fusion, aims at producing a low density plasma, $n \sim 10^{19}m^{-3}$, which however is confined for a much longer time in order to satisfy the constraint imposed by (1.2), typically $\tau_E \sim\ s$. We present magnetic fusion in some more detail in the next section.

1.2 Magnetic confinement

A promising approach to reach the required energies for fusion reaction is to heat a mixture of deuterium and tritium gas to sufficiently high temperatures, of the order of 100-200 million K, corresponding to an average thermal energy of 10-20 keV. In these conditions, a large fraction of the tails of the Maxwellian distribution characterizing each plasma species is clearly at energies exceeding the Coulomb repulsion and fusion reactions can occur. A mean to confine and isolate the hot plasma by avoiding any contact with the surrounding walls must be found. Otherwise the rapid transfer of energy from the plasma to the walls is likely to result in structural damages and in an instantaneous cooling of the plasma thus preventing any fusion reaction to further occur.

Although globally neutral, each of the particles constituting a plasma can interact with any electromagnetic field **E** and **B**, and the resulting motion is determined by the Lorentz force:

$$m\frac{d\mathbf{v}}{dt} = q\left(\mathbf{E} + \mathbf{v} \times \mathbf{B}\right), \tag{1.3}$$

where q, m, and $\mathbf{v}$ are respectively the charge, mass and velocity of the particle. Magnetic confinement exploits this property of a plasma in order to confine it in a finite volume with a specific shape.

In order to understand the basic principles behind the design of a magnetic fusion device and its configuration, it is useful to discuss the most basic properties of the motion of a single charged particle in electromagnetic fields [4]. In the presence of only a magnetic field **B**, as a consequence of Eq. (1.3), a particle is free to move along one magnetic field line but constrained to gyrate around it in the perpendicular direction. Therefore, if the

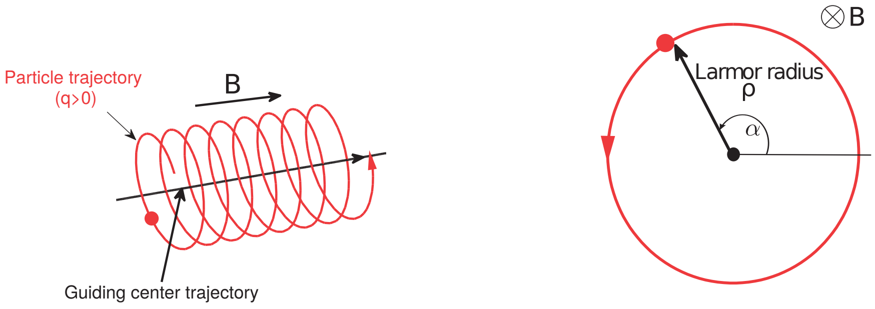

Figure 1.1 : Cartoon sketching the gyromotion of a positively charged particle in a uniform magnetic field B (left) and its projection on a plane perpendicular to the magnetic field (right).

magnetic field is homogeneous and constant, the resulting trajectory of the particle is an helix wrapping around a field line, as sketched in Figure 1.1. The resulting *gyromotion* is characterized by the gyrofrequency Ω and the so-called Larmor radius ρ, respectively given by:

$$\Omega = \frac{qB}{m}, \qquad \rho = \frac{v_\perp}{\Omega}. \tag{1.4}$$

where $v_\perp$ indicates the velocity of the particle in the direction perpendicular to the magnetic field. On the other hand, when electric and magnetic fields are present at the same time, particles are no longer bound to one field line, but instead move as well in a direction perpendicular to both fields, undergoing the so called $\mathbf{E} \times \mathbf{B}$ drift. Its velocity is given by

$$\mathbf{v}_{\mathbf{E}\times\mathbf{B}} = \frac{\mathbf{E} \times \mathbf{B}}{|\mathbf{B}|^2}, \tag{1.5}$$

which is independent from mass and charge, and therefore goes in the same direction for all plasma species without creating any net current. Other particle drifts arise from curvature and inhomogeneities of the magnetic field, and are respectively given by:

$$\mathbf{v}_c = \frac{mv_\parallel^2}{qB} \left(\nabla \times \mathbf{b}\right)_\perp, \qquad \mathbf{v}_{\nabla B} = \frac{mv_\perp^2}{2q} \frac{\nabla B \times \mathbf{B}}{B^3}. \tag{1.6}$$

Here $v_\parallel$ indicates the velocity parallel to the magnetic field $\mathbf{B} = B\mathbf{b}$. Note that these drifts are charge dependent.

Early designs of fusion devices were essentially linear machines employing inhomogeneities in the magnetic field to create a mirror force to reflect particles at both ends. Such devices however suffer from the so-called ”loss cone” problem, that is the loss of particles at both end, making the confinement insufficient. Hence they have been abandoned in favor of configurations where the magnetic field lines are closed.

The simplest geometry in which magnetic field lines can close on themselves is a torus. However, because of curvature and gradient drifts the magnetic field lines cannot be simple rings. The configuration will otherwise be intrinsically unstable. Being charge dependent, $\mathbf{v}_c$ and $\mathbf{v}_{\nabla B}$ lead to drifts in opposite directions for ions and electrons. The resulting vertical charge separation produces an electric field which in turn causes a radial plasma expulsion because of $\mathbf{E} \times \mathbf{B}$ drifts. Magnetic field lines thus need to be twisted into an helical shape around the torus. In this way, because the motion of a particle along a magnetic field line is much faster than the one in the perpendicular direction, curvature and gradient drifts cancel and the individual particle trajectories can be effectively confined. Two different technical ways of obtaining twisted field lines exist: by internal currents in tokamaks or by external coils in stellarators.

The tokamak (Russian acronym for toroidal chamber with magnetic field coils), is schematically presented in Fig. 1.2. It is an axisymmetric device characterized by a

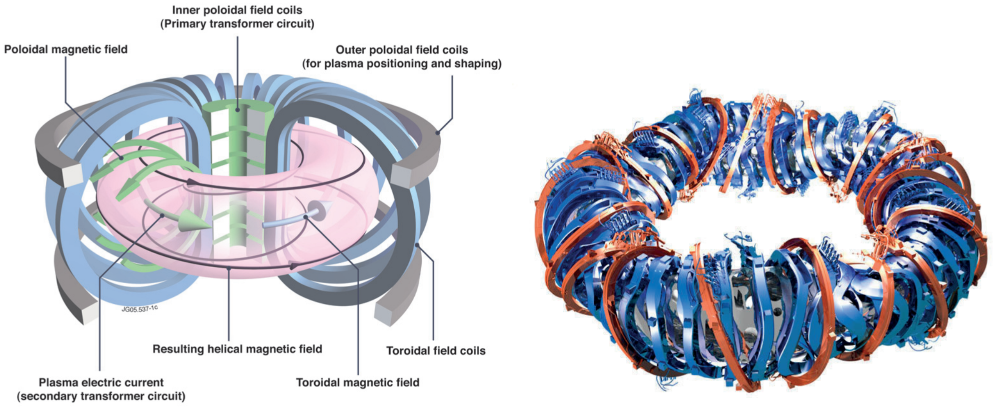
Inner poloidal field coils
(Primary transformer circuit)
Poloidal magnetic field
Outer poloidal field coils
(for plasma positioning and shaping)
JG05.537-1c
Resulting helical magnetic field
Toroidal field coils
Plasma electric current
(secondary transformer circuit)
Toroidal magnetic field

Figure 1.2 : Cartoons sketching the basic configuration on the left of Tokamak, and on the right of a Stellarator. The different magnetic coil systems leading to a different plasma shape are shown.

strong toroidal magnetic field generated by external coils and a smaller poloidal magnetic field which is generated by a current flowing in the plasma. Such current is induced by a a central transformer, the plasma itself being the secondary winding. The plasma current constitutes also a natural heating system through Ohmic dissipation (which however is limited by the fact that plasma resistivity decreases with increasing temperature and therefore other complementary heating solutions must be adopted). One of several problems facing the tokamak is the fact that a fusion reactor will need to operate as a steady state device, a requirement which is incompatible with an ohmic transformer. External current drive is required, which in turn involves costly and technologically complex systems such as microwaves or neutral beams, whose efficiency is not very high. To this end, in tokamaks there is a natural transport-driven current, the so-called bootstrap current, which is generated by the Coulomb friction between trapped and passing particles [5]. It can provide a significant fraction of the required current and is considered as a critical element towards the realization of a fusion reactor. Finally, one must also remember that plasma currents can drive dangerous instabilities (e.g. kink modes) that set operational limits [3].

A stellarator instead adopts a complex set of coils to obtain the desired twisting of magnetic field lines without the need of any plasma current (right side of Fig. 1.2). The main advantage of such approach is the possibility of steady state operation, as there is no need of an ohmic transformer. As a drawback, this configuration is inherently three dimensional and the set of coils is extremely more complicated than the one required for a tokamak.

Both approaches to magnetic confinement fusion are currently under active investigation. The major next step for tokamak research is represented by the ITER project currently under construction in Cadarache, in the south of France. ITER is a joint worldwide collaboration with the aim of demonstrating the technological and scientific feasibility of fusion energy [6]. The machine is designed to produce a ten fold return on energy (Q=10), that is produce 500 MW with an input power of 50 MW for discharges of $\sim 400s$. In addition, ITER is also meant to explore the steady state operation of a burning plasma, a plasma where fusion reactions are self-sustained, as well as test solutions for integrating into a future power plant the tritium breeding modules.

The most advanced stellarator experiment is currently ongoing in Greifswald, Germany, where in December 2015 the first plasma was created in Weldenstein 7-X. This machine is the first example of a quasi-isodynamic stellarator [7]. Its specific goal is to prove the capability of this advanced configuration to effectively confine fast particles, such as the fusion born α, and to operate at zero bootstrap current [8].

1.3 Transport in confined plasmas

Even when macroscopic MHD instabilities (e.g. disruptions, sawtooth activity, tearing modes) are stabilized, one of the main problems of any confined plasma that still prevents it reaching the limits imposed by the Lawson criterion is associated to radial transport of particles and energy, which dramatically reduce the plasma confinement time. Phenomena like conduction, convection and radiation can significantly degrade the performance of any fusion device [9]. The main object of transport theory is thus to investigate, and possibly control, such phenomena.

Transport processes are often considered of diffusive nature, therefore characterized by a particle and heat diffusivities of the form

$$D, \chi = \frac{a^2}{\tau_E}, \tag{1.7}$$

such that, assuming a Fick's type law, the particle and heat fluxes can be expressed as

$$\begin{aligned} \Gamma &= -D\nabla n, \\ Q &= -n\chi\nabla T. \end{aligned} \tag{1.8}$$

Here, the minor radius of the plasma a gives a measure of the distance that energy and particles have to cross before actually leaving the system.

Transport is often classified by considering its origin. The most obvious, but also the one that in fact contributes less to the experimentally measured fluxes, is collisional diffusion, leading to the so-called *classical* transport. Particles undergo collisions between each others and therefore diffuse across the magnetic field [10]. Collisions are equally probable in every direction, but because of the density being higher in the core plasma, one obtains a net outward flux. A simple random walk model can be used to describe this process. The particle diffusivity e.g. can be expressed as

$$D = \frac{\Delta x^2}{\Delta t}, \tag{1.9}$$

where Δx represents the typical step size and Δt the time step. For a diffusion across a straight magnetic field $\Delta x \sim \rho$, ρ being the Larmor radius, and $\Delta t \sim 1/\nu_c$, with ν_c the Coulomb collisional frequency. Under typical fusion relevant conditions (a magnetic field B of few T, a temperature $T \sim$10 keV and a density $n \sim 10^{20}$ m^{-3}) one finds D$_{\text{class}} \sim 10^{-3}$ m^2/s, which is in fact negligible compared to experimentally measured values of ~ 1 m^2/s. Note that the classical diffusion is equal for ion and electrons since the smaller electron step size, by a factor $\sqrt{m_e/m_i}$, is balanced by a collision frequency higher by a factor m_i/m_e. The energy diffusion can be computed in a similar way and again one finds a discrepancy with the experimental values of several orders of magnitude. The toroidal geometry of a tokamak causes, because of the particle drifts related to curvature and ∇B, modified collisionless particle trajectories, with excursion transverse to the magnetic field significantly larger than ρ and consequently larger associated heat and particle diffusivity. Transport induced by the toroidal geometry is known as *neoclassical*, and a comprehensive description can be found in e.g. Ref. [10]. One of the most important effects of toroidicity on particle trajectories is that particles can be trapped because of inhomogeneity of the magnetic field amplitude B. In the so-called circular large aspect ratio limit, the magnetic field of a tokamak can be expressed as

$$\mathbf{B} = \frac{B_0 R_0}{R}\left(\mathbf{e}_\varphi + \frac{r}{R_0 q_s}\mathbf{e}_\theta\right), \tag{1.10}$$

where $\mathbf{e}_\varphi$ and $\mathbf{e}_\theta$ are the unit vectors in the toroidal and poloidal direction, see also Figure 2.1, and $q_s \sim rB_0/R_0B_\theta$ (more details about the plasma equilibrium B_0 are provided in section 2.1). At zeroth order the poloidal field B_θ is small compared to the toroidial one $B \sim 1/R$, thus the magnetic field strength is weak on the outside of the torus and strong on the inside. Because of conservation of the kinetic energy $\mathcal{E} = mv^2/2$ and of the magnetic moment $\mu = mv_\perp^2/2B$, particles starting on the outside of the torus with a small $v_\parallel/v_\perp$ are mirror reflected as their parallel motion brings them towards the inside of the torus in the high field region. These particles are trapped on the outside of the torus. Particles with a sufficiently high $v_\parallel/v_\perp$ are instead free to move, they are the so-called passing particles. For a particle starting at the low field side, the trapped-passing boundary can be written as

$$\frac{v_\parallel^2}{v^2} < 1 - \frac{B_{\text{min}}}{B_{\text{max}}} = 1 - \frac{R_0 - r}{R_0 + r} \sim 2\frac{r}{R_0} \tag{1.11}$$

defining the so-called trapping-cone, shown in Figure 1.3. The angle θ_t is defined by $\cos(\theta_t) = v_\parallel/v \sim \sqrt{2r/R_0} \sim \sqrt{2\epsilon}$, where $\epsilon = r/R_0$ is the ratio between the minor radius r and major radius R_0 of the machine. The fraction of trapped particles for a Maxwellian distribution is given by

$$\alpha_t \sim \sqrt{2\epsilon}. \tag{1.12}$$

These particles bounce between their reflection points and the resulting motion projected

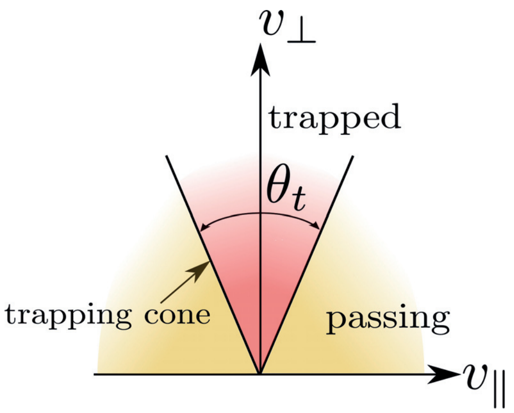
$v_\perp$
trapped
θ_t
trapping cone
passing
$v_\parallel$

Figure 1.3 : Velocity space showing the trapped-passing boundary and the resulting trapping cone.

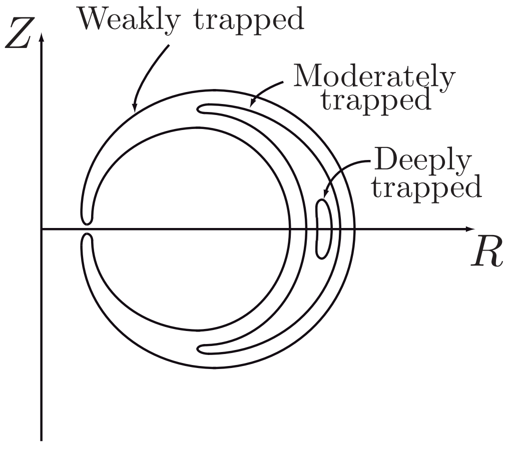
Z
Weakly trapped
Moderately trapped
Deeply trapped
R

Figure 1.4 : Banana orbits of trapped particles. Different values of $v_\parallel/v_\perp$ lead to different bounce angles corresponding to deeply trapped particles, moderately trapped particles, and barely trapped particles. From Ref. [5].

on a poloidal plane resembles the shape of a banana, see Figure 1.4, hence the name *banana* regime. The banana width r_b can be estimated considering the radial excursion due to drift velocities associated to magnetic field gradient and curvature:

$$r_b \sim \frac{B_\varphi}{B_\theta}\frac{|\Delta v_\parallel|}{\Omega} \sim \frac{q_s}{\epsilon}\frac{|v_\parallel|}{\omega} \sim \frac{q\rho}{\sqrt{\epsilon}}, \tag{1.13}$$

typically larger than the Larmor radius. The bounce frequency of trapped particles ω_b can then be estimated as

$$\omega_b \sim \frac{v_d}{r_b} \sim \frac{v_{\text{th}}}{q_s R_0} \sim \sqrt{\epsilon/2}v_{\text{th}}/(qR_0) \tag{1.14}$$

where v_d is the total drift velocity, which in a typical tokamak configuration satisfies the ordering $v_d/v_{\text{th}} \sim \rho/R_0 \ll 1$. Hence, collisional detrapping leads to larger step size than the classical one. Moreover, the effective collisional frequency is also enhanced by $1/\epsilon$ because the scattering angle required in velocity space to go from one trapped trajectory to another is within the trapping cone $\Delta\theta_t$. The diffusion in the so-called banana regime, i.e. $\omega_b \gg \nu_c$ (one often defines this regime introducing an effective collisionality $\nu^* = (\nu_c/\epsilon)/\omega_b \lesssim 1$), can thus be expressed as

$$D_{\text{neo}} = \alpha_t \frac{\nu_c}{\epsilon} w_b^2. \tag{1.15}$$

In practice D_{neo} can be up to two orders of magnitude larger than the corresponding classical estimate, setting a lower limit of transport for any toroidal machine. We also recall that when collisionality increases, collisional detrapping happens, on average, before a banana orbit is completed, thus reducing the effective radial step. This is the so called plateau regime, where transport does not depend on collisionality. At even higher collisionality one finally enters the so-called Pfirsch-Schlüter regime [10] where diffusivity is again proportional to ν_c.

Even though toroidal geometry can increase by two orders of magnitude the transport estimated by classical collisional estimates, the experimentally measured diffusivities are still usually larger by one or two orders of magnitude and one refers to this additional plasma transport as being *anomalous.* Nowadays, it is widely accepted that anomalous transport is due to plasma turbulence, in turn caused by instabilities that develop on microscopic scale lengths, known as microinstabilites. An intuitive description of the mechanism at place is as follows. In order to meet the conditions necessary to reach fusion, the plasma is in a statistically steady state very far from a thermodynamic equilibrium. In particular, an extreme pressure gradient, ∼ 1 atm in the core, vacuum at the edge, is built radially across the plasma, providing a source of free energy which in particular destabilizes small-scale plasma waves, i.e. with characteristic wavelengths perpendicular to the magnetic field of the order of the ion and electron Larmor radius. These instabilities involve density and temperature fluctuations, δn and δT respectively, as well as electrostatic or electromagnetic fluctuations, $\delta\phi$ and δA. As a result of nonlinear coupling, these instabilities drive a low amplitude turbulent state, $\delta n/n \sim \delta T/T \sim e\phi/T \sim 1\%$. The fluctuating electromagnetic fields lead to additional radial drifts. When the fluctuations of e.g. density are in phase with these drifts, then a net flux of particles Γ_{turb} can develop. In a similar way, pressure perturbations lead to a net flux of energy Q_{turb} across the plasma. Even though microturbulent fluctuations are very small in amplitude, typically 10^{-3} in the core of large devices, the associated transport fluxes can be sufficiently large to explain experimental measurements. Typically one relates these fluxes to the gradients via turbulent diffusivities:

$$Q_{\text{turb}} = -n\chi_{\text{turb}}\nabla T \qquad \Gamma_{\text{turb}} = -D_{\text{turb}}\nabla n \tag{1.16}$$

where a simple local relation has been assumed. More generally, it should be remembered that turbulent fluxes can exhibit a non-local nature. Furthermore, when relating fluxes to gradients, off-diagonal terms can play a significant role, e.g. density gradients driving heat fluxes, as well as non-diffusive pinch terms.

1.4 Scope and outline of the thesis

The main goal of this thesis is to study turbulent transport in conditions relevant to the Tokamak à Configuration Variable (TCV), which is located at the Swiss Plasma Center. In the last two decades microinstabilities and the associated turbulence have been actively studied with the help of numerical simulations, carried out in the framework of the so-called gyrokinetic theory. This model allows to average the trajectory of particles over their fast gyromotion around magnetic field lines, thus reducing the phase space from six to five dimensions. A variety of codes have been developed to tackle this subject, and different numerical methods have been used to carry out simulations [11]. In the Eulerian, or grid-based, description, the gyrokinetic equation is first discretized on a fixed grid in phase space, obtaining a system of ordinary differential equations, which are then numerically solved. The Particle In Cell (PIC) method instead uses a Lagrangian description of the plasma. A statistical sampling of markers in phase space is performed and particle trajectories are followed. A third approach, the so-called semi-Lagrangian, can be seen as a combination of grid-based and PIC methods. At each time step, the distribution function is discretized in phase space, however the update of the distribution function is obtained integrating particle trajectories. Each of the aforementioned methods have advantages and disadvantages. For instance, the Eulerian method is usually computationally more demanding than the PIC method, however it does not suffer from numerical noise arising from the statistical sampling.

In this work we shall make use of the Eulerian gyrokinetic code GENE [12], in both its local and global versions. The local approach, based on a complete separation between the spatial scales of turbulent and background equilibrium profiles, allows one to reduce the simulated physical volume to a narrow tube aligned with the magnetic field. While this approach leads to a strong reduction of the computational effort, it might not be adequate for small size machines like TCV, where the scale separation assumption is not clearly satisfied. In this case a global approach, where the radial variation of equilibrium quantities like temperature and density profiles, as well as of the magnetic geometry, are retained, might be necessary.

TCV is a so-called medium-size tokamak, a device whose minor and major radius are respectively 30 cm and 0.88 m, with a confining magnetic field of 1.4 T and plasma current up to 1.2 MA. An essential feature of this machine is the high flexibility of the magnetic coils system, which allows one to create plasmas with very different shapes. In particular it has been experimentally shown [13] that negative triangularity δ of the Last Closed Flux Surface (LCFS) has a strong beneficial effect on the electron energy confinement in L-mode discharges, which, in spite of the finite radial penetration depth of δ, is increased by approximately a factor of two at all radial locations when changing the sign of δ_{LCFS} from positive to negative. The origin of this improvement remains not completely understood, and numerical simulations are a suited tool for such an investigation, the gyrokinetic theory providing the ideal framework for studying microturbulence.

Other relevant observations made in TCV are related to the Geodesic Acoustic Mode, which may play an important role in saturating turbulence, thus helping lowering transport. This mode is experimentally observed as “eigenmode”, that is a global radially coherent oscillation of e.g. plasma electron density over a significant fraction of the minor radius, while analytic theory predicts a scaling of the mode frequency with the local temperature. Only in specific conditions this latter condition of a “dispersive” mode is experimentally observed.

This work is structured as follows. In chapter 2, the theoretical background is described. The plasma magnetic equilibrium is presented, and the key elements of the derivation of the gyrokinetic equations and associated electromagnetic fields are given. The so-called local and global approaches are introduced, as well as further simplifications that can be made under specific conditions to reduce the computational effort. A phenomenological description of the microinstabilities mostly relevant in the case of interest for us is provided.

The numerical implementation of the gyrokinetic equations in GENE is presented in chapter 3, where specific local and global code features are discussed.

Chapter 4 is dedicated to a series of local and global benchmarks that have been carried out in order to validate the interface of GENE with the MHD equilibrium solver CHEASE, in view of carrying out simulations that consider the realistic magnetic geometry of TCV.

An investigation of profile stiffness, addressing its dependence on shaping which can potentially explain the observed confinement improvement, is carried out with the local version of the code in Chapter 5. It will be shown that, even if the most complete model is used, local simulations appear inadequate to reproduce TCV transport level and global effects should be retained.

Chapter 6 is thus devoted to global simulations of TCV. For the original parameter set, simulations are unable to reproduce the observed heat transport, a discrepancy that is understood as a consequence of the too large error bars in the measured density and temperature profiles. The analysis of another experimentally better diagnosed discharge, still addressing the effect of negative triangularity, has been initiated and, in this case, simulations indeed show a much better agreement with measurements.

In Chapter 7, GAM dynamics are studied in TCV relevant conditions with both local and global simulations, aiming at reproducing the experimental trends, and partly addressing the coherent-dispersive regime transition.

Finally, conclusions are drawn in chapter 8.

Appendices are present at the end of the thesis. Appendices A and B contain a brief description of the GKW and GS2 codes, providing the necessary information for carrying out the local benchmarks of chapter 4. Appendix C describes the implementation, in form of a post processing tool of GENE simulations, of synthetic diagnostics for the Phase Contrast Imaging and correlation-ECE currently installed on TCV, and, finally, Appendix D provides more details about local simulations carried out in chapter 7.

2 Theoretical background

The aim of this chapter is to provide a brief description of the theoretical framework and of the basic equations used in order to describe microturbulence in a confined plasma.

2.1 Tokamak plasma equilibrium

The background magnetic field $\mathbf{B}_0$ that appears within the gyrokinetic description, is the magnetic field which confines the plasma. A tokamak is in principle a perfectly axisymmetric device. Deviations from this abstract model can arise because of non-ideal coil systems, externally induced magnetic perturbations or internal perturbations (see e.g. helical cores), which will however be both neglected throughout this work.
The equilibrium state of the plasma can be characterized using a fluid model. In particular, it can be described by the time independent ideal MHD equations:

$$\mathbf{j} \times \mathbf{B}_0 = \nabla p, \tag{2.1}$$

$$\nabla \times \mathbf{B}_0 = \mu_0 \mathbf{j}, \tag{2.2}$$

$$\nabla \cdot \mathbf{B}_0 = 0. \tag{2.3}$$

Here $\mathbf{j}$ is the current density and p the total plasma pressure. Equation (2.1) simply expresses the force balance between the magnetic and plasma pressure at equilibrium. Background flows have been neglected.

Assuming a cylindrical coordinate system (R, Z, φ), as the one depicted in Figure 2.1, all background quantities are independent from φ in case of a tokamak. The most general form of a divergence-free magnetic field satisfying this condition can be written as

$$\mathbf{B}_0 = F(\psi)\nabla\varphi + \nabla\varphi \times \nabla\psi. \tag{2.4}$$

The magnetic field has been decomposed into the toroidal $\mathbf{B}_\varphi = F(\psi)\nabla\varphi$ and poloidal

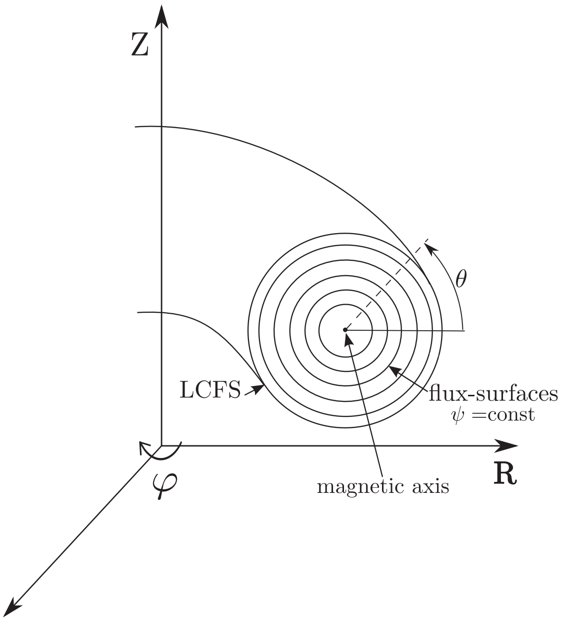

Figure 2.1 : Cylindrical coordinate system (R, Z, φ) as employed in GENE. Indicated are also the location of the magnetic axis, the flux surfaces (ψ=const) and the Last Closed Flux Surface (LCFS), separating the confined plasma from the Scrape Off Layer.

$\mathbf{B}_\theta = \nabla\varphi \times \nabla\psi$ components, with φ the poloidal flux function defined as the poloidal flux through a ribbon between the magnetic axis and a given radial location [14]:

$$\psi(R, Z) = \frac{1}{2\pi}\int_S \mathbf{B}_0 \cdot d\mathbf{S} = \frac{1}{2\pi}\int_S \mathbf{B}_\theta \cdot d\mathbf{S}. \tag{2.5}$$

From Equation (2.4) one immediately sees that $\mathbf{B} \cdot \nabla\psi = 0$, implying that magnetic field lines lie on ψ =const surfaces. Furthermore, from (2.1) one has $\mathbf{B} \cdot \nabla p$=0 and $\mathbf{j} \cdot \nabla p$=0. Hence, $\mathbf{B}$ and $\mathbf{j}$ are tangent to p=const surfaces. These surfaces can be uniquely labelled by ψ and are the so-called *flux-surfaces*. The plasma pressure is thus a flux-surface quantity, $p = p(\psi)$. The magnetic axis is defined as the center of these nested flux surfaces, i.e. where the magnetic surface reduces to a toroidal magnetic field line ($\psi = 0$). The last of these nested surfaces is known as the Last Closed Flux surface (LCFS), setting a boundary between the confined plasma and the so called Scrape-Off Layer.

Combining Eqs. (2.4) with the force balance, Equation (2.1) and Ampére's law (2.2), one obtains the following relation:

$$-R^2\nabla\left(\frac{1}{R^2}\nabla\psi\right) = \mu_0 R^2 p' + FF', \tag{2.6}$$

with

$$p' = \frac{\mathrm{dp}}{\mathrm{d}\psi}, \qquad F' = \frac{\mathrm{dF}}{\mathrm{d}\psi}. \tag{2.7}$$

Equation (2.6) is known as the Grad-Shafranov equation [15], describing the magnetic equilibrium of a confined plasma provided a pressure gradient $p'(\psi)$ and a current $F(\psi)$ profiles.
One of the essential features of a tokamak is the fact that magnetic lines must be twisted around the torus in order to achieve stability [3]. This twisting, related to the strength of the poloidal field compared to the toroidal one, is measured by the safety factor q:

$$q(\psi) = \frac{1}{2\pi} \oint_0^{2\pi} \left.\frac{\mathrm{d}\varphi}{\mathrm{d}\theta}\right|_{\text{along B}_0} \mathrm{d}\theta = \frac{1}{2\pi} \oint_0^{2\pi} \frac{\mathbf{B}_0 \cdot \nabla\varphi}{\mathbf{B}_0 \cdot \nabla\theta} \mathrm{d}\theta. \tag{2.8}$$

where θ is the geometrical poloidal angle. Physically, the safety factor is associated to the number of toroidal turns required in order to cover one poloidal turn along a magnetic field line lying on a given ψ=const flux surface.

Experimentally, the shape of the flux-surfaces can be varied and, besides being relevant for plasma stability with respect to MHD modes, this is in fact one of the potential ways to possibly reduce turbulent transport. Additional magnetic coils are normally installed on a Tokamak so as to provide the freedom to vary the shape of the plasma. In practice, one aims at a given shape of the LCFS and then adapts the external magnetic fields such as to maintain the desired geometry.

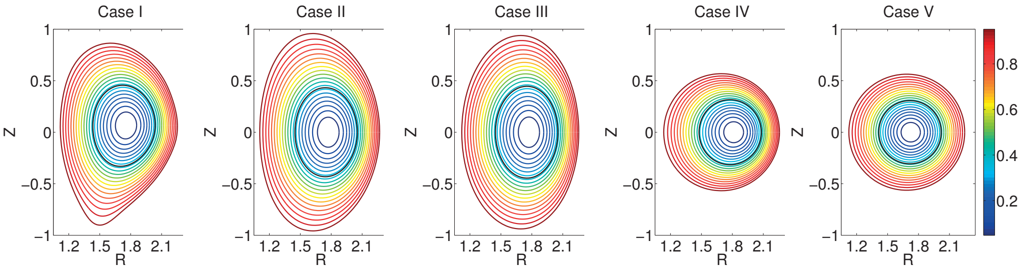

Figure 2.2 : Different MHD equilibria, labelled as Cases I to V, characterized by different degrees of shaping complexity. Shown are constant contours of the poloidal magnetic flux function ψ/ψ(LCFS). The contour of the flux surface at $r/a = 0.5$ is depicted in black.

As an illustrative example, in Figure 2.2 we show five different plasma geometries corresponding to different degrees of shaping complexity. They are labelled as Case I to V, and will be used for the benchmarks presented in Chapter 4, where a detailed description of these equilibria will also be provided. It suffices to note that Case I is in fact very close to an actual experimental plasma (it is inspired by a real DIII-D discharge [16]), while all the other equilibria have been obtained by artificially modifying the LCFS. A typical approach for describing a given flux-surface is by taking its poloidal Fourier decomposition. In this case one can write the (R, Z) contour of a given flux-surface (labelled by its minor radius r) as

$$\begin{aligned}
R(\theta) &= R_0 + r\cos(\theta) - \Delta(r) + \sum_{m=2} S_m(r)\cos\left[(m-1)\theta\right] + P(r)\cos(\theta) \\
Z(\theta) &= r\sin\theta - \sum_{m=2} S_m(r)\sin\left[(m-1)\theta\right] - P(r)\sin(\theta),
\end{aligned} \tag{2.9}$$

where R_0 indicates the location of the magnetic axis (assuming for simplicity that its elevation is Z=0), while Δ indicates the so-called Shafranov shift, related to the compression of magnetic surfaces at the outboard midplane induced by toroidicity. Finally, $P(r)$ is a higher order correction term. With this parametrization, one can express the magnetic field amplitude as [17]

$$B = B_0 \left\{ \frac{F}{R_0 B_0} - \epsilon\cos(\theta) + \epsilon^2\left(\cos^2(\theta) + \frac{1}{2q^2}\right) + \frac{\Delta}{R_0} - \sum_{m=2} \frac{S_m}{R_0}\cos\left[(m-1)\theta\right] \right\}, \tag{2.10}$$

with $F = R_0 B_0 + \mathcal{O}(\epsilon^2)$ and $\epsilon = r/R_0$ the inverse aspect ratio. The coefficients S_m provide a measure of the shaping of the actual flux-surface, see Figure 2.3.

In particular, S_2 is associated to the elongation κ, S_3 to the triangularity δ,

$$\kappa(r) = \frac{r - S_2}{r + S_2} \qquad \text{and} \qquad \delta(r) = \frac{4S_3}{r},$$

and so on for higher order terms. Each of these coefficients can be evaluated by introducing Eq. (2.9) in the Grad-Shafranov equation and decomposing into Fourier modes $\cos(m\theta)$. Neglecting higher order corrections, one gets (see Ref. [18] for details)

$$r^2 S_m'' + (3 - 2s(r))rS_m' + (1 - m^2)S_m = 0 \tag{2.11}$$

which, under the assumption of flat q profile can be solved as

$$S_m(r) = S_m(a)\left(\frac{r}{a}\right)^{m-1}, \tag{2.12}$$

leading for elongation and triangularity

$$\kappa(r) = \kappa_{\mathrm{LCFS}} \qquad \text{and} \qquad \delta(r) = \delta_{\mathrm{LCFS}}\frac{r}{a},$$

already illustrating how different shaping parameters have a different penetration depths. The penetration of the shaping into the core is also affected by the magnetic shear $s(r)$, whose increase decreases the penetration in the core and vice versa.

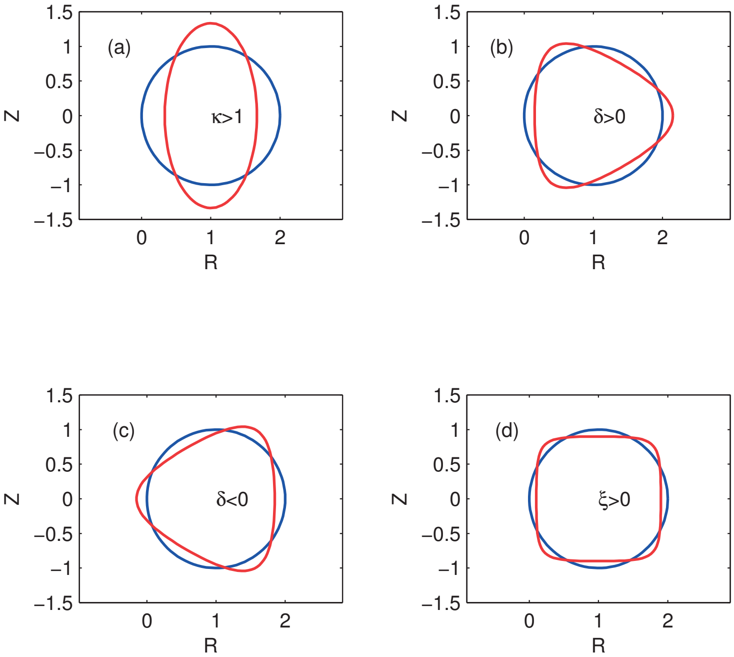

Figure 2.3 : Examples of shaped flux surfaces. The actual contours shown in red are obtained from the parametrization (2.10) starting from a circular flux surface (depicted in blue) and adding (*a*) elongation κ which is corresponding to S_2, (*b*) positive triangularity δ associated to S_3, (*c*) negative δ and (*d*) finite squareness ξ associated to S_4.

2.2 Kinetic plasma modeling and Vlasov-Maxwell system

In a kinetic description, each plasma species j is characterized by a distribution function $f_j(\mathbf{x}, \mathbf{v}, t)$ which depends on position $\mathbf{x}$, velocity $\mathbf{v}$ and time t. Estimating $f_j(\mathbf{x}, \mathbf{v}, t)\mathrm{d}^3\mathbf{x}\mathrm{d}^3\mathbf{v}$ provides the number of particle which are located in the infinitesimal six dimensional phase space volume $\mathrm{d}^3\mathbf{x}\mathrm{d}^3\mathbf{v}$ around the position $(\mathbf{x}, \mathbf{v})$ at time t. The time evolution of f_j is governed by the following equation:

$$\frac{\mathrm{d}}{\mathrm{d}t} f_j(\mathbf{x}, \mathbf{v}, t) = \left[\frac{\partial}{\partial t} + \mathbf{v}\frac{\partial}{\partial \mathbf{x}} + \frac{q_j}{m_j}\left(\mathbf{E}(\mathbf{x}, t) + \mathbf{v} \times \mathbf{B}(\mathbf{x}, t)\right)\frac{\partial}{\partial \mathbf{v}}\right] f_j(\mathbf{x}, \mathbf{v}, t) = \mathcal{C}\left[f_j(\mathbf{x}, \mathbf{v}, t)\right], \tag{2.13}$$

where q_j and m_j are respectively the charge and the mass of species j, $\mathbf{E}(\mathbf{x}, t)$ and $\mathbf{B}(\mathbf{x}, t)$ the electromagnetic fields and $\mathcal{C}$ is an operator used to model the effect of binary collisions. The operator $\mathrm{d}/\mathrm{d}t$ appearing in (2.13) represents the total time derivative along unperturbed trajectories in phase space. For high temperature plasmas, as is the case for the core conditions of most fusion plasmas, the collision frequency is very small compared

to the characteristics time scales of many phenomena of interest, e.g. microturbulence in our case, and collisions can therefore be neglected in first approximation. In this case Eq. 2.13 reduces to $\mathrm{d}f_j/\mathrm{d}t = 0$, and is normally referred to as the Vlasov equation. It simply states that the distribution function is constant along particle trajectories in phase space.
The electromagnetic fields $\mathbf{E}(\mathbf{x}, t)$ and $\mathbf{B}(\mathbf{x}, t)$ appearing in Eq. (2.13) obey Maxwell's equations:

$$\begin{aligned} &\nabla \cdot \mathbf{E} = \frac{1}{\epsilon_0} \sum_j \rho_j, \qquad && \nabla \times \mathbf{E} = -\frac{\partial \mathbf{B}}{\partial t} \\ &\nabla \cdot \mathbf{B} = 0, && \nabla \times \mathbf{B} = \mu_0 \left(\sum_j \mathbf{j}_j + \epsilon_0 \frac{\partial \mathbf{E}}{\partial t} \right) \end{aligned} \tag{2.14}$$

where the source terms, the charge density ρ_j and the current charge density $\mathbf{j}_j$, are evaluated as respectively zeroth and first velocity moments of the distribution function f_j:

$$\rho_j = q_j \int f_j \mathrm{d}^3\mathbf{v}, \qquad \mathbf{j}_j = q_j \int f_j \mathbf{v} \mathrm{d}^3\mathbf{v}. \tag{2.15}$$

A self-consistent description of the plasma evolution requires therefore to solve Equations (2.13) and (2.14), which form the so called Vlasov-Maxwell system. This system of nonlinear integro-differential equations formulated in 6-dimensional phase space cannot be solved analytically except in few simplified and idealized situations. For a typical tokamak, the complete solution to this system of equations would in principle account for plasma dynamics involving different spatial and temporal scales varying by several orders of magnitude: from the machine size down to the electron Larmor radius and Debye length ($\sim$ 5 orders of magnitude) and from confinement time sales to the cyclotron frequency of electrons ($\sim$ 11 orders of magnitude). Even for today's supercomputers this problem remains out of practical reach and it is therefore necessary to introduce a set of approximations so as to retain only the spatial and temporal scales relevant for microturbulence and associated transport. Gyrokinetic theory provides the analytic framework to systematically derive a set of approximate equations that allow one to reach this goal. The main ideas and the steps required to obtained the *gyrokinetic* Vlasov-Maxwell system, constituting the theoretical basis of this work, will be presented in the next section.

2.3 The gyrokinetic model: the basic idea and corresponding ordering

Several approximations are systematically carried out to derive the gyrokinetic Vlasov-Maxwell system, based on the so-called gyrokinetic ordering. These approximations are not mere mathematical expansions, but reflect experimentally measured properties of microturbulence in the core of magnetically confined plasmas [19–21]. In particular, in the core of a Tokamak the microinstabilities are drift-wave type instabilities [22] characterized by the following:

- **Small amplitude**
  The relative amplitude of any fluctuating quantity e.g. density and temperature, in the core of a confined plasma is very small compared to the background equilibrium, typically only a few percent. This relative amplitude typically increases moving towards the LCFS, up to several tens of percent in the SOL. Introducing a dimensionless expansion parameter ϵ_δ, the aforementioned ordering can be formally expressed as:

  $$\frac{\delta f}{f} \sim \frac{q\delta\phi}{T_e} \sim q\frac{v_\parallel \delta A_\parallel}{T_e} \sim \frac{\delta B_\parallel}{B} \sim \epsilon_\delta \tag{2.16}$$

  where all perturbation quantities have been indicated with a δ. Note that the index j of species dependent quantities has been dropped to lighten notations. Here $\phi(\mathbf{x}, t)$ and $\mathbf{A}(\mathbf{x}, t)$ are the scalar and vector potentials used to describe the electromagnetic fields, $\mathbf{E} = -\nabla\phi - \partial\mathbf{A}/\partial t$ and $\mathbf{B} = \nabla \times \mathbf{A}$. Finally, from hereon parallel and perpendicular directions are to be evaluated with respect to the stationary background magnetic field $\mathbf{B}_0(\mathbf{x}, t)$.

- **High anisotropy**
  The parallel wavelength is much larger than the one perpendicular to the magnetic field. Typical correlations lengths are of the order of a few gyroradii in the perpendicular direction, $k_\perp \rho_l \sim 1$ ($k_\perp \rho_i \sim 1$ characterizes fluctuations developing on the ion scale, while $k_\perp \rho_e \sim 1$ fluctuations on the electron one). Much longer distances, of the order of a connection length ($\sim 2\pi R_0 q$) which can be up to several meters, characterize instead the parallel direction. This observation results from the fact that the motion of particle is much faster along a magnetic field line than across it, and can be expressed as

  $$\frac{|k_\parallel|}{|k_\perp|} \sim \epsilon_\parallel \qquad \text{and} \qquad k_\perp \rho_l \sim 1. \tag{2.17}$$

- **Typical frequencies much smaller than the gyrofrequency**
  The frequency spectrum of microturbulence is typically broadband with a mean frequency of the same order as the diamagnetic drift frequency $\omega_D = \mathbf{k} \cdot \mathbf{v}_D$ for a given wave vector $\mathbf{k}$ and drift velocity $|\mathbf{v}_D| \simeq (T/qB)|\nabla_\perp \ln P|$, P being the pressure of a given species. The diamagnetic frequency of both ion and electron scale fluctuations, respectively $\omega_D \sim v_{th,i}/L_c$ and $\omega_D \sim v_{th,e}/L_c$ with $1/L_c = \mathrm{d}\log\mathrm{n}/\mathrm{dx}, \mathrm{d}\log\mathrm{T}/\mathrm{dx}$, is much smaller than the corresponding cyclotron

frequencies $\Omega_{i,e}$:

$$|\omega| \ll |\Omega|. \tag{2.18}$$

Furthermore, one assumes also that equilibrium quantities are stationary in time and slowly varying in space:

$$\rho_i \frac{\nabla f_0}{f_0} \sim \rho_i \frac{\nabla B_0}{B_0} \sim \epsilon_B. \tag{2.19}$$

All the previously listed properties of microturbulence allow one to systematically carry out a gyroaveraging procedure thanks to which the information about the fast gyration is averaged out while keeping the slower timescales of turbulence dynamics. The original Vlasov-Maxwell problem formulated in six-dimensional phase phase space is thus approximated by a set of equations in a reduced five-dimensional phase space (three space and two velocity dimensions). In this description only the information about the average motion of the gyrocenter of each particle is retained. These trajectories result from the gyro-averaged stationary and fluctuating electromagnetic fields, and as $k_\perp \rho_l \sim 1$, finite Larmor radius effects are kept for the gyroaveraged fluctuating fields. This is equivalent to replacing the full particle motion with the dynamics of charged rings along field lines subjected to perpendicular drifts.

2.4 Modern derivation of the collisionless gyrokinetic equation

Even if it appears intuitive to consider the gyrokinetic description as basic equations of motion for particles resulting from an averaging procedure over the gyroangle, in order to correctly derive the corresponding equations, ensuring also conservation properties, a sophisticated mathematical approach must be followed. The original derivation of the non-linear gyrokinetic equation by Frieman and Chen [23] was obtained as an ordering expansion in the small parameter ϵ ($\epsilon_\delta \sim \epsilon_B \sim \epsilon_{||} \sim \epsilon$). Modern gyrokinetic theory instead is based on variational methods, where Lie transforms are used to introduce appropriate phase-space coordinate transformations such as to explicitly remove the dependence on the gyroangle, which thus remains a cyclic variable. The first application of Lie transforms to guiding center is due to Littlejohn [24]. The approach was then extended to electrostatic and electromagnetic fluctuations, and to nonlinear gyrokinetic equations. In the following, the main steps required to derive the collisionless gyrokinetic equations will be presented. For a detailed and comprehensive description of modern nonlinear gyrokinetic theory we refer the reader to the review by Brizard and Hahm [25]. How the effect of collisions is modeled in practice will be briefly discussed in section 2.5.

For an Hamiltonian system, the equations of motion can be derived minimizing the action given by the time integral of its Lagrangian $\mathcal{L}$ along particles trajectories, according to the following variational principle:

$$\delta \int \mathcal{L} \mathrm{d}t = 0. \tag{2.20}$$

The Lagrangian $\mathcal{L}(z, \dot{z}, t)$ is the so-called phase space Lagrangian, which is obtained from the Lagrangian $L(\mathbf{p}, \mathbf{q}, t) = \mathbf{p} \cdot \dot{\mathbf{q}} - \mathrm{H}(\mathbf{p}, \mathbf{q}, \mathrm{t})$, expressed in canonical coordinates $(\mathbf{p}, \mathbf{q})$, H being the Hamiltonian of the system, with an arbitrary change of variables $\mathbf{z} = \mathbf{z}(\mathbf{p}, \mathbf{q})$. The advantage of using the variational principle given by Eq. 2.20 is that it is valid for any choice of phase space coordinates, including non-canonical variables.

It proves convenient to use a one-form formulation:

$$\gamma = \gamma_\mu dz^\mu = \mathcal{L} dt, \tag{2.21}$$

with $z^\mu = \{z^i, t\}$, where $i = 1, 2, 3$ spans the spatial and $i = 4, 5, 6$ the velocity directions. Here the Einstein summation rule over repeated indexes is assumed.

A description of differential k-forms and their properties is clearly outside the scope of this work and can be found elsewhere, see *e.g.,* Ref. [25]. Here it suffices to remember that k-forms are fundamental objects defined on an n-dimensional space with coordinates $\mathbf{z} = \{z^1, \ldots, z^n\}$ of the form

$$\gamma_k = \frac{1}{k!} \gamma_{i_1 \ldots i_k} \mathrm{d}z^{i_1} \wedge \cdots \wedge \mathrm{d}z^{i_k}. \tag{2.22}$$

One defines in particular the external derivative d of a k-form, which is a $(k + 1)$-form, as

$$\mathrm{d}F \equiv \partial_\mu F \mathrm{dz}^\mu \tag{2.23}$$

for zero-forms (scalars), and as

$$\mathrm{d}\gamma \equiv \mathrm{d}\gamma_\mu \wedge \mathrm{d}z^\nu \tag{2.24}$$

for one-forms. One introduces also an inner product between a vector $\mathbf{v}$ and a $k-$form, which results in a $(k - 1)$-form. It is defined as

$$\mathbf{v} \cdot \gamma \equiv v^\mu \gamma_\mu \tag{2.25}$$

for one-forms and as

$$\mathbf{v} \cdot \gamma \equiv v^\mu \gamma_{\mu\nu} \mathrm{d}z^\nu. \tag{2.26}$$

for two-forms.

Making use of the one-form formulation, the variational principle of Eq. (2.20) leads to the generalized Euler-Lagrange equations of motion [26]:

$$\omega_{\mu\nu}\frac{dz^\nu}{dt} = 0 \tag{2.27}$$

where

$$\omega_{\mu\nu} = \frac{\partial\gamma_\nu}{\partial z^\mu} - \frac{\partial\gamma_\mu}{\partial z^\nu} \tag{2.28}$$

is the so-called Lagrange tensor. For the following, it is also useful to remember that a one-form γ in z can be expressed as Γ in a new coordinate system Z according to:

$$\gamma_\mu dz^\mu = \gamma_\mu \frac{\partial z^\mu}{\partial Z^\mu}\mathrm{d}Z^\mu = \Gamma_\mu \mathrm{d}Z^\mu \tag{2.29}$$

and that the equations of motion are invariant with respect to a phase space gauge transformation of the one form $\gamma \to \gamma + dS$, where $\mathrm{d}S$ is the exact differential of a scalar function $S(z^\mu)$, referred to as the phase space gauge function.
For the case of interest to us, one starts considering the motion of charged particles in given electromagnetic fields. In this case the Lagrangian and Hamiltonian, expressed using the non-canonical coordinates $(\mathbf{x}, \mathbf{v})$, assume the following well known expressions:

$$\mathcal{L}(\mathbf{x}, \mathbf{v}) = (m\mathbf{v} + q\mathbf{A}(\mathbf{x})) \cdot \mathbf{v} - \mathcal{H}(\mathbf{x}, \mathbf{v}), \tag{2.30}$$

$$\mathcal{H}(\mathbf{x}, \mathbf{v}) = \frac{1}{2}mv^2 + q\phi(\mathbf{x}). \tag{2.31}$$

The scalar and vector potential, ϕ and $\mathbf{A}$ respectively, are associated to the electric and magnetic fields:

$$\mathbf{E} = -\nabla\phi - \frac{\partial\mathbf{A}}{\partial t} \quad \text{and} \quad \mathbf{B} = \nabla \times \mathbf{A}. \tag{2.32}$$

The corresponding one-form therefore reads

$$\gamma = (m\mathbf{v} + q\mathbf{A}) \cdot \mathrm{d}\mathbf{x} - \left(\frac{1}{2}mv^2 + q\phi\right)\mathrm{d}t. \tag{2.33}$$

The derivation of the gyrokinetic equation proceeds then in three steps. First a transformation is applied to Eq. 2.33 such as to derive the one-form for guiding center motion in a stationary magnetic field $\mathbf{B}_0 = \nabla \times \mathbf{A}_0$. Then, field perturbations characterized by $\delta\phi$ and $\delta\mathbf{A}_0$ are allowed (as necessary in order to model turbulent fluctuations) obtaining a new set of equations which describe the particle motion in these fluctuating fields retaining the effect of the gyromotion but without explicitly depending on the gyroangle. Finally, from the gyrocenter distribution one can evaluate the moments required for estimating sources to Maxwell's equation, thus allowing to consistently compute the electromagnetic fields and obtain the gyrokinetic Vlasov-Maxwell system.

2.4.1 The unperturbed guiding center equations

The guiding center transformation involves an expansion in the small parameters $\epsilon_B \sim \rho/L_B$ in order to remove the fast gyroscale associated with the time-independent background magnetic field $\mathbf{B}_0 = \nabla \times \mathbf{A_0}$. For the sake of simplicity, we will neglect in the following derivation any background electric field which is associated to plasma rotation. In this case the single particle one-form reads:

$$\gamma_0(\mathbf{x}, \mathbf{v}) = (m\mathbf{v} + q\mathbf{A}_0) \cdot \mathrm{d}\mathbf{x} - \frac{1}{2}mv^2 \mathrm{d}t. \tag{2.34}$$

One aims at rewriting Eq. (2.34) using a new set of coordinates $(\mathbf{X}_{\mathrm{GC}}, v_{\|,\mathrm{GC}}, \mu_{\mathrm{GC}}, \alpha_{\mathrm{GC}})$, the so-called guiding center coordinates (GC), such that thanks to a proper choice of the gauge function S one can then explicitly eliminate the dependency on the gyroangle α at all orders from the resulting one form.

Here $\mathbf{X}_{\mathrm{GC}}$ is the position of the guiding center around which particles gyrate, $v_{\|\mathrm{GC}}$ the component of velocity parallel to the magnetic field and $\mu_{\mathrm{GC}} = mv^2_{\perp\mathrm{GC}}/(2B_0)$ the magnetic moment. Having assumed that the background electromagnetic fields vary on a much larger scale than the gyroradius, the gyromotion can be approximately considered circular.

In order to describe particle motion it is thus convenient to use a local Cartesian coordinate system $(\mathbf{e_1}, \mathbf{e_2}, \mathbf{b})$ at each point $\mathbf{x}$ of coordinate space, where $\mathbf{b} = \mathbf{B}_0/B_0$ points in the direction of the magnetic field and $(\mathbf{e_1}, \mathbf{e_2})$ are two orthogonal unit vectors in the perpendicular plane, see Figure 2.4.

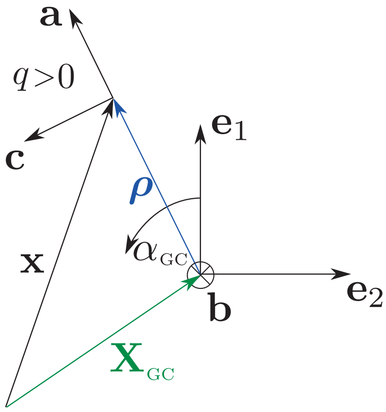

Figure 2.4 : Local Cartesian coordinate system $(\mathbf{e_1}, \mathbf{e_2}, \mathbf{b})$ used to described the gyromotion of a positively charged particle at the position $\mathbf{x}$. The position of the guiding center $\mathbf{X}_{\mathrm{GC}}$ is indicated in green and the Larmor radius $\boldsymbol{\rho}$ in blue.

Defining the radial and tangential directions

$$\mathbf{a}(\alpha_{\mathrm{GC}}) = \mathbf{e_1}\cos(\alpha_{\mathrm{GC}}) - \mathbf{e_2}\sin(\alpha_{\mathrm{GC}}), \tag{2.35}$$

$$\mathbf{c}(\alpha_{\mathrm{GC}}) = -\mathbf{e_1}\sin(\alpha_{\mathrm{GC}}) - \mathbf{e_2}\cos(\alpha_{\mathrm{GC}}), \tag{2.36}$$

the particle coordinates $(\mathbf{x}, \mathbf{v})$ can be expressed as function of the guiding center coordinates according to

$$\mathbf{x} = \mathbf{X}_{\mathrm{GC}} + \rho(\mathbf{X}_{\mathrm{GC}}, \mu_{\mathrm{GC}})\mathbf{a}(\alpha_{\mathrm{GC}}), \tag{2.37}$$

$$\mathbf{v} = v_{\|\mathrm{GC}}\mathbf{b} + v_{\perp\mathrm{GC}}(\mathbf{X}_{\mathrm{GC}}, \mu_{\mathrm{GC}})\mathbf{c}(\alpha_{\mathrm{GC}}). \tag{2.38}$$

The original unperturbed one-form given in Eq. 2.34 can then be transformed in a straightforward way according to the rule given by Eq. (2.29). Expanding the background magnetic field in the small parameter ϵ_B,

$$\mathbf{A}_0(\mathbf{x}) = \mathbf{A}_0(\mathbf{X}_{\mathrm{GC}}) + \rho\mathbf{a}(\alpha_{\mathrm{GC}}) \cdot \nabla\mathbf{A}_0(\mathbf{X}_{\mathrm{GC}}) + \mathcal{O}(\epsilon_B^2), \tag{2.39}$$

one obtains at first order in ϵ_B:

$$\begin{aligned}\Gamma_0^{\mathrm{GC}} = \Big(&mv_{\|\mathrm{GC}}\mathbf{b} + mv_{\perp\mathrm{GC}}\mathbf{c}(\alpha_{\mathrm{GC}}) + q\mathbf{A}_0(\mathbf{X}_{\mathrm{GC}}) + \rho\mathbf{a}(\alpha_{\mathrm{GC}}) \cdot \nabla\mathbf{A}_0(\mathbf{X}_{\mathrm{GC}})\Big) \\ &\cdot (\mathrm{d}\,[\mathbf{X}_{\mathrm{GC}} + \rho\mathbf{a}(\alpha_{\mathrm{GC}})]) - \left(\frac{1}{2}mv_{\|\mathrm{GC}}^2 + \mu_{\mathrm{GC}}B_0\right)\mathrm{d}t.\end{aligned} \tag{2.40}$$

The gyrophase dependence in Γ_0^{GC} (i.e., all terms depending on α_{GC}) can then be systematically removed at any order by a proper phase space gauge transformation involving a gauge function S. For instance, at order zero there is no dependence on the gyroangle, while choosing $\mathrm{d}S = -q\mathrm{d}\,(\rho\mathbf{a}) \cdot \mathbf{A}_0 - q\rho\mathbf{a} \cdot (\mathrm{d}\mathbf{X}_{\mathrm{GC}} \cdot \nabla\mathbf{A}_0)$, allows to cancel all terms depending on the gyroangle at order one, obtaining

$$\Gamma_0^{\mathrm{GC}} = \Big(mv_{\|\mathrm{GC}}\mathbf{b} + q\mathbf{A}_0\Big) \cdot \mathrm{d}\mathbf{X}_{\mathrm{GC}} + \frac{\mu_{\mathrm{GC}}B_0}{\Omega}\mathrm{d}\alpha_{\mathrm{GC}} - \left(\frac{1}{2}mv_{\|\mathrm{GC}}^2 + \mu_{\mathrm{GC}}B_0\right)\mathrm{d}t. \tag{2.41}$$

We note that the same result can be obtained by explicitly applying a gyroaverage operator defined as

$$\langle\cdots\rangle = \frac{1}{2\pi}\int \mathrm{d}\alpha_{\mathrm{GC}} \tag{2.42}$$

to the one-from in (2.40).

2.4.2 The gyrocenter equations

In order to describe turbulent phenomena, one must allow for perturbations of the electromagnetic fields and consequently extend the equations previously derived. According to the gyrokinetic ordering, such perturbations are small compared to their background counterpart, i.e., of order $\mathcal{O}(\epsilon_\delta)$. Hence, the electromagnetic potentials as well as the one-form, can be conveniently split into a background and a perturbation:

$$\phi(\mathbf{x},t) = \phi_1(\mathbf{x},t), \tag{2.43}$$

$$\mathbf{A}(\mathbf{x},t) = \mathbf{A}_0(\mathbf{x}) + \mathbf{A}_1(\mathbf{x},t), \tag{2.44}$$

$$\gamma = \gamma_0 + \gamma_1, \tag{2.45}$$

with

$$\gamma_1 = q\mathbf{A}_1(\mathbf{x},t) \cdot \mathrm{d}\mathbf{x} - q\phi_1(\mathbf{x},t)\mathrm{d}t. \tag{2.46}$$

If now one proceeds as detailed in the previous section and computes the perturbed guiding center one-form Γ_1, one obtains

$$\begin{aligned}\Gamma_1^{\mathrm{GC}} =& q\mathbf{A}_1(\mathbf{X}_{\mathrm{GC}} + \rho, t) \cdot \left[\mathrm{d}\mathbf{X}_{\mathrm{GC}} + \frac{1}{qv_{\perp\mathrm{GC}}}\mathbf{a}(\alpha_{\mathrm{GC}})\mathrm{d}\mu_{\mathrm{GC}} + \frac{mv_{\perp\mathrm{GC}}}{qB_0}\mathbf{c}(\alpha_{\mathrm{GC}})\mathrm{d}\alpha_{\mathrm{GC}}\right] \\ &- q\phi_1(\mathbf{X}_{\mathrm{GC}} + \rho, t)\mathrm{d}t,\end{aligned} \tag{2.47}$$

which is clearly function of the fast varying gyroangle because of the rapidly fluctuating nature in space of the perturbed electromagnetic fields $\mathbf{A}_1(\mathbf{x},t)$ and $\phi_1(\mathbf{x},t)$. This gyroangle dependency cannot be removed by means of a simple gauge transformation alone. Intuitively, one cannot replace the actual particle position $\mathbf{x}$ with the gyrocenter one $\mathbf{X}_{\mathrm{GC}}$ in the fields as they are rapidly varying over the gyroradius scale. Instead, another set of coordinates, the *gyrocenter* (GY) coordinates $(\mathbf{X}, v_\parallel, \mu, \alpha)$, for which the associated perturbed one-form Γ_1^{GY} is independent of the gyroangle, must be introduced.

The transformation to the new coordinate system (denoted here with an overbar) involves continuous near-identity phase space coordinate transformations of the form:

$$\mathcal{T}_\epsilon : Z \to \bar{Z}(Z,\epsilon) \equiv T_\epsilon Z \quad \text{with} \quad \bar{Z}(Z,0) = Z, \tag{2.48}$$

and their inverse

$$\mathcal{T}_\epsilon^{-1} : \bar{Z} \to Z(\bar{Z},\epsilon) \equiv T_\epsilon^{-1}\bar{Z} \quad \text{with} \quad Z(\bar{Z},0) = \bar{Z}, \tag{2.49}$$

where ϵ denotes an ordering parameter.
Using the Lie transform technique, one can introduce the so-called generating vectors $\mathbf{G}$ such as to express the coordinate transformation as

$$\mathcal{T}_\epsilon^{\pm 1} \equiv \exp\left(\pm \sum_n \epsilon^n \mathbf{G}_n \cdot \mathrm{d}\right). \tag{2.50}$$

The n-th generator $\mathbf{G}_n$ is used to remove the fast time scale of order ϵ^n from the perturbed system. One can therefore explicitly rewrite to order ϵ^2 the coordinate transformations given in (2.48) and (2.49) as

$$\bar{Z}^\mu = Z^\mu + \epsilon G_1^\mu + \epsilon^2 \left(G_2^\mu + \frac{1}{2} G_1^\nu \frac{\partial G_1^\mu}{\partial Z^\nu} \right) + \mathcal{O}(\epsilon^3), \tag{2.51}$$

$$Z^\mu = \bar{Z}^\mu - \epsilon G_1^\mu - \epsilon^2 \left(G_2^\mu - \frac{1}{2} G_1^\nu \frac{\partial G_1^\mu}{\partial \bar{Z}^\nu} \right) + \mathcal{O}(\epsilon^3). \tag{2.52}$$

The transformation defined by (2.50) induces *pull-back* T_ϵ and *push-forward* T_ϵ^{-1} operators which are used to transform scalar fields F. The pull-back operator transforms a scalar field $\bar{F}$ defined in a phase-space with coordinates $\bar{Z}$ into a scalar field F in a phase space with coordinates Z. The push-forward instead operates the inverse transformation i.e., from a scalar field $F(Z)$ to $\bar{F}(\bar{Z})$. These operators can be formally expressed with the help of the generating vectors $\mathbf{G}$ according to

$$T_\epsilon^{\pm 1} \equiv \exp \left(\pm \sum_n \epsilon^n \mathbf{G}_n \mathrm{d} \right) = \exp \left(\pm \sum_n \epsilon^n L_G \right). \tag{2.53}$$

Here we have introduced the Lie derivative L_G, which is a differential operator acting on a k-form γ along the vector G according to

$$L_G \gamma \equiv \mathbf{G} \cdot \mathrm{d}\gamma + \mathrm{d}(\mathbf{G} \cdot \gamma). \tag{2.54}$$

One immediately notes that the Lie derivative preserves the tensorial nature of the object on which it is applied, i.e. the Lie derivative of a scalar is a scalar and the derivative of a one-form is a one-form. Making use of eqs. (2.23) to (2.26), one can easily show that the Lie derivative of a one-form can be expressed as:

$$(L_G \gamma)_\mu = G^\nu \left(\frac{\partial \gamma_\mu}{\partial Z^\nu} - \frac{\partial \gamma_\nu}{\partial Z^\mu} \right). \tag{2.55}$$

In order eliminate the dependence on the gyroangle from the guiding center one-form Γ^{GC} and obtain the corresponding gyrocenter one form, Γ^{GY}, one makes use of the transformation given in 2.55 properly choosing the generating vectors and the Gauge. Different choices are available in order to accomplish this goal, see e.g., Refs. [27–29]. Here we follow [30], employing the so-called parallel-symplectic approach [25] which allows the simplectic part of the gyrocenter one-form to retain gyroangle-independent perturbed fields. The advantage is that the parallel momentum coordinate will not depend on perturbed magnetic fields. Up to first order in ϵ one can write

$$\Gamma^{\mathrm{GY}} = (1 - \epsilon L_G) \Gamma^{\mathrm{GC}} + \mathrm{d}S \tag{2.56}$$

or, introducing a separation between equilibrium and perturbed contributions,

$$\Gamma_0^{\mathrm{GY}} = \Gamma_0^{\mathrm{GC}} + \mathrm{d}S_0 \tag{2.57}$$

$$\Gamma_1^{\mathrm{GY}} = \Gamma_1^{\mathrm{GC}} - L_G \Gamma_0^{\mathrm{GC}} + \mathrm{d}S_1 \tag{2.58}$$

Here, Γ_0^{GC} is the unperturbed guiding center one-form derived in the previous section and given by (2.41). Therefore, one has $\mathrm{d}S_0 = 0$. At first order the generating vectors G_1 and the gauge $\mathrm{d}S_1$ are chosen such as to obtain

$$\Gamma_1^{\mathrm{GY},\mathbf{X}} = q\langle A_{1\parallel}\rangle \mathbf{b}. \tag{2.59}$$

One assumes $\Gamma_1^{\mathrm{GY},\mu} = 0$ in order to establish the gyrocenter magnetic moment as an adiabatic invariant. For the same reason, also $\Gamma_1^{\mathrm{GY},\alpha} = 0$ is imposed. In the perturbed guiding center $\Gamma_0^{\mathrm{GY},v_\parallel \mathrm{GC}} = 0$, which is maintained in the gyrocenter counterpart. The following generators are therefore chosen [30]:

$$G_1^{\mathbf{X}} = \frac{1}{B^*_{0\parallel}}\left[\mathbf{b}\times\left(\mathbf{A}_1 + \frac{1}{q}\nabla S_1\right) + \frac{\mathbf{B}_0^*}{m}\frac{\partial S_1}{\partial v_\parallel}\right], \tag{2.60}$$

$$G_1^{v_\parallel} = \frac{\Omega}{B}\frac{\mathbf{B}_0^*}{B^*_{0\parallel}}\left(\mathbf{A}_1 - \mathbf{b}\langle A_{1\parallel}\rangle + \frac{1}{q}\nabla S_1\right), \tag{2.61}$$

$$G_1^{\mu} = \frac{\Omega}{B}\left(\frac{m}{B}\mathbf{A}_1\cdot\mathbf{v}_\perp + \frac{\partial S_1}{\partial \alpha}\right), \tag{2.62}$$

$$G_1^{\alpha} = -\frac{\Omega}{B}\left(\frac{1}{v_\perp}\mathbf{A}_1\cdot\mathbf{a} + \frac{\partial S_1}{\partial \mu}\right), \tag{2.63}$$

where

$$S_1 = \frac{1}{\Omega}\int_\alpha \left(q\tilde{\phi}_1 + \frac{1}{B^*_{0\parallel}}\left(\mathbf{b}\times\tilde{\mathbf{A}}_1\right)\cdot\mu\nabla B_0 - q v_\parallel \frac{\mathbf{B}_0^*}{B^*_{0\parallel}}\cdot\tilde{\mathbf{A}}_1 - q v_\perp \widetilde{\mathbf{A}\cdot\mathbf{c}}\right)\mathrm{d}\alpha', \tag{2.64}$$

and

$$\mathbf{A}_0^* = \mathbf{A} + \frac{m}{q}v_\parallel \mathbf{b}, \qquad \mathbf{B}_0^* = \nabla\times\mathbf{A}_0^*. \tag{2.65}$$

In equation (2.64) we have introduced the notation $\tilde{\mathcal{F}}$ to indicate the difference between a given quantity $\mathcal{F}$ and its gyroaverge:

$$\tilde{\mathcal{F}} = \mathcal{F} - \langle\mathcal{F}\rangle. \tag{2.66}$$

2.4.3 The gyrokinetic equation

In order to derive the gyrokinetic Vlasov equation, one can invoke the invariance of the distribution function along its characteristics. From the previously derived gyrocenter one-form, one can compute the equations of motion of each single gyrocenter thanks to the Euler-Lagrange equations:

$$\dot{\mathbf{X}} = \frac{\mathbf{b}}{qB^*_{0\|}} \times \nabla H + mv_\| \frac{\mathbf{B}^*}{mB^*_{0\|}}, \tag{2.67}$$

$$\dot{v}_\| = -\frac{\mathbf{B}^*}{mB^*_{0\|}} \cdot \left(\nabla H + q\mathbf{b}\dot{\bar{A}}_{1\|}\right), \tag{2.68}$$

where, in order to simplify the notation, we have explicitly introduced the perturbed gyrocenter Hamiltonian H:

$$H = \frac{1}{2}mv_\|^2 + \mu B_0 + q\bar{\phi}_1 + \mu \bar{B}_{1,\|}. \tag{2.69}$$

From here on we denote the gyroaveraged quantities appearing in the equation of motion with an overbar, while the notation $\langle \ldots \rangle$ will be kept for field equations. This is done in order to explicitly distinguish between gyroaverages taken about the gyrocenter position $\mathbf{X}$, as they appear in the equations of motion, from the ones about the particle position $\mathbf{x}$ (in the fields).

The effective magnetic field $\mathbf{B}^*$ appearing in the equation of motion,

$$\mathbf{B}^* = \mathbf{B}_0 + \frac{B_0}{\Omega} v_\| \nabla \times \mathbf{b} + \nabla \times \left(\mathbf{b}\bar{A}_{1\|}\right), \tag{2.70}$$

can be recast into the more convenient form

$$\mathbf{B}^* = B^*_{0\|}\mathbf{b} + \frac{B}{v_\|}\mathbf{v}_c + \frac{B}{v_\|}\mathbf{v}_{A_{1\|}} \tag{2.71}$$

where a term of order $\mathcal{O}(\epsilon_B)$ has been neglected. In writing Equation (2.71) we have also introduced the curvature drift velocity

$$\mathbf{v}_c = \frac{v_\|^2}{\Omega} \left(\nabla \times \mathbf{b}\right)_\perp, \tag{2.72}$$

and the magnetic flutter

$$\mathbf{v}_{A_{1\|}} = -\frac{1}{m\Omega}\mathbf{b} \times \left(qv_\| \nabla \bar{A}_{1\|}\right). \tag{2.73}$$

Combining Eqs. (2.67) and (2.71), defining the modified gyroaveraged potential $\bar{\xi}_1$ as

$$\bar{\xi}_1 = \bar{\phi}_1 - v_\| \bar{A}_{1\|} + \frac{\mu}{q}\bar{B}_{1\|}, \tag{2.74}$$

introducing the grad-B drift velocity

$$\mathbf{v}_{\nabla B} = \frac{\mu}{m\Omega}\mathbf{b} \times \nabla B \tag{2.75}$$

and the generalized $\mathbf{E}\times\mathbf{B}$ velocity, which contains also the magnetic flutter contribution,

$$\mathbf{v}_\xi = \frac{1}{B_0}\mathbf{b}\times\nabla\bar{\xi}_1 \tag{2.76}$$

the equations of motions can finally be rewritten as

$$\dot{\mathbf{X}} = v_\parallel\mathbf{b} + \frac{B_0}{B^*_{0\parallel}}\left(\mathbf{v}_\xi + \mathbf{v}_c + \mathbf{v}_{\nabla B}\right) \tag{2.77}$$

$$\dot{v}_\parallel = -\left(\frac{1}{m}\mathbf{b} + \frac{1}{mv_\parallel}\frac{B_0}{B^*_{0\parallel}}\left(\mathbf{v}_\xi + \mathbf{v}_c + \mathbf{v}_{\nabla B}\right)\right)\cdot\left(\mu\nabla B_0 + q\nabla\bar{\phi}_1 + \mu\nabla\bar{B}_{1\parallel}\right) - \frac{q}{m}\dot{\bar{A}}_{1\parallel}. \tag{2.78}$$

These equations can be substituted into the Vlasov equation invoking, as already mentioned, the invariance of the distribution function along characteristics in phase space:

$$\frac{D\bar{F}}{Dt} = \frac{\partial\bar{F}}{\partial t} + \dot{\mathbf{X}}\cdot\frac{\partial\bar{F}}{\partial\mathbf{X}} + \dot{v}_\parallel\frac{\partial\bar{F}}{\partial v_\parallel} = 0. \tag{2.79}$$

By construction the Vlasov operator does not contain derivatives with respect to μ as $\dot{\mu} = 0$, while the term $\partial_\alpha\bar{F}$ drops because $\bar{F}$ is independent of the gyroangle[1]. Again the species index has been dropped to lighten notations. This is the so-called full-f gyrokinetic equation, which describes the dynamics of the gyrocenter distribution $\bar{F}$.
A common procedure used to further simplify Eq. (2.79) is the so-called delta-f splitting, in which one writes $\bar{F} = \bar{F}_0 + \bar{F}_1$ i.e. the distribution function is split into a time independent background $\bar{F}_0$ and a fluctuating part $\bar{F}_1$. Employing the gyrokinetic ordering and assuming that all ordering parameters are of the same magnitude, one can separate Eq. (2.79) into terms of zeroth, first and second order.
At order zero, one obtains:

$$v_\parallel\mathbf{b}\cdot\left(\nabla\bar{F}_0 - \frac{1}{mv_\parallel}\mu\nabla B_0\frac{\partial\bar{F}_0}{\partial v_\parallel}\right) = 0, \tag{2.80}$$

which imposes a constraint on the background distribution, which is not explicitly evolved in time.

---

[1] For clarity of notations, the distribution function is indicated as $\bar{F}$ when expressed in gyrocenter variables, as F in guiding center variables and as f in particle phase space variables.

At order one Eq. (2.79) reads:

$$\begin{aligned}\frac{\partial \bar{F}_1}{\partial t}+&\left\{\frac{\mathbf{b}}{qB^*_{0\|}}\times\nabla(\mu B_0+q\bar{\xi}_1)+\frac{B_0}{B^*_{0\|}}\mathbf{v}_c\right\}\\ &\cdot\left[\nabla(\bar{F}_0+\bar{F}_1)-\frac{1}{mv_\|}(\mu\nabla B_0+q\nabla\bar{\phi}_1+\mu\bar{B}_{1\|})\frac{\partial\bar{F}_0}{\partial v_\|}\right]\\ &+v_\|\mathbf{b}\cdot\left[\nabla\bar{F}_1-\frac{1}{mv_\|}(q\nabla\bar{\phi}_1+\mu\bar{B}_{1\|})\frac{\partial\bar{F}_0}{\partial v_\|}-\frac{1}{mv_\|}\mu\nabla B_0\frac{\partial\bar{F}_1}{\partial v_\|}\right]\\ &-\frac{q}{m}\dot{\bar{A}}_{1\|}\frac{\partial\bar{F}_0}{\partial v_\|}=0.\end{aligned} \tag{2.81}$$

Second and higher order terms in Eq. (2.79) give rise to the so-called parallel nonlinearity, which are neglected in the current version of the GENE code.

Throughout this work the background distribution will be assumed as a local[2] Maxwellian i.e.

$$F_0(x,v_\|,\mu)=\frac{n(x)}{\pi^{3/2}v_{th}^3(x)}\exp\left[\frac{\frac{1}{2}mv_\|^2+\mu B}{T(x)}\right] \tag{2.82}$$

where $T(x)=mv_{\mathrm{th}}^2(x)$. With this choice, neglecting curvature and grad-B drifts, the zeroth order gyrokinetic equation is automatically satisfied, as can be seen by a direct substitution in Eq. (2.80). A true solution accounting for the finite orbit widths resulting from aforementioned drifts is given by the so-called Canonical Maxwellian, i.e. function of the constant of motion of the unperturbed axisiymmetric system: kinetic energy, magnetic moment and canonical angular momentum. The reader is referred to Ref. [31] for a detailed study of the consequences of taking a local distribution instead of a canonical Maxwellian. The first order (2.81) can be greatly simplified by explicitly evaluating the derivatives of the F_0:

$$\nabla F_0=\left[\frac{\nabla n_0}{n_0}+\frac{\nabla T_0}{T_0}\left(\frac{mv_\|^2/2+\mu B_0}{T_0}-\frac{3}{2}\right)-\mu\frac{\mu\nabla B_0}{T_0}\right]F_0, \tag{2.83}$$

$$\frac{\partial F_0}{\partial v_\|}=-\frac{m_j v_\|}{T_{0j}}F_0, \tag{2.84}$$

$$\frac{\partial F_0}{\partial \mu}=-\frac{B_0}{T_0}F_0. \tag{2.85}$$

---

[2] Local here indicates that the radial dependency of temperature and density is kept.

Substituting these expressions into (2.81), one obtains

$$\begin{aligned}\frac{\partial \bar{F}_1}{\partial t} &+ \frac{B_0}{B_{0\|}^*}\left(\mathbf{v}_\xi + \mathbf{v}_{\nabla B} + \mathbf{v}_c\right)\cdot\left[\nabla F_0 - \mu\nabla B_0\frac{F_0}{T_0}\right]\\ &+ \frac{B_0}{B_{0\|}^*}\left(\mathbf{v}_\xi + \mathbf{v}_{\nabla B} + \mathbf{v}_c\right)\cdot\left[\nabla \bar{F}_1 - (q\nabla\bar{\phi}_1 + \mu\bar{B}_{1\|})\frac{F_0}{T_0}\right]\\ &+ v_\|\mathbf{b}\cdot\left[(q\nabla\bar{\phi}_1 + \mu\bar{B}_{1\|})\frac{F_0}{T_0} + \nabla\bar{F}_1 - \frac{1}{mv_\|}\mu\nabla B_0\frac{\partial\bar{F}_1}{\partial v_\|}\right]\\ &- qv_\|\dot{\bar{A}}_{1\|}\frac{F_0}{T_0} = 0,\end{aligned} \tag{2.86}$$

where we have also introduced the drift velocities defined in Eqs. (2.76), (2.75) and (2.72). Finally, for numerical implementation it runs out convenient to combine the time derivative of the distribution function with the one acting on the perturbed magnetic potential $\bar{A}_{1\|}$. Therefore, introducing the modified distribution function

$$g_1 = \bar{F}_1 + qv_\|\dot{\bar{A}}_{1\|}\frac{F_0}{T_0}, \tag{2.87}$$

Equation (2.86) becomes

$$\begin{aligned}\frac{\partial g_1}{\partial t} =& - \frac{B_0}{B_{0\|}^*}\left(\mathbf{v}_\xi + \mathbf{v}_{\nabla B} + \mathbf{v}_c\right)\cdot\left[\nabla F_0 - \mu\nabla B_0\frac{F_0}{T_0}\right]\\ &- \frac{B_0}{B_{0\|}^*}\left(\mathbf{v}_\xi + \mathbf{v}_{\nabla B} + \mathbf{v}_c\right)\cdot\left[\nabla \bar{F}_1 - (q\nabla\bar{\phi}_1 + \mu\bar{B}_{1\|})\frac{F_0}{T_0}\right]\\ &+ v_\|\mathbf{b}\cdot\left[(q\nabla\bar{\phi}_1 + \mu\bar{B}_{1\|})\frac{F_0}{T_0} + \nabla\bar{F}_1 - \frac{1}{mv_\|}\mu\nabla B_0\frac{\partial\bar{F}_1}{\partial v_\|}\right].\end{aligned} \tag{2.88}$$

The GENE code implements and solves this equation, with specific numerical techniques and further simplifications that will be detailed in the next chapter. We remark that the only remaining nonlinearity in (2.88) stems from the term proportional to $\mathbf{v}_\xi \cdot \nabla\bar{F}_1 = (\mathbf{b}/B_{0\|}^* \times \nabla\bar{\xi}_1)\cdot\nabla\bar{F}_1$.

2.4.4 The field equations

In order to solve the gyrokinetic equations of motion, the self-consistent electromagnetic fields must be evaluated from the following reduced form of the Maxwell's equations (considering Coulomb gauge):

$$-\nabla^2\phi = \frac{1}{\epsilon_0}\sum_j q_j\int f_{1j}(\mathbf{x},\mathbf{v},t)\mathrm{d}^3\mathbf{v} = \frac{1}{\epsilon_0}\sum_j q_j n_{1j}(\mathbf{x}), \tag{2.89}$$

$$-\nabla^2\mathbf{A} = \mu_0\sum_j q_j\int f_{1j}(\mathbf{x},\mathbf{v},t)\mathbf{v}\mathrm{d}^3\mathbf{v} = \mu_0\sum_j n_j\mathbf{j}_j(\mathbf{x}), \tag{2.90}$$

where the displacement current contribution has already been neglected in Ampére's law (2.90). Here we consider only the fluctuating parts of ϕ and $\mathbf{A}$ originated from the perturbed particle distribution. The plasma current density $\mathbf{j}_0$ which produces the confining magnetic field is neglected, as well as the vector potential generated by the external coils. Given that the moment of the particle distribution function appearing at the right-hand-side of Maxwell's equations (2.89) and (2.90) are expressed in terms of the particle distribution function variables, while the distribution provided by the gyrokinetic equation is expressed in gyrocenter variables, one needs to properly evaluate these moments with the help of the pullback operator defined in Eq. (2.53), such as to transform the distribution in gyro-center variables in the one in particle variables.

Poisson equation

With the choice of generators and gauge detailed in the previous section, the pullback operator T_ϵ acting on the gyrocenter distribution $\bar{F}_1$ at first order in ϵ_δ reads:

$$\begin{aligned} F &= T_\epsilon \bar{F}_1 \\ &= F_1 + \frac{\mathbf{b}\times\mathbf{A}_1}{B^*_\parallel}\cdot\nabla F_0 + \frac{\Omega}{B}\frac{\mathbf{B}^*}{B^*_\parallel}\cdot\left(\mathbf{A}_1 - \mathbf{b}\bar{A}_{1\parallel}\right)\frac{\partial F_0}{\partial v_\parallel} + \frac{\Omega}{B}\left(\frac{m}{B}\mathbf{A}_1\cdot\mathbf{v}_\perp + \frac{\partial S_1}{\partial\alpha}\right)\frac{\partial F_0}{\partial\mu}, \end{aligned} \tag{2.91}$$

with S_1 given by Eq. (2.64). Considering the local Maxwellian background, (2.91) leads to the following simplified form:

$$T_\epsilon \bar{F}_1 = F_1 - \left(q\tilde{\phi} - \mu\bar{B}_{1\parallel}\right)\frac{F_0}{T_0}. \tag{2.92}$$

Given the distribution in gyrocenter variables, the pullback operator enables to obtain the distribution in guiding center variables. The change of coordinates from guiding center to particle variables can be then obtained with the help of a delta function $\delta(\mathbf{X}+\boldsymbol{\rho}-\mathbf{x})$, such that the generic moment of the $j-$th species distribution function of order m and n in $v_\parallel$ and $v_\perp$ respectively can be expressed as

$$M_{j,mn}(\mathbf{x}) = \frac{1}{m_j}\int\delta(\mathbf{X}+\boldsymbol{\rho}-\mathbf{x})\left[F_{1,j} - q_j\left(\tilde{\phi_1} - \mu\bar{B}_{1\parallel}\right)\frac{F_{0j}}{T_{0j}}\right]B^*_{0\parallel}v^m_{\parallel j}v^n_{\perp j}\mathrm{d}\mathbf{X}\mathrm{d}v_{\parallel j}\mathrm{d}\mu_j\mathrm{d}\alpha. \tag{2.93}$$

Here, one has made use of the guiding center phase-space Jacobian [32]:

$$J^{\mathrm{GC}} = \left|\frac{\partial(\mathbf{x},\mathbf{v})}{\partial(\mathbf{X}_{\mathrm{GC}}, v_{\parallel,\mathrm{GC}}, \mu_{\mathrm{GC}}, \alpha_{\mathrm{GC}})}\right| = \frac{B^*_{0\parallel}}{m_j}. \tag{2.94}$$

The zeroth order moment i.e., the particle density $n_{1j}(\mathbf{x})$, is required in order to solve Poisson's Equation (2.89). By noting that

$$B^*_{0\parallel} = B_0 + \frac{m_j}{q_j} v_\parallel \mathbf{b} \cdot (\nabla \times \mathbf{b}) \,, \tag{2.95}$$

it is possible to write

$$\begin{aligned} n_{1j}(\mathbf{x}) = M_{j,00}(\mathbf{x}) = \frac{1}{m_j} \int \Bigg\{ \delta(\mathbf{X} + \rho - \mathbf{x}) \left[F_{1,j} - q_j \left(\tilde{\phi}_1 - \mu \bar{B}_{1\parallel} \right) \frac{F_{0j}}{T_{0j}} \right] \\ \left(B_0 + \frac{m_j}{q_j} v_{\parallel j} \mathbf{b} \cdot (\nabla \times \mathbf{b}) \right) \Bigg\} \mathrm{d}\mathbf{X} \mathrm{d}v_{\parallel j} \mathrm{d}\mu_j \mathrm{d}\alpha. \end{aligned} \tag{2.96}$$

Dropping the term proportional to $\mathbf{b} \cdot (\nabla \times \mathbf{b})$ which is of order $\mathcal{O}(\epsilon_B)$, expressing $\tilde{\phi}$ as the difference between the potential and its gyroaverage, Eq. (2.66), and integrating over $\mathbf{X}$, one obtains

$$\begin{aligned} \nabla^2 \phi_1 = -\frac{1}{\epsilon_0} \sum_j 2\pi \frac{q_j}{m_j} \int \Bigg[\Big\langle \{B_0 F_{1,j}\}|_{\mathbf{X}=\mathbf{x}-\boldsymbol{\rho}} \Big\rangle - q_j \phi_1 B_0 \frac{F_{0j}}{T_{0,j}} \\ + \left\langle \left\{ \left[q_j \bar{\phi}_{1j} + \mu \bar{B}_{1\parallel j} \right] B_0 \frac{F_{0,j}}{T_{0,j}} \right\} \Bigg|_{\mathbf{X}=\mathbf{x}-\boldsymbol{\rho}} \right\rangle \Bigg] \mathrm{d}v_\parallel \mathrm{d}\mu, \end{aligned} \tag{2.97}$$

where the integral over $\mathrm{d}\alpha$ has been explicitly replaced with a gyroaverage operation. We note that consecutive gyroaverages of both the electrostatic potential and the parallel magnetic fluctuation have to be computed when solving the previous equation. The notation $\{\cdots\}|_{\mathbf{X}=\mathbf{x}-\boldsymbol{\rho}}$ indicates that the bracketed expression is to be evaluated at the position $\mathbf{x} - \boldsymbol{\rho}_j$.

Thanks to the parallel wavenumber ordering, the Laplacian can be approximated with its perpendicular component. Rearranging the terms, the gyrokinetic Poisson's equation finally reads:

$$\begin{aligned} \nabla^2_\perp \phi_1 - \frac{1}{\epsilon_0} \sum_j 2\pi \frac{q_j^2}{m_j} \int \left[\phi_1 B_0 \frac{F_{0j}}{T_{0,j}} - \left\langle \left\{ B_0 \bar{\phi}_{1j} \frac{F_{0,j}}{T_{0,j}} \right\} \Bigg|_{\mathbf{X}=\mathbf{x}-\boldsymbol{\rho}} \right\rangle \right] \mathrm{d}v_\parallel \mathrm{d}\mu = \\ -\frac{1}{\epsilon_0} \sum_j 2\pi \frac{q_j}{m_j} \int \left[\Big\langle \{B_0 g_{1,j}\}|_{\mathbf{X}=\mathbf{x}-\boldsymbol{\rho}} \Big\rangle + \left\langle \left\{ \mu B_0 \bar{B}_{1\parallel j} \frac{F_{0,j}}{T_{0,j}} \right\} \Bigg|_{\mathbf{X}=\mathbf{x}-\boldsymbol{\rho}} \right\rangle \right] \mathrm{d}v_\parallel \mathrm{d}\mu. \end{aligned} \tag{2.98}$$

In the final step, we have also replaced $F_{1,j}$ with the corresponding modified distribution function $g_{1,j}$ thanks to the symmetry of the equilibrium distribution F_0 with respect to $v_\parallel$ (F_0 is even with respect to $v_\parallel$).

Ampére's Law

The parallel component of Ampére's law can be evaluated following an equivalent procedure. Thanks to the pullback operator, one can write it as a function of the perturbed gyrocenter distribution as

$$\nabla_\perp^2 A_{1\parallel} = -\mu_0 \sum_j 2\pi \frac{q_j}{m_j} \int v_\parallel \langle \{B_0 f_{1,j}\}|_{\mathbf{X}=\mathbf{x}-\boldsymbol{\rho}} \rangle \mathrm{d}v_\parallel \mathrm{d}\mu. \tag{2.99}$$

In this case the substitution $f_{1,g} \to g_{1,j}$ introduces an additional term:

$$\nabla_\perp^2 A_{1\parallel} = -\mu_0 \sum_J 2\pi \frac{q_j}{m_j} \int v_\parallel \left\langle \left\{ B_0 g_{1,j} - q_j v_\parallel B_0 \bar{A}_{1\parallel,j} \frac{F_{0,j}}{T_{0,j}} \right\}\Bigg|_{\mathbf{X}=\mathbf{x}-\boldsymbol{\rho}} \right\rangle \mathrm{d}v_\parallel \mathrm{d}\mu. \tag{2.100}$$

Rearranging once again the terms such that all contributions involving $A_{1\parallel}$ appear on the left hand side, the final form of Ampére's law can be expressed as:

$$\begin{aligned} &\nabla_\perp^2 A_{1\parallel} - \mu_0 \sum_J 2\pi \frac{q_j^2}{m_j} \int v_\parallel^2 \left\langle \left\{ B \bar{A}_{1\parallel,j} \frac{F_{0,j}}{T_{0,j}} \right\}\Bigg|_{\mathbf{X}=\mathbf{x}-\boldsymbol{\rho}} \right\rangle \mathrm{d}v_\parallel \mathrm{d}\mu = \\ &- \mu_0 \sum_J 2\pi \frac{q_j}{m_j} \int v_\parallel \langle \{B g_{1,j}\}|_{\mathbf{X}=\mathbf{x}-\boldsymbol{\rho}} \rangle \mathrm{d}v_\parallel \mathrm{d}\mu. \end{aligned} \tag{2.101}$$

One is thus left with finding an equation for $B_{1\parallel}$ which appears in (2.98) whenever compressional electromagnetic fluctuations are considered. This relation can be obtained from the perpendicular component of Ampére's law:

$$(\nabla \times B_1)_\perp = \mu_0 \mathbf{j}_\perp \tag{2.102}$$

The perpendicular current $\mathbf{j}_\perp$ can be as well expressed as a function of the perturbed gyrocenter distribution. After some algebra, one gets:

$$\begin{aligned} &(\nabla \times B_1)_\perp \\ &= \mu_0 \sum_j 2\pi q_j \left(\frac{2}{m_j} \right)^{3/2} \int \left\langle \left\{ \mathbf{c} B^{3/2} \left[f_{1j} - (q_j \tilde{\phi}_1 - \mu \bar{B}_{1\parallel,j}) \frac{F_{0,j}}{T_{0,j}} \right] \right\}\Bigg|_{\mathbf{X}=\mathbf{x}-\boldsymbol{\rho}} \right\rangle \sqrt{\mu} \mathrm{d}v_\parallel \mathrm{d}\mu, \end{aligned} \tag{2.103}$$

where $\mathbf{c}$ is the unit vector defined in (2.36). Equation (2.103) can then be rearranged and solved together with (2.98) for ϕ_1 and $B_{1\parallel}$ [33].

2.4.5 Further simplifications

Depending of the particular case study, further simplifications can be applied to the field equations resulting potentially also in a relevant reduction of the computational cost of a simulation.

Quasi-neutrality

For typical Tokamak parameters, the Debye length λ_D is much smaller than the wave length of microinstabilities. One can thus neglect the Laplacian appearing in Eq. (2.98), obtaining the so-called quasi-neutrality equation:

$$\sum_j q_j n_{1j}(\mathbf{x}) = 0. \tag{2.104}$$

Expressing the perturbed densities with the help of the moments of the distribution function, one finally gets

$$\begin{aligned}\sum_j \frac{q_j}{m_j} \int \Bigg[& \langle \{B_0 g_{1,j}\} \,|_{\mathbf{X}=\mathbf{x}-\boldsymbol{\rho}} \rangle - q_j \phi_1 B_0 \frac{F_{0j}}{T_{0,j}} + q_j \left\langle \left\{ B_0 \bar{\phi}_{1j} \frac{F_{0,j}}{T_{0,j}} \right\} |_{\mathbf{X}=\mathbf{x}-\boldsymbol{\rho}} \right\rangle \\ & + \left\langle \left\{ \mu \bar{B}_{1\parallel j} B_0 \frac{F_{0,j}}{T_{0,j}} \right\} \Bigg|_{\mathbf{X}=\mathbf{x}-\boldsymbol{\rho}} \right\rangle \Bigg] \mathrm{d}v_\parallel \mathrm{d}\mu = 0. \end{aligned} \tag{2.105}$$

The first term in Eq.(2.105) is the so called gyrodensity, while the following two are referred to as the polarization density, which reflect the difference between guiding-center and gyrocenter coordinates. The last one is associated to the compressional magnetic fluctuations. We remark that GENE can handle a finite Debye length, which will however be neglected in this work and the limit $k_\perp \lambda_D \to 0$ assumed.

Adiabatic electron model

For studying some types of modes, like e.g. ITG (see sec. 2.6.2), given their much lighter mass in comparison to the one of ions, proton/electron masses ~ 1836, electrons can be assumed mass-less and therefore able to respond infinitely fast to an electrostatic perturbation along the magnetic field. This constitutes the so-called *adiabatic electron* limit. In this approximation, in a fluid-like description, a perfect balance is established at all times between the parallel pressure gradient and the parallel electric field deriving from the electrostatic potential ϕ. In this case the electron density is represented by a Boltzmann distribution

$$n_e(\mathbf{x}) = N(x) \exp\left(\frac{e\phi_1(\mathbf{x})}{T_{0e}(x)}\right) = N(x)\left(1 + \frac{e\phi_1(\mathbf{x})}{T_{0e}(x)}\right) + \mathcal{O}(\epsilon^2) \tag{2.106}$$

where in the last step we have assumed small amplitude fluctuations in order to linearize the electron response. $N(x)$ is evaluated assuming that the perturbed electron density cancels over a flux surface:

$$\langle n_e(\mathbf{x})\rangle_{\mathrm{fs}} = \langle n_{0,e}(x) + n_{1,e}(\mathbf{x})\rangle_{\mathrm{fs}} = n_{0,e}(x) \tag{2.107}$$

Here $\langle\cdots\rangle_{\mathrm{fs}}$ indicates the flux surface average of a quantity $\mathcal{A}$ and is defined by

$$\langle\mathcal{A}\rangle_{\mathrm{fs}} = \lim_{\Delta\psi\to 0}\frac{1}{\Delta V}\int_{\Delta V}\mathcal{A}\, d^3x, \tag{2.108}$$

where $\Delta V(\psi)$ is the volume between the flux surface ψ=const and $\psi + \Delta\psi$ = const. Combining equations (2.106) and (2.107) one arrives at

$$n_{1,e}(\mathbf{x}) = \frac{n_{0,e}(x)}{T_{0,e}(x)} e\left(\phi_1 - \langle\phi_1\rangle_{\mathrm{fs}}\right), \tag{2.109}$$

In this case the electron distribution does not need to be advanced in time. Equation (2.109) can then be directly inserted in Eq. (2.105), which becomes

$$\begin{aligned}\sum_{j\neq e} 2\pi\frac{q_j}{m_j}\int\Bigg[&\left\langle\{B_0 g_{1,j}\}|_{\mathbf{X}=\mathbf{x}-\boldsymbol{\rho}}\right\rangle - q_j\phi_1 B_0\frac{F_{0j}}{T_{0,j}}\\ &+q_j\left\langle\left\{B_0\bar{\phi}_{1j}\frac{F_{0,j}}{T_{0,j}}\right\}\Bigg|_{\mathbf{X}=\mathbf{x}-\boldsymbol{\rho}}\right\rangle\Bigg]\mathrm{d}v_\parallel\mathrm{d}\mu = e^2\frac{n_{0e}}{T_{0e}}\left(\phi_1 - \langle\phi_1\rangle_{\mathrm{fs}}\right).\end{aligned} \tag{2.110}$$

The Ampére equation is not solved in the adiabatic electron limit, since in this case a Maxwellian dependency is assumed for the electron distribution in velocity space, thus excluding any current.

Hybrid electron model

The assumption of a fully adiabatic response of electrons can be partly relaxed in the so-called *hybrid electron* model, where passing particles are still assumed to respond adiabatically, while the trapped electrons are handled with a fully gyrokinetic approach. The gyrokinetic description is also used for treating the ion dynamics.

The trapped-passing boundary can be identified based on the conservation of kinetic energy and magnetic moment; the trapped region, see Fig. 1.3, is thus defined in velocity space at a given point (ψ, χ) n the poloidal plane by the relation

$$v_\parallel(\mu) < \left\{\frac{2}{m_e}\left[B_{0,\max}(\psi) - B_0(\psi,\chi)\right]\mu\right\}^{1/2}, \tag{2.111}$$

where $B_{0,\mathrm{max}}$ indicates the maximum value of the magnetic field on the flux surface $\psi = \mathrm{const}$. One can then estimate the fraction of trapped particles α_t as

$$\alpha_t = \sqrt{1 - \frac{B_0(\psi, \chi)}{B_{0,\mathrm{max}}(\psi)}}. \tag{2.112}$$

In the hybrid model, the distribution function of trapped electrons is clearly required in order to evaluate the associated density fluctuations required for solving the field equation. The passing electron contribution is instead enforced to be adiabatic. The full electron distribution function must nevertheless be evolved in time according to the gyrokinetic model because turbulent fields can cause passing particles to get trapped and vice versa. The evolution of passing particles is however passive, as the passing electron distribution function does not appear explicitly in the field equations, where it is replaced by the adiabatic response weighted by α_t.
Equation (2.105) reads in this case

$$\begin{aligned}
&(1-\alpha_t)\frac{1}{2\pi}e^2\frac{n_{0,e}}{T_{0,e}}\left(\phi_1 - \langle\phi_1\rangle_{\mathrm{fs}}\right) + \frac{e}{m_e}\int\limits_{\mathrm{trap}} \Big\langle \{B_0 g_{1,e}\}\big|_{\mathbf{X}=\mathbf{x}-\boldsymbol{\rho}}\Big\rangle \mathrm{d}v_\parallel \mathrm{d}\mu \\
&+ \frac{e^2}{m_e}\int\limits_{\mathrm{trap}} \left[\phi_1 B_0 \frac{F_{0e}}{T_{0,e}} - \left\langle \left\{ B_0 \bar{\phi}_{1e} \frac{F_{0,e}}{T_{0,e}} \right\}\Big|_{\mathbf{X}=\mathbf{x}-\boldsymbol{\rho}} \right\rangle\right] \mathrm{d}v_\parallel \mathrm{d}\mu \\
=& \sum_{j\neq e}\frac{q_j}{m_j}\int \Big\langle \{B_0 g_{1,j}\}\big|_{\mathbf{X}=\mathbf{x}-\boldsymbol{\rho}}\Big\rangle \mathrm{d}v_\parallel \mathrm{d}\mu \\
&- \sum_{j\neq e}\frac{q_j^2}{m_j}\int \left[\phi_1 B_0 \frac{F_{0j}}{T_{0,j}} - \left\langle \left\{ B_0 \bar{\phi}_{1j} \frac{F_{0,j}}{T_{0,j}} \right\}\Big|_{\mathbf{X}=\mathbf{x}-\boldsymbol{\rho}} \right\rangle\right] \mathrm{d}v_\parallel \mathrm{d}\mu,
\end{aligned} \tag{2.113}$$

having neglected terms proportional to $B_{1\parallel}$ as the hybrid model is inadequate to address electromagnetic fluctuations. The velocity space integral appearing on the left hand side (and indicated as $\int_{\mathrm{trap}}$) is only carried out over the trapped region defined in Eq. (2.111).

Adiabatic ion model

In the limit of short perpendicular wavelengths compared to the ion Larmor radius, the effective response on ions become adiabatic. In this case the response $n_{1,j}$ of ions to an electrostatic perturbation ϕ_1 thus reads:

$$\frac{n_{1,j}}{n_{0,j}} = -\frac{q_j}{T_{0,j}}\phi_1 \tag{2.114}$$

At such short wavelengths, finite $k_\perp \lambda_D$ can become important and one must consider the full Poisson equation instead of the reduced quasi-neutrality relation:

$$\begin{aligned}
&\nabla_\perp^2 \phi_1 - \frac{1}{\epsilon_0} \sum_j q_j^2 \frac{n_{0,j}}{T_{0,j}} \phi_1 + \frac{1}{\epsilon_0} \frac{2\pi}{m_e} e^2 \int \left\langle \left\{ B_0 \bar{\phi}_{1j} \frac{F_{0,e}}{T_{0,e}} \right\} \Big|_{\mathbf{X}=\mathbf{x}-\boldsymbol{\rho}} \right\rangle \mathrm{d}v_\parallel \mathrm{d}\mu = \\
&\frac{1}{\epsilon_0} \frac{2\pi}{m_e} e \int \left[\left\langle \{B_0 g_{1,e}\}|_{\mathbf{X}=\mathbf{x}-\boldsymbol{\rho}} \right\rangle + \left\langle \left\{ \mu B_0 \bar{B}_{1\parallel e} \frac{F_{0,e}}{T_{0,e}} \right\} \Big|_{\mathbf{X}=\mathbf{x}-\boldsymbol{\rho}} \right\rangle \right] \mathrm{d}v_\parallel \mathrm{d}\mu,
\end{aligned} \tag{2.115}$$

In the adiabatic ion limit, parallel and perpendicular Ampére's law are given by Eqs. (2.101) and (2.103) respectively, where the sums are limited to the electron species.

2.4.6 The local limit

Besides simplifications in the field equations valid when studying particular turbulent regimes, an important simplification can be made considering the turbulent transport as being essentially a local process. In this case one assumes the limit $\rho^* \to 0$, where $\rho^* = \rho_i/a$, and neglects the variation of all equilibrium quantities over typical turbulence correlation lengths, which are assumed to scale proportionally to the Larmor radius. This is the so-called "*local*", or flux-tube, approach [34] in contrast to the "*global*", where this approximation is not made. Under this limit, the simulation domain can be reduced to a narrow tube elongated along a magnetic field line but covering only a small fraction of the perpendicular cross-section.

The local gyrokinetic equations can be derived by removing the radial dependence of equilibrium quantities in Eq. (2.88) and in the corresponding field equations (2.98), (2.101) and (2.103). Their gradient is however retained and assumed constant across the computational domain. As a result, all the equilibrium quantities exit from gyroaverages, which can then be evaluated simply by multiplying with the Bessel function $J_0(k_\perp \rho_j)$ as shown in e.g. Ref. [33]. Temperature and density are considered constant across the simulation domain, while their gradient is retained as the main turbulence driving term. It should be noted that even if the flux-tube domain is representative of a very thin radial fraction of the minor radius of the confined plasma, the numerical representation, which employs radial periodic boundary conditions (see also section 3.2), must be carried out assuming a sufficiently large radial computational domain in comparison to turbulent radial correlation lengths. This, for the core conditions of machines of the size of TCV ($\rho^* \sim 1/80$), can result in a simulation domain even larger than the actual plasma minor radius.

2.5 The collision operator

The gyrokinetic model derived so far describes a collisionless plasma, that is a plasma in which particles collectively interact between each other only via the self-consistent electromagnetic wavefields. This is a typical approximation valid for high temperature fusion plasmas, where the collision frequency is much smaller than the typical frequencies of microinstabilities. Binary interactions between particles can nevertheless play an important role in determining the actual dynamics of microturbulent fields. As will be discussed in the following chapters, for TCV relevant conditions, collisionality can lead to a significant stabilization of microturbulence, and therefore to a reduction of the associated heat and particle fluxes. In this work the effect of collisions is modeled via a linearized Landau-Boltzmann operator $\mathcal{C}$ which is added as a correction to the right-hand-side of the Vlasov equation, Eq. (2.13), leading to the so-called Fokker-Plank equation. A detailed description of the collision operator and of its current implementation in the GENE code can be found in Ref. [35]. Here we will summarize its essential properties. In particle space, the collision operator for the j-th species assumes the form

$$\mathcal{C}\left[f_j\right] = \sum_{j'} \mathcal{C}_{jj'}\left[f_j, f_{j'}\right] \tag{2.116}$$

where $\mathcal{C}_{jj'}$ represents collision of species j on another species j', including self collisions ($j = j'$). Thanks to the gyrokinetic ordering, assuming $|\delta f/f_0| \ll 1$. the collision operator can be linearized as follows:

$$\mathcal{C}_{jj'}\left[f_j, f_{j'}\right] \simeq \mathcal{C}_{jj'}\left[f_{1j}, f_{0j'}\right] + \mathcal{C}_{jj'}\left[f_{0j}, f_{1j'}\right], \tag{2.117}$$

having neglected both the collision contribution from the background species $\mathcal{C}_{jj'}\left[f_{0j}, f_{0j'}\right]$, as it describes a thermalization process happening on much longer timescales than microturbulence, as well as the higher order nonlinear correction from $\mathcal{C}_{jj'}\left[f_{1j}, f_{1j'}\right]$. One often writes Eq. (2.117) as

$$\mathcal{C}\left[f_j, f_{j'}\right] = \sum_{j'} \frac{\partial}{\partial \mathbf{v}} \cdot \left(\bar{\bar{\mathcal{D}}}_{jj'} \cdot \frac{\partial}{\partial \mathbf{v}} - \mathbf{R}_{jj'}\right) f_j \tag{2.118}$$

where $\bar{\bar{\mathcal{D}}}_{jj'}$ is a diffusion tensor while the vector $\mathbf{R}$ represents drag, explicitly showing that the Landau-Boltzmann equation is an advection-diffusion operator in particle velocity space. It can also be shown that the operator of Eq. (2.118) ensures local conservation of particles, energy and momentum, as well as the H-theorem for entropy production [36]. In order to derive a consistent collisional gyrokinetic model, one needs to transform the operator given in Eq. (2.118) first to guiding center and then to gyrocenter coordinates to be able to integrate it into Eq. (2.88). As a result, one obtains a collision operator which is a mixed operator in configuration and velocity gyrocenter variables. This complication is avoided in the GENE code by ignoring the difference between F and $\bar{F}$ when evaluating collisions in the gyrocenter equations. Furthermore, the guiding center collision operator still has a gyroangle dependency, as the guiding center transformation is designed to remove the gyrophase only from the collisionless Vlasov equation only. This dependence is also neglected accounting only for the gyroangle-independent part.

2.6 Microinstabilites

A proper description of microinstabilities with the purpose of understanding and estimating the related transport, requires to solve the nonlinear gyrokinetic Vlasov-Maxwell system of equations previously derived. This task is extremely challenging and can lead to a large variety of instabilities depending on the particular considered plasma parameters. These modes are characterized by a wide range of frequencies and wavelengths. Nevertheless, some classification among them can be made. One usually distinguishes between electrostatic and electromagnetic instabilities, depending on the nature of the dominant fluctuating field. Other typical distinctions are made considering the type of wave dynamics e.g. drift waves, sound waves or Alfvénic modes. One can also separate between instabilities driven by trapped or passing particles. As a result, a large number of microinstabilities have been identified in literature, for which dispersion relations are derived under specific limits. It must however be emphasized that all these distinctions are usually made possible thanks to model simplifications (in particular linearization), as well as the choice of a specific subset of plasma parameters. Under realistic conditions, many of these instabilities coexist: they are unstable at the same time and interact linearly and nonlinearly with each other. Therefore, for most practical purposes a numerical approach must be considered and it might not always be obvious how to classify a specific result. In the following, the most relevant microinstabilities for this work are briefly discussed focusing mainly on physical interpretation rather than on mathematical derivations. A more detailed description can be fond elsewhere, see e.g. Ref. [22].
Besides the single particle drifts, collective diamagnetic drifts can result from the plasma pressure gradient. Considering a Maxwellian distribution and expanding to first order in ρ/L_c, one can evaluate a fluid-like average velocity as

$$\mathbf{v}_{\text{dia}} = \int \mathbf{v} f_0 \mathrm{d}\mathbf{v} = -\frac{\nabla p \times \mathbf{B}}{nqB^2}. \tag{2.119}$$

The diamagnetic drift can thus be expressed as $\mathbf{F} \times \mathbf{b}/qB$, where the force $\mathbf{F} = -\nabla p/n$ is the macroscopic force related to temperature and density gradients. The inhomogeneous magnetic field can thus lead to the so-called drift waves and microinstabilities which propagate perpendicularly to $\mathbf{B}$ at a velocity $\sim \mathbf{v}_{\text{dia}}$. One therefore defines the corresponding diamagnetic drift frequency $\omega^* = \mathbf{k} \cdot \mathbf{v}_{\text{dia}}$, where $\mathbf{k}$ is the mode wavevector. The drift frequency can be further decomposed into a density and a temperature drift frequency, $\omega^* = \omega_n + \omega_T$, where $\omega_n = k_\theta T \nabla n / nqB$ and $\omega_T = k_\theta \nabla T/qB$, k_θ being the poloidal wavenumber.

In a toroidal system, any perturbed quantity $\mathcal{A}(\psi, \chi, \varphi)$ can be represented as a superposition of poloidal and toroidal Fourier modes m and n respectively as:

$$\mathcal{A}(\psi, \chi, \varphi) = \sum_{m,n} \hat{\mathcal{A}}(\psi) \mathrm{e}^{\mathrm{i}(m\chi + n\varphi)}, \tag{2.120}$$

where χ is the so-called straight-field-line poloidal angle, a modified poloidal angle such that the magnetic pitch $\mathrm{d}\varphi\mathrm{d}/\chi = q(\psi)$ is constant and equal to the safety factor $q(\psi)$ on a given flux-surface labelled by ψ (see also Equation (3.1) for the actual definition of χ). The relation $\nabla\mathcal{A} \sim \mathrm{i}\mathbf{k}\mathcal{A}$ provides the wavevector associated to a given (m, n) Fourier mode: $\mathbf{k} = m\nabla\chi + n\nabla\varphi$. The projection along the magnetic field gives the parallel wavenumber $k_\parallel$:

$$k_\parallel = \frac{\mathbf{k}\cdot\mathbf{B}_0}{B_0} = \frac{1}{B_0 J^{\psi,\chi,\varphi}}(nq(\psi) - m) \simeq \frac{1}{R_0 q(\psi)}(nq(\psi) - m), \tag{2.121}$$

with $J^{\psi,\chi,\varphi}$ is the Jacobian of the (ψ, χ, φ) coordinate system:

$$J^{\psi,\chi,\varphi} = \frac{1}{|(\nabla\psi\times\nabla\chi)\cdot\nabla\varphi|} = \frac{Rq(\psi)}{B_\varphi}. \tag{2.122}$$

In the last expression we have made use of the safety factor $q(\psi)$ defined in Eq. (2.8). For field-aligned modes $k_\parallel \sim 0$, therefore $m \sim nq$. Fluctuations thus acquire a phase dependence $\sim \exp[\mathrm{i}(n(\varphi - q\chi)]$ and are associated to the wavevector

$$\mathbf{k} = n\left[\frac{\mathrm{d}q}{\mathrm{d}\psi}\chi\nabla\psi + q\nabla\chi + \nabla\varphi\right]. \tag{2.123}$$

Finally, the time dependence of microinstabilities is typically expressed as $\sim \exp(-\mathrm{i}\omega_r t + \gamma t)$, where ω_r provides the real frequency and γ the damping of the mode.

2.6.1 Drift waves

In slab geometry, where the magnetic field has no curvature, drift waves are together with the slab-ITG and -ETG (which will be discussed in the following) the dominant instability. They are electrostatic fluctuations, driven unstable by a plasma density gradient. Since their wavelength and frequency are in agreement with experimental observation of turbulent transport, drift waves are often considered as the paradigm of microturbulence in a magnetized plasma.

The basic principle of a drift wave is represented in Figure 2.5. Consider a homogeneous magnetic field $\mathbf{B}$ and a plasma characterized by a background density gradient ∇n in the direction perpendicular to $\mathbf{B}$. We are interested in the evolution of a density potential perturbation δn possessing a finite parallel wave vector $k_\parallel$. Its dynamics is entirely determined by the behaviour of the electrons. If one assumes that the response of the electrons is adiabatic, then any density perturbation is in phase with an electrostatic potential perturbation $\delta\phi$, see Eq. (2.106). As a result, the potential will increase inside the regions of positive density fluctuation and vice-versa, resulting in a net electric field leading in turn to an $\mathbf{E}\times\mathbf{B}$ drift. As a consequence of the background density gradient, the particle flux associated to the $\mathbf{E}\times\mathbf{B}$ velocity results in an increase of the initial perturbation in the region where $v_{\mathbf{E}\times\mathbf{B}}$ and ∇n are anti-parallel and in a decrease

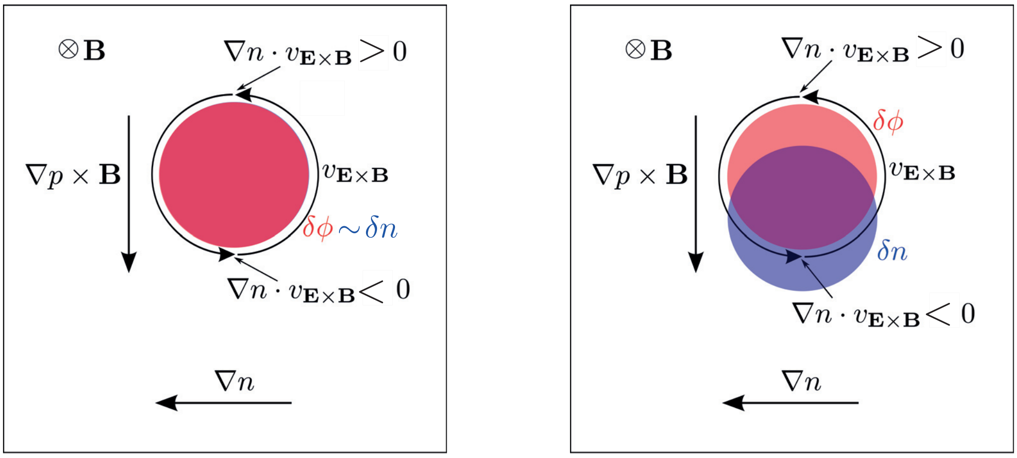
$\otimes\mathbf{B}$
$\nabla n \cdot v_{\mathbf{E}\times\mathbf{B}} > 0$
$\nabla p \times \mathbf{B}$
$v_{\mathbf{E}\times\mathbf{B}}$
$\delta\phi \sim \delta n$
$\nabla n \cdot v_{\mathbf{E}\times\mathbf{B}} < 0$
∇n
$\otimes\mathbf{B}$
$\nabla n \cdot v_{\mathbf{E}\times\mathbf{B}} > 0$
$\delta\phi$
$\nabla p \times \mathbf{B}$
$v_{\mathbf{E}\times\mathbf{B}}$
δn
$\nabla n \cdot v_{\mathbf{E}\times\mathbf{B}} < 0$
∇n

Figure 2.5 : Cartoon of a drift wave in a plasma with a background density gradient. On the left, the density and potential perturbations (respectively δn and $\delta\phi$) are in phase, hence the advection due to $\mathbf{E} \times \mathbf{B}$ velocity cause the perturbations to propagate in the electron diamagnetic direction $v_{d,e}$. On the right, the perturbations are out of phase. In this case the density perturbation is sustained by the $\mathbf{E} \times \mathbf{B}$ flow, thus resulting in an instability. Picture inspired by [22].

where they are parallel. This causes the initial perturbation to propagate in the electron diamagnetic direction, given by $v_{d,e} = \nabla p_e/(n_{0,e}eB^2) \times \mathbf{B}$.
The drift wave can become unstable if the assumption of adiabatic electrons is relaxed. In particular accounting for the resonant wave-particle interactions. In this case, δn and $\delta\phi$ are characterized by a non-zero cross phase and if the density perturbation is out of phase with the potential perturbation, then the $\mathbf{E} \times \mathbf{B}$ flow leads to an amplification of δn and to a net outwards transport.
When extending the drift wave picture to a tokamak one has to realize that, as a result of a more complex magnetic geometry, particles are now subject to drifts associated to curvature and gradients of the magnetic field. Furthermore, the inhomogeneity of the magnetic field leads to a separation of particles into trapped and passing. Both the aforementioned effects are at the origin of the destabilization of two of the experimentally most relevant microinstabilities, namely Ion Temperature Gradient modes and Trapped Electron Modes.

2.6.2 ITG

Ion Temperature Gradient (ITG) instabilities are drift-wave type modes driven by the temperature gradient of ions. Contrary to pure density gradient driven drift waves, ITGs are non-resonant waves. They have first been identified by Horton, Choi and Tang [37], and are believed to be one of the main microinstabilities responsible for the ion temperature and density fluctuations measured in the core of today's tokamaks.
The so-called slab-ITG is an ion acoustic wave that may become unstable in a plasma

with a uniform magnetic field may because of the ion temperature gradient. The toroidal geometry of a tokamak modifies the slab-ITG into an interchange-like instability, the so-called toroidal-ITG, whose nature is similar to the Rayleigh-Taylor instability that develops when a denser fluid is above a lighter one.

Toroidal-ITG modes can become unstable when the ion temperature gradient∇T_i is parallel to the gradient of the magnetic field amplitude ∇B while it is stable if ∇T_i and ∇B are anti-parallel. Therefore, when looking at the toroidal geometry of a tokamak one refers to a region of *good curvature*, the inner part of the machine corresponding to the high B field side, where pressure and magnetic field gradients point in opposite directions, and a *bad curvature* region, corresponding to the low B field side, where they are parallel. A simple picture of the instability is as follows. Assuming an initial pressure perturbation δp, because of the vertical ∇B and curvature drifts (see Eqs. (2.75) and (2.72) respectively), a charge separation is generated, which in turn induces a charge independent $\mathbf{E} \times \mathbf{B}$ drift. At the high field side, this drift acts against the perturbation therefore stabilizing it, but at the low field side it amplifies it, as depicted in Figure 2.6. The temperature and density perturbations grow and become unstable (this mechanism is equivalent to the one described in Section 2.6.1).

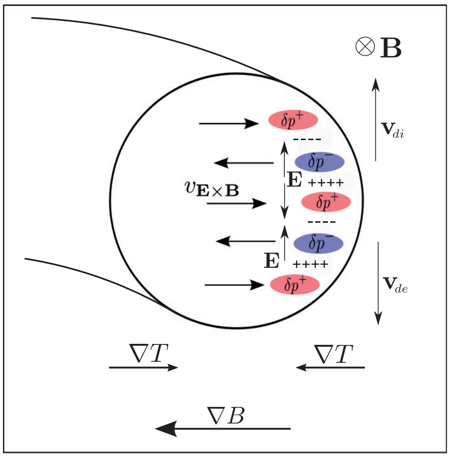

Figure 2.6 : Schematic representation of an ITG instability at the low field side of a tokamak. Assuming an initial pressure perturbation δp, the vertical drifts associated to ∇B and curvature cause a charge separation which produces a perturbed electric field $\mathbf{E}$. As a result of the $\mathbf{E} \times \mathbf{B}$ flow, the perturbation grows. At the high field side, ∇T and ∇B point in opposite directions, therefore the $\mathbf{E} \times \mathbf{B}$ advection cancels the initial perturbation. Adapted from [38].

In order to derive a dispersion relation for toroidal ITG modes, we follow Ref. [39]. Being an ion instability, one needs a kinetic model only for describing the ion dynamics while an adiabatic electron response can be assumed. From the quasineutrality condition one obtains:

$$\epsilon(\mathbf{k},\omega) = \frac{1}{k^2\lambda_{De}^2} + \frac{1}{k^2\lambda_{Di}^2}\left[1 + (\omega - \omega'_{Ti}) \int \mathrm{d}^3 v \frac{f_{0i}}{n_{0i}} \frac{J_0^2(\frac{k_\theta v_\perp}{\Omega})}{k_\parallel v_\parallel + \omega_{di} - \omega}\right] = 0, \qquad (2.124)$$

where $\epsilon(\mathbf{k},\omega)$ is the plasma dielectric function, $\lambda_{Di,e}$ the Debye length of ions and electrons, and J_0 the Bessel function of the first kind describing Finite Larmor Radius (FLR) effects. Moreover, ω'_T is an operator providing the temperature drift frequency, $\omega'_{Ti} = (k_\theta T_i \nabla T_i/qB)\partial/\partial T_i$, while ω_{di} is the drift frequency $\omega_{di} = \mathbf{k}\cdot(\mathbf{v}_{\nabla B} + \mathbf{v_c})$ related to ∇B and curvature drifts. Note that the density gradient has intentionally been neglected to point out how the ion temperature gradient is sufficient to generate the plasma instability.

Taking a fluid-like limit $|\omega/(k_\parallel v_{th,i})| \ll 1$, assuming $|\omega/\omega_{di}| \ll 1$ and neglecting all FLR corrections, $J_0 \sim 1$, Eq. (2.124) reduces to

$$1 - \left(1 - \frac{\omega_T}{\omega}\right)\left[\left(\frac{k_\parallel c_s}{\omega} + \frac{T_e}{T_i}\frac{\langle\omega_{di}\rangle}{\omega}\right)\right] = 0 \tag{2.125}$$

where $\langle\omega_{di}\rangle = 2T_i k_\theta |\nabla_\perp \log B|/eB$, and the temperature derivative contained in ω'_T has been explicitly carried out.

Equation (2.125) provides an instability even in the limit $k_\parallel \to 0$, as assuming $|\omega| \ll |\omega_T|$ it reduces to

$$1 + \frac{T_e}{T_i}\frac{\langle\omega_{di}\rangle}{\omega^2} = 0, \tag{2.126}$$

which admits the solutions

$$\omega = \pm\sqrt{-2\frac{T_e}{T_i}(k_\theta\rho_i)^2\nabla\log T\cdot\nabla\log B}. \tag{2.127}$$

The toroidal-ITG is thus unstable if $\nabla T_i \cdot \nabla B > 0$, which, as already mentioned, is the case at the low field side of a tokamak.

2.6.3 ETG

At sufficiently short perpendicular wavelengths, the perpendicular perturbation felt by the ions is averaged out by their gyromotion. As a result, their response becomes essentially adiabatic. At the same time, electrons do not respond adiabatically anymore, and a kinetic model must be used to describe their dynamics. Under these conditions, a sufficiently large gradient in the electron temperature can develop an instability, the Electron Temperature Gradient (ETG) mode. In the linear, electrostatic, adiabatic limit, ETGs are basically isomorphic to ITGs i.e. they can be considered equivalent switching the role of ions with the one of electrons. Even though the associated turbulence develops on hyperfine scale in comparison with ITG, it has been shown that it can lead to significant electron heat fluxes [40]. Moreover, modes developing at ion scales can interact non-linearly with modes at the electron scales making numerical modeling of such conditions particularly challenging.

2.6.4 TEM

Trapped Electron Modes (TEM) are waves that can become unstable in a magnetically confined plasma as a result of a resonant interaction between an electrostatic perturbation and the toroidal precessional drift of trapped electrons. First described by Kadomtsev and Pogutse in Ref. [41], they are nowadays the main candidate invoked to explain the anomalous heat and particle transport through the electron channel.

A simple physical picture of the instability is as follows. Because of the inhomogeneity of the magnetic field, one can distinguish between trapped and passing particles. We focus here on instabilities associated to trapped electrons; one can develop a similar model for the Trapped Ion Mode (referred to in literature as TIM). The former class of particles, thanks to their high parallel velocity, are free to move along a magnetic field line and ensure an adiabatic response to slow waves ($|\omega/k_\parallel v_{th}| \ll 1$). Trapped particles instead are forced to bounce back and forth in the outer low field side of the tokamak because of the mirroring effect induced by the confining magnetic field. As already mentioned, they describe a trajectory whose projection on a poloidal plane assumes the shape of a banana. Because of the combination of parallel motion and vertical drifts, once an average over many bounces is evaluated, it turns out that trapped particles drift in the toroidal direction with a velocity $\langle\dot{\varphi}\rangle_b$. Thus, in the presence of a perturbation they do not average out the effect of the associated field but instead may interact resonantly with it, giving rise to an instability.

In order to derive a dispersion relation valid for TEM, which can then be used to intuitively illustrate how the plasma shaping can play a key role in controlling such instability, we shall follow Ref. [42].

Electron dynamics can be modeled using the drift kinetic equation i.e. particle positions are assumed to be equivalent to their guiding centers. Furthermore, typical perturbation frequencies are usually much smaller than the bounce frequency ω_{be}.

It is therefore possible to replace the drift kinetic equation for electrons with its bounce averaged equivalent:

$$\left(\frac{\partial}{\partial t} + \langle\dot{\varphi}\rangle_b \frac{\partial}{\partial \varphi}\right)\tilde{g}_e = -\left(\frac{e f_{0e}}{T_e}\frac{\partial}{\partial t} - \frac{1}{B_p}\frac{\partial f_{0e}}{\partial x}\frac{\partial}{\partial \varphi}\right)\langle\phi\rangle_b, \tag{2.128}$$

which is obtained by averaging the original equation over a bounce period [42]. Here $\langle\dot{\varphi}\rangle_b$ is the toroidal precessional drift frequency, while $\langle\cdots\rangle_b$ indicates a bounce-averaging procedure, defined as:

$$\langle\cdots\rangle_b = \frac{\omega_b}{2\pi}\int\limits_{\text{orbit}} \frac{\mathrm{d}l}{v_\parallel}. \tag{2.129}$$

The background electrons distribution f_{0e} is assumed Maxwellian, while $\tilde{g}_e$ indicates the fluctuating non-adiabatic part of the electron distribution:

$$\tilde{g}_e = \tilde{f}_e - \frac{e\phi}{T_e} f_{0e} \tag{2.130}$$

Considering now a perturbation of the form $\exp\left[\mathrm{i}(\omega t - n\varphi)\right]$, one can solve Eq. (2.128) (see Ref. [42] for details) obtaining for the non-adiabatic perturbed distribution function:

$$\tilde{g}_e = -\frac{e f_{0e}}{T_e} \frac{\omega - \omega_e^*}{\omega - n\langle\dot{\varphi}\rangle_b} \langle\phi\rangle_b \tag{2.131}$$

where

$$\omega_e^* = \omega_{ne} + \omega'_{Te} = \frac{k_\theta T_e}{eB}\left(\frac{\mathrm{d}\log n_e}{\mathrm{d}x} + \nabla T_e \frac{\partial}{\partial T_e}\right). \tag{2.132}$$

The quasineutrality condition allows one to derive the relevant dispersion relation. Assuming for simplicity $\langle\phi\rangle_b \simeq \phi$ and carrying out the necessary velocity space integrals, one finally obtains

$$\begin{split}\frac{T_i}{T_e} + \frac{T_i}{T_e}\frac{2\alpha_t}{\omega_{\varphi,e}}\left[\left(\omega - \omega_{ne}\left(1 - \frac{3}{2}\eta_e\right)\right)W(z_{b,e}) - \omega_{n,e}\eta_e\left(\frac{\omega}{\omega_{\varphi,e}}W(z_{b,e}) + \frac{1}{2}\right)\right] + \\ + 1 - \int \mathrm{d}\mathbf{v}\frac{f_{0i}}{n_{0i}}\frac{\omega - \omega_i^*}{\omega - k_\parallel v_\parallel - \omega_{di}} = 0.\end{split} \tag{2.133}$$

where α_t is the fraction of trapped particles and $\eta_e = \mathrm{d}\log T_e/\mathrm{d}\log n_e$. $W(z)$ is the plasma dispersion function while $z_b = \mathrm{sign}(\omega_\varphi)\sqrt{2\omega/\omega_\varphi}$, with $\omega_\varphi = n\langle\dot{\varphi}\rangle_b$.
The previous relation in fact describes not only TEM modes but also ITG, showing how those modes can be strongly coupled depending on their relative drives. Indeed neglecting trapped particles ($\alpha_t = 0$) one recovers in the proper limit the dispersion relation provided by (2.124), in this case retaining in ω_i^* also the effect of a ion density gradient, which previously was neglected.
A dispersion relation for a pure TEM mode can be obtained from Eq. (2.133) by dropping the parallel and perpendicular ion drives ($k_\parallel, \omega_{gi} = 0$). In this case Eq. (2.133) becomes

$$\frac{T_i}{T_e} + \frac{T_i}{T_e}\frac{2\alpha_t}{\omega_{\varphi,e}}\left[\left(\omega - \omega_{ne}\left(1 - \frac{3}{2}\eta_e\right)\right)W(z_{b,e}) - \omega_{n,e}\eta_e\left(\frac{\omega}{\omega_{\varphi,e}}W(z_{b,e}) + \frac{1}{2}\right)\right] + \frac{\omega_{ni}}{\omega} = 0. \tag{2.134}$$

Assuming also $|\omega_{\varphi,e}/\omega| \ll 1$, considering isothermal ions and electrons, one can estimate a typical growth rate and frequency as:

$$\omega_r \simeq \omega_{n,e} \qquad \gamma \simeq \sqrt{\frac{3}{2}\alpha_t \omega_{\varphi,e}\omega_{n,e}\left(1 + \frac{\mathrm{d}\log T_e}{\mathrm{d}\log n_e}\right)}. \tag{2.135}$$

Equations (2.133) and (2.135) clearly show how the toroidal precessional drift is the crucial element in determining the instability of TEM modes and their growth rate. It is therefore also a way of controlling this kind of modes, as by modifying $\langle\dot{\varphi}\rangle_b$ one can in turn strongly affect the growth rate of the mode.

One first notes that the resonant process behind the instability takes place only if the toroidal drift is in the same direction as the propagation direction of the perturbation. Hence, changing the drift direction will naturally lead to a TEM suppression. As shown in Ref. [42], in the limit of large aspect ratio, circular concentric flux surfaces (zero Shafranov shift), the precessional drift can be expressed in terms of elliptic integrals, related to particle energy, and it is a function of the magnetic shear $\hat{s}$. In particular, one finds that barely passing and deeply trapped particles drift in opposite directions regardless of the values of $\hat{s}$. More generally, trapped particles can drift in different directions depending on the magnetic shear and their pitch angle, thus resonating or not with a given perturbation.

Plasma shaping is another way of actively changing $\langle\dot{\varphi}\rangle_b$, as single particle motion, and therefore also its precessional drift, is ultimately related to the magnetic geometry. The effect of each single shaping parameter on the actual drift frequency is in general dependent on all the other shaping coefficients, and furthermore dependent on whether one is considering deeply or barely passing particles. For a detailed discussion, we refer the reader to Refs. [17] and [43]. Some general trends can nonetheless be identified: elongation κ acts reducing the drift of deeply trapped particles while it increases the one of barely passing. An increase of triangularity δ increases the drift frequency of deeply trapped particles, while lowers the toroidal drift of barely trapped. As an illustrative example we plot the toroidal drift frequency as a function of the bouncing angle in Figure 2.7 for a triangularity scan. These simulations have been performed with the VENUS [44] code, which solves for the particle orbits in a confining magnetic field. Starting from the plasma shape of a TCV discharge with $\delta_{|rmLCFS} = 0.4$ (see also 5), the magnetic geometry is modified by varying the LCFS while keeping the q profile fixed. According to the parametrization of Eq. (2.9), only elongation and triangularity are kept as shaping coefficients.

One has also to remember that when changing triangularity, one is also changing the penetration of κ towards the core, which is favoured by lower δ, and, at the same time, increasing the Shafranov shift, resulting in a larger flux compression at the low field side. In this respect, evaluating the effect of shaping on trapped particle instabilities is a complicated exercise, and a numerical approach must be used.

In addition to the effect on drifts, plasma shaping changes also the turbulent drives, as for given density and temperature profiles $n(x)$, $T(x)$, the true gradients leading to instabilities are $\langle|\nabla(n,T)|\rangle_{\mathrm{fs}} = |\mathrm{d}(n,T)/\mathrm{d}x|\langle|\nabla x|\rangle_{\mathrm{fs}}$, with $\langle|\nabla x|\rangle_{\mathrm{fs}}$ modified by the actual magnetic geometry. Moreover, one has to consider the whole range of particle energies and in particular examine the behaviour of the particles which contribute dominantly to the nonlinear fluxes.

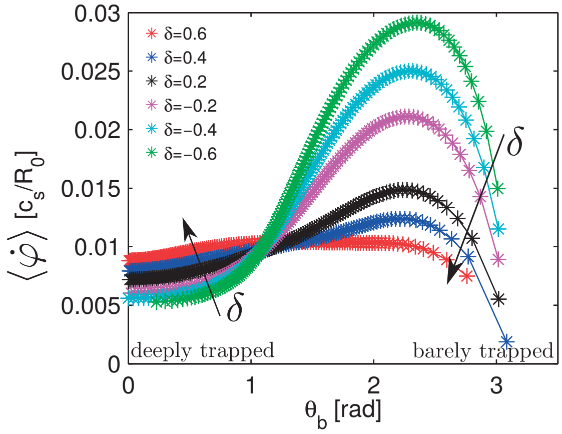

Figure 2.7 : Toroidal precessional drift frequency $\langle\dot{\varphi}\rangle$ as a function of the bounce angle θ_b. The shape of the LCFS is varied starting from a TCV experimental discharge with $\kappa_{\mathrm{LCFS}} = 1.2$ and $\delta_{\mathrm{LCFS}} = 0.4$ by the triangularity of the plasma boundary. The drift are then simulated following thermal electrons ($\mathcal{E}$ =568 eV as measured in TCV) from their initial radial location $\rho_{tor} = 0.75$. Arrows indicate increase in δ. Results obtained with the VENUS code.

2.6.5 Other instabilities

Many other important microinstabilities have been studied in recent years, thanks also to numerical simulations. Among them, an important class that one needs to point out is the *electromagnetic* one, for which, as the name suggests, fluctuations are dominantly magnetic. Examples of this kind of modes are Micro-Tearing Modes (MTM), the equivalent on a microscopic scale of the MHD tearing mode and which have been recently suggested as another possible candidate to explain transport through the electron channel [45], or Kinetic Ballooning Modes (KBM) [46]. Other physically relevant instabilities are Resistive Ballooning Modes (RBM), recently suggested as a possible candidate to describe turbulence in the edge region of tokamak plasmas [47], or Parallel Velocity Gradient (PVG) modes [48], instabilities whose drive is the gradient of the parallel velocity.

2.7 Zonal Flows and the Geodesic Acoustic Mode

Zonal flows are collective plasma flows of particular interest because in certain regimes they are able to self-regulate turbulence. Similar flows have been observed in meteorology in form of large scale flows along latitudinal lines. In the context of magnetic confinement, zonal flows indicate a plasma flow resulting from a difference between the electrostatic potential on neighbouring flux surfaces. The corresponding radial electric field $\mathbf{E}_r$ consequently leads to an $\mathbf{E} \times \mathbf{B}$ rotation of the plasma in the poloidal direction. If this flow is stationary, then it is normally referred to as Zonal Flow (ZF).

What makes zonal flows of particular interest for fusion research is their capability to

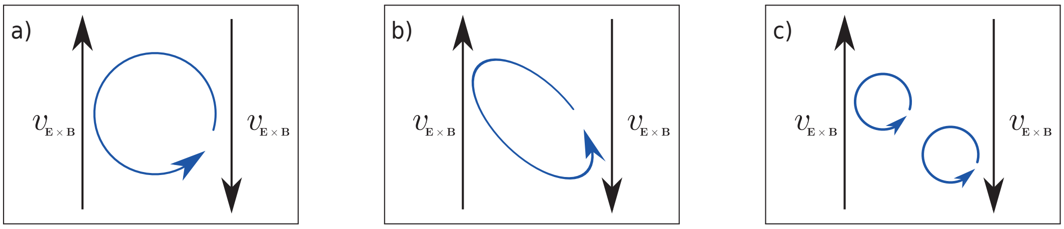

Figure 2.8 : Schematic representation of the zonal flows shearing turbulent eddies. (*a*) A vortex moves across a region of strong sheared flows, (*b*) it gets sheared, and (*c*) eventually is torn apart into smaller scale vortices.

reduce the turbulent diffusion via turbulent eddy-shearing. The mechanism leading to this suppression is sketched in Figure 2.8. A detailed description can be found in e.g. Refs. [49, 50]. Let us consider a series of radial layers with alternating poloidal $v_{\mathbf{E}\times\mathbf{B}}$ flow directions. When turbulent eddy move radially across them, they get distorted as a result of the different flow speed, leading to the so-called shearing rate $\omega_{\mathbf{E}\times\mathbf{B}} = \mathrm{d}v_{\mathbf{E}\times\mathbf{B}}/\mathrm{d}r$. Provided that the shearing rate is sufficiently high, vortices will eventually break into smaller scale ones. This dynamics is clearly reducing the radial correlation length over which turbulence can develop.

Zonal flows can be excited nonlinearly by the turbulence itself, thus providing a self-regulating mechanism for the associated transport. The stabilizing effect is proportional to the shearing rate, however there is a level above which ZFs themselves become unstable. The maximum amplitude level is associated to a Kelvin-Helmholtz-type instability, which transfers energy back from the zonal flows to the turbulent fields. A balance between microinstabilities driving the turbulence and flows leading to its suppression therefore develops, and can be described via a predator-prey model [49].

In general, the interaction of zonal flows with turbulence and their efficiency in tearing apart turbulent structures, thus reducing transport, is strongly related to the type of modes at play. While for ITG-driven turbulence it is well established that zonal flows are indeed the main saturation mechanism [51], for TEM dominated plasmas the picture it is not yet fully understood. Depending on plasma parameters, one can distinguish regimes where ZFs are more or less relevant in setting their saturated transport level [52], and other mechanisms might be required in order to explain the nonlinear saturation [53].

The Geodesic Acoustic Mode (GAM) is a finite frequency Zonal Flow, characterized by a dominant $n = 0$, $m = 1$ density fluctuation component. As its name suggests, it is associated to the geodesic curvature of a given flux surface, that is the component of the curvature vector tangent to the magnetic surface, enabling it to couple to sound waves. From the definition of the curvature vector $\boldsymbol{\kappa}$, making use of the MHD radial

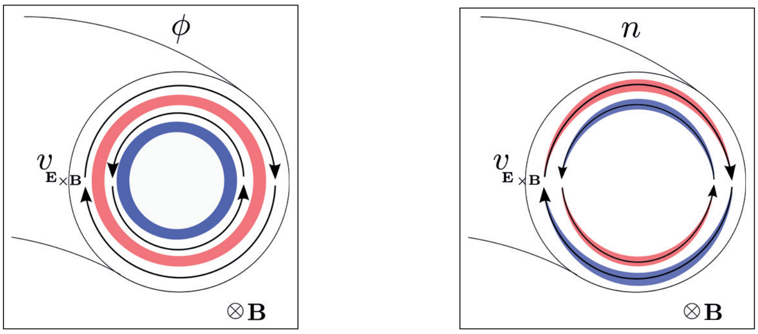
ϕ
$v_{\mathbf{E}\times\mathbf{B}}$
$\otimes\mathbf{B}$
n
$v_{\mathbf{E}\times\mathbf{B}}$
$\otimes\mathbf{B}$

Figure 2.9 : Schematic representation of $\mathbf{E}\times\mathbf{B}$ zonal flows. On the left, the electrostatic potential, characterized by $n = m = 0$ toroidal and poloidal components is shown, together with the resulting $\mathbf{E}\times\mathbf{B}$ flows. On the right it is depicted the resulting density fluctuation in case of finite frequency ZFs, which in case of circular flux surfaces is dominated by the $m = 1$ harmonic.

force balance given in Eq. (2.1) and of Ampére's law, one can write

$$\boldsymbol{\kappa} \equiv (\mathbf{b}\cdot\nabla)\mathbf{b} = \frac{1}{B^2}\nabla_\perp\left(\frac{B^2}{2} + \mu_0 p\right). \tag{2.136}$$

It thus clearly appears that $\boldsymbol{\kappa}$ is always perpendicular to the magnetic field, and any contribution to the geodesic curvature must come from the gradient in the magnetic field strength B ($\nabla_\perp p = \nabla p = \mathrm{d}p/\mathrm{d}\psi\nabla\psi$). Therefore any component of the geodesic curvature is either parallel or anti-parallel to the $\mathbf{E}\times\mathbf{B}$ direction. The origin of the oscillating nature of the flow associated to the GAM can then be intuitively understood with the help of ideal MHD. Because of magnetic flux conservation [3], any flux tube gets compressed when they moving into region of high magnetic field and vice versa. A parallel flow naturally allows to compensate this compression. Therefore, zonal flows are associated to the divergence of the corresponding density flows. If the parallel flow is sufficient to cancel the density flow divergence, then a stationary zonal flow develops. Otherwise a pressure perturbation builds up eventually leading to the inversion of the flow which then becomes oscillatory. In the limit of circular flux-surfaces, the curvature is essentially along the negative major radius direction, thus the divergence of the density flux is maximum (resp. minimum) at the top (resp. bottom) of the plasma resulting in an $m = 1$ poloidal dependency, as schematically depicted in Figure 2.9.
The GAM has been first predicted by Winsor *et al.* [54] when studying the MHD model in a toroidal geometry. The mode frequency ω_{GAM} was identified as

$$\omega_{\mathrm{GAM}} = \sqrt{\frac{2(T_e + \gamma_i T_i)}{m_i}}\frac{1}{R_0}\sqrt{2 + q^{-2}}, \tag{2.137}$$

with γ_i the adiabatic index of ions. Since then, many investigations, both theoretical and experimental, have been carried out, in particular motivated by the experimental GAM measurements in the edge of various tokamaks (see Ref. [55] and references therein for a

review).
From a theoretical point of view, one has to remember that zonal flows are primarily poloidal flows, therefore they are, at least linearly, not affected by the radial pressure gradient and cannot cause any radial transport. In other words, they are linearly stable.
As already mentioned, turbulence can however nonlinearly excite these modes affecting also their frequency. The original linear frequency estimate proposed by Winsor (2.137) has been generalized adopting a kinetic model (see e.g. Ref. [56]) and also to non-circular plasma equilibria [57].
Equation (2.137), and the more accurate estimates mentioned, provide a frequency which in the presence of magnetic shear or temperature gradients is function of the radial location. Therefore, the GAM appears as a radially localized oscillating plasma flow.
Regimes in which discrete eigenmodes exist, i.e. the GAM frequency is predicted to be constant over a finite radial extent, have been identified, and related to both finite ion Larmor radius effects [58] and electromagnetic fluctuations [59, 60]. In general, predicting the nonlinear frequency and location of the GAM is a very challenging exercise because it requires the knowledge of the turbulent drives [61].
Finally, motivated also by experimental evidence [62], the magnetic perturbation associated to the GAM has been investigated as well, identifying a dominant m=2 poloidal [63] component, with higher poloidal harmonics possibly excited in shaped plasmas [60].

2.8 Summary

In this chapter, the gyrokinetic system of equations has been derived. It constitutes the basis for all the numerical simulations that will be discussed in this work. The equations are correct up to order ϵ and can be used to describe electrostatic and electromagnetic fluctuations in a confined plasma, taking into account radial variations of background density and temperature profiles. Simplifications, leading to the so-called local (flux-tube) limit have been discussed together particular with limits of the gyrokinetic model for which field equations can be greatly simplified. The following chapter will present the numerical implementation of the gyrokinetic equations in the GENE code.

3 Numerical simulation model: the GENE code

The GENE (Gyrokinetic Electromagnetic Numerical Experiment) code is the numerical tool used for carrying out all the microturbulence simulations that will be presented in the following chapters. It is an Eulerian gyrokinetic code which solves the time evolution of the distribution function of each plasma species on a fixed grid in phase space.

Initiated by F. Jenko [12] and further developed by T. Dannert [29], the code was originally solving the time evolution of both electrostatic and electromagnetic fluctuations on a flux-tube following a field line around the tokamak. This constitutes the so-called *local* approach introduced in section 2.4.6. The first implementation of the collision operator, as well as the possibility of running the code in its spectral version thus determining the eigenvalues of the system, is due to F. Merz [33]. The code has then been furthermore generalized so as to be able to account for radial variations of background profiles (geometrical coefficients as well as temperature and density profiles) in the so-called *global* approach by T. Görler [64, 65] and X. Lapillonne [32], together with a first implementation of the required heat sources. Improvements of the collision operator, in particular ensuring conservation properties, as well as the implementation of a neoclassical solver for solving only the axisymmetric modes, are due to H. Doerk [35]. Additional developments, including among others the possibility of simulating background flows in the local limit, as well as particle sources required for carrying out global simulations with gyrokinetic electrons, have been introduced by D. Told [30].

In this work GENE has been exploited in order to model plasmas under TCV relevant conditions, and only minor modifications to the code have been made. The aim of this chapter is thus to provide a brief description of the essential features of the code and the fundamental numerical techniques employed. A more detailed description can be found in the specific GENE documentation [66], and in all aforementioned references.

All simulations presented here are carried out considering axisymmetric geometries. We remark that GENE can currently handle also non-axysimmetric (i.e. stellarator-like) systems in its so-called y-global version [67], a capability that will not be addressed here.

3.1 Phase space coordinate system

Configuration space

As already discussed, turbulence is characterized by a strong anisotropy, with much longer wavelengths in the parallel than in the perpendicular direction ($k_\| \ll k_\perp$). It is therefore very convenient for any numerical representation to use a coordinate system which reflects this property, so as to reduce the computational cost otherwise required to properly resolve turbulent structures. This can be obtained adopting the so-called *field-aligned* coordinates. A description of how such a coordinate system can be introduced for any magnetic configuration can be found in e.g. Ref. [14].

For an axisymmetric system, one first introduces a straight-field-line coordinate system (ψ, χ, φ) where ψ is the poloidal flux function given in Eq. (2.5), χ is the straight-field-line poloidal angle, defined in terms of the geometrical poloidal angle θ as

$$\begin{aligned}\chi &= 2\pi \int_0^\theta \frac{\mathbf{B}\cdot\nabla\varphi}{\mathbf{B}\cdot\nabla\theta'} d\theta' \Bigg/ \oint \frac{\mathbf{B}\cdot\nabla\varphi}{\mathbf{B}\cdot\nabla\theta'} d\theta' \\ &= 2\pi \int_0^\theta \frac{1}{R^2}\frac{1}{\mathbf{B}\cdot\nabla\theta'} d\theta' \Bigg/ \oint \frac{1}{R^2}\frac{1}{\mathbf{B}\cdot\nabla\theta'} d\theta' \\ &= \frac{F(\psi)}{q(\psi)} \int_0^\theta \frac{1}{R^2}\frac{1}{\mathbf{B}\cdot\nabla\theta'} d\theta',\end{aligned} \tag{3.1}$$

and φ is the toroidal angle. The field-aligned coordinate system (x, y, z) adopted in GENE is then defined as

$$\begin{cases} x - x_0 = C_x(\psi), \\ y = C_y\left[q(\psi)\chi - \varphi\right], \\ z = \chi, \end{cases} \tag{3.2}$$

where the x coordinate defines the radial direction, while y is called the binormal one. Finally, z parametrizes the position along a field line and therefore is referred to as the "parallel" direction. It is to be noted that in practice the choice of the radial coordinate x is dependent on the specific magnetic equilibrium used. C_y is a normalization constant, chosen as $C_y = x_0/q_s$, in order to establish y as a length rather than an angle-like quantity. $q_s = q(x_0)$ indicates the local safety factor evaluated at $x = x_0$, a reference radial position usually assumed as the center of the simulation domain. Note that both (ψ, χ, φ) and (x, y, z) are non-orthogonal coordinate systems.

The magnetic field $\mathbf{B}$ can be written with respect to either (ψ, χ, φ) or (x, y, z) as follows

$$\mathbf{B} = F\nabla\varphi + \frac{1}{2\pi}\nabla\varphi \times \nabla\psi = \mathcal{C}(\nabla x \times \nabla y), \tag{3.3}$$

where $F(\psi) = RB_\varphi$, with B_φ the toroidal component of the magnetic field, and

$$\mathcal{C} = \frac{1}{[2\pi(dC_x/d\psi)C_y]}. \tag{3.4}$$

It is clear from Eq. 3.3 that $\mathbf{B}\cdot\nabla x = \mathbf{B}\cdot\nabla y = 0$, so that ($x = \text{const}$, $y = \text{const}$) define a magnetic field line, and (x, y, z) indeed defines a field-aligned coordinate system.

Velocity space

The parallel velocity $v_\|$ and magnetic moment $\mu = mv_\perp^2/2B$ are the variables used in GENE to discretize the velocity space of each species distribution function.

Details about how these directions are represented and discretized, together with the relative boundary conditions, will be presented in the next section.

3.2 Numerical representations and boundary conditions of phase space directions

Radial direction

When simulations are carried out in the local approach, radially periodic boundary conditions are assumed, therefore a spectral representation of the x direction is used. For a given fluctuation quantity A, the Fourier back and forth transforms are defined according to

$$\hat{A}_{k_x}(y,z) = \frac{1}{L_x}\int_0^{L_x} \mathrm{d}x e^{-\mathrm{i}k_x x} A(x,y,z) \qquad A(x,y,z) = \sum_{k_x} e^{\mathrm{i}k_x x}\hat{A}_{k_x}(y,z). \tag{3.5}$$

Derivatives are computed in Fourier space, ensuring accuracy up to machine precision. In the *global* approach instead one retains the radial variation of background profiles and Dirichlet or Neumann boundary conditions are applied. The former consists in assuming the perturbed distribution function to be zero outside the radial domain. The latter corresponds to the same assumption with the exception that a zero derivative condition is applied to the flux-surface-averaged perturbation. This allows the background profiles to evolve in time under the action of specific heat and particle sources. Further details will be discussed in sections 3.6 and 6.1. Having relaxed the assumption of periodic boundary conditions, a direct space representation is required for the radial direction in the global version of the code. In this case derivatives are computed according to a centered fourth order finite difference scheme, see Ref. [33].

Binormal direction

In (x, y, z) coordinates, axisymmetry translates to invariance with respect to y so that linear eigenmodes have an exact wave-number k_y with respect to y because the linearized equations for the k_y Fourier modes are decoupled. Periodicity with respect to the toroidal direction

$$A(\psi, \chi, \varphi + 2\pi) = A(\psi, \chi, \varphi) \tag{3.6}$$

indeed translates in (x, y, z) coordinates to periodicity in the y direction:

$$A(x, y, z) = A(x, y + 2\pi C_y, z). \tag{3.7}$$

The binormal direction and the required derivatives are thus represented in Fourier space in both local and global versions of the code. The standard size of the simulation domain in the y direction is therefore $L_y = 2\pi C_y$. It should be noted that in many cases turbulent correlation lengths in the binormal direction ∇y are smaller than a full binormal turn. Therefore, simulation volumes do not necessarily account for the full toroidal angle, so that the simulation box length L_y does not necessarily coincides with $2\pi C_y$. On the other hand, $z = \chi$ is the coordinate along a magnetic field line and since parallel correlation lengths are very large, one cannot truncate the z coordinate (see also the next section where parallel boundary conditions are discussed). One nonetheless imposes periodicity in y, which therefore in general reads $A(x, y, z) = A(x, y + L_y, z)$.
The corresponding Fourier representation of a given mode therefore reads

$$A(x, y, z) = e^{\mathrm{i}k_y y} \hat{A}_{k_y}(x, z) \sim e^{-\mathrm{i}n\varphi} \tag{3.8}$$

yielding together with Eq. (3.2) the relation between k_y and the toroidal mode number n:

$$n = k_y C_y \qquad k_y = \frac{n}{C_y} = \frac{n q_s}{x_0} \sim k_\theta, \tag{3.9}$$

where k_θ is an estimate of the effective poloidal wave number for field-aligned fluctuations.

Parallel direction

Periodicity in the poloidal direction

$$A(\psi, \chi + 2\pi, \varphi) = A(\psi, \chi, \varphi) \tag{3.10}$$

implies the following pseudo periodic relation in the z direction:

$$A(x, y, z + 2\pi) = A(x, y - 2\pi q C_y, z). \tag{3.11}$$

Introducing the Fourier representation of the y coordinate Eq. (3.11) is equivalent to

$$\hat{A}_{k_y}(x, z + 2\pi) = \hat{A}_{k_y}(x, z)e^{-\mathrm{i}2\pi n q(x)}, \tag{3.12}$$

which can be already enforced as a boundary condition in the global code. In the flux-tube version, Eq. (3.11) has to be recast in a form that is compatible with radially periodic boundary conditions. After linearizing the safety factor profile, $q(x) = q_s(1 + \hat{s}x/x_0) = q_s\hat{s}/x_0\ (x + x_0/\hat{s})$ around the reference position x_0, one can show that for a given δk_x and k_y, the set of radial Fourier components

$$k_x = p\Delta k_x + \delta k_x, \qquad p \in \mathbb{Z}, \tag{3.13}$$

are coupled together, with $\Delta k_x = 2\pi\hat{s}k_y$, such that any linear fluctuation mode in the flux-tube limit reads:

$$\begin{aligned} A(x, y, z) &= e^{\mathrm{i}k_y y} e^{\mathrm{i}\delta k_x x} \textstyle\sum_p \hat{A}_{\delta k_x + p\Delta k_x}(z) e^{\mathrm{i}p\Delta k_x x}, \\ \text{with} \qquad & \hat{A}_{\delta k_x + p\Delta k_x}(z + 2\pi) = \hat{A}_{\delta k_x + (p+1)\Delta k_x}(z). \end{aligned} \tag{3.14}$$

In deriving Eq. (3.14), it has been assumed that the phase factor $e^{\mathrm{i}2\pi n q_s(x_0)}$ is unity, which in fact corresponds to centering the simulation domain around the mode rational surface nearest to x_0 for the considered $k_y = n/C_y$ (the distance between two neighboring rational surfaces, Δ_{MRS}, being $1/k_y\hat{s}$).

Velocity space

A uniform grid in the parallel velocity interval $-L_{v_\parallel,max} \leq v_\parallel \leq L_{v_\parallel,max}$ is used to discretize the parallel velocity direction, and integration is carried out considering a modified Simpson scheme. In the δf method, one assumes that the perturbed distribution function retains a near Maxwellian behaviour, *i.e.* with exponentially decaying tails in velocity space. Sufficiently large maximum velocities must therefore be assumed when defining simulation grids, such that all relevant contributions to the perturbed distribution function are retained. A typical choice, based on experience, consists in assuming $L_{v_\parallel,max} = 3v_{th}$ for a flux-tube simulation, while for global runs one has to adapt the grids according to the specific temperature profiles (an illustrative example will be given in section 6.1). Under this assumption it is reasonable to assume the perturbation to be zero outside the domain when evaluating derivatives with respect to $v_\parallel$. Two options are available for the discretization of the derivatives along z and $v_\parallel$. One can use a fourth order centered scheme, similar to the one adopted for the radial direction in the global code. Alternatively, the terms involving these derivatives can be combined and cast into a Poisson bracket which is in turn discretized according to an Arakawa scheme [68]. This second option, which preserves analytic conservation properties, is preferable when looking at turbulent energetics, e.g. free energy conservation. Further details can

be found in Ref. [30].
Along the magnetic moment direction one needs to evaluate derivatives only for the implementation of the collision operator. In this case derivatives are computed assuming a finite volume scheme with vanishing fluxes across the outer domain, see Ref. [35]. Again, one has to assume a sufficiently large maximum value for L_μ, usually $9T_j/B_0$ for local runs. Different choices for the distribution of the μ integration points are available, with the default set-up consisting in a Gauss-Laguerre quadrature rule.

3.3 Further numerical details

3.3.1 Time stepping scheme and eigenvalue solver

The gyrokinetic equation can be formally written as

$$\frac{\partial g}{\partial t} = L[g] + N[g], \tag{3.15}$$

where L indicates a linear operator, including collisions, while the nonlinearity has been included in the nonlinear operator N.
Discretizing the right hand side of Eq. (3.15) on the previously described phase space grid, the original partial differential equation is recast into a system of ordinary differential equations that can be solved as an initial problem. GENE evolves the distribution function in time using an explicit fourth order Runge-Kutta scheme, starting from an initial condition g^0.
This initial value solver can be used for linear and nonlinear computations. The time step limit is determined by the stability analysis of the time stepping scheme, see Ref. [33] for further details. For linear computations the maximum stable time step can be evaluated from the spectral radius of the operator L, while in case of nonlinear runs one has to take into account the extra limit imposed by the Courant-Friedrichs-Levy (CFL) condition arising from the nonlinear advection term.
Switching off the nonlinear term N, Eq. (3.15) becomes an eigenmode equation. In this case, assuming modes with a time dependency of the form $\exp[\mathrm{i}\omega t + \gamma t]$, an initial value computation allows to determine only the most unstable eigenvalue, which will eventually dominate. Alternatively, one can solve the linear gyrokinetic equation as an eigenvalue problem. This approach allows one to solve for a subset of eigenmodes and corresponding eigenfunctions. GENE implements an interface to the SLEPc library [69], which makes use of iterative solvers to identify specific subsets of the complete eigenmode spectrum. A direct solver, based on ScaLAPACK is also available for computing the entire spectrum. This latter option is, however, practically feasible only for very small problem sizes.

3.3.2 Magnetic equilibrium

GENE currently supports a wide class of magnetic equilibria. Two analytic models are frequently used in the literature for carrying out gyrokinetic simulations, the so-called $s - \alpha$ model and the *ad-hoc* geometry. Both implement circular flux-surfaces, however an inconsistent implementation in the gyrokinetic context makes the first one incorrect for all tokamaks having a small but finite aspect ratio [70].
Whenever dealing with experimental conditions, the equilibrium is usually reconstructed with the help of magnetic measurements. In this case an ideal MHD equilibrium solver is required in order to solve the Grad-Shafranov equation and provide GENE with the background magnetic geometry. Currently, interfaces to the ideal MHD equilibrium codes CHEASE [71], g-eqdsk provided by Efit [72], GIST [73] and TRACER [67] are available. Finally, an interface to Miller's equilibrium [74], allowing the user to freely specify the shape of a given flux surface via its values of elongation, triangularity and squareness, is implemented for the local version of the code. It will be used and presented in more detail in chapter 4.

3.3.3 Discretization of the nonlinearity

When computing the nonlinear term, derivatives are, whenever possible, evaluated in Fourier space. Multiplications are instead carried out after going back to $x - y$ real space. This avoids the expensive computation of convolutions as would otherwise be required. The conservation properties of the nonlinear term are preserved at machine precision in the local code thanks to the Fourier $k_x - k_y$ representation. In the global version, this is achieved through a mixed Fourier-real space version of the Arakawa scheme, similar to the one used to represent parallel derivatives. More details can be found in Ref. [30].

3.3.4 Numerical hyperdiffusion and anti-aliasing

Finite difference centered schemes, as the one employed in GENE for computing derivatives, are non-dissipative. They also tend to decouple neighbouring points, potentially leading to spurious effects. In order to limit this effect, numerical hyperdiffusion terms are added to the right hand side of the Vlasov equation. They are typically fourth order derivatives terms with an amplitude that can be adjusted by the user. Hyper diffusive terms can be added in the radial and binormal directions, as well as in z and $v_\parallel$ Details regarding the actual implementation and the influence on results can be found in Refs. [46, 75].
Hyperdiffusion terms provide also the necessary damping of sub-grid fluctuations (dealiasing), that can otherwise appear and potentially lead to numerical instabilities. When a Fourier representation is employed, dealiasing is obtained applying the so-called 3/2 rule, which introduces 50% more Fourier modes with vanishing amplitude before back-

transforming to real space in order to evaluate the nonlinearity. Afterwards these modes are again removed.

3.3.5 Gyroaveraging

As we have seen in the derivation of the gyrokinetic model, two kinds of gyroaveraging operations are required:

$$\bar{\phi}_{1j}(\mathbf{X}) = \frac{1}{2\pi}\int \phi_1(\mathbf{X} + \boldsymbol{\rho}_j)\mathrm{d}\alpha \tag{3.16}$$

and, for the field equations,

$$\langle\phi_{1j}(\mathbf{x})\rangle = \frac{1}{2\pi}\int \delta(\mathbf{X} + \boldsymbol{\rho}_j - \mathbf{x})\phi_1(\mathbf{X} + \boldsymbol{\rho}_j)\mathrm{d}\mathbf{X}\mathrm{d}\alpha \tag{3.17}$$

In the global version of the code, the gyroaveraging is carried out using a finite element interpolation involving neighbouring grid points. All quantities are expanded on a set of basis functions

$$\phi_1 = \sum \phi_{1i}\Lambda_i(x), \tag{3.18}$$

such that the gyroaveraging can be evaluated thanks to the gyromatrix $\mathcal{G}_j$ acting on the grid values of e.g. ϕ_1. Formally one can thus rewrite Eq. (3.16) as

$$\bar{\phi}_{1j}(\mathbf{X}) = \boldsymbol{\mathcal{G}}_j \cdot \phi_1(\mathbf{x}), \tag{3.19}$$

with $\boldsymbol{\mathcal{G}}_j$ representing a gyroaverage operator for species j . Details regarding the choice of the basis functions Λ_i and the actual implementation in the code can be found in Ref. [64]. It can be shown, see Ref. [30] that the second kind of gyroaveraging given in Eq. (3.17) can be expressed as $\langle\phi_{1j}(\mathbf{X})\rangle = \boldsymbol{\mathcal{G}}_j^\dagger \cdot \phi_1(\mathbf{X})$, with $\boldsymbol{\mathcal{G}}_j^\dagger$ the hermitian conjugate of $\boldsymbol{\mathcal{G}}_j$.

In order to preserve the analytic symmetry properties of the gyro-operator, and avoid potential numerical instabilities (see Ref. [30] for details), when evaluating the double gyroaverages appearing in the field equation one has to evaluate them as

$$\langle\bar{\phi}_{1j}P\rangle(\mathbf{x}) = \boldsymbol{\mathcal{G}}_j^\dagger \cdot \{P_j\boldsymbol{\mathcal{G}}_j \cdot \phi_1(\mathbf{x})\}. \tag{3.20}$$

Here P_j indicates a factor containing equilibrium terms, which can be taken out from the gyroaverage in the local limit. In this latter case the gyromatrix is diagonal and can be represented in terms of Bessel functions. Moreover, in this limit the two gyro-operations in Eqs. (3.16) and (3.17) are equivalent, see e.g. Ref. [33], and can be evaluated as:

$$\bar{\phi}_{1j} = \langle\phi_{1j}\rangle = J_0(k_\perp\rho_j)\phi_1. \tag{3.21}$$

3.4 Normalizations

The normalizations in GENE are chosen such that all dimensionless quantities are of order unity. Therefore, in configuration space, the independent variables x and y used for representing fluctuating fields are normalized to a reference gyroradius ρ_{ref}, while the already dimensionless field connection length along z is kept to be $2\pi \sim \mathcal{O}(1)$. A macroscopic length L_{ref} is used to normalize gradients of equilibrium quantities. In velocity space, in order to account for potentially differing temperatures, the normalization has to be species dependent. Furthermore, magnetic fields, temperatures, densities and masses are normalized with respect to the reference values B_{ref}, T_{ref}, n_{ref} and m_{ref}. The user is free to specify these reference values. Derived reference quantities such as the sound velocity c_{ref}, the Larmor frequency Ω_{ref} and radius ρ_{ref} are defined as

$$c_{\mathrm{ref}} = \sqrt{\frac{T_{\mathrm{ref}}}{m_{\mathrm{ref}}}}, \qquad \Omega_{\mathrm{ref}} = \frac{eB_{\mathrm{ref}}}{m_{\mathrm{ref}}}, \qquad \rho_{\mathrm{ref}} = \frac{c_{\mathrm{ref}}}{\Omega_{\mathrm{ref}}}.$$

Indicating the normalized quantities with a hat, one has for the j-th species

$$x = \hat{x}\rho_{\mathrm{ref}}, \qquad y = \hat{y}\rho_{\mathrm{ref}}, \qquad z = \hat{z},$$

$$v_{\parallel,j} = \hat{v}_{\parallel}\hat{v}_{\mathrm{th},j}c_{\mathrm{ref}}, \qquad \mu_j = \hat{\mu}\,\hat{T}_j\,\frac{T_{\mathrm{ref}}}{B_{\mathrm{ref}}}, \qquad t = \hat{t}\,\frac{L_{\mathrm{ref}}}{c_{\mathrm{ref}}},$$

where the thermal velocity $\hat{v}_{\mathrm{th},j}$ of the $j-$species is defined as

$$\hat{v}_{\mathrm{th},j} = \sqrt{2T_j/m_j}. \tag{3.22}$$

Typical choices are $T_{\mathrm{ref}} = T_e$, $n_{\mathrm{ref}} = n_e$ and $m_{\mathrm{ref}} = m_i$, such that $c_{\mathrm{ref}} = c_s$, while B_{ref} is typically the magnetic field on axis, $B_{\mathrm{ref}} = B_{mag}$. One also has $\beta_{\mathrm{ref}} = 2\mu_0 n_{\mathrm{ref}} T_{\mathrm{ref}}/B_{\mathrm{ref}}^2$. The macroscopic distance L_{ref} is usually taken to be either the major radius R_0 or the minor radius a of the Tokamak.

Field fluctuations are normalized according to:

$$\phi = \hat{\phi}\frac{T_{\mathrm{ref}}}{e}\frac{\rho_{\mathrm{ref}}}{L_{\mathrm{ref}}}, \qquad A_{\parallel} = \hat{A}_{\parallel}\rho_{\mathrm{ref}}B_{\mathrm{ref}}\frac{\rho_{\mathrm{ref}}}{L_{\mathrm{ref}}}, \qquad B_{\parallel} = \hat{B}_{\parallel}B_{\mathrm{ref}}\frac{\rho_{\mathrm{ref}}}{L_{\mathrm{ref}}},$$

where the factor $\rho_{\mathrm{ref}}/L_{\mathrm{ref}}$ is introduced in order to account for the small nature of such fluctuations. Background temperature and density profiles are normalized with respect to the respective reference values at the position x_0, and can therefore be written as

$$T_{0,j} = \hat{T}_{pj}(x)\hat{T}_{0j}(x_0)T_{\mathrm{ref}} \qquad n_{0j} = \hat{n}_{pj}(x)\hat{n}_{0j}(x_0)n_{\mathrm{ref}}$$

where $\hat{T}_{0j}(x_0)$ accounts for the species dependence i.e. $\hat{T}_{0j}(x_0) = 1$ for the reference species, and $\hat{T}_{pj}(x)$ the radial dependence. Normalized background gradients are indicated with the following notations:

$$\hat{\omega}_{nj} = -\frac{L_{\mathrm{ref}}}{n_{0j}}\frac{\mathrm{d}n_{0j}}{\mathrm{d}x} \qquad \text{and} \qquad \hat{\omega}_{Tj} = -\frac{L_{\mathrm{ref}}}{T_{0j}}\frac{\mathrm{d}T_{0j}}{\mathrm{d}x}.$$

Finally, one normalizes the distribution function as

$$F_{0,j} = \hat{F}_{0,j}\left.\frac{n_{\mathrm{ref}}}{c_{\mathrm{ref}}^3}\frac{\hat{n}_{0,j}}{\hat{v}_{Tj}^3}\right|_{x_0} \qquad f_{0,j} = \hat{f}_{0,j}\left.\frac{n_{\mathrm{ref}}}{c_{\mathrm{ref}}^3}\frac{\hat{n}_{0,j}}{\hat{v}_{Tj}^3}\right|_{x_0}\frac{\rho_{\mathrm{ref}}}{L_{\mathrm{ref}}}.$$

The application of these normalizations rules leads to the normalized version of the gyrokinetic equation previously derived, as well as to the normalized electromagnetic field equations. They can be found in e.g. Ref. [64].

3.5 Macroscopic observables

3.5.1 Turbulent fluxes

The amount of information contained in the time evolution of the perturbed distribution function is huge. It can be regularly reduced by taking appropriate moments over the phase space, such as to provide quantities useful for a comparison with experiments. As detailed in Ref. [32], one can start from the gyrokinetic equation and introduce e.g. a gyrocenter particle flux and derive the corresponding radial conservation law. Strictly speaking, one is however interested in the fluxes evaluated at the particle positions $\mathbf{x}$:

$$\begin{aligned}
\mathbf{\Gamma}_j(\mathbf{x}) &= \int \mathbf{v} f_j(\mathbf{x},\mathbf{v},t)\mathrm{d}\mathbf{v} \\
\mathbf{Q}_j(\mathbf{x}) &= \int \frac{1}{2}mv^2\mathbf{v} f_j(\mathbf{x},\mathbf{v},t)\mathrm{d}\mathbf{v} \\
\mathbf{\Pi}_{\parallel j}(\mathbf{x}) &= \int mv_\parallel \mathbf{v} f_j(\mathbf{x},\mathbf{v},t)\mathrm{d}\mathbf{v}
\end{aligned} \tag{3.23}$$

where $\mathbf{\Gamma}_j$, $\mathbf{Q}_j$ and $\mathbf{\Pi}_{\parallel,j}$ are the particle, heat and parallel momentum fluxes of the $j-$th species, which are in general different from the gyrocenter ones because of diamagnetic and polarization terms. We also note that the parallel momentum can be assumed as an approximation of the toroidal momentum flux in the case if $B_\varphi \gg B_\theta$. Otherwise, the toroidal projection can be obtained by multiplying with $qR\mathcal{C}/JB$.

In GENE, the turbulent fluxes given by the relations in Eq. (3.23) are approximated by taking the moments of the distribution function with the generalized drift velocity, $\mathbf{v}_D = \mathbf{v}_\xi + \mathbf{v}_{\nabla B} + \mathbf{v}_c$ in lieu of $\mathbf{v}$, where $\mathbf{v}_\xi$, $\mathbf{v}_{\nabla B}$ and $\mathbf{v}_c$ are respectively the generalized $\mathbf{E}\times\mathbf{B}$ velocity, the ∇B and the curvature drift velocities defined in Equations (2.76), (2.75) and (2.72). For all the geometries possessing a weak up-down asymmetry, as the ones considered here, $\mathbf{v}_\xi$ is the dominant contribution to $\mathbf{v}_D$ and therefore the other terms can be neglected[1]. Moreover, one makes use of the parallel gyrokinetic ordering such as to approximate

$$\mathbf{v}_\xi \cdot \nabla x \simeq -\frac{1}{\mathcal{C}}\frac{\partial \xi}{\partial y}. \tag{3.24}$$

Noting that all equilibrium quantities are independent of y, and therefore, as will be explained in the next section, do not contribute to turbulent transport, one can finally express the fluxes given in Eq. (3.23) as moments $M_{j,mn}$ of the perturbed distribution function, already introduced in Equation (2.93). When evaluating fluxes associated to the compressional magnetic perturbation $B_{1\|}$, a functionality currently implemented only in the local code, additional moments $N_{j,mn}(\mathbf{x})$ are required. They are defined according to

$$N_{j,mn}(\mathbf{x}) = \pi \left(\frac{2B_0}{m_j}\right)^{n/2+1} \int \left[F_1 + q_j \left(\bar{\phi}_1 + \mu_j \bar{B}_{1\|}\right) \frac{F_{0j}}{T_{0j}}\right] \mu I_{1j} v_{\|j}^n \mu_j^{m/2} \mathrm{d}v_{\|j} \mathrm{d}\mu_j, \tag{3.25}$$

where the external gyroaverage leads to a multiplication with $\mu_j I_{1j}$, with

$$I_{1j}(k_\perp \rho_j) = 2\frac{J_1(k_\perp \rho_j)}{k_\perp \rho_j}. \tag{3.26}$$

The normalized version of both $M_{j,mn}$ and $N_{j,mn}$ can be found in e.g., Ref. [64]. We report them here for completeness:

$$\begin{aligned}
\hat{M}_{j,mn}(\mathbf{x}) =& \frac{M_{j,mn}(\mathbf{x})}{n_\mathrm{ref}\hat{n}_{0j}(x_0) c_\mathrm{ref}^{m+n} v_{\mathrm{th},j}^{m+n}(x_0) \frac{\rho_\mathrm{ref}}{L_\mathrm{ref}}} \\
=& \pi \hat{B}_0^{\frac{n}{2}} \int \hat{B}_{0\|}^* \langle \hat{F}_{1j}(\mathbf{x}-\boldsymbol{\rho})\rangle \hat{v}_\|^m \hat{\mu}^{n/2} \mathrm{d}\hat{v}_\| \mathrm{d}\hat{\mu} \\
& - \frac{\hat{n}_{pj}\hat{T}_{pj}^{\frac{m+n}{2}}}{\hat{T}_{0j}} \left[\mathcal{I}(m) + \beta_\mathrm{ref}\frac{\hat{T}_{0j}}{\hat{B}_0^2 \hat{q}_j \hat{v}_{\mathrm{th},j}} \hat{j}_{0\|}\mathcal{I}(m+1)\right] \Bigg[(n/2)! \hat{q}_j \hat{\phi}_1(\mathbf{x}) \\
& - \left(\frac{\hat{B}_0}{\hat{T}_{pj}}\right)^{\frac{n}{2}+1} \int \left(\hat{q}_j \langle \hat{\bar{\phi}}_1(\mathbf{x}-\boldsymbol{\rho}\rangle + \hat{T}_{0j}(x_0)\hat{\mu}\langle \hat{\bar{B}}_{1\|}(\mathbf{x}-\boldsymbol{\rho})\rangle\right) \mathrm{e}^{\frac{-\hat{\mu}\hat{B}_0}{\hat{T}_{pj}}} \hat{\mu}^{n/2} \mathrm{d}\hat{\mu} \Bigg],
\end{aligned} \tag{3.27}$$

---

[1] This is in general not the case for neoclassical computations, where the ∇B and curvature terms must be retained. Moreover, the parallel ordering cannot be used, as clearly discussed in Ref. [35] where the expression of neoclassical GENE fluxes are provided.

and

$$\begin{aligned}\hat{N}_{j,mn}(\mathbf{x}) &= \frac{N_{j,mn}(\mathbf{x})}{p_{\mathrm{ref}}p_{0j}(x_0)c_{\mathrm{ref}}^{m+n}v_{\mathrm{th},j}^{m+n}(x_0)\frac{\rho_{\mathrm{ref}}}{L_{\mathrm{ref}}}} \\ &= \pi\hat{B}_0^{n/2+2}\int \hat{v}_{\parallel j}^{m}\hat{\mu}_j^{n/2}\hat{\mu}_j I_{1j}\Big[\hat{F}_{1j} \qquad (3.28) \\ &+ \left(\hat{q}_j J_{0j}\hat{\phi}_1 + \hat{T}_{0j}(x_0)\hat{\mu}_j I_{1j}\hat{B}_{1\parallel}\right)\frac{\hat{F}_{0j}}{\hat{T}_{0j}}\Big]\,\hat{v}_{\parallel j}^{m}\hat{\mu}_j^{n/2}\mathrm{d}\hat{v}_{\parallel j}\mathrm{d}\hat{\mu}_j,\end{aligned}$$

where, to lighten the notation, we have dropped the species index j in the velocity space variables, indicated that double gyroaveraged fields in the global version are to be evaluated at the position $\mathbf{x}-\boldsymbol{\rho}$ by showing their spatial dependency, and carried out the $v_{\parallel}$-integrals involving the Maxwellian background. Finally, $\mathcal{I}(m)$ indicates

$$\mathcal{I}(m) = \begin{cases} 0, & m \text{ odd} \\ \frac{1\cdot 3\cdots(m-1)}{2^{m/2}}, & m \text{ even} \end{cases} \tag{3.29}$$

By separating $\mathbf{v}_{\xi}$ into its field components, one furthermore distinguishes between electrostatic and magnetic contributions to transport (the latter being the sum of longitudinal and compressional magnetic fluctuations), each involving moments of different order.

Applying GENE normalization rules, one finally writes for each species

$$\hat{\Gamma}_j = \frac{\boldsymbol{\Gamma}_j\cdot\nabla x}{\Gamma_{\mathrm{GB}}} = -\frac{\hat{n}_{0j}}{\hat{\mathcal{C}}}\left(\frac{\partial\hat{\phi}}{\partial\hat{y}}\hat{M}_{00} - \hat{v}_{T,j}\frac{\partial\hat{A}_{1\parallel}}{\partial\hat{y}}\hat{M}_{20} + \frac{\hat{T}_{0j}}{\hat{q}_j}\frac{\partial\hat{B}_{1\parallel}}{\partial\hat{y}}\hat{N}_{10}\right) \tag{3.30}$$

$$\begin{aligned}\hat{Q}_j = \frac{\mathbf{Q}_j\cdot\nabla x}{Q_{\mathrm{GB}}} = -\frac{\hat{n}_{0j}\hat{T}_{0j}}{\hat{\mathcal{C}}}\Bigg(&\frac{\partial\hat{\phi}}{\partial\hat{y}}(\hat{M}_{20}-\hat{M}_{02}) - \hat{v}_{\mathrm{th}j}\frac{\partial\hat{A}_{1\parallel}}{\partial\hat{y}}(\hat{M}_{30}+\hat{M}_{12}) \\ &+\frac{\hat{T}_{0j}}{\hat{q}_j}\frac{\partial\hat{B}_{1\parallel}}{\partial\hat{y}}(\hat{N}_{20}+\hat{N}_{02})\Bigg)\end{aligned} \tag{3.31}$$

$$\hat{\Pi}_{\parallel,j} = \frac{\boldsymbol{\Pi}_{\parallel,j}\cdot\nabla x}{\Pi_{\mathrm{GB}}} = -\frac{\hat{m}_{0j}\hat{n}_{0j}\hat{v}_{\mathrm{th}j}}{\hat{\mathcal{C}}}\left(\frac{\partial\hat{\phi}}{\partial\hat{y}}\hat{M}_{10} - \hat{v}_{T,j}\frac{\partial\hat{A}_{1\parallel}}{\partial\hat{y}}\hat{M}_{10} + \frac{\hat{T}_{0j}}{\hat{q}_j}\frac{\partial\hat{B}_{1\parallel}}{\partial\hat{y}}\hat{N}_{10}\right) \tag{3.32}$$

where the so-called GyroBohm units, respectively reading $\Gamma_{\mathrm{GB}} = n_{\mathrm{ref}}c_{\mathrm{ref}}\rho_{\mathrm{ref}}^2/L_{\mathrm{ref}}^2$, $Q_{\mathrm{GB}} = p_{\mathrm{ref}}c_{\mathrm{ref}}\rho_{\mathrm{ref}}^2/L_{\mathrm{ref}}^2$ and $\Pi_{\mathrm{GB}} = n_{\mathrm{ref}}m_{\mathrm{ref}}c_{\mathrm{ref}}^2\rho_{\mathrm{ref}}^2/L_{\mathrm{ref}}^2$, have been introduced.

3.5.2 Spatial averages and radial conservation laws

The previously derived fluxes are still function of the position $\mathbf{x}$, therefore an appropriate spatial average must be taken in order to provide a measure of radial fluxes, which ultimately have to be compared to experimental values. Considering e.g. the three-dimensional continuity equation involving particle density, in absence of sources, one can write it as :

$$\frac{\partial}{\partial t} n(\mathbf{x}, t) + \frac{\partial}{\partial \mathbf{x}} \mathbf{\Gamma}(\mathbf{x}, t) = 0. \tag{3.33}$$

Integrating Eq. (3.33) over the volume $V(x)$ within a given flux-surface defined by $x = \text{const}$, and taking the radial derivative with respect to x, one obtains the relevant radial conservation law:

$$\frac{\partial}{\partial t} n_x(x, t) + \frac{\partial}{\partial x} \left[S \left\langle \frac{\mathbf{\Gamma} \cdot \nabla x}{|\nabla x|} \right\rangle_S \right] = 0. \tag{3.34}$$

Here we have indicated with n_x the radial particle density

$$n_x(x, t) = \frac{\partial}{\partial x} \int\limits_{V(x)} \mathrm{d}\mathbf{x} n(\mathbf{x}, t) \tag{3.35}$$

and with $\langle \cdots \rangle_S$ the average over the surface at $x = \text{const}$:

$$\langle \cdots \rangle_S = \frac{1}{S} \int\limits_{\partial V(x)} \cdots \mathrm{d}\sigma \qquad \text{and} \qquad S = \int\limits_{\partial V(x)} \cdots d\sigma. \tag{3.36}$$

The total radial particle flux is therefore defined by

$$\Gamma(x, t) = \left\langle \frac{\mathbf{\Gamma} \cdot \nabla x}{|\nabla x|} \right\rangle_S . \tag{3.37}$$

Similar expressions can be obtained for the heat and parallel momentum fluxes.
Assuming a Fick type relation between fluxes and gradients and considering turbulent diffusivities to be constant on a given flux surface, one can finally derive:

$$D_j = -\left(\frac{\mathrm{d}n}{\mathrm{d}x} \right)^{-1} \frac{\left\langle \frac{\mathbf{\Gamma} \cdot \nabla x}{|\nabla x|} \right\rangle_S}{\langle |\nabla x| \rangle_S} \tag{3.38}$$

and

$$\chi_j = -\frac{1}{n_0} \left(\frac{\mathrm{d}T}{\mathrm{d}x} \right)^{-1} \frac{\left\langle \frac{\boldsymbol{Q} \cdot \nabla x}{|\nabla x|} \right\rangle_S}{\langle |\nabla x| \rangle_S}. \tag{3.39}$$

Applying the rules of section 3.4, the normalized counterparts read

$$
\begin{aligned}
\hat{D}_j &= \frac{D_j}{D_{\mathrm{GB}}} = \frac{1}{\hat{n}_{0j}\hat{\omega}_{nj}\left\langle|\nabla\hat{x}|\right\rangle_S}\left\langle\frac{\hat{\Gamma}_j}{|\nabla\hat{x}|}\right\rangle_S \\
\hat{\chi}_j &= \frac{\chi_j}{\chi_{\mathrm{GB}}} = \frac{1}{\hat{n}_{0j}\hat{T}_{0j}\hat{\omega}_{Tj}\left\langle|\nabla\hat{x}|\right\rangle_S}\left\langle\frac{\hat{Q}_j}{|\nabla\hat{x}|}\right\rangle_S
\end{aligned}
\tag{3.40}
$$

with $D_{\mathrm{GB}} = \chi_{\mathrm{GB}} = c_{\mathrm{ref}}\rho_{\mathrm{ref}}^2 L_{\mathrm{ref}}$.

3.6 Other specific features of the global code

3.6.1 Heat and particle sources

Global simulations allow turbulent heat and particle fluxes to relax the background temperature and density plasma profiles until sub-critical values of the gradients are reached. Sources and sinks are therefore required in order to reach a turbulent stationary state. With this aim, two different approaches, both implemented in GENE, can in general be adopted.

The first one, normally referred to *gradient-driven*, consists in imposing background profiles which are then maintained during the time evolution thanks to Krook-type sources. This kind of heat sources have been introduced in the PIC code ORB5 as described in Ref. [76]. Due to the specific choice of velocity space variables, GENE sources are expressed as function of a symmetrized distribution function

$$
F_{1,j}(\mathbf{X}, |v_\parallel|, \mu) = \frac{F_{1,j}(\mathbf{X}, v_\parallel, \mu) + F_{1,j}(\mathbf{X}, -v_\parallel, \mu)}{2},
\tag{3.41}
$$

such as to ensure no parallel momentum injection.

An heat source of the form

$$
\begin{aligned}
S_{H,j} = &-\gamma_H \Bigg(\left\langle F_{1,j}(\mathbf{X}, |v_\parallel|, \mu)\right\rangle_{\mathrm{fs}} \\
&- \left\langle F_{0,j}(\mathbf{X}, |v_\parallel|, \mu)\right\rangle_{\mathrm{fs}} \frac{\left\langle \int \left\langle f_{1,j}(\mathbf{X}, |v_\parallel|, \mu)\right\rangle_{\mathrm{fs}} \mathrm{d}\mathbf{v}\right\rangle_{\mathrm{fs}}}{\left\langle \int F_{0,j}(\mathbf{X}, |v_\parallel|, \mu)\mathrm{d}\mathbf{v}\right\rangle_{\mathrm{fs}}}\Bigg)
\end{aligned}
\tag{3.42}
$$

is added to the right hand side of the Vlasov equation for the $j-$th species. Here $\langle\cdots\rangle_{\mathrm{fs}}$ indicates a flux-surface average, defined in Eq. (2.108). The second term in Eq. (3.42) ensures that no density perturbation is introduced in the system, while the coefficient γ_H is a user-defined input value that can be interpreted as a relaxation rate towards the prescribed background distribution. Similarly, the particle source is given by

$$\begin{aligned}S_{P,j} = &- \gamma_P \left(\left\langle f_{1,j}(\mathbf{X}, |v_\parallel|, \mu) \right\rangle_{\text{fs}} \right. \\ &\left. - \left\langle F_{0,j}(\mathbf{X}, |v_\parallel|, \mu) \right\rangle_{\text{fs}} \frac{\sum_{i=1}^{n_s} q_i \left\langle \int \left\langle f_{1,i}(\mathbf{X}, |v_\parallel|, \mu) \right\rangle_{\text{fs}} \mathrm{d}\mathbf{v} \right\rangle_{\text{fs}}}{q_j n_{\text{s}} \left\langle \int F_{0,j}(\mathbf{X}, |v_\parallel|, \mu) \mathrm{d}\mathbf{v} \right\rangle_{\text{fs}}} \right),\end{aligned} \tag{3.43}$$

where the correction given from the second term is added in order to fulfill the quasineutrality equation

$$\sum_{j=1}^{n_s} q_j \left\langle \int S_{P,j} \mathrm{d}\mathbf{v} \right\rangle_{\text{fs}} = 0, \tag{3.44}$$

and avoid introducing artificial electrostatic potentials. Once again, γ_P is a user defined prefactor providing a relaxation rate. The heat input due to S_P is compensated by GENE, as detailed in Ref. [30], such that the overall input heat can be evaluated as the second velocity moment of the heat source:

$$Q_{H,j} = \left\langle \int \frac{1}{2} m_j v^2 S_{H,j} \mathrm{d}\mathbf{v} \right\rangle_{\text{fs}}. \tag{3.45}$$

Alternative to gradient-driven runs, one can perform *flux-driven* simulations, where given sources and sinks are prescribed and the system is evolving till a steady state is reached. In this case, profiles might during their evolution significantly deviate from the prescribed background, thus violating the assumption $|\delta f / f_0| \ll 1$. An automatic adaptation of the background F_0 to the full f is therefore implemented in GENE, see Ref. [77]. Localized heat sources S_L are modeled according to

$$S_L = S_0 S_x S_E, \tag{3.46}$$

where

$$S_{E,j} = \frac{2}{3} \frac{1}{p_{0,j}(x)} \left(\frac{E}{T(x)} - \frac{3}{2} \right) F_{0,j} \tag{3.47}$$

with $E = v_\parallel^2 + \mu B$, such that no particles and no parallel momentum are introduced in the system. S_x allows the user to specify a radial profile of the source. Currently a Gaussian and a broader peak profile, similar to the one described in Ref. [78] are available. Finally, S_0 specifies the amplitude of the source. When reproducing an experimental scenario where the externally applied heating is known, S_0 can be set by noting that the total power injected by the source in (3.46) is

$$Q_{ext} = S_0 \int \mathrm{d}^3 x \int \mathrm{d}^3 v E S_e S_x. \tag{3.48}$$

3.6.2 Radial buffers

When performing gradient-driven runs, Dirichlet boundary conditions are employed in the radial direction, therefore the temperature and density at both ends of the simulation are constrained to their initial value. This can lead to large unphysical profile variation very close to the boundaries, in turn generating a strong turbulence in the edge regions. In order to avoid such behaviour, and ensure numerical stability, radial buffers regions are used where an artificial Krook damping operator is applied. This operator has the form

$$\hat{h} = -\nu \hat{g}, \tag{3.49}$$

where the amplitude ν is set to zero outside the buffer regions and is a polynomial ramp inside. When instead one carries out a flux-driven simulation, as already mentioned a zero derivative boundary condition is applied to the flux-surface-averaged fluctuation. The outer buffer can in this case be used as a sink by damping the $k_y = 0$ mode.

3.7 Summary

In this chapter, a description of the GENE code and the numerical techniques that are employed has been given. The coordinate system, together with their numerical representation and the boundary conditions along each phase space direction have been presented. Code specific normalizations have been discussed as well as how to extract macroscopic turbulent fluxes from a simulation to be compared with experimental measurements. Finally, the specific features of the global version of the code have been presented.

In the next chapter a benchmarking effort, involving both the local and the global versions of the code, will be discussed.

4 Code verification

Verification is the fundamental step that any turbulence simulation code has to be submitted to in order to assess the proper implementation of the underlying equations, regardless of the specific numerical algorithm adopted to solve them. The work by Dimits *et al.* [16] can be considered among the first systematic benchmark effort of gyrokinetic codes based on a standard test case, the so-called Cyclone Base Case (CBC). Since then, various efforts have already been successfully carried out involving different codes, both in the local limit as well as considering a global representation [79–86]. With some exceptions, e.g. Refs. [82–84], these comparisons often use an approximate analytical circular model to describe the plasma equilibrium and ad-hoc temperature and density profiles. Moreover a simplified adiabatic model for describing the electron dynamics has usually been considered, with the main purpose of reducing the overall required computational cost.

Given that whenever aiming at reproducing experimental observations with gyrokinetic simulations one is normally dealing also with experimental geometries, a series of benchmarks, of both the local and global version of GENE, have been carried out with the specific aim of verifying the implementation of the interface to the MHD equilibrium solver CHEASE [71]. These tests will be presented and discussed in this chapter.

The results of local benchmarks have been published in [87]. Verification of the global code is still ongoing and some first results have been reported in [88].

4.1 Local benchmarks

4.1.1 Magnetic geometries and profile details

For all the benchmarks we consider five different numerical plasma equilibria obtained using the ideal MHD solver CHEASE [71], which provides the axisymmetric equilibrium magnetic field **B** with a pressure profile obtained from given density and temperature profiles for the different plasma species. A detailed description of the cases can already be found in Ref. [89]. For the sake of clarity we briefly present them again here. These equilibria are inspired by the DIII-D shot underlying the Cyclone Base Case [16] which was a fully shaped plasma corresponding to a Single Null Diverted (SND) configuration. The CBC benchmark, however, just considers circular concentric flux surfaces with only plasma and safety factor profiles taken from the experiment. Among the shapes we consider here, Case I has the most complex geometry and is derived directly from the DIII-D experimental equilibrium i.e. a plasma with up-down asymmetry, positive triangularity δ, elongation κ greater than unity and realistic Shafranov shift Δ. The shape complexity is then progressively reduced by removing one shaping effect in each subsequent equilibrium. This is achieved by modifying the Last Closed Flux Surface (LCFS) shape. Therefore Case II is an up-down symmetric triangular plasma, Case III corresponds to an elongated geometry (triangularity δ_{LCFS}=0), Case IV is a circular plasma (elongation $\kappa_{\text{LCFS}} = 1$), and finally Case V is a zero β plasma with almost concentric flux surfaces (Shafranov shift $\Delta_{\text{LCFS}} \simeq 0$). The flux surface contours for the five equilibria are the ones depicted in Figure 2.2, while the geometrical parameters describing the LCFS are reported in Table 4.1.

Regarding the triangularity of the up-down asymmetric Case I, this shaping parameter has been estimated separately for the upper and lower halves of the corresponding magnetic geometry. This was carried out by considering two separate up-down *symmetric* equilibria, respectively based on the upper and lower half of the LCFS of Case I, and providing $\delta_{\text{LCFS}}(\text{upper}) = 0.15$ and $\delta_{\text{LCFS}}(\text{lower}) = 0.35$ (see also Table 4.1). Note that the triangularity of Case II is set to $\delta_{\text{LCFS}} = 0.15$, i.e. the upper value of Case I.

Case	q_{95}	κ_{LCFS}	δ_{LCFS}	Δ_{LCFS}
I	3.92	1.68	$0.15(u)/0.35(l)$	-0.0443
II	3.87	1.68	0.15	-0.0531
III	3.70	1.68	-0.002	-0.0534
IV	3.66	1.00	0.015	-0.0752
V	3.72	1.00	0.0	-0.0262

Table 4.1 : Parameters characterizing the Last Closed Flux Surface of the five equilibrium cases. For the up-down asymmetric geometry of Case I, the values of upper (u) and lower (l) triangularity are provided.

In order to completely describe the plasma equilibrium it is necessary to specify, in addition to the shape of the LCFS, the safety factor profile as well as the total pressure profile. This is done by choosing similar profiles with respect to the minor radius r for the different equilibria and built such that at the radial position r/a=0.5, the one used to carry out flux-tube benchmarks, the local values of safety factor q_s, magnetic shear $\hat{s} = (r/q)(dq/dr)$ and of temperature and density gradients are as close as possible to the CBC ones (q_s=1.4 and $\hat{s}$=0.8, R_0/L_n=2.22 and R_0/L_T=6.91 respectively). Here, r indicates the geometric local minor radius of a given flux surface, defined as $r = [R_{max} - R_{min}]/2$, R_{max} and R_{min} being respectively the maximum and minimum major radius of the flux surface evaluated at the elevation of the magnetic axis. One in particular also defines the minor radius a of the LCFS as $a = r(\text{LCFS})$. The geometric center of a given flux surface in turn is defined as $R_{geom} = [R_{max} + R_{min}]/2$, such that the major radius of the machine is given by $R_0 = R_{geom}(\text{LCFS})$ while the position of the magnetic axis corresponds to $R_{axis} = R_{geom}(0)$. The local aspect ratio is therefore defined as $\epsilon(r) = r/R_0$. For all the cases, $a = 0.6$ m and $R_0 = 1.68$ m have been taken, corresponding to an inverse aspect ratio $a/R_0 = 0.36$, and the flux tube considered in the gyrokinetic simulations has been centered at r/a=0.5, such that ϵ=0.18. For all the simulations, a deuterium plasma is considered (assuming real mass ratio m_D/m_e=3670, m_D and m_e being respectively deuterium and electron masses), and as the benchmark is carried out in the flux tube limit, only the values of normalized inverse temperature and density gradient lengths $R_0/L_{T,n} = R_0 d\log(T,n)/dr$ at the position of interest are required. As already mentioned, these values are set to R_0/L_T=6.91 and R_0/L_n=2.22 for all the five cases. The same temperature is assumed for ions and electrons ($\tau = T_e/T_i = 1$). Collisions are neglected and no background flows are considered. Note that the inverse gradient lengths $R_0/L_{T,n}$ are evaluated as derivatives of the profiles with respect to the geometric minor radius r. The true normalized gradients driving the instabilities at a given position on a magnetic surface are however given by $R_0|\nabla\log(T,n)| = R_0 d\log(T,n)/dr|\nabla r|$, where the geometrical factor $|\nabla r|$ is in general different from unity and not constant on a magnetic surface in a shaped plasma. One may thus estimate on a given flux surface an effective flux-surface-averaged gradient given by $\langle R_0|\nabla\log(T,n)|\rangle = R_0/L_{T,n}\langle|\nabla r|\rangle_{fs}$. The corresponding values of $\langle|\nabla r|\rangle_{fs}$ evaluated at r/a=0.5 are listed in Table 4.2 and shown as a function of elongation in Figure 4.1. Note that in all the graphs comparing results pertaining to different geometries, the same color coding has been used: red for Case I, blue for Case II, black for Case III, green for Case IV and magenta for Case V. The nice alignment of the data in this plot already hints towards elongation being the most important shaping parameter considered here. Note that for all the Cases with elongation, the mid-radius values differ while the edge elongations are kept constant $\kappa_{LCFS} = 1.68$ (see Tables 4.1 and 4.3). We also remark that the higher triangularity that characterizes Case I is due to an effectively higher $\delta_{\text{LCFS}} = [\delta_{\text{LCFS}}(\text{upper}) + \delta_{\text{LCFS}}(\text{lower})]/2 = 0.25$ of the fully shaped plasma compared to Case II. Elongation penetrates differently with different edge triangularities, as noted in Ref. [90], and a lower δ leads to a larger κ in the core (Case III). Of particular interest in this benchmark is the possibility to study the effect of the usual shaping parameters on plasma behaviour by simply comparing the five Cases. We note that when moving from one case to another, although one specific

Case	I	II	III	IV	V
$\langle\|\nabla r\|\rangle$	0.907	0.871	0.864	1.040	1.003
$\langle R_0\|\nabla\log n\|\rangle$	2.014	1.933	1.918	2.308	2.226
$\langle R_0\|\nabla\log T\|\rangle$	6.269	6.017	5.969	7.184	6.929

Table 4.2 : Values of flux surface averaged $\langle|\nabla r|\rangle$ and the corresponding values of effective flux-surface averaged temperature and density gradient lengths for the five Cases ($R_0\langle|\nabla\log(T,n)|\rangle$=$R_0/L_{n,T}\langle|\nabla r|\rangle$).

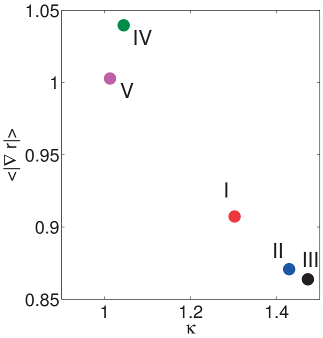

Figure 4.1 : Flux surface averaged $\langle|\nabla r|\rangle$ evaluated at $r = 0.5$ versus elongation κ. Numbers identify the corresponding case.

edge shaping parameter is sensibly varied intentionally, all the other parameters change to some degree as well.

In order to facilitate the understanding of the effect of the various shaping parameters, an interface with Miller's equilibrium [74] will be exploited in few cases (results shown in Figs. 4.5 and 4.14) using the GENE code. The Miller parametrization considered in GENE parametrizes in a poloidal plane $\varphi =$ const the contour of a given magnetic surface with geometric minor radius $r =$ const by a poloidal angle θ (in general different from the geometric angle) and is given in cylindrical coordinates (R, Z, φ) by [91]

$$R(r,\theta) = R_{geom}(r) + r\cos\left\{\theta + \arcsin\left[\delta(r)\sin\theta\right]\right\}, \tag{4.1}$$

$$Z(r,\theta) = Z_{axis}(r) + \kappa(r) r \sin\left[\theta + \zeta(r)\sin(2\theta)\right], \tag{4.2}$$

where the elongation κ, triangularity δ and squareness ζ have been introduced. Z_{axis} indicates the elevation of the magnetic axis with respect to the equatorial mid-plane. In order to evaluate these parameters, the global CHEASE equilibrium is fitted according to Eqs. (4.1) and (4.2) and the radial derivatives of the shaping parameters $[\kappa'(r), \delta'(r), \zeta'(r)]$, also required for implementing the Miller equilibrium in the gyrokinetic equations, are evaluated in the neighborhood of the flux surface of interest. The parametrization given by Eqs. (4.1) and (4.2) does not require to specify the value of the Shafranov shift, instead it requires the value of dR_{geom}/dr to build all the geometrical quantities required to solve

Case	q_s	s	κ	δ	ζ	Δ	α_{MHD}
I	1.382	0.804	1.3015	0.0812	$9.01\ 10^{-4}$	-0.0127	0.515
II	1.382	0.778	1.4287	0.0260	$5.22\ 10^{-4}$	-0.0132	0.5338
III	1.389	0.751	1.4723	-0.0070	$2.83\ 10^{-3}$	-0.0139	0.5425
IV	1.450	0.764	1.0443	0.0065	$5.13\ 10^{-4}$	-0.0206	0.5552
V	1.427	0.847	1.0124	0.0014	$1.04\ 10^{-4}$	-0.0045	0.0

Table 4.3 : Parameters characterizing the five flux surfaces of interest computed according to Eqs.(4.1) and (4.2).

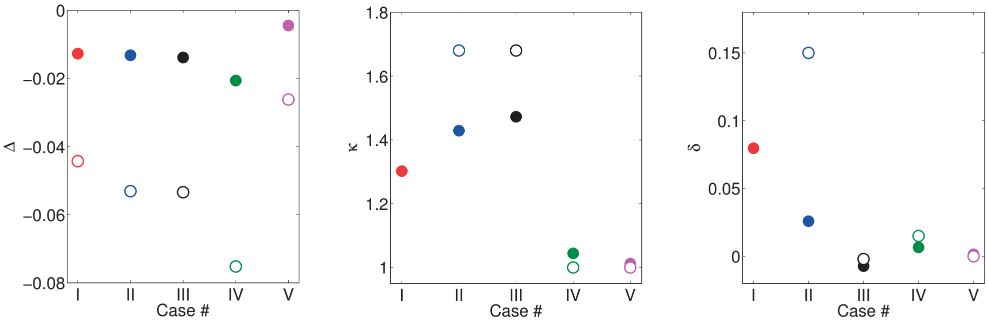

Figure 4.2 : Values of the usual shaping parameters: (a) Shafranov shift Δ, (b) elongation κ and (c) triangularity δ evaluated at the position $r/a = 0.5$ for the five test cases. The values at the LCFS are shown with empty symbols with the exception of Case I where the Miller parametrization given in Eqs.(4.1) and (4.2) is not suited for the LCFS.

the gyrokinetic equations. The actual parameters characterizing the flux surface $r/a = 0.5$ are listed in Table 4.3 for the five equilibria considered. For completeness the values of the Shafranov Shift Δ, defined as $[R_{geom}(r) - R_{axis}]/R_{axis}$, and $\alpha_{\mathrm{MHD}} = -q_s^2 R_0 (d\beta/dr)$ where $\beta = 2\mu_0 p/B_{mag}^2$, p and $B_{mag}^2/2\mu_0$ being respectively the local thermal pressure provided by the MHD equilibrium and the magnetic pressure estimated with the magnetic field B_{mag} on axis, are tabulated as well. As depicted in Figure 4.2 and quantified in Table 4.3, the different shaping parameters have different radial penetration depths. In particular it is to be noted for Case II, with finite triangularity $\delta_{\mathrm{LCFS}} = 0.15$ at the LCFS, that the remaining triangularity at r/a=0.5 is reduced by more than 80% to $\delta = 0.026$, illustrating the weak penetration depth of this shaping parameter. Elongation however, which remains finite down to the magnetic axis and as noted above is favored by small δ, is for example reduced only by $\approx$ 10% in Case III , going from κ_{LCFS}=1.68 to κ=1.47 at $r/a = 0.5$.

4.1.2 Linear k_θ-spectra

First, a linear electrostatic benchmark is performed, considering instability spectra with wave-numbers up to the electron Larmor radius scales. All the five cases are characterized by a mixed Ion Temperature Gradient (ITG) - Trapped Electron Modes (TEM) regime at the ion Larmor radius scale, as already shown in Ref. [89], while Electron Temperature Gradient (ETG) driven modes dominate the spectra at electron Larmor radius scales. Even though only purely electrostatic fluctuations are considered, the finite pressure gradient contribution is kept in computing the curvature drift $\mathbf{v}_c$. The value of β is computed consistently with the CHEASE equilibrium. The effect of the pressure gradient is small but not negligible, especially at the ITG to TEM transition, which is shifted to lower wave-numbers when this pressure term is accounted for.

At ion scales, the GENE code has been run in its eigenvalue (spectral) version [92–94] in order to recover not only the most unstable mode but the subdominant branches of the dispersion relation as well. At ETG scales, because of the absence of strong subdominant modes, the initial value (time evolution) approach was used for being significantly more effective than the eigenvalue procedure in determining the growth rates of the most unstable modes. All the simulations have been carried out considering $n_{k_x} = 32$ radial modes connected because of the parallel boundary condition, while $n_z = 64$ points have been used to discretize the "parallel" direction z. For the velocity space, unless specified differently, a uniform grid composed of $n_{v_\parallel}$=128 points between $0 < v_\parallel < 4.24 v_\mathrm{j}$ was used to discretize $v_\parallel$ direction, while n_μ=32 Gauss-Laguerre integration points between $0 < \mu < 9T_j/B_0$ were used for the μ direction. Here $v_\mathrm{j} = \sqrt{T_j/m_j}$ stands for the thermal velocity of species j.

The GKW code also considers a field-aligned coordinate system noted (r, ζ, s) built from the Hamada coordinates. Here r is the radial direction, ζ the binormal and s (one of the Hamada coordinates) is referred to as the "parallel" direction; as for the GENE code, parallel velocity $v_\parallel$ and magnetic moment μ are used for discretizing the velocity space. The GKW coordinate system is briefly presented in Appendix A, while a detailed description of the code is given in Ref. [95]. Similarly to GENE, a Fourier decomposition is used for the flux-tube representation in both r and ζ directions. The simulations have been carried out considering n_{k_r}=25 radial modes k_r connected via the parallel boundary condition, while n_s=35 points were used to discretize the s direction. Uniform grids in both $v_\parallel$ and μ, with the same upper limits as considered for GENE, have been adopted for the velocity space and discretized using $n_{v_\parallel} \times n_\mu = 128 \times 8$ points respectively.

Finally, the GS2 coordinate system (X, Y, θ) and its Fourier representation are directly related to the ballooning representation of a fluctuating field (see Appendix B and Ref. [96] for the details). All the simulations shown here have been performed considering n_{k_X}=15 connected radial modes, while a parallel resolution of $n_\theta = 32$ has been used to discretize a magnetic field line along one poloidal turn. Differently from GENE and GKW, in the GS2 code energy $\mathcal{E}$ and pitch angle $\lambda = v_\perp^2/(v^2 B_0)$ are used as velocity space variables to represent the distribution function, while the integration is carried out according to a Gauss-Legendre distribution of points. For these simulations $n_\lambda = 24$ points are used to discretize the λ direction while $n_\mathcal{E} = 18$ for $\mathcal{E}$. The maximum value of the $\mathcal{E}$-grid is set to 11.3 $m_j v_j^2/2$.

We point out that the simulations performed with the GENE code have been carried out with an higher resolution in both the radial and "parallel" directions with respect to GKW and GS2 with the aim of providing reference results well converged in all directions. We nevertheless remark that using a lower resolution e.g. $n_{k_x} \times n_z \times n_{v_\parallel} \times n_\mu = 32 \times 32 \times 64 \times 16$ in GENE is sufficient to provide growth rates and frequencies converged within 5% for all the microturbulence regimes and plasma shapes being considered here. We also note that the efficient parallelization scheme adopted in GENE allows to carry out the most resolved runs without a significant increase of the computational cost. A similar approach was used for the discretization of the velocity space, which as will be shown turns out to be crucial, especially as one needs to correctly resolve the trapped-passing particle boundary. The choice of $(v_\|, \mu)$ naturally requires a higher number of points to resolve this boundary compared to a discretization along $(\mathcal{E}, \lambda)$, which explains the difference between the GENE and GKW setups with respect to GS2. The trapped-passing boundary is indeed aligned to a Cartesian $(\mathcal{E}, \lambda)$ grid while it is diagonal to a $(v_\|, \mu)$ grid.

One of the main difficulties arising when comparing different codes is the dependence of the corresponding results on code-specific coordinate systems. This is particularly critical when considering plasmas with non-circular shapes, as differences between various coordinate systems become significant. We recall that for linear modes in an axisymmetric systems, n is an exact mode number, while this is not the case for poloidal mode numbers m. Nonetheless, as the fluctuations are field aligned, poloidal wave numbers can be estimated as $k_\theta \sim m/r$ with $m \sim nq_s$. Therefore we plot the real frequencies ω_r and the growth rates γ of the modes (in units of v_i/R_0) with respect to the effective poloidal mode number estimate $k_\theta = nq_s/r_0$ normalized to the ion Larmor radius $\rho_i = v_i/\Omega_i$. This quantity can be evaluated from each code's specific representation (see Eq. (3.9) for GENE and Appendixes A and B for details respectively to GKW and GS2 codes):

$$n = k_y C_y \qquad \text{for GENE} \tag{4.3}$$

$$n = \frac{k_\zeta}{2\pi} \qquad \text{for GKW} \tag{4.4}$$

$$n = k_Y \frac{1}{B_a} \frac{d\psi}{dr} \qquad \text{for GS2} \tag{4.5}$$

When plotting the results, we conform to GENE conventions on the sign of the real frequency of the mode: a positive value indicates a propagation in ion diamagnetic drift direction while a negative value corresponds to propagation in the electron diamagnetic direction.

The results obtained for the k_θ-spectra using the three codes are shown in Figure 4.3 at the ion scales ($k_\theta \rho_i \sim 1$), while in Figure 4.4 the linear spectra at the electron scales ($k_\theta \rho_e \sim 1$) are compared for Case I. All results shown here consider zero ballooning angle $\chi_0 = 0$, where χ is the straight field-line poloidal angle defined in Eq. (3.1). With the previously specified setup, GENE, GKW and GS2 agree between each other within 3% on both real frequency ω_r and growth rate γ of the most unstable modes, at all scales and independently from shaping. Separate convergence studies have been performed at the different scales and the difference between the codes was further reduced to 1% when higher resolutions, similar to the GENE ones, were considered by the different codes. We note that the transition from ITG to TEM cannot be taken as a practical benchmark point as its position is very sensitive to the resolution used and a convergence study is particularly expensive.

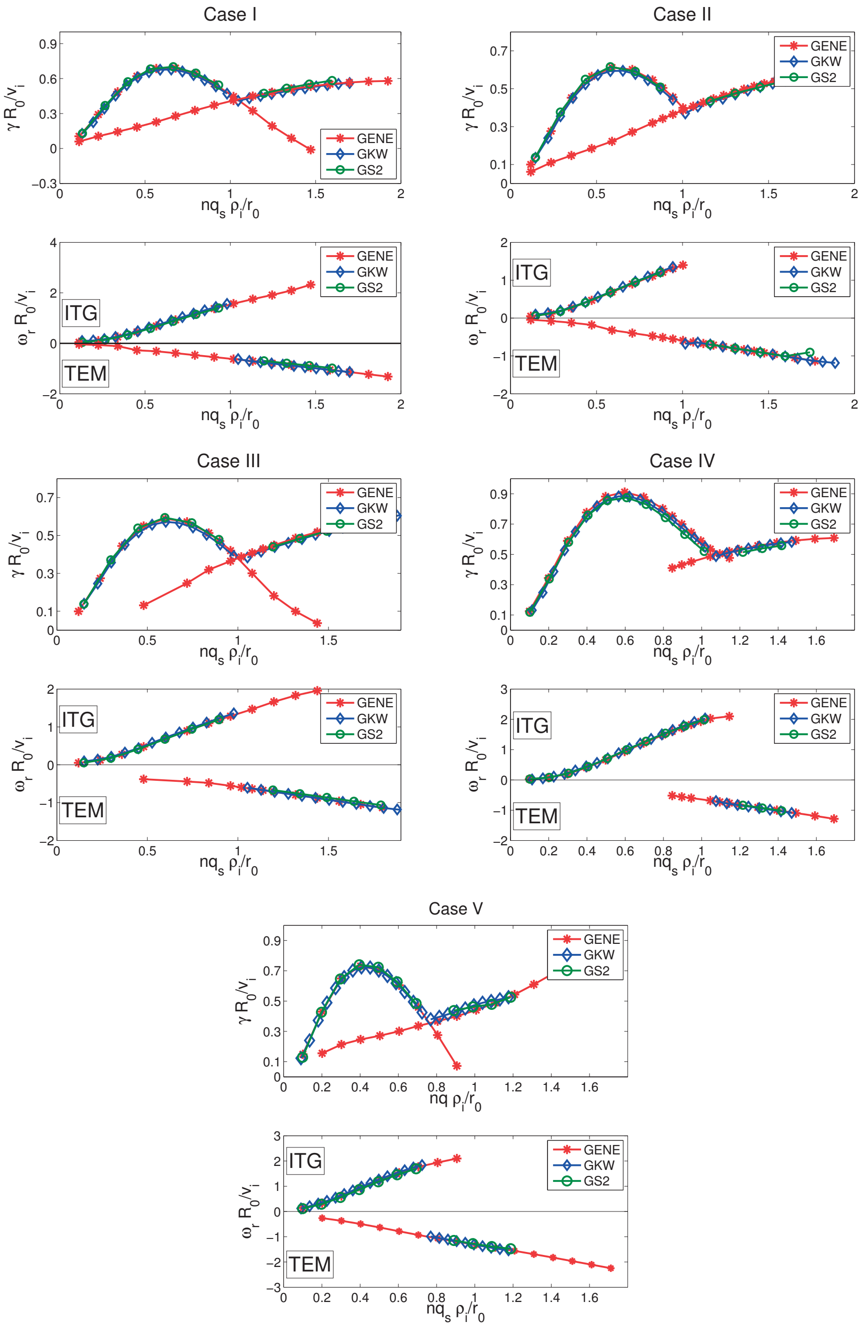

Figure 4.3 : Real frequency ω_r and growth rates γ normalized to R_0/v_i as a function of the effective poloidal mode number $k_\theta\rho_i = nq_s\rho_i/r_0$ for the five CHEASE equilibrium test cases. Shown are the results obtained with the GENE (red stars), GKW (blue diamonds) and GS2 (green circles) codes. Sub-dominant modes are only provided for GENE results.

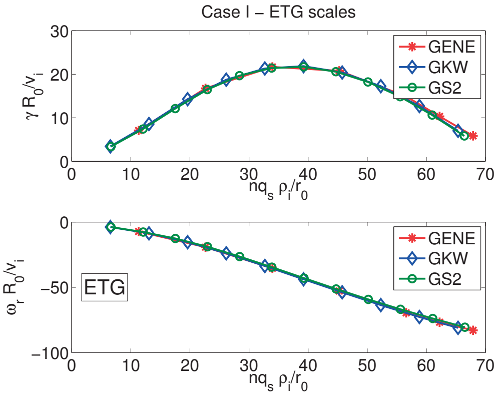

Figure 4.4 : Benchmark at electron scales for Case I. Results from GENE (red stars), GKW (blue diamonds) and GS2 (green circles).

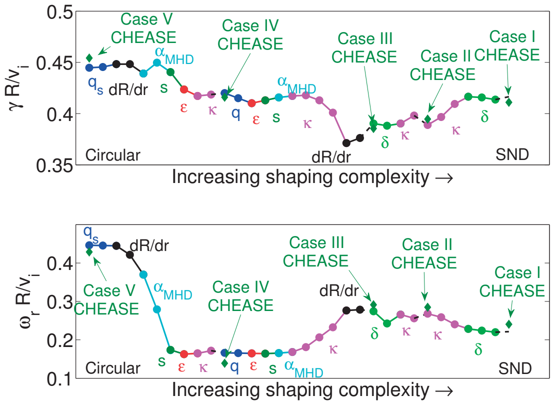

Figure 4.5 : Variation of growth rate γ and real frequency ω_r for fixed $k_y\rho_i = 0.3$ (according to GENE convention) continuously increasing shaping complexity from Case V (circular, $\beta = 0$) to I (SND, $\beta \neq 0$) making use of the Miller equilibrium representation. Labels indicate the parameter being changed at each step. Results obtained for the five cases with the MHD equilibrium are shown for comparison and labeled "CHEASE" (green diamonds). All results have been obtained with the GENE code.

As already discussed in Sec. 4.1.1, when going from one equilibrium case to the other, all the parameters characterizing the actual local flux surface geometry are changed. The interface to the Miller equilibrium given in Eqs. (4.1) and (4.2) has therefore been used to study the effect of each parameter separately. Starting from the representation of the flux surface of Case V, one geometrical parameter is changed at the time, until reaching the values characteristic of Case I. The results, obtained with GENE for $k_y\rho_i = 0.3$, are presented in Figure 4.5, where the labels indicate the particular parameter being changed (either q_s, $\hat{s}$, ϵ, κ, δ or dR/dr). Dashed lines are used for illustrating the combined variation related to parameters inducing only smaller effects. We note that having performed this scan at fixed $k_y\rho_i$, the equivalent $k_\theta\rho_i$ as defined in Eqs. (4.3-4.5) is not constant because of the variation in both n and q_s ($k_\theta\rho_i$ varies between 0.296 and 0.451).

From Figure 4.5 it appears, as expected, that any variation of the parameters used to describe the plasma equilibrium contributes to a change in the linear spectra. For each change of equilibrium between Cases V and III it is possible to identify one parameter which leads to the most significant variation: α_{MHD} going from Case V to IV (responsible for the Shafranov shift), elongation κ going from Case IV to III. Note that going from Case III to II, very little variation arises from the change in triangularity, while the effect of the variation of κ is comparable to the results of changing all the other parameters. Going from Case II to I, where despite the up-down asymmetry the Miller parametrization still is a good approximation, elongation appears once again as the main reason for change in growth rate and frequency of the mode. Triangularity δ, despite the significant relative variation at the considered reference surface (see table 4.3), has only a little effect.

Considering the relative variation of the growth rate for a given relative variation of the various shaping parameters considered here, elongation appears the most important, and the change in linear stability from Case IV to I can be explained mainly by a variation in κ. As an example, in Figure 4.6 we plot γ of the most unstable mode in the ITG regime for the five test Cases versus the corresponding effective temperature gradient (which is determined mainly by elongation, as shown in Fig. 4.1). A trend is clearly recovered; we plot also the result obtained for Case V which appears not as much aligned as the other points. This happens because of the strong effect exerted by $\alpha_{\text{MHD}} = 0$ and dR_{geom}/dr in going from Case IV to V.

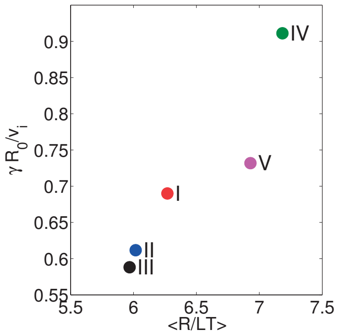

Figure 4.6 : Maximum linear growth rate in ITG regime for all five Cases versus the flux surface averaged temperature gradient length. Values in units of R_0/v_i. Numbers identify the corresponding case. Results from the GENE code.

4.1.3 Ballooning angle scan

The ballooning representation [97] of a given fluctuating field $\mathcal{A}(x,\chi,\varphi)$ in straight field line coordinate system reads

$$\mathcal{A}(x,\chi,\varphi) = \hat{\mathcal{A}}(\chi)e^{-\mathrm{i}n\{\varphi - q(x)[\chi-\chi_0]\}}. \tag{4.6}$$

The exponential term in (4.6) represents the fast phase factor for field-aligned fluctuations, while χ_0 corresponds to the so-called ballooning angle, angle at which the fast phase does not vary radially through $q(x)$. $\hat{\mathcal{A}}(\chi)$ is the so-called ballooning envelope and accounts for the slow variation of the fluctuation along the magnetic field line. Any radial modulation of the envelope has already been neglected. Equation (4.6) does not ensure periodicity with respect to χ which is therefore enforced by expressing the actual field $A(x,\chi,\varphi)$ in terms of $\mathcal{A}(x,\chi,\varphi)$ as follows:

$$\begin{aligned} A(x,\chi,\varphi) &= \sum_{p=-\infty}^{+\infty} \mathcal{A}(x,\chi+p2\pi,\varphi) \\ &= e^{-\mathrm{i}n[\varphi-q(x)\chi]} \sum_{p=-\infty}^{+\infty} \hat{\mathcal{A}}(\chi+p2\pi)e^{\mathrm{i}nq(x)[p2\pi-\chi_0]} \end{aligned} \tag{4.7}$$

Identifying $k_y y = -n\,[\varphi - q(x)\chi]$ according to Eqs. (3.2) and (3.9), and after again linearizing the safety factor profile, one obtains

$$\begin{aligned} A(x,\chi,\varphi) &= e^{\mathrm{i}k_y y} \sum_{p=-\infty}^{+\infty} \hat{\mathcal{A}}(\chi+p2\pi)e^{\mathrm{i}k_y\hat{s}x(p2\pi-\chi_0)}, \\ &= e^{\mathrm{i}k_y y}e^{-\mathrm{i}k_y\hat{s}\chi_0 x} \sum_{p=-\infty}^{+\infty} \hat{\mathcal{A}}(\chi+p2\pi)e^{\mathrm{i}p2\pi\Delta_{k_x}x}. \end{aligned} \tag{4.8}$$

In deriving equation (4.8) the radial coordinate has been radially shifted *i*.e., $x + x_0/\hat{s} \to x$. Comparing equation (3.14) to (4.8), one thus identifies

$$\begin{cases} \chi_0 = -\dfrac{\delta k_x}{k_y\hat{s}}, \\ \hat{\mathcal{A}}(\chi+p2\pi) = \hat{A}_{\delta k_x + p\Delta k_x}(z). \end{cases} \tag{4.9}$$

The effect of a finite ballooning angle χ_0 is usually neglected in linear studies and benchmarks, which are normally carried out under the assumption of zero χ_0. However, linearly [98–100] and non linearly correctly taking into account ballooning angle is crucial to accurately predict the transport level, thus the reason for benchmarking this effect. We recall also that the ballooning angle is the angle at which turbulent eddies point radially.

A finite ballooning angle can be introduced in the Fourier representation of all the codes used. As already discussed, for a given k_y (resp. k_ζ, k_Y) linear mode, GENE (resp. GKW, GS2) code couples the radial Fourier modes $k_x = \delta k_x + p\Delta k_x$ (resp. $k_r = \delta k_r + p\Delta k_r$, $k_X = \delta k_X + p\Delta k_X$), $p \in \mathcal{Z}$, where δk_x, δk_r andδk_X are related to the straight field poloidal ballooning angle χ_0 by the relations (see also Appendixes A and B for further details about resp. GKW and GS2):

$$\chi_0 = -\frac{\delta k_x}{k_y \hat{s}} \qquad \text{for GENE} \tag{4.10}$$

$$\chi_0 = -2\pi \frac{\delta k_r}{k_\zeta dq/dr} \qquad \text{for GKW} \tag{4.11}$$

$$\chi_0 = -\frac{\delta k_X}{k_Y \hat{s}} \qquad \text{for GS2} \tag{4.12}$$

For each of the five test cases, a scan of χ_0 has been carried out at given toroidal mode number, $k_\theta|_{\mathrm{GKW}}\ \rho_i = 0.2$ according to GKW definitions, the corresponding values of $nq_s\rho_i/r_0$ are listed in Tab. 4.4. For the sake of completeness the input values of $k_y\rho_i|_{\mathrm{GENE}}$ and $k_Y\rho_i|_{\mathrm{GS2}}$ used for the equivalent GENE and GS2 runs are reported as well. The resolution $n_{k_x} \times n_z \times n_{v_\parallel} \times n_\mu = 32 \times 64 \times 128 \times 32$ has been used for the simulations performed with the GENE code, while GKW runs have been carried out considering $n_{k_r} \times n_s \times n_{v_\parallel} \times n_\mu = 27 \times 35 \times 128 \times 32$. GS2 runs have been performed using $n_{k_X} \times n_\theta \times n_\lambda \times n_\mathcal{E} = 63 \times 48 \times 24 \times 18$ grid points. The results obtained are shown in Figure 4.7, where growth rates and frequencies are plotted as a function of χ_0 for the five geometries.

We note that increasing the ballooning angle the ITG mode, which is the most unstable one associated to $\chi_0 = 0$, is first stabilized. Then at larger values of χ_0 ($\chi_0 \sim \pm 0.3$) a transition to TEM is found for all Cases except Case IV, where the mode is stable. With the GENE code, used in its initial value mode of operation, we resolved the mode transition systematically for all geometries. As can be seen from Fig. 4.7 a good agreement is again recovered between the codes, within 3% on both frequency and growth rate. As for the k_θ-spectra, the transition point is strongly dependent on the resolution adopted and cannot be taken as an exact benchmark point (a convergence study being too costly).

Case	I	II	III	IV	V
$nq_s\rho_i/r_0$	0.180	0.222	0.308	0.312	0.276
$k_y\rho_i\|_{\mathrm{GENE}}$	0.231	0.246	0.251	0.227	0.179
$k_\theta\rho_i\|_{\mathrm{GKW}}$	0.2	0.2	0.2	0.2	0.2
$k_Y\rho_i\|_{\mathrm{GS2}}$	0.197	0.196	0.201	0.223	0.183

Table 4.4 : Equivalent poloidal mode number $nq_s\rho_i/a$ used for the finite ballooning angle scan in the five test Cases. The corresponding GENE, GKW and GS2 input binormal wave vectors $k_y\rho_i|_{\mathrm{GENE}}$, $k_\theta\rho_i|_{\mathrm{GKW}}$ and $k_Y\rho_i|_{\mathrm{GS2}}$, are tabulated as well.

We also remark that for this particular value of $nq_s\rho_i/r_0$ in spite of the up-down edge asymmetry, the most unstable modes for Case I are indeed associated to zero ballooning

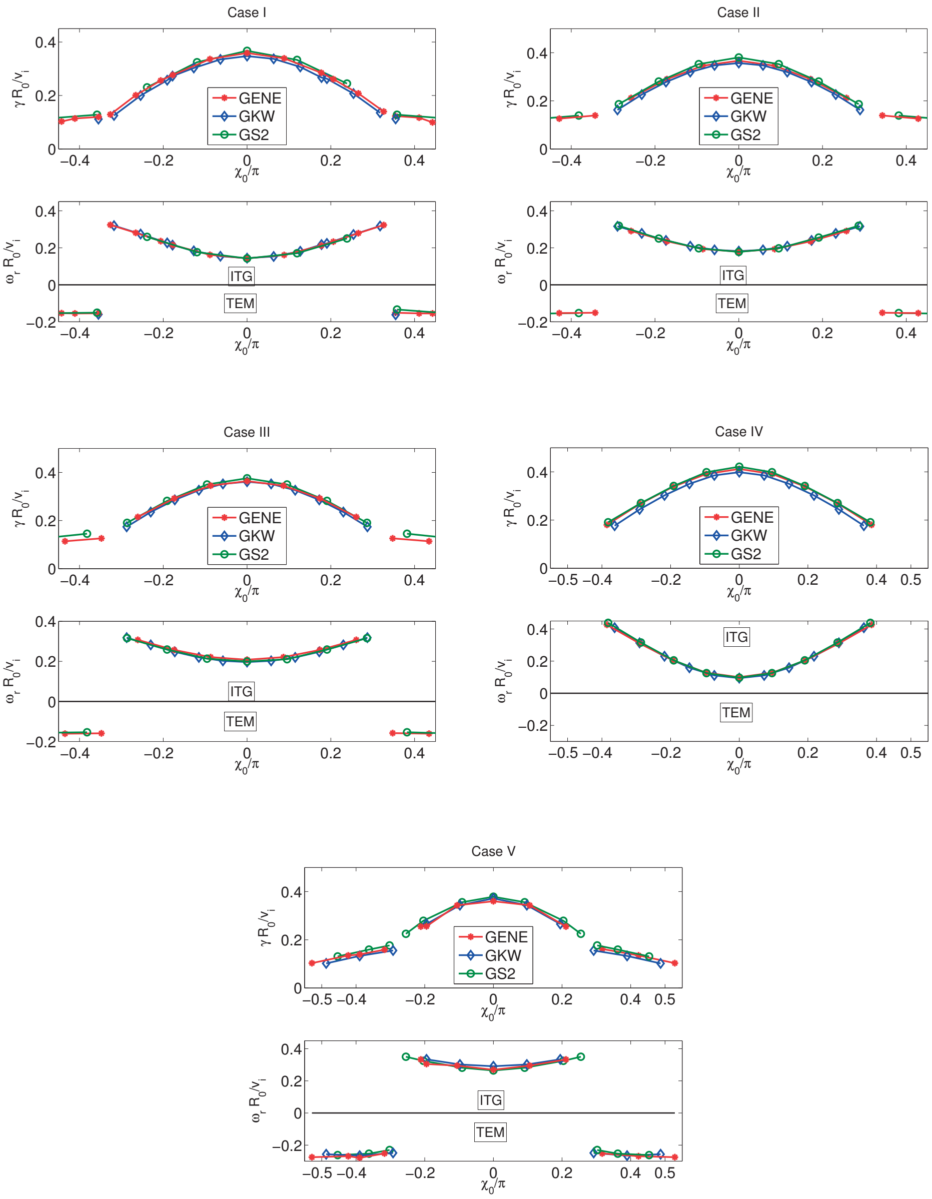

Figure 4.7 : Ballooning angle scan for the five test cases. From Case I to V growth rates and frequency in units of v_i/R_0 are shown for the GENE code (red) code, GKW (blue) and GS2 (green).

angle (the difference between growth rates at positive and negative χ_0 is of the order of $\simeq 2\%$, with more unstable modes at positive angles). This is because the flux surface of interest is relatively inside the plasma cross section, such that the effective up-down asymmetry is very weak.

Finally, we benchmark the mode structure of the electrostatic potential ϕ associated to some of the modes for which frequency and growth rate have been computed in the previous Section. In order to compare the results from different codes, amplitudes and phases of the fields must be appropriately renormalized; we therefore plot $\phi(\chi)$ renormalized such that $\Re\{\phi(\chi = 0)\} = 1$ and $\Im\{\phi(\chi = 0)\} = 0$.

Benchmarking the ballooning structure turns out to be very challenging, more than the growth rate and frequency of the mode. In particular, we note that when growth rate and frequency of the mode are converged within few percents ($\sim 5\%$), then the most ballooned part of the mode, *i*.e., $-\pi \leq \chi \leq \pi$ is also converged and a good agreement between the codes is recovered. An example is given in Figure 4.8, where the eigenfunction of the mode $nq_s\rho_i/r_0 = 0.276$, computed considering the magnetic geometry of Case V and $\chi_0 = 0$, is compared. The results of Fig. 4.8 have been obtained using the same resolutions as adopted for computing real frequency and growth rate of the mode, and one observes differences in the tails of the eigenfunction, for $\chi > 2\pi$. We nevertheless remark that even if the local differences can be up to 30%, they remain small compared to the maximum amplitude of the mode.

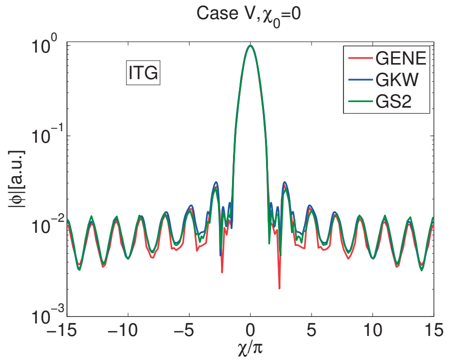

Figure 4.8 : Ballooning representation of the electrostatic potential ϕ computed with GENE (red), GKW (blue) and GS2 (green) for the mode $nq_s\rho_i/r_0 = 0.276$ and $\chi_0 = 0$. Magnetic geometry of Case V.

In order to converge the mode structure and have the same good match between codes over a wider range of χ values, the resolution has to be significantly increased. Besides a sufficiently large number of connections along the field line, corresponding *e*.g., to the number of k_x modes in GENE, the velocity space resolution turns out to be crucial for recovering a good agreement over the complete ballooning structure. This is especially true for the TEM modes, for the same reasons as described in Sec. 4.1.2. This turns out to be a challenging and computationally significant effort, therefore it has been limited to GENE and GKW codes only. No particular reason prevents from doing the same also

with GS2. Also, this benchmark is carried out considering only Case V and I, viz. the circular and the fully shaped geometry, while values of χ_0 have been selected such that both ITG and TEM regime are studied.
The results obtained are shown in Figure 4.9 for Case V and Figure 4.10 for Case I. All these simulations have been performed considering 64 n_{k_x} modes in GENE and 64 n_{k_r} in GKW, while 70 points have been used to discretize along the magnetic field line. The runs associated to ITG modes have been carried out discretizing the phase space with $n_{v_\parallel} \times n_\mu$=128 × 32 points in both codes, while for TEM modes the velocity space resolution has been further increased to 192 × 48 in GENE and 256 × 64 in GKW. With these grids the frequency obtained from the two codes agree within less than 1%. The different number of grid points required for velocity space is explained by their different distribution. We note that the two codes adopt different boundary conditions at the beginning and end of a magnetic field line: in GENE, the default setting is assuming zero perturbation at the domain boundaries (other options are available). In GKW a zero derivative condition is applied (see Refs. [33, 95] for more details on the actual implementation). We have verified by further increasing the number of connected radial modes that the boundary condition is not affecting the results. We also note that reducing parallel dissipation in GKW appears to further improve the agreement. However, this requires to set a smaller time step increasing the cost of the runs, so we have carried out all the simulations setting the dissipation to 0.02 without further pushing the convergence.

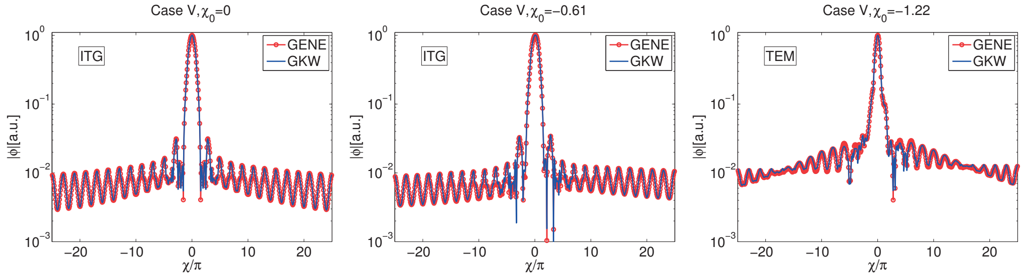

Figure 4.9 : Ballooning representation of the electrostatic potential ϕ computed with GENE (red) and GKW (blue) for three different values of ballooning angle χ_0. Shown are the results obtained for (a) zero ballooning angle, (b) finite χ_0 in the ITG regime and (c) finite χ_0 for TEM. The value of χ_0 is reported in each plot.

4.1.4 Rosenbluth - Hinton test

Correctly describing Zonal Flows is essential for any turbulence simulation as they are one of the main mechanisms of saturation in non-linear regime, at least in ITG dominated plasmas. The Rosenbluth-Hinton test [101] allows to study linear dynamics of ZFs by computing the residual level of e.g. the potential and at the same time characterize the properties (real frequency ω_{GAM} and damping γ_{GAM}) of the Geodesic Acoustic Mode

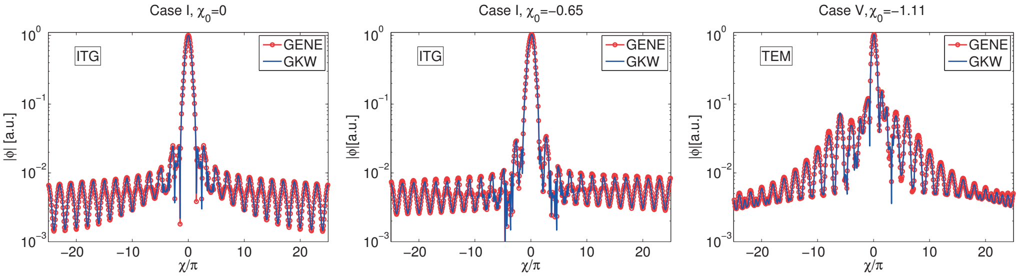

Figure 4.10 : Same as Figure 4.9, but for Case I.

(GAM) [54]. Several theoretical works are available providing estimates for both the residual level and the GAM properties under various limits. Thus in addition to code benchmarking it is also possible to validate simulation results against such estimates, in their proper limit.
In order to avoid the numerical problem of small recurrence time due to light electrons, this particular test has been carried out considering the adiabatic response of the electrons. Fully kinetic simulations show the same level of residual potential, confirming the validity of the approach.

GENE simulations have been performed evolving an ion density perturbation associated to the mode $k_x\rho_i = 0.05$, $k_y = 0$ and solved on grids involving up to $n_z \times n_v \times n_\mu = 64 \times 400 \times 32$ points. No hyperdiffusion has been used in order to avoid any effect on the frequency of the GAM [102]. Density and temperature gradients have been set to zero. The same set up was used for carrying out GKW simulations, which have been performed using $n_s \times n_{v_\parallel} \times n_\mu = 140 \times 256 \times 27$ grid points. Hyperdiffusion has been switched off as well. GS2 adopts a different initial condition for Zonal Flow investigations, consisting in evolving in time an initial zonal electrostatic field without initiating any density perturbation. These different initial conditions are found to lead to the same final results. The runs performed with GS2 have been carried out considering $n_\theta \times n_\lambda \times n_\mathcal{E} = 64 \times 32 \times 48$ grid points.

We benchmark the value of the residual potential $\langle\phi(\infty)\rangle/\langle\phi(0)\rangle$, defined as the flux surface averaged electrostatic potential $\langle\phi\rangle$ normalized to its initial value $\langle\phi(0)\rangle$. This quantity is computed after the GAM oscillation is completely damped. Simulations are run well beyond this limit, typically up to $150R_0/v_i$, to ensure a true stationary state and check that the recurrence problem is not affecting the results. The obtained residual levels computed with GENE, GKW and GS2, are shown in Figure 4.11, and compared with several theoretical estimates available in the literature. These are all of the form

$$\frac{\langle\phi(\infty)\rangle}{\langle\phi(0)\rangle} = \frac{1}{1 + Sq_s^2/\sqrt{\epsilon}} \tag{4.13}$$

where S is a shaping function dependent on the model used for describing the magnetic geometry. For circular concentric magnetic surfaces in large aspect ratio Tokamaks, Eq. (4.13) reduces to the well known expression by Rosenbluth and Hinton $1/(1{+}1.6q_s^2/\sqrt{\epsilon})$ valid to first order in ϵ. For shaped Tokamaks, Xiao and Catto [103] derived a shaping function valid up to second order in ϵ in which all shaping parameters explicitly appear

$$\begin{aligned} S_{XC} = \frac{1}{1+\kappa^2}\Bigg(&3.27 + \sqrt{\epsilon} + 0.722\,\epsilon - 1.44\,\delta - 2.945\frac{\Delta}{\epsilon} \\ &+ \frac{0.692k^2 - 0.722}{q_s^2}\epsilon\Bigg) \end{aligned} \tag{4.14}$$

while Zhou and Yu [104] adopted a Miller equilibrium to obtain

$$\begin{aligned} S_{ZY} =& \frac{1}{\kappa^2\left(1+3\delta\epsilon/8\right)^2 I_0}\left\{\frac{25}{16} - \frac{53}{256}\delta + \frac{\sqrt{\epsilon}}{2} - \epsilon\right. \\ &\left.\times\left[\frac{3}{64} - \frac{93}{256}\delta + \frac{9\kappa^2}{8q_s^2}\left(\frac{3I_0}{4} + I_1\right)\right]\right\} \end{aligned} \tag{4.15}$$

I_0 and I_1 are two geometrical quantities defined in Ref. [104], q_s,ϵ, κ, δ and Δ are the local values at $q = q_s$. We note that the definition of ϵ, elongation κ triangularity δ and Shafranov shift Δ appearing in equations (4.14) and (4.15), depend on the particular parametrization used for describing the flux surface. Therefore their value is computed by fitting the CHEASE equilibrium accordingly to each specific magnetic geometry model. The agreement obtained between the codes is very good, within 1% and independent from shaping. A systematic deviation from analytic estimates is found in all shaped cases (Case I to IV), among which the one by Zhou and Yu (Eq. (4.15)) is found to give the estimate closest to our numerical simulation (≈ 10% lower).

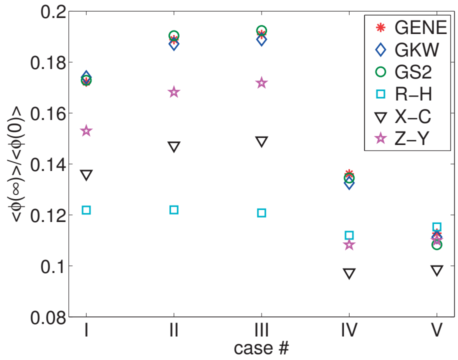

Figure 4.11 : Residual potential computed with GENE (red stars), GKW (blue diamonds) and GS2 (green circles) normalized to its initial value for each equilibrium Case, I to V. For comparison, the theoretical estimates given by Rosenbluth-Hinton [101] (R-H), Xiao-Catto [103] (X-C) and Zhou-Yu [104] (Z-Y) are shown as well with cyan squares, black triangles and magenta pentagrams respectively.

When performing the Rosenbluth-Hinton test, the GAM is excited and its real frequency and damping can be extracted from the time trace of the simulated potential. The damping γ_{GAM} is obtained upon fitting the maxima and minima of the residual to an exponential envelope. The frequency is subsequently extracted via inverse Hilbert transform. An example is shown in Figure 4.12. When comparing different codes the same time window is used. This is necessary especially when evaluating the damping which is strong in the cases considered here and therefore only few GAM oscillations are contained in the simulated time trace. The three codes agree between each other on ω_{GAM} within 1%. The numerical results, together with the numerical solution to the dispersions relations proposed in Refs. [56] and [57] are shown in Figure 4.13. The first analytical estimate, valid only for circular plasmas, agrees with the simulation only for Case V, while the latter which retains shaping effects, matches the simulation in all Cases with less than 5% difference. The strong GAM damping found in all shaped plasmas (Cases I to IV) makes its estimation from the simulation difficult. Nevertheless the codes agree between each other, while a sensible difference is found when comparing to analytical estimates.

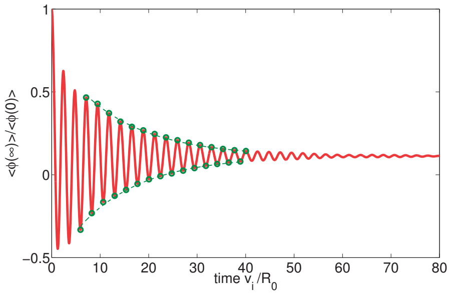

Figure 4.12 : Time trace of electrostatic potential normalized to its initial value for Case V (values obtained with the GENE code). The points used to estimate GAM real frequency and damping are shown with green circles together with the corresponding estimated exponentially decaying envelope.

The same analysis as described in Section 4.1.2 of interfacing the flux surfaces with the Miller equilibrium for studying the effect of all parameters, has been repeated for the Rosenbluth-Hinton test. Figure 4.14, showing the residual potential level and the GAM properties, confirms that when going from one case to the other all the parameters play a role but whenever κ is varied, it is responsible for the major part of the change. This is true in particular for Case II where, despite considering a triangular plasma, most of the difference is originated by a variation of elongation from Case II, and also for Case I. Note that in Fig. 4.14 the values have been normalized to $R_{geom}(r)/v_i$ for simplicity. We can therefore plot the results of this test with respect to elongation, as shown in Figure 4.15. The results are nicely aligned and show how an increase of κ leads to an increase of the residual level while at the same time the GAM frequency is reduced and the mode is more strongly damped.

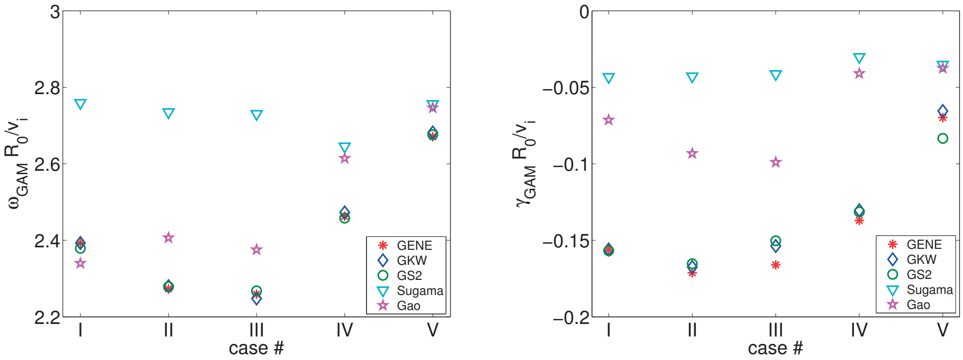

Figure 4.13 : GAM real frequency ω_{GAM} and damping rate γ_{GAM} for the five test Cases. Shown are GENE results (red stars), GKW ones (blue diamonds) and GS2 (green circles). The analytic predictions by Sugama [56] (cyan triangles) and the one from Gao [57] (magenta pentagrams) are shown as well.

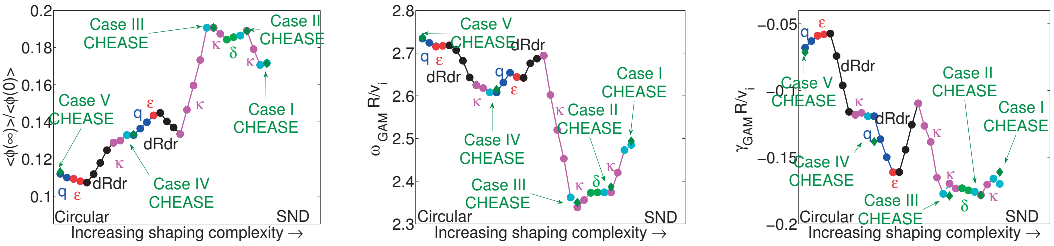

Figure 4.14 : Effect of the shaping parameters on (*a*) ZF residual, (*b*) GAM frequency ω_{GAM} and (*c*) GAM damping γ_{GAM}. Results obtained with the GENE code performing the RH test after fitting the equilibria according the parametrization given by Eqs. (4.1) and (4.2). One parameter is varied at each time as indicated by labels, the values are listed in Table 4.3. For comparison, the values obtained when using the CHEASE equilibrium are reported as well (green).

4.2 Global benchmarks

The same five geometries are currently being employed for benchmarking the CHEASE interface for the global version of GENE. This benchmark is carried out within the framework of an international validation effort, the EUROFusion Enabling Research project *"Verification and validation of global gyrokinetic codes"*. This effort currently involves the GENE and ORB5 codes.

Carrying out a similar exercise as the one described in the previous sections, but employing global gyrokinetic codes, appears of great interest, among others because it has not been carried out systematically before. The need of having at least an heat source for carrying out a global turbulence simulation, naturally makes extremely valuable carrying out not only linear but also nonlinear simulations.

Assuming a given resolution, global runs are significantly more expensive than flux-tube ones. Hence, in order to define a series of benchmarks that are meaningful for verification

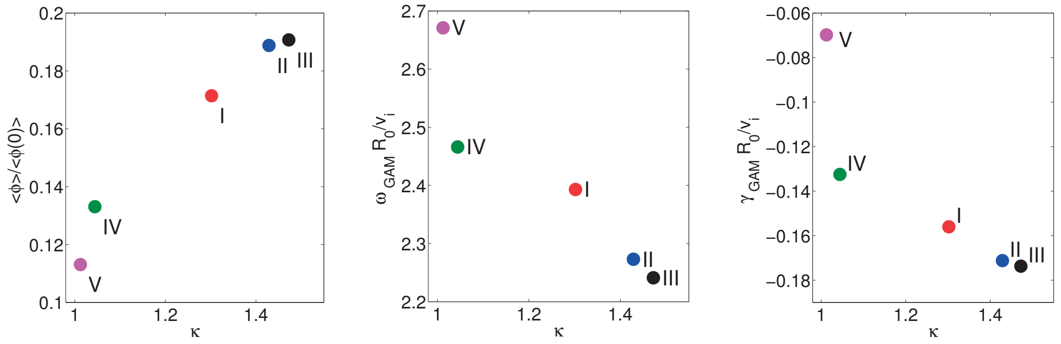

Figure 4.15 : Results of the Rosenbluth-Hinton represented versus elongation κ of each test Case. Shown are (a) the residual level, (b) the GAM real frequency ω_{GAM} and (c) the damping γ_{GAM}. Numbers indicate the corresponding test case.

purposes, in particular of the magnetic geometry, but with a limited (and affordable) computational cost, only a subset of the five cases will be used and in most cases an adiabatic electron response assumed. This greatly reduces the overall cost of the runs.
Analytic temperature and density profiles are chosen instead of realistic ones. On the one hand, this allows to avoid simulating the edge region where gradients are typically very large and therefore the simulation very demanding. On the other hand it makes the definition of the profiles unique and reproducible by any code. We choose to use profiles of the form [64]:

$$\hat{T}_{i,e}(\rho) = \left[\frac{\cosh\left(\frac{\rho-\bar{\rho}+\delta T}{\Delta T}\right)}{\cosh\left(\frac{\rho-\bar{\rho}-\delta T}{\Delta T}\right)}\right]^{-\kappa_T\epsilon\Delta T/2} , \quad \hat{n}_{i,e}(\rho) = \left[\frac{\cosh\left(\frac{\rho-\bar{\rho}+\delta n}{\Delta n}\right)}{\cosh\left(\frac{\rho-\bar{\rho}-\delta n}{\Delta n}\right)}\right]^{-\kappa_n\epsilon\Delta n/2} . \quad (4.16)$$

Here δT and ΔT (and δn, Δn respectively) are characteristic profiles widths shown in in Figure 4.16, while κ_T and κ_n are the maximum value of temperature and density gradient. Finally, ϵ is the inverse aspect ratio of the machine $\epsilon = a/R_0$. The radial coordinate is based on the normalized plasma volume enclosed inside a given flux surface, $\rho = \rho_{vol} = \sqrt{V(r)/V_{\mathrm{LCFS}}}$, and $\bar{\rho}$ indicates the radial location at which the profiles are centered, in all cases 0.5.

While the maximum gradients are chosen to be CBC like ($\kappa_T = 6.91$ and $\kappa_n = 2.22$), different profiles widths are taken for linear and nonlinear benchmarks, with once again the aim of reducing the cost of the runs. In particular, in order to avoid beating between modes linearly unstable at different radial locations, a more localized gradient is assumed in linear runs compared to nonlinear ones.
One final aspect that has to be carefully taken into account, is the orientation of the equilibrium toroidal magnetic field and plasma current. The only equilibrium which is explicitly built such as to possess an up-down asymmetry is Case I, one might be tempted to assume that a transformation $Z \to -Z$, which is equivalent to flipping the sign of the

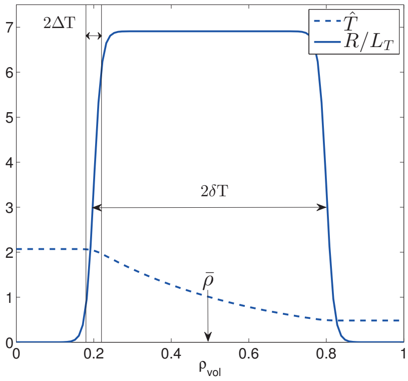

Figure 4.16 : Example of a normalized temperature profile $\hat{T}$ (dashed line) and associated normalized logarithmic gradient length R/L_T (solid line) computed according to Eq. (4.16). The characteristic profile widths (δT and ΔT), as well as the center position $\bar{\rho}$ have been indicated with arrows.

torodal field B_φ or of the plasma current I_p in a perfectly up-down symmetric geometry, will not affect the results. It turns out that in all cases the effect of such transformation is not negligible and one must use the same orientation of the two aforementioned quantities in order to recover the desired agreement between the different codes. In practice, this can be achieved thanks to the CHEASE code itself, which allows to freely change the orientation of both B_φ and I_p. We note that all equilibria considered assume a negative magnetic field orientation and a positive plasma current, thus resulting in a negative q profile according to GENE conventions and a positive one in ORB5 coordinates. Unless this condition is not met, a small difference ($\sim 10\%$) on the frequency and growth rate is found even in the Cases II to V.

4.2.1 Linear runs with adiabatic electrons

As a first step, the linear growth rares and frequencies of the most unstable mode for a toroidal mode number scan are compared. For these tests, $\delta T = 0.075$ and $\Delta T = 0.02$ (the same values are chosen for the density profile as well) have been assumed.
GENE simulations are carried out considering an annulus centered at $\rho_{vol} = 0.5$ and covering half minor radius of the plasma. A single machine size, with $\rho^* = \rho_i/a = 1/180$ where ρ_i is the ion Larmor radius measured at the center of the simulation domain, is considered. Separate convergence studies have been carried out for different values of n_0 in order to ensure the convergence of the results within 3%. A typical GENE grid reads $n_x \times n_z \times n_v \times n_\mu = 256 \times 48 \times 96 \times 32$. Finer grids grids are required for higher n_0 modes. ORB5 simulations have been performed considering the same radial domain, discretized with $n_r \times n_\chi \times n_\varphi = 200 \times 1024 \times 512$ points along respectively the radial, poloidal and toroidal directions.

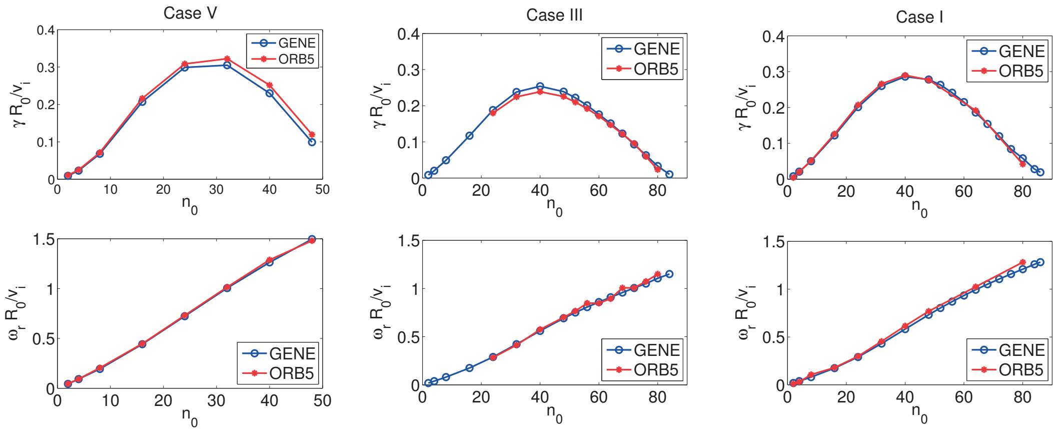

Figure 4.17 : Growth rate γ and real frequency ω_r, in units of R_0/v_i, of the most unstable mode for a scan over toroidal mode number n_0. Shown are the results obtained with GENE (blue circles) and ORB5 (red stars) for Case V (a), Case III (b) and Case I (c).

The results for Case V (circular with $\beta \sim 0$), Case III (elongated) and Case I (fully shaped) obtained with GENE and ORB5 are compared in Figure 4.17. A good agreement is recovered, for all shapes and values of n_0 on both growth rate and frequency. A small difference $\sim 5\%$ is observed on the value of the growth rate, which is however within the error bars associated to the determination of this quantity. In order to make the comparison more robust and detailed, the eigenfunction of the most unstable mode has been compared as well. An example, obtained considering the magnetic geometry of Case I (which because of the up-down asymmetry is the most challenging shape), is depicted in Figure 4.18 where the electrostatic potential ϕ is shown on a poloidal plane. To further quantify any difference between the two codes, we looked at the field amplitude as a function of the the parallel and radial coordinates. This is accomplished by comparing ϕ as function of the straight field line angle χ on the flux surface at $\rho_{vol} = 0.5$, as well as comparing it as a function of ρ at few specific poloidal location ($\chi = 0, \pi$ and $\pm\pi$), as show in Figure 4.19. The fields are obtained at the end of a linear simulation i.e. when the growth rate is converged. As a consequence, the amplitude and the phase of the fields are not relevant and in general different. In order to effectively carry out such comparison, the fields have thus to be properly renormalized. This is achieved writing the field as

$$\phi(\rho_{vol} = 0.5, \chi) = \frac{1}{2} \sum_{m=-M/2}^{M/2} \left(\phi_m + \phi^*_{-m}\right) e^{\mathrm{i}m\chi}. \tag{4.17}$$

such as to isolate the dominant poloidal mode at the location of interest. Upon having verified that the two codes indeed agree about the dominant mode m, one can then match the relative phases and conveniently normalize the maximum amplitude. For the n_0=40 and the magnetic geometry of Case I, the results are depicted in Figure 4.19. The

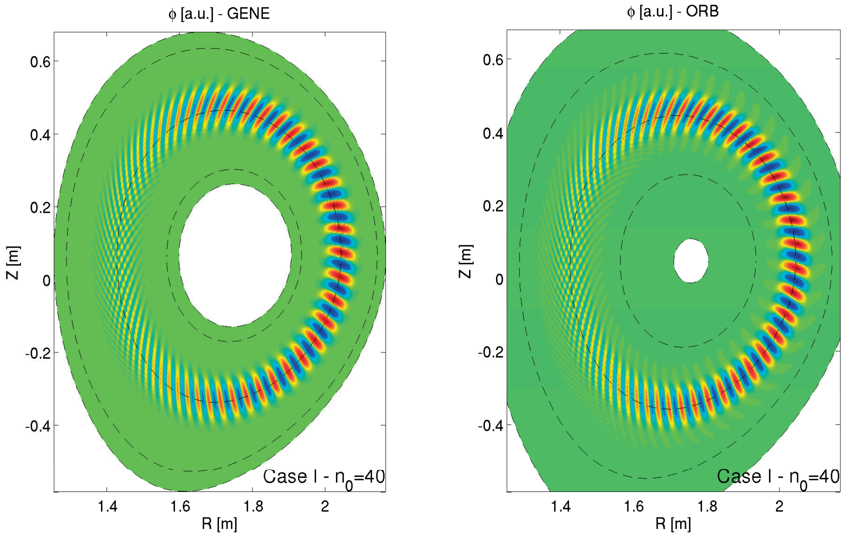

Figure 4.18 : Projection on a poloidal plane of the electrostatic potential associated most unstable mode for n_0=40. On the left, the mode structure obtained with the GENE is shown, while on the right the one provided by ORB5. The magnetic geometry used is Case I (fully shaped plasma). The flux surfaces corresponding to ρ_{vol}=0.3, 0.5 and 0.7 are indicated with dashed lines.

agreement is astonishingly good, with a difference on field amplitude below 10%.

Linear GENE simulations have been carried out for all the five geometries. The obtained growth rates are shown in Figure 4.20. One sees that, in agreement with the local results, Case IV is the shape characterized by the highest growth rates. Compared to Case V, one observes that the inclusion of a finite Shafranov shift leads also to a destabilization of higher n_0 modes and to a strong reduction of the real frequency for a given n_0. The short scale destabilization is further enhanced by elongation, which at the same time is found to reduce the maximum growth rate by 15%. Among the elongated magnetic geometries, Cases I to III, no significant effect is observed because of finite triangularity, while up-down asymmetry appears to slightly increase γ.

4.2.2 Nonlinear runs with adiabatic electrons

Nonlinear simulations have been performed considering a wider profile ($\delta T = \delta n = 0.04$, $\Delta n = \Delta T = 0.3$). The same radial and parallel resolutions as the one used for linear runs have been assumed, while 48 modes have been used to discretize the binormal direction, representing half torus. The minimum $k_y \rho_i$ retained is thus 0.030. The velocity grids have been extended from the linear runs ones in order to accommodate the new temperature profile in use to $\hat{L}_{v_\parallel} \times \hat{L}_\mu = 4.24 \times 18$ and discretized with 96×32 points. ORB5 runs have instead been carried out considering $n_r \times n_\chi \times n_\varphi = 280 \times 512 \times 256$ points and retaining 32 toroidal modes. Once again, as done for the local benchmarks,

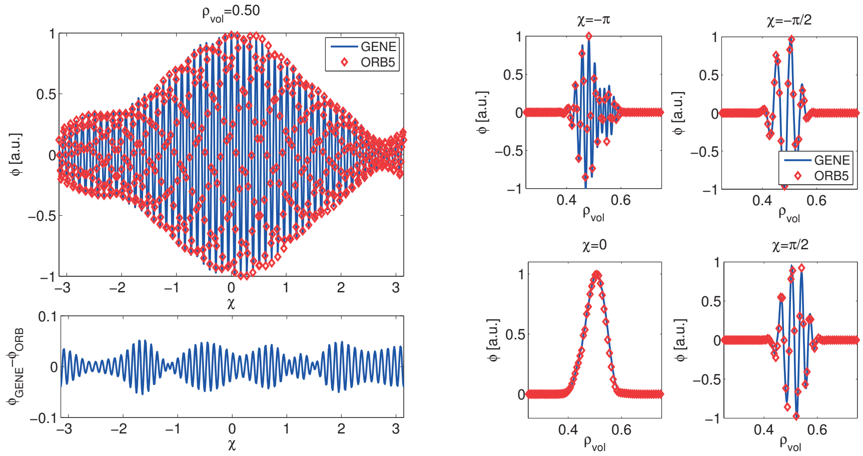

Figure 4.19 : Comparison of the amplitude of ϕ as obtained from GENE (blue curve) and ORB5 (red diamonds) at different radial and poloidal locations. On the left, the amplitude of the electrostatic potential is shown as a function of the straight field line angle χ on the flux-surface $\rho_{vol} = 0.5$. On the right, the radial dependence of ϕ is compared at difference poloidal angles χ.

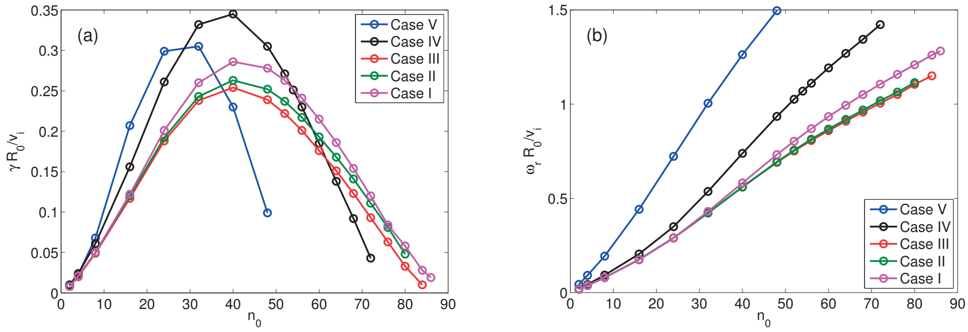

Figure 4.20 : Comparison between the linear spectra obtained for the five magnetic geometries. Shown are (a) growth rates γ_r and (b) real frequencies ω_r as a function of the toroidal mode number n_0.

particularly fine grids have been used for the GENE runs, especially in the binormal direction, with the aim of providing reference results. We remark that using $n_{k_y} = 32$ modes and simulating only a third of the torus is sufficient to converge nonlinear fluxes within 10%.

Following the same logic as what done in Ref. [32], the heat diffusivity, averaged over the radial domain $0.45 < \rho_{vol} < 0.55$, are compared as a function of time in Figure 4.21, together with the time averaged temperature gradient profiles. One observes a good agreement between the two codes, with time averaged values differing for $\sim 10\%$. This is further exemplified in Figure 4.22, where the time evolution of the ion heat flux is shown as a function of time and radius. Both codes reproduce a turbulent behaviour dominated by inward propagating avalanche like structures. Looking at the temperature

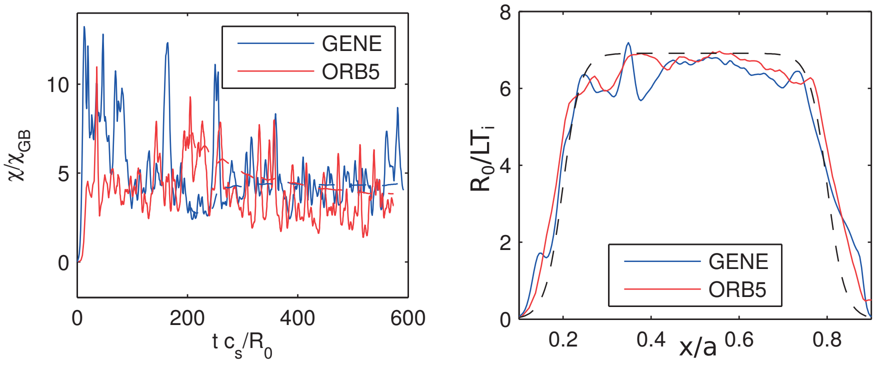

Figure 4.21 : On the left, heat diffusivities in GyroBohm units averaged over $0.45 < \rho_{vol} < 0.55$, on the right time averaged temperature gradient profiles.

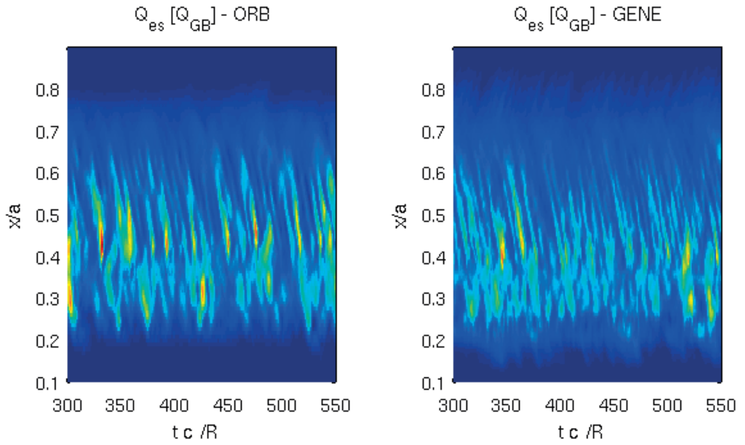

Figure 4.22 : Heat flux profiles (in units of Q_{GB}) obtained, on the left, from GENE and, on the right, from ORB5.

gradient profiles, one observes a much stronger relaxation in the GENE results around x/a=0.37. The effect of the strength of the heat source (an approximately 15% lower value of γ_k was used in GENE runs) is currently under investigation.

Finally, in Figure 4.23 we plot the time evolution of the $\mathbf{E} \times \mathbf{B}$ shearing rate profiles, defined as [105]:

$$\omega_{\mathbf{E}\times\mathbf{B}} = \frac{1}{2q}\left(\frac{\mathrm{d}^2\phi_0}{\mathrm{d}\psi^2} - \frac{1}{s}\frac{\mathrm{d}\phi_0}{\mathrm{d}\psi}\right) \tag{4.18}$$

where ψ is the poloidal flux.

Both codes qualitatively agree in reproducing different behaviour in different radial zones. A strong modulation of the shearing rate is found in both cases around x/a=0.2 and 0.35, while a large region of inwards propagating avalanches characterizes region $0.5 < x/a > 0.8$. Finally, both codes predict an outwards propagation close to the plasma edge. However, the discrepancy observed in the gradient profiles is reflected also in the

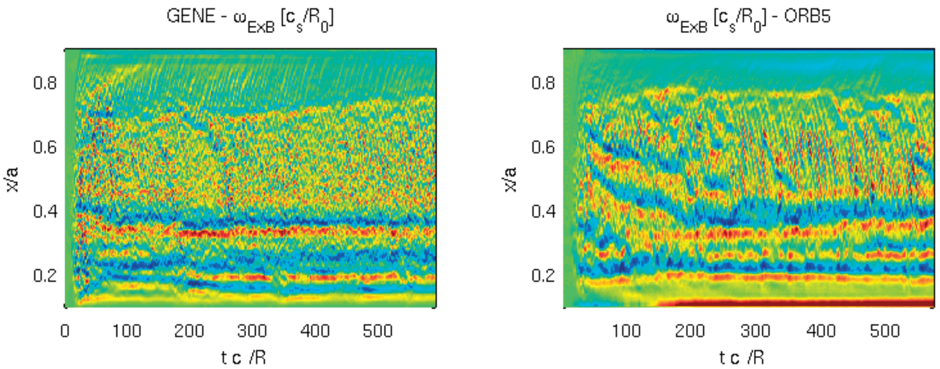

Figure 4.23 : Space-time evolution of the $\mathbf{E} \times \mathbf{B}$ shearing rate profiles, on the left obtained from GENE results, on the right from ORB5. Different color scales have bee used to highlight the avalanche like behaviour.

much strong modulation found in GENE around x/a=0.37.

4.2.3 Linear runs with kinetic electrons

Few linear simulations, still with verification purposes, have been performed assuming a kinetic response of the electrons. Those simulations have been carried out in strict collaboration with ORB5 developers, in particular J. Dominski. Specific aim of these runs was to compare GENE results with the ones obtained with the new ORB5 field solver [88], which, thanks to an integral representation of the quasineutrality equation, is valid to all orders in the Larmor radius. GENE solver already accounts for this.

Even without considering instabilities developing at the electron scales ($k_\perp \rho_e \sim 1$), correctly accounting for the electron dynamics at all radial scales plays a crucial role also for modes with $k_\perp \rho_i \sim 1 - 10$. When the non-adiabatic response of electrons is included, TEM modes can become unstable. Moreover, ITG growth rates are typically modified as well. From a purely computational point of view, the major drawback associated to a (fully) kinetic electron model, is the significant increase of the resolution requirements, and therefore of the cost, of each run. Let us first recall why.

One of the most important consequences of retaining a kinetic dynamics of electrons, is that they do not respond adiabatically around mode rational surfaces. As a consequence, small radial structures develop around specific MRSs [32, 106] and one needs to properly resolve them. Adopting too coarse grids typically results in overestimated linear growth rates and the corresponding real frequency is poorly converged. The relevance of these structures on nonlinear transport level is still debated, as they are typically broader and therefore more easily resolved. However, they can also cause numerical instabilities to appear if not properly treated.

Considering a mode with frequency ω and parallel wave vector $k_\parallel$, electrons respond adiabatically in the limit $\omega/k_\parallel \simeq 0$. The mode wave vector can be related to the poloidal and toroidal Fourier components according to

$$k_{\parallel} = (n\nabla\chi + m\nabla\phi)\cdot\mathbf{b} \sim \frac{1}{Rq}(nq-m), \tag{4.19}$$

which clearly shows how the adiabatic response breaks down around mode rational surfaces where $q = m/n$. One can estimate the width of the region where electrons are non-adiabatic, as well as the resolution requirements [32]. Typically one needs up to $\Delta x/\rho_s \sim 10^{-2} - 10^{-3}$ for properly resolving short scale modes, which makes the simulation cost particularly high.

Both GENE and ORB5 have currently implemented both an hybrid and a fully kinetic electrons model, which have both been benchmarked. The geometry of Case V has been considered, assuming the same temperature and density profiles as the one presented in Section 4.2.1. Artificially heavy electrons (m_e/m_i=400) have been assumed in order to allow for a larger time step.

The obtained mode frequency and growth rate are compared in Figure 4.24, showing

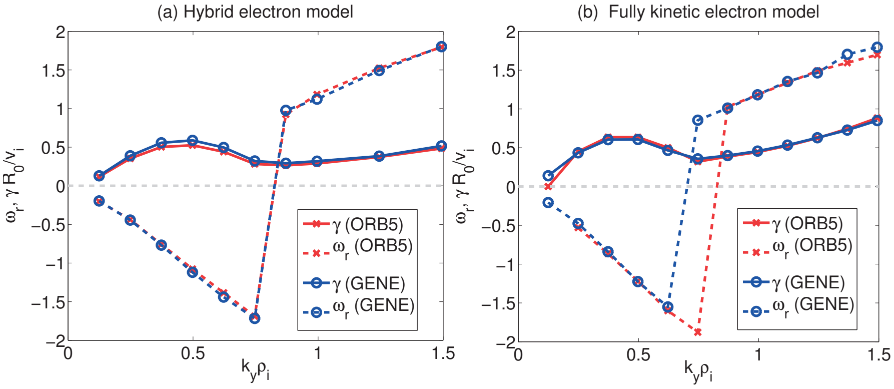

Figure 4.24 : Comparison of GENE and ORB5 linear growth rates γ and frequencies ω_r. Results have been obtained considering the magnetic of geometry of Case V and assuming (a) an hybrid and (b) fully kinetic electron model. note that in this case ITG (resp. TEM) are characterized by negative (resp. positive) frequencies as the magnetic field is negative in the GENE coordinate system.

on the left panel results valid for the hybrid electron model and on right side for fully kinetic. A remarkably good agreement is obtained, in both the ITG and TEM regimes. Note that in this case ITG are the negative real frequency branches as the magnetic geometry assumes a negative magnetic field. As already remarked when discussing local benchmarks, the position at which the turbulence regime transition happens cannot be considered a good reference point because it is too sensitive to the adopted resolution. The small differences appearing in the obtained real frequency for high k_y modes are within the error bars of the results. GENE simulations (and similarly the ORB5 ones, see Ref. [88] for more details) have been carried out considering up to 1400 radial gridpoints for the ITG modes ensuring results converged within 1%. Even higher resolutions have been used for the TEM modes where however the radial annulus retained in the simulation has been narrowed to a third of the minor radius in order to reduce the simulation cost. An example of the fine radial structures associated to non-adiabatic electrons are shown

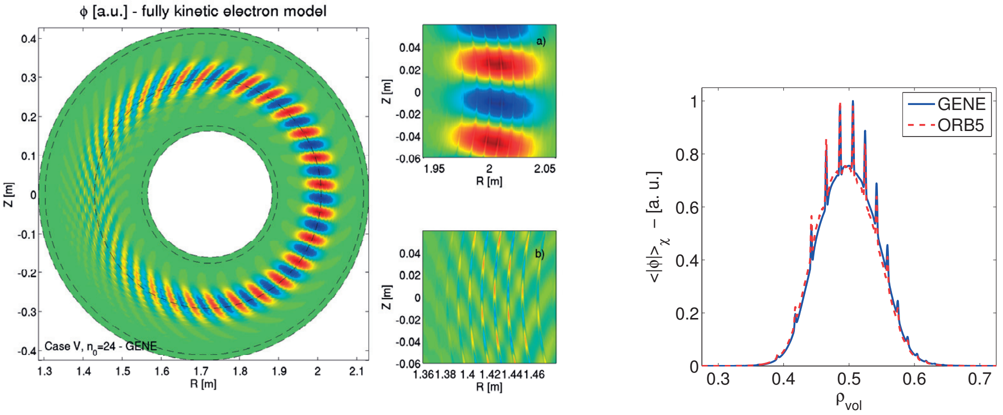

Figure 4.25 : Eigenfunction of the electrostatic potential ϕ associated to the n_0=24 mode for Case V. Shown on the left side is the poloidal projection of ϕ (in arbitrary units) together with zooms *a*) on the high field side and *b*) at the low field side to illustrate the fine radial structures appearing around MRS because of the non-adiabatic electron response. Results have been obtained with GENE code. On the right side, the mode structures provided by GENE and ORB5, averaged over the parallel direction, are compared.

in Figure 4.25, where the eigenfucntion of the $n_0 = 24$ (ITG) mode is depicted on a poloidal plane. The width and the location of this structure, being uniquely related to the safety factory profile, is can be used for benchmarking, as shown on the right side of Fig. 4.25 illustrating the excellent agreement obtained between the codes.

4.3 Conclusions

We have developed a series of benchmarks with the aim of testing the interface of gyrokinetic codes with kinetic ions and electrons and realistic shaped MHD equilibria, the latter being provided by the MHD equilibrium code CHEASE.

These tests have been used to successfully benchmark against each other the three gyrokinetic codes GENE [12, 65, 66], GKW [95] and GS2 [96] in the linear flux-tube limit. A fully kinetic model for describing the electron dynamics was considered, while collisions and electromagnetic effects have been neglected. This exercise, which at first glance might appear trivial, requires in fact to pay attention to several subtleties that normally do not need to be faced when carrying out similar benchmarks but adopting circular analytic geometry. In particular, one has to be very careful regarding the particular choice of coordinates used within each code, not only to correctly define the location of the flux tube volume, but also because it determines how to correctly recast the results in a common representation for comparison. We have put a specific effort in identifying all the details that have to be taken into account such as any other code can undergo the same benchmarks without uncertainties. The results have been published in [87], while all codes inputs and outputs, together with all useful information, are also made public available in Ref. [107] for any other code interested in carrying out the same series of tests.

Several benchmarks have successfully been carried out looking at linear k_θ spectra, at the effect of a finite ballooning angle and studying the linear dynamics of ZFs and GAMs via the standard Rosenbluth-Hinton test. In all the tests that we have performed, the codes agree within 3%, a difference that can be further reduced by properly increasing the resolution.

This benchmark cannot be considered an exhaustive study of plasma shaping effects, but nevertheless it has demonstrated that among the parameters that we have considered, elongation plays the strongest stabilizing role and at the same time it increases the ZF residual level and reduces GAM frequency.

The natural extension of this benchmark exercise is towards global simulations. The equilibria that we have considered were designed for carrying out this kind of simulations and are explicitly built such that local and global results can be compared. A gloabl benchmarking exercise has thus been initiated as well.

Carrying out the same exercise as the one done with the flux-tube code for the global one is a long and computationally expensive effort, also because non linear simulations are desirable. Hence, in order to limit the overall cost of the foreseen benchmarks, still keeping them relevant for verification purposes, global runs are carried out considering the adiabatic electrons limit. This verification effort is currently ongoing, involving GENE and ORB5. Linear simulations have been performed and the two codes agree between each together within less than 10% for all shapes. Nonlinear comparisons have been started as well and already a very good agreement has been recovered for the simplest geometry.

Finally, a limited number of linear simulations adopting a gyrokinetic response of the electrons (both hybrid and fully kinetic) have been performed with the aim of comparing GENE results whit the ones obtained with the new ORB5 field solver [88].

5 Local investigation of the effect of triangularity on turbulent transport

In this chapter we will present and discuss results obtained using the local version of GENE in order to investigate the origin of the confinement improvement experimentally observed in TCV when flipping the sign of triangularity of the plasma. These results have been reported in Refs. [108] and [109]. We shall start first reviewing the experimental observation that motivated such an investigation.

5.1 Overview of TCV experimental observations

5.1.1 Reversing LCFS triangularity in the TCV tokamak

The TCV tokamak [110] (major radius R=0.88 m, minor radius at midplane a=0.25 m, magnetic field on axis B_0=1.44 T and plasma current I_p up to 1.0 MA) offers a unique plasma shaping capability. Indeed, discharges with an edge elongation κ up to 2.8 and triangularity $-0.7 \leq \delta_{\rm LCFS} \leq 1$ have been obtained. The effect of negative δ in limited L-mode discharges has been investigated with a dedicated triangularity scan in EC-heated plasmas with $\delta_{\rm LCFS}$ ranging from -0.4 to 0.4. The interested readers are referred to [13, 111] for a detailed description of the experimental set-up. Let us recall here that in those discharges a specific effort was made in order to keep all other plasma parameters, and especially elongation [112], constant in order to highlight the effect of triangularity. The electron heat transport was experimentally determined by a power balance analysis. We note that the experimental error bars lead to an uncertainty of $\sim$ 20% in the determination of the electron temperature and density gradients. This uncertainty is particularly important towards the plasma edge where the error bars in the extrapolation of the ion temperature profiles can reach up to 80-100%. Furthermore, at these radial locations the radiated power can represent a non-negligible fraction of the total electron heat flux (20-30%). The main result was that the same electron temperature and density profiles were achieved in plasmas with $\delta_{\rm LCFS} = +0.4$ and -0.4 but injecting in the latter case half as much heating power compared to the former. This was interpreted as a better energy confinement at all plasma radii, by a factor of two, when flipping the sign of δ_{LCFS}.

We will focus our attention on the discharges #28014 ($\delta_{\mathrm{LCFS}} = 0.4$) and #28008

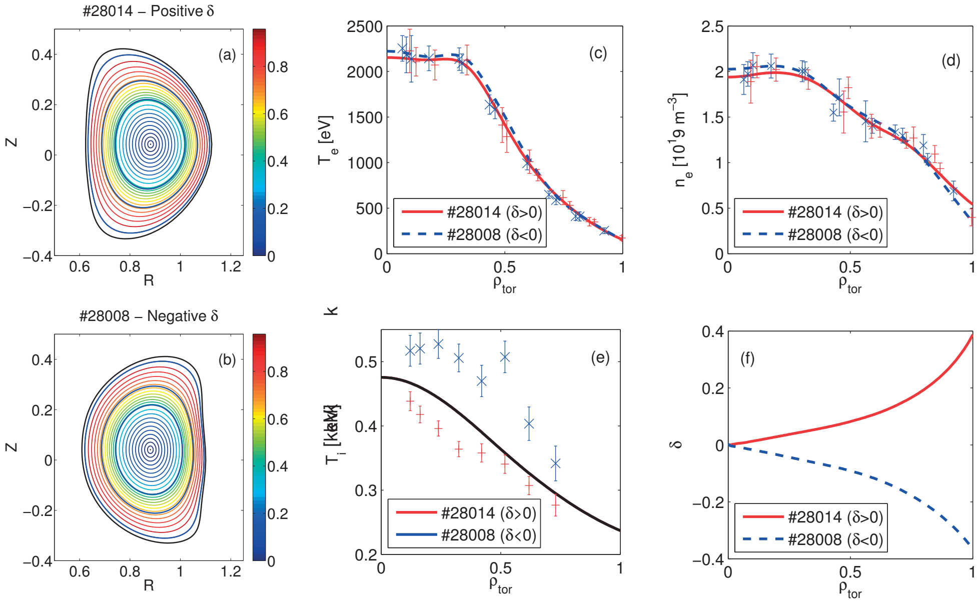

Figure 5.1 : TCV discharges #28014 and #28008 with resp. positive ($\delta_{\mathrm{LCFS}} = +0.4$) and negative ($\delta_{\mathrm{LCFS}} = -0.4$) triangularity of the LCFS. Corresponding flux surface contours of constant normalized poloidal flux $\Psi/\Psi_{\mathrm{LCFS}}$ are shown in (a) and (b) (blue curves indicate the the radial positions $\rho_{tor} = 0.5$, 0.7 and 0.95 where flux-tube simulations have been performed). Shown as a function of ρ_{tor} are the experimentally measured profiles of (c) electron temperature T_e and (d) electron density n_e as well as (e) the ion temperature T_i profile used for the simulations and (f) the triangularity δ as obtained from MHD equilibrium reconstructed with CHEASE.

($\delta_{\mathrm{LCFS}} = -0.4$), for which the same profiles have been obtained with the injection of respectively 1.3 MW and 0.65 MW. The radial profiles of electron temperature T_e, electron density n_e and ion temperature T_i, together with the radial profile of triangularity, are shown in figure 5.1. Figure 5.1.f clearly shows the rapid decrease of triangularity from the LCFS towards the magnetic axis: from the edge value, a $\sim 70\%$ reduction is found already at mid radius, independently from the sign of δ. As already noted, this is different from other shaping parameters like e.g. elongation which remains essentially constant up to the magnetic axis. We note that the experimentally measured ion temperature profiles are available only in the core plasma region and between the two discharges they are up to $\sim 40\%$ different, T_i being higher in the negative δ plasma. All the simulations presented here have been carried out considering an intermediate profile, depicted in black in figure 5.1.e, as already done in Ref. [90]. We have verified with linear simulations that this choice is not affecting the results, as only a maximum $\sim 3\%$ variation of the linear growth rates is found when changing the T_i profile between the experimental values.

5.1.2 Profile stiffness

A more recent observation, based on a large database of TCV discharges, showed that temperature and density profiles appear to be characterized over a wide range of plasma parameters (e.g. LCFS shape, plasma current, q profile and heating power) by constant *logarithmic gradients* $R|\nabla \log(T, n)|$ in the core plasma, while constant *gradients* $|\nabla(T, n)|$, whose values vary with plasma parameters, characterize the edge [108]. Here the core plasma is identified as the region between the sawtooth inversion radius and a radial location ρ_{vol} of about 0.8. The edge region, on the other hand, is the outermost part of the plasma but still inside the LCFS, namely $0.8 \lesssim \rho_{vol} < 1$. This observation is directly related to profile stiffness, i.e. the local slope of the flux versus normalized gradient curves, which thus appears to be strong and plasma parameters independent in the core and weaker and parameter dependent in the edge.

One can thus speculate that this radially varying stiffness, possibly together with varying values of the non-linear critical gradients $R/L_{T_{e,crit}}$ for instability, can be related to the beneficial effect of negative δ. Two limiting cases of such a relation are depicted in the two cartoons of figure 5.2. A first possibility, shown in cartoon (a), is that the level of edge stiffness is triangularity-dependent and is reduced going from positive to negative $\delta_{\mathrm{LCFS}} < 0$, while $R/L_{T_{e,crit}}$ does not depend on triangularity. The second limiting case is that the degree of edge non-stiffness is not related to δ, however the critical gradient $R/L_{T_{e,crit}}$ depends on shape and is larger for plasmas with negative triangularity. This second case is depicted in cartoon (b) of Figure 5.2. In both these limiting cases, or any combination in between, the confinement improvement would rely entirely on the edge region where the triangularity is indeed strong. In both cases, a stiff core profile leading to the same logarithmic gradient even when the heat flux varies by a factor of 2, explains the transport behaviour in this inner region.

The goal of this investigation is therefore to study profile stiffness in conditions relevant

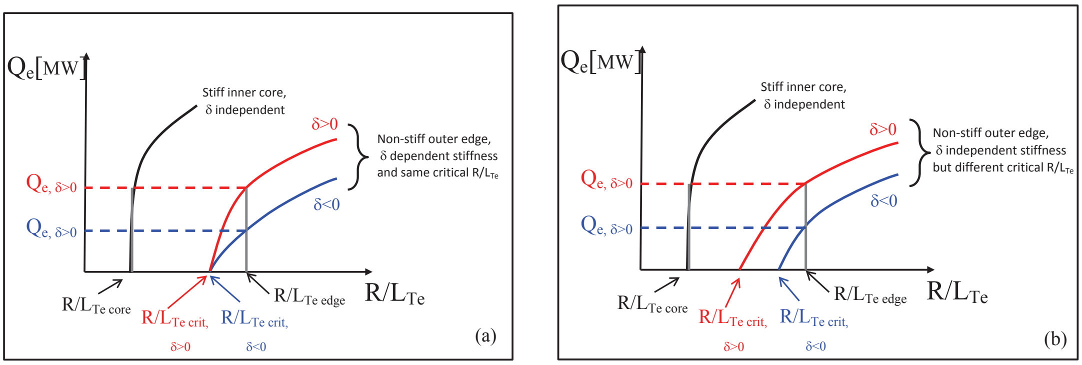
Q$_e$[MW]
Stiff inner core, δ independent
δ>0
Non-stiff outer edge, δ dependent stiffness and same critical R/L$_{Te}$
Q$_{e, δ>0}$
δ<0
Q$_{e, δ>0}$
R/L$_{Te}$
R/L$_{Te\ core}$
R/L$_{Te\ crit,}$ δ>0
R/L$_{Te\ crit,}$ δ<0
R/L$_{Te\ edge}$
(a)
Q$_e$[MW]
Stiff inner core, δ independent
δ>0
Non-stiff outer edge, δ independent stiffness but different critical R/L$_{Te}$
Q$_{e, δ>0}$
δ<0
Q$_{e, δ>0}$
R/L$_{Te}$
R/L$_{Te\ core}$
R/L$_{Te\ crit,}$ δ>0
R/L$_{Te\ crit,}$ δ<0
R/L$_{Te\ edge}$
(b)

Figure 5.2 : Cartoons describing two limiting ways of relating the confinement improvement associated with negative triangularity to profile stiffness. (a) via enhanced edge non-stiffness when $\delta_{\mathrm{LCFS}} < 0$ but same critical gradients, and (b) higher $R/L_{T_{e,crit}}$ at the same edge non-stiffness.

to the TCV tokamak, with the final objective of verifying the hypotheses of a radially varying and triangularity-dependent stiffness. At the same time, the dependence of critical gradients $R/L_{T,n_{,crit}}$ on δ can be addressed. Flux tube simulations are the natural tool to be used for such a study, as they allow to easily vary the local electron temperature and density gradients $R/L_{T_e,n_e}$ and compute the associated turbulent heat fluxes. Global simulations are computationally more expensive, and the interpretation of the results in terms of local stiffness might not be obvious. A first attempt to study profile stiffness with global simulations is presented in Ref. [113], where for a given TCV plasma shape the relation between increased heating and profiles evolution was studied in the ITG regime, obtaining a qualitative agreement with the experimental findings present in Ref. [108].

This study is thus complementary to what was already published in Ref. [90], where the issue of profile stiffness was not addressed and it is also a further step towards aiming at quantitatively reproducing experimental measurements with gyrokinetic modeling.

5.2 Simulation details

In order to model conditions relevant for studying stiffness and the confinement improvement associated to negative δ plasma, the two TCV discharges #28014 and #28008 described in section 5.1.1 are considered. Three different radial positions $\rho_{tor} = 0.5$, 0.7 and 0.95 have been considered for both discharges. They are representative of core, intermediate and edge conditions. Here ρ_{tor} is the radial coordinate based on the toroidal flux Φ, $\rho_{tor} = \sqrt{\Phi/\Phi_{\mathrm{LCFS}}}$. The magnetic equilibrium reconstructed with CHEASE has been used. The physical parameters describing the two discharges at the three considered radii, and used for the simulations, are listed in table 5.1. Temperature and density gradient lengths are defined according to the following relation:

$$R/L_{T,n} = -R/\alpha d\log(T,n)/d\rho_{tor}. \tag{5.1}$$

with $\alpha = \sqrt{\Phi_{\mathrm{LCFS}}/\pi B_0}$. The plasmas are Deuterium discharges. The effective charge, defined as $Z_{\mathrm{eff}} = \sum_i n_i Z_i^2/n_e$ where the sums are over all ion species, takes on the value $Z_{\mathrm{eff}} \approx 3.6$, with carbon ($Z_C = 6$) the dominant impurity. Three fully kinetic species have thus been considered in the GENE simulations: Deuterium ions, electrons and carbon ions. Deuterium and carbon concentrations are estimated so as to respect quasineutrality, i.e. $n_D + Z_C n_C = n_e$ and in agreement with the experimentally measured value of Z_{eff}. As Z_{eff} is assumed to be radially constant, one has $R/L_n = R/L_{n_e} = R/L_{n_D} = R/L_{n_C}$. When considering electromagnetic effects, the experimental value of $\beta_e = 2\mu_0 p_e/B_0^2$ is used; p_e is the local electron pressure. For the simulations in which finite collisionality is accounted for, it is evaluated based on the experimental values. Inter- and intra-species collisions are retained and all collision frequencies are consistently derived from the value of ν_{ei} and local values of temperature and density.

In particular, $\nu_{ei} = \sum_i 3\sqrt{\pi}/4\tau_{e,i}$, where $\tau_{e,i}$ is the electron collision time of the i-th ion species, $\tau_{e,i} = 3(2\pi)^{3/2}\epsilon_0^2 T_e^{3/2} m_e^{1/2}/n_i Z_i^2 e^2 \log\Lambda$, m_e is the electron mass and $\log\Lambda$ is the Coulomb logarithm. In order to conform to the experimental observation that within error bars the electron temperature and density profiles are the same, we used in all simulations, for both positive and negative δ, the measurements associated to the positive δ discharge, but keeping the relevant equilibrium depending on δ_{LCFS}.

	ρ_{tor}=0.5	ρ_{tor}=0.7	ρ_{tor}=0.95
q	1.18(1.26)	1.81(1.92)	3.58(3.66)
$\hat{s}$	0.82(0.78)	1.73(1.67)	3.31(2.53)
δ	0.09(-0.09)	0.15(-0.15)	0.33(-0.31)
T_i/T_e	**0.252**(0.289)	**0.43**(0.47)	**1.13**(1.11)
R/L_n	**3.75**(2.99)	**3.61**(4.39)	**10.4**(19.2)
R/L_{T_e}	**8.99**(8.89)	**10.52**(12.56)	**17.2**(18.8)
R/L_{T_i}	2.59	2.49	1.8
$\nu_{ei}[c_s/R]$	0.32(0.30)	1.12(1.02)	5.18(4.07)
β_e	0.41(0.44) $\times 10^{-2}$	0.16(0.16) $\times 10^{-2}$	0.26(0.21) $\times 10^{-3}$

Table 5.1 : Experimental parameters describing the three radial positions considered for flux-tube simulations. q = safety factor, $\hat{s}$ shear and other parameters defined in main text. Listed are the values referring to the TCV discharge #28014, positive δ, while the corresponding values for negative δ are provided in parenthesis. The values related to temperature and density profiles used for both $\delta > 0$ and $\delta < 0$ simulations are highlighted in bold.

5.3 Linear simulations

GENE has first been used in its linear version in order to identify for both considered triangularities the most unstable eigenmodes for the three radial positions ρ_{tor}=0.5, 0.7 and 0.95. Wavenumbers $k_y\rho_s$ up to the electron scale have been considered. The growth rate γ and the real frequency ω_r, normalized to R/c_s, are shown as a function of $k_y\rho_s$ in Figure 5.3. The results are shown in Figures 5.3 *a*), *c*) and *e*) in log-log plots over both ions and electron scales. To emphasize the difference between the results at the ion scale obtained with the two triangularities, the corresponding growth rates are also shown in lin-lin plots in Figs. 5.3 *b*), *d*) and *f*). Here $c_s = \sqrt{T_e/m_i}$ is the ion sound speed and ρ_s the ion sound Larmor radius $\rho_s = c_s/\Omega_i$ where $\Omega_i = eB_0/m_i$ is the ion cyclotron frequency. Note that the normalization factors are all based on the local value of the sound speed. The mode real frequency is depicted with a dashed line, and for all the wavenumbers considered it has a negative sign, indicating, in agreement with to GENE conventions, that the mode propagates in the electron diamagnetic direction. According to the GENE definition of the y variable, each k_y can be associated to a given toroidal mode number $n = k_y\rho_{tor}/q$, where ρ_{tor} is the radial position at which the flux tube is centered. The k_y associated to the $n = 1$ mode can be thus considered as the smallest

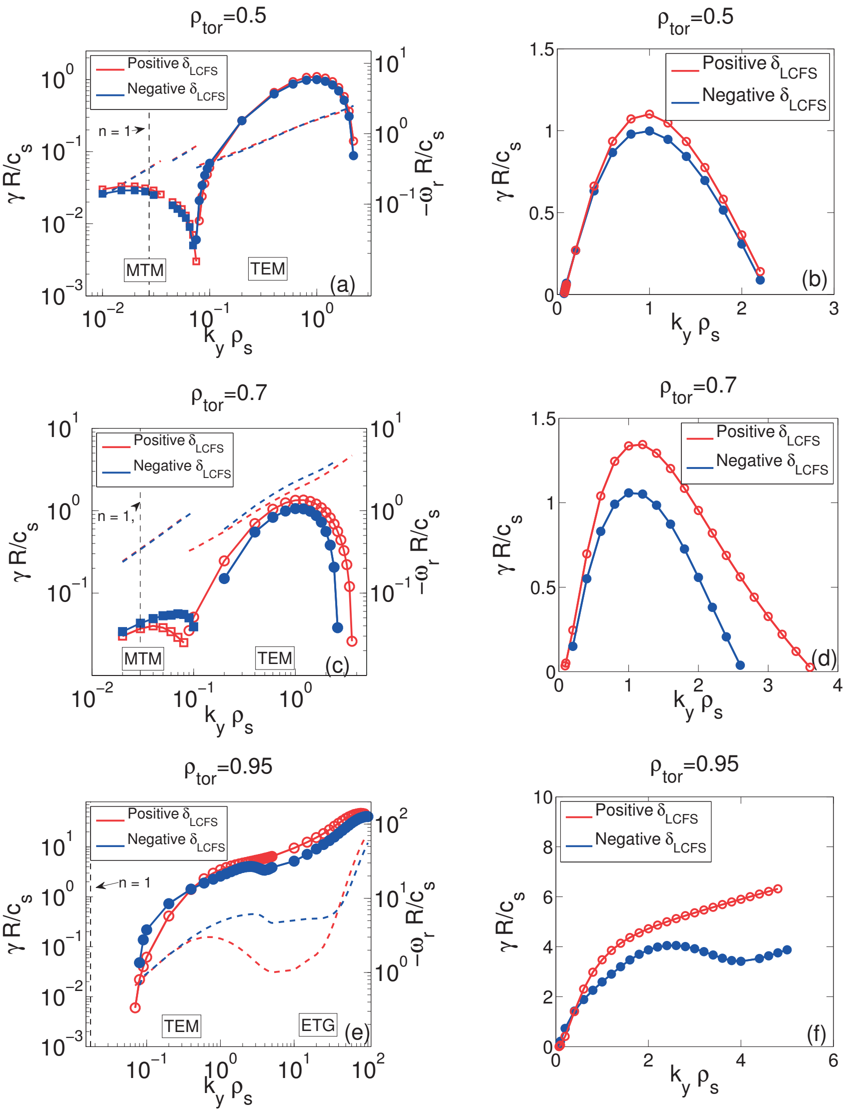

Figure 5.3 : Linear growth rates (continuous lines) and real frequency (dashed lines) in units of c_s/R as a function of the wavenumber $k_y\rho_s$ for (a,b) ρ_{tor}=0.5, (c,d) ρ_{tor}=0.7 and (e,f) ρ_{tor}=0.95. (a), (c) and (e) plots in log-log scale, (b) and (d) and $f)$ in lin-lin scale limited to the ion scale. Frequency ω_r are shown only in log-log plots. Shown are the results obtained for TCV discharges #28014 (red, empty symbols) and #28008 (blue, solid simbols). All modes propagate in the electron diamagnetic direction; MTM instabilities are marked with a square while TEM/ETG with circles. Vertical dashed lines indicate the approximate wavenumber corresponding to the n=1 toroidal mode number.

physical wavenumber. A typical grid size for these simulations is $n_{k_x} \times n_z \times n_{v_\parallel} \times n_\mu =$ $64 \times 64 \times 64 \times 16$. Convergence studies have been performed at the various radial locations and for the different turbulent regimes by increasing the resolution in turn for each dimension in phase space. The aforementioned grid is enough to ensure the convergence of all the growth rates, and in particular the ones at $\rho_{tor} = 0.95$, within 10%. Electromagnetic fluctuations (without $B_\parallel$ contribution), finite collisionality and the experimentally measured Carbon content have all been retained. These physical effects correspond to the "*full physics*" model set-up used for non-linear simulations and presented in section 5.4.

At all the considered positions, for both positive and negative δ, trapped electron modes (TEMs) are the most unstable instability at the ion scale. The negative triangularity discharge is found to have lower growth rates than the one with positive δ_{LCFS} at all $k_y\rho_s$ scales, with the exception of the $\rho_{tor} = 0.95$ position where for $k_y \lesssim 0.2$ the behaviour is inverted. For essentially all $k_y\rho_s$, the difference between the growth rates for the two triangularity cases increases as one moves towards the plasma edge, i.e. when the absolute magnitude of triangularity gets larger. This result is in agreement with the similar study reported in Ref. [90], where different radial locations were also considered.

At large scales ($k_y\rho_s < 0.1$), for the two innermost positions $\rho_{tor} = 0.5$ and $\rho_{tor} = 0.7$ microtearing modes (MTMs) [45] are the most unstable. The nature of these modes is determined by inspecting the parity of the ϕ and $A_\parallel$ fields with respect to the radial position of the mode rational surfaces. The growth rate is nevertheless small compared to TEM ones and it turns out that their contribution to the non-linear turbulent heat flux, which is essentially electrostatic, is negligible. At ρ_{tor}=0.95, MTMs are still unstable, but with a smaller growth rate compared to TEMs. Varying the electron temperature gradient at this location, one finds a transition from TEMs to MTMs for a gradient smaller than the experimental one, as can be seen in Figure 5.4*c*).

We also studied instabilities at the electron scale. Electron temperature gradient (ETG) modes are destabilized only at $\rho_{tor} = 0.95$ by the strong gradients characteristic of this location [40]. For the other considered radii, the low T_i and large Z_{eff} are stabilizing to ETG modes. Despite the fact that for both positive and negative δ the TEM branch continuously evolves to the ETG one when going from ion ($k_y\rho_s \lesssim 1$) to electron scales ($k_y\rho_s \gg 1$), a stronger hump at the ion scale is found in the $\delta < 0$ case, reflecting a different interplay between the two scales according to the plasma shape considered.

Determining a linear critical gradient is a difficult exercise for the two discharges being considered here. For all cases, we have performed a scan of both electron temperature and density gradient for $k_y\rho_s = 0.3$ (the mode at which we expect the largest contribution to non-linear fluxes, ρ_s being the local value of the Larmor radius). The results are shown in Figure 5.4, where the same aspect scale has been used when plotting the results relative to a given position (Figures 5.4 $(a-d)$, $(b-e)$ and $(c-f)$) in order to allow the comparison of the sensitivity of the linear growth rates to a variation of temperature and density gradient. Almost no difference between the two shapes is found for the innermost core position where there is no critical temperature gradient, the TEMs being driven

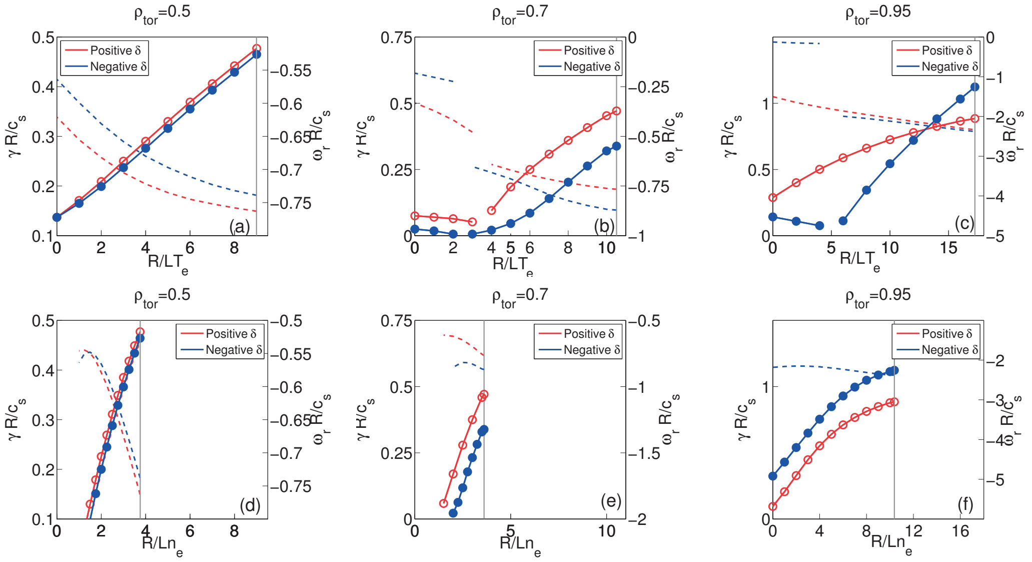

Figure 5.4 : Linear growth rates γ (continuous lines) and real frequency ω_r (dashed lines) of the $k_y\rho_s = 0.3$ mode in units of c_s/R as a function of (a, b, c) electron temperature gradient R/L_{T_e} and (d, e, f) density gradient R/L_{n_e}. Shown are the results for positive (red, empty symbols) and negative triangularity (blue, solid symbols) evaluated at (a, d) ρ_{tor}=0.5, (b, e) ρ_{tor}=0.7, and (c, f) ρ_{tor}=0.95. Vertical lines indicate the experimentally measured gradient.

by both density and temperature gradients, while we find essentially the same critical density gradient length for the TEM ($R/L_n \simeq 1$). At $\rho_{tor} = 0.7$, no critical gradient is found for TEM when scanning the electron temperature gradient (for both shapes different TEMs branches exist at different value of $k_y\rho_s$ as shown in Fig. 5.4.b), while scanning the density gradient one finds a linear critical gradient for TEMs at $R/L_n \simeq 1$ (resp. $R/L_n \simeq 2$) for positive (resp. negative) triangularity. Finally, at $\rho_{tor} = 0.95$ the difference between the two plasma shapes is most evident. For both positive and negative triangularity, no critical density gradient is found and at all R/L_n the growth rate of the most unstable mode for the negative triangularity shape turns out to be for the considered $k_y\rho_s$ bigger than the corresponding one for positive triangularity. When scanning R/L_{T_e} we find that for the experimental value of the gradients, the positive δ_{LCFS} discharge is more stable than the negative one, but as one further reduces R/L_{T_e} the $\delta_{\mathrm{LCFS}} < 0$ one returns to be more stable. We note that these orderings of the growth rates for the two triangularities are specific to the particular $k_y\rho_s$ that we considered. If one repeats the same exercise of varying the gradients but at different k_y (e.g. the one at which the linear growth rate is maximum), the results will look different. Especially, increasing k_y, we find that growth rates of TEMs become relatively larger and the negative δ discharge has lower growth rates at all positions and all temperature and density gradients. The results obtained scanning both temperature and gradient lengths are summarized for all the considered radial locations in Figure 5.5, from which it appears clear how the

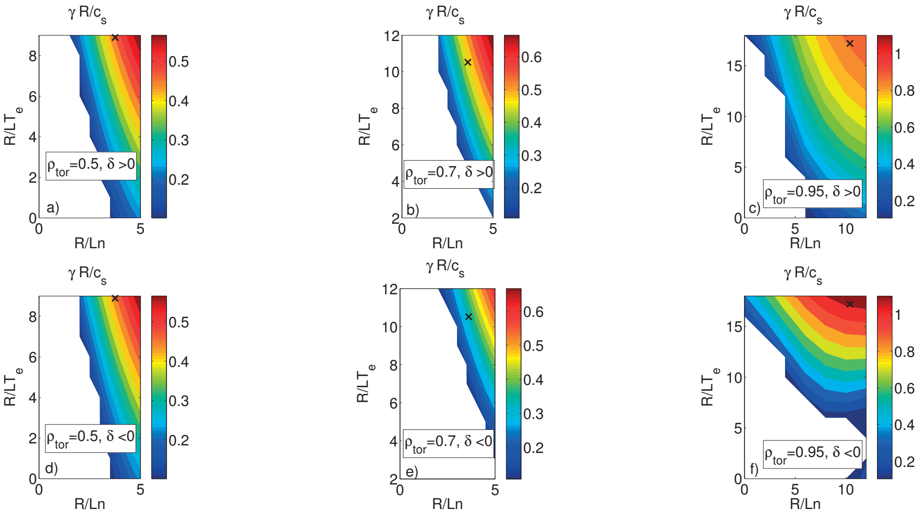

Figure 5.5 : Linear growth rates γ of the $k_y\rho_s = 0.3$ mode in units of c_s/R as a function of temperature and density gradient lengths. Shown are the results obtained for (a, b, c) positive δ plasma at respectively ρ_{tor}=0.5, 0.7 and 0.95, and (e, d, f) negative δ at the same radial location. The experimentally measured gradients are reported for each position with a black cross.

maximum linear growth rate is more sensitive to a variation of the density gradient with respect to a variation of the temperature one. This difference is reduced moving from the core (ρ_{tor}=0.5) to the edge (ρ_{tor}=0.95), where independently from plasma triangularity a given variation of temperature or density gradient appears to induce the same change of the growth rate.

5.4 Non-linear simulations

Non-linear simulations have been performed for the two TCV discharges at the three aforementioned radial locations. Two different simulation models have been considered. The first one, referred to in the following as "*simple physics*" model, considers only deuterium and electrons, the latter with an reduced ion-to-electron mass ratio (m_D/m_e=400). Furthermore, impurities, finite collisionality and electromagnetic effects have all been neglected. These approximations are made in order to reduce the cost of the runs, allowing more extensive parameter scans. As will be shown, this simple model has its limitations and all of above mentioned neglected effects have therefore been retained in a second series of simulations. These runs, referred to as "*full physics*" model, are fully-kinetic, electromagnetic, collisional runs, with the realistic electron mass and the experimental content of Carbon accounted for. All the simulations have been limited to the ion gyroradius scale; numerical hyperdiffusion is used to avoid spectral pile-ups due to medium k_y ETGs. The grid resolution used for these runs are reported in table

	L_x/ρ_s, $\delta > 0$	L_x/ρ_s, $\delta < 0$	L_y/ρ_s	$k_{x,\max}\rho_s$, $\delta > 0$	$k_{x,\max}\rho_s$, $\delta < 0$
ρ_{tor}=0.5	145(145)	153(153)	126(126)	2.76(5.52)	2.62(5.25)
ρ_{tor}=0.7	139(151)	143(155)	126(126)	4.33(5.33)	4.20(5.18)
ρ_{tor}=0.95	115(115)	120(120)	126(126)	10.52(10.52)	10.17(10.17)

Table 5.2 : Flux-tube dimensions adopted for non-linear simulations. Listed are the values for the *"simple physics"* runs, while in parenthesis for the *"full physics"*. Lengths are normalized to the local sound larmor radius ρ_s. $k_{x,\max}\rho_s$ indicates the maximum radial wave vector retained in the simulation.

	n_{k_x}	n_{k_y}	n_z	$n_{v_\parallel}$	n_μ
ρ_{tor}=0.5	128(256)	64(64)	32(32)	48(64)	8(16)
ρ_{tor}=0.7	192(256)	64(64)	32(32)	48(64)	8(16)
ρ_{tor}=0.95	384(384)	64(64)	32(32)	48(64)	8(16)

Table 5.3 : Resolutions adopted for non-linear simulations. Listed are the values for the *"simple physics"* runs, while in parenthesis for the *"full physics"*.

5.3. Higher radial resolutions are required for flux-tube simulations with radial position towards the plasma edge in conjunction with the increase of magnetic shear $\hat{s}$, see table 4.3 leading to a coupling of k_x modes that are further apart in k-space than at low shear [64]. At the same time, to limit the cost of these runs, the radial extent L_x of the box has been reduced in comparison with the more inner radial positions, but still ensuring a domain large enough compared to the turbulent eddy size, as shown in Figure 5.6. Finally, retaining collisions requires a higher resolution in velocity space, explaining the different set-up of *"full physics"* runs.

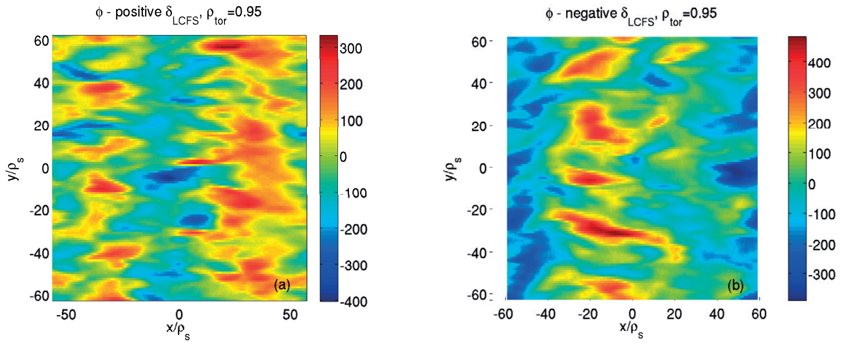

Figure 5.6 : Snapshots of the electrostatic potential (in units of $\frac{T_e}{e}\frac{\rho_s}{R}$) taken at the end of the simulation. Shown are the contours obtained with the "*full physics*" model at $\rho_{tor} = 0.95$, for (a) positive and (b) negative δ_{LCFS} and evaluated at the outboard midplane $(z = 0)$.

5.4.1 "Simple physics" model

The time traces of the simulated electron heat power $\langle Q_e \rangle \cdot S$ in MegaWatts are shown in figure 5.7. The heat flux density $\langle Q_e \rangle$ is defined as the average over the flux-tube volume, $\langle Q_e \rangle = \int \mathbf{Q} \cdot \nabla x \; J^{xyz} \; dxdydz \Big/ L_x L_y \int |\nabla x| \; J^{xyz} \; dz$, J^{xyz} being the Jacobian of the (x, y, z) coordinate system, while S is the area of the flux surface of interest. The ion heat flux is negligible, and therefore not shown, in agreement with the fact that TEMs are the dominant instabilities. Note that each simulation time is normalized using the local values of the sound speed $c_{s,loc}$. Given the fact that the simulations at $\rho_{tor} = 0.95$ are significantly more expensive than the ones at the other positions, somewhat less statistics have been acquired for these outer radial runs. The corresponding turbulent k_y-spectra are shown in Figure 5.8, where for each radial position the results from the two shapes are compared. A reduction of the integrated fluxes is found when flipping δ sign for larger ρ_{tor} (Fig. 5.7 and in agreement with [90]). However there is not a systematic reduction of the contribution to the fluxes from a given k_y, as seen in Fig. 5.8.

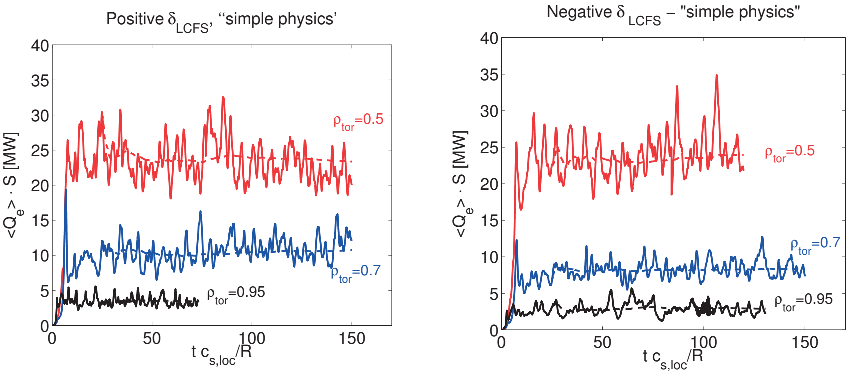

Figure 5.7 : Time traces of the simulated electron heat power $\langle Q_e \rangle \cdot S$ in MW for (a) positive δ_{LCFS} and (b) negative δ_{LCFS} discharges. Shown are the results obtained for the radial positions $\rho_{tor} = 0.5$ (red), 0.7 (blue) and 0.95 (black). These simulations have been performed with the *"simple physics"* model. Dashed lines indicate the running averages.

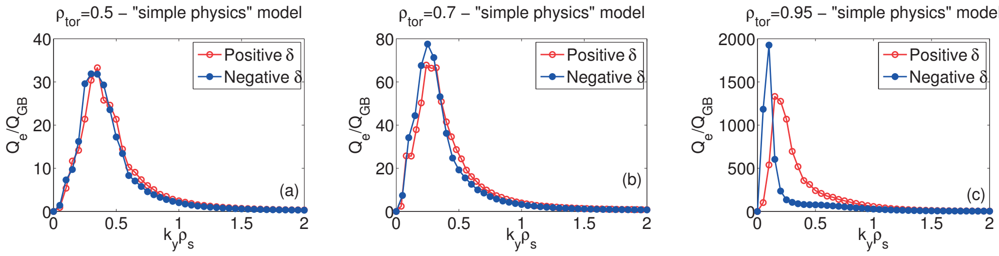

Figure 5.8 : Electron heat flux spectra evaluated at (a) $\rho_{tor} = 0.5$, (b) $\rho_{tor} = 0.7$ and (c) $\rho_{tor} = 0.95$. The heat fluxes are normalized to the local value of $Q_{\mathrm{GB}} = c_s T_e n_e (\rho_s / R)^2$. Experimental temperature gradients are considered.

We also note that the value of k_y which contributes most to the transport is reduced as one moves towards the LCFS, independently from triangularity. At $\rho_{tor} = 0.95$ the difference between the two discharges appears strongest.

For each position, the electron temperature gradient was both reduced and increased from the experimental value in order to address stiffness. The results are shown in Figure 5.9. In this plot, and in all the following Figures, the same color coding is used to help the reader. Red curves (color online) refer to the shape with positive triangularity, blue ones to the negative. Circles are used to mark $\rho_{tor} = 0.5$ position, stars $\rho_{tor} = 0.7$ and squares $\rho_{tor} = 0.95$. Finally, full-colored markers indicate the experimental value of the temperature gradient. The heat flux is plotted against the effective flux surface-averaged temperature gradient $\langle R/L_{T_e} \rangle = -R\, d\log(T, n)/d\rho_{tor} \langle |\nabla \rho_{tor}| \rangle$ which can be considered the effective normalized gradient driving the instabilities [112]. The different plasma shapes lead to a different value of $\langle |\nabla \rho_{tor}| \rangle$, which is larger when $\delta > 0$.

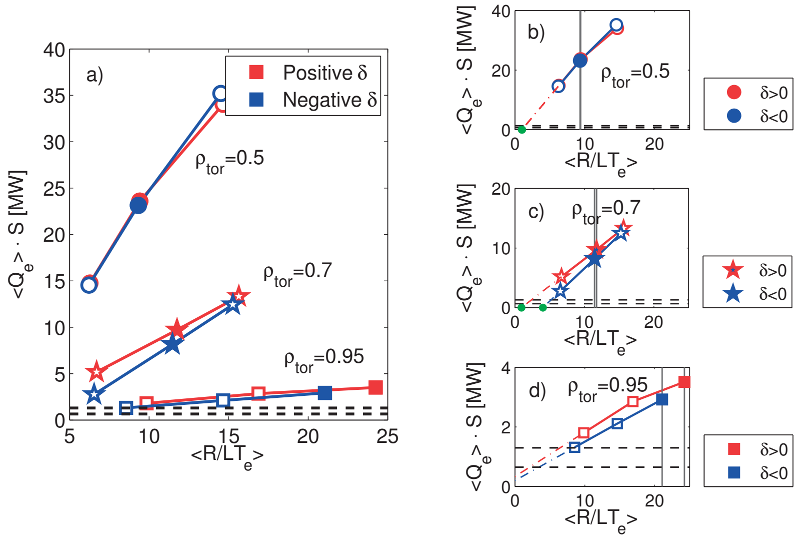

Figure 5.9 : (Color online) Electron heat power in MW versus the flux surface-averaged logarithmic temperature gradient $\langle R/L_{T_e} \rangle$ obtained with "*simple physics*" model. Shown are the results obtained for positive (red) and negative δ (blue) at $\rho_{tor} = 0.5$ (circles), $\rho_{tor} = 0.7$ (stars) and $\rho_{tor} = 0.95$ (squares). Full markers correspond to the experimental value of the gradient (further pointed out also with vertical lines), while horizontal lines indicate the input heating power for both positive and negative δ (1.3 MW and 0.65 MW respectively). For the sake of clearness, the same results are shown separately for each radial position, (a) $\rho_{tor} = 0.5$, (b) $\rho_{tor} = 0.7$ and (c) $\rho_{tor} = 0.95$. Linearly extrapolated critical gradients have been highlighted with dashed lines and green dots.

One immediately notes that the simulated powers for the experimental gradients are not radially constant, as would be expected under the assumption that all the input EC power is radially transported outwards across all flux surfaces between the radial location of power deposition ($\rho_{tor} = 0.4$ in this case) and the plasma edge. Also, and more importantly, the simulated transport levels are strongly overestimating the experimentally measured ones. This overestimation is particularly important in the core region (by a factor ~ 20 and ~ 40 for positive and negative δ respectively) and clearly not compatible with possible uncertainties in the input profiles. In agreement with [90], a radially dependent reduction of the heat transport when moving from positive to negative triangularity is found, however the results from the "*simple physics*" flux-tube model are obviously inadequate for modeling TCV discharges and a more accurate description is required.

5.4.2 "Full physics" model

The same series of runs as described in section 5.4.1 were repeated with the more comprehensive "*full physics*" model. In Figure 5.10, the turbulent spectra for the experimental gradient cases are presented, showing the same radial dependence of different k_y modes contribution depending on δ as the ones described for the "*simple physics*" model. However we clearly see the reduction at negative δ for large ρ_{tor} values and not for $\rho_{tor} = 0.5$. The results obtained from the R/L_{T_e} scan are summarized in Figure 5.11. With respect to the results obtained considering the "*simple physics*" model, there is a strong reduction of the electron heat flux $\langle Q_e \rangle$ when carrying out the more realistic simulations. We studied the relative importance of every physical effect introduced with this more accurate model by switching on each term one after the other and monitoring the resulting variation of the heat flux. This exercise has been performed for the experimental conditions of the positive triangularity discharge at $\rho_{tor} = 0.5$ and $\rho_{tor} = 0.7$. For those two positions we also studied the effect of finite collisionality depending on δ.

Among the different effects that have been retained in this new series of runs, finite collisionality, because of its stabilizing role on TEMs [38], is the most important one. It contributes up to $\sim 60\%$ of the "*simple*" to "*full physics*" model reduction. As already shown in Ref. [90], its effect is strongest in the cases with $\delta_{\text{LCFS}} < 0$ and is relatively more important as one moves from the core to the edge. Similar trends have been also experimentally observed, where a strong reduction of electron heat transport with increasing collisionality and decreasing triangularity is found, see e.g. Fig. 6 in Ref. [13]. Real electron to ion mass ratio and impurities, both contribute to further reducing heat

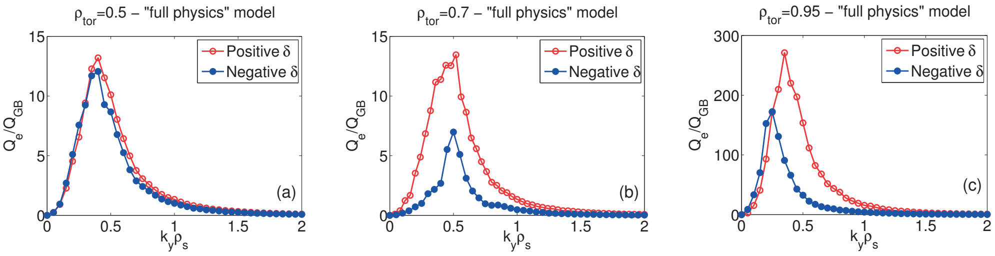

Figure 5.10 : Same as figure 5.8 but for the "*full physics*" model results.

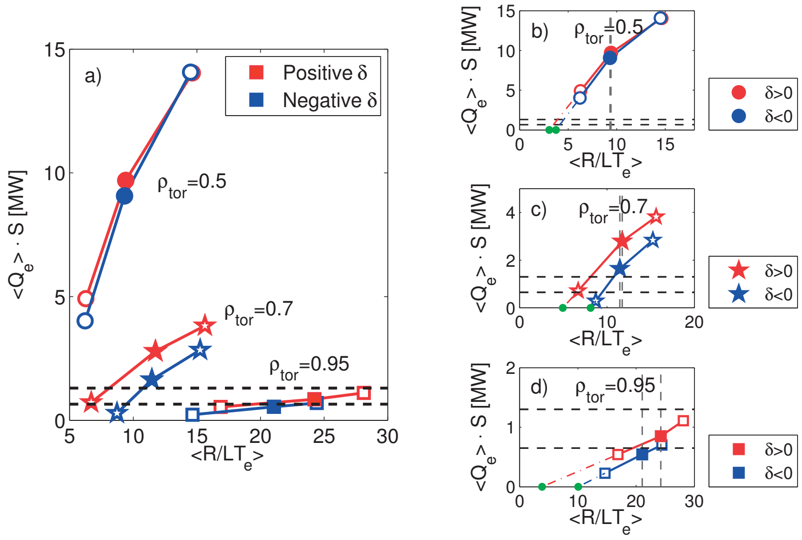

Figure 5.11 : Same as figure 5.9 but for the "*full physics*" model results.

transport. In particular, approximately 40% of the transport reduction is related to realistic m_D/m_e and another 10% to the impurities (this latter estimate is an average between the results at $\rho_{tor} = 0.5$ and 0.7). A minor effect is played by finite β effects, which in fact induce an *increase* in the heat flux by $\sim 10\%$. The actual electromagnetic contribution to transport related to magnetic field fluctuations is however negligible (less than a few percents of the total heat flux). Similarly low levels are found for the ion heat transport.

Despite the significant reduction of the electron heat transport going from "*simple*" to "*full physics*", a large overestimation of the simulated fluxes compared to the experimental ones, by at least a factor 6 (resp. 12), still remains for the core position (ρ_{tor}=0.5) of TCV plasma with positive (resp. negative) δ. Part of it might be explained by the high sensitivity of the heat transport to R/L_n as discussed below. On the other hand, at $\rho_{tor} = 0.95$ the simulated heat transport is in fact smaller than the measured one, an observation that we explain as a consequence of having artificially suppressed the contribution of ETG turbulence there. Preliminary simulations limited to the electron gyroradius scales (not shown here) have been performed, showing that a non-negligible contribution to the transport is provided by ETG modes. These same simulations however also point out that the scale separation is probably not fully justified and a multi-scale approach is necessary towards the plasma edge.

In order to complete the stiffness study, we scanned also the density gradient, upward and downward from the experimental value of temperature gradient. The results are shown in Figure 5.12. At $\rho_{tor} = 0.95$ a $\pm 20\%$ variation of R/L_{n_e} does not change the heat transport level significantly as reflected in Figure 5.12.*d* by curves which are non-stiff. At ρ_{tor} =0.5 and 0.7 instead, the sensitivity of the heat flux to a relative variation of the density gradient is stronger than the one to a variation of the temperature gradient as

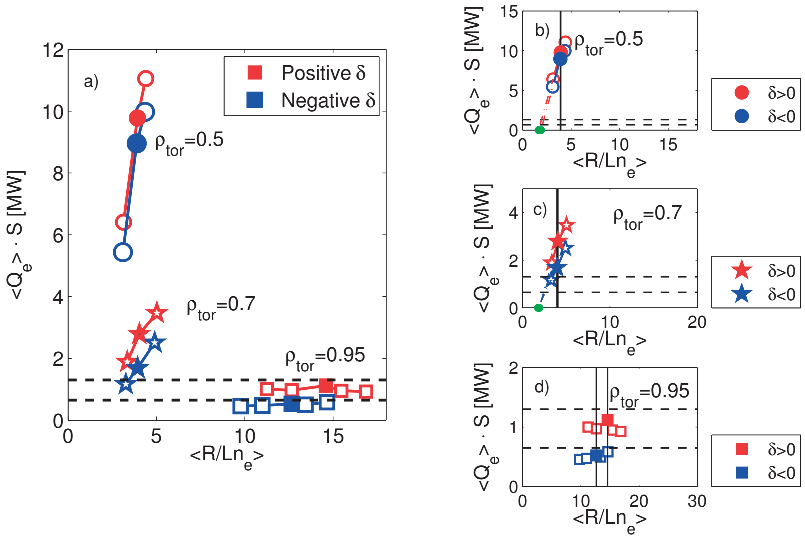

Figure 5.12 : Same as figure 5.9 but using the "*full physics*" model set-up and scanning $\langle R/L_{n_e}\rangle$.

reflected by relatively stiff curves in Figs. 5.12.*b*) and 5.12.*c*). Note that the aspect ratio of the axis of the subplots 5.11.(*b*) and 5.12.(*b*), as well as of subplots 5.11.(*c*) and 5.12.(*c*) and 5.11.(*d*) and 5.12.(*d*), has been kept, in order to allow the comparison between local stiffness with respect to a variation of R/L_{T_e} to stiffness with respect to a variation of R/L_n.

5.5 How to interpret local runs and look at stiffness?

As seen in the previous sections, the most accurate physical modeling, is necessary in order to reproduce the TCV transport level. Nonetheless, a non-negligible discrepancy between simulations and experiments persists. A significant overestimation of the heat transport level, by at least a factor 5, remains when simulating TCV core conditions, and it cannot be explained by uncertainties in the input values of the gradients, which are at most of the order of $\sim 20\%$. A better agreement is found for the edge simulations. For the outermost position considered ($\rho_{tor} = 0.95$), the simulations carried out at the ion scale, *i.e.* neglecting ETG contribution, are in fact underestimating the experimental electron heat flux. Our analysis however points out that a multiscale approach, resolving at the same time ion and electron scales, is required. Regarding the effect of negative triangularity, we do find a reduction by a factor $\sim$2 in the heat transport only for $\rho_{tor} \gtrsim 0.7$, in agreement with [90].

All these results show the intrinsic limit of flux-tube simulations applied to machines of similar size as TCV, where finite ρ^* effects are expected to be strong and need to be accounted for in the simulations in order to match experiments. It is already well established that the smaller $1/\rho^*$ the bigger the overestimation from flux-tube compared to global simulations [114–116]. If one considers just the radial profile of ρ_s, because of the decrease of temperature moving towards the LCFS, one can speculate that finite machine size stabilization is expected to be stronger in the plasma core with respect to the edge, i.e in agreement with our results. It is also known that for idealized cases one should in fact consider an effective $\rho^*_{\text{eff}} = \rho_s/\Delta_r$, accounting for gradient profile shapes [116] (Δ_r is the width of the gradient profile). How to correctly estimate Δ_r when dealing with experimental profiles (as well the dependence of finite ρ^* effects on all other plasma parameters) is still an open question that requires further dedicated investigations. Moreover, when transport is dominated by nonlocal effects, the concept of local profile stiffness as the local slope of the flux vs. normalized gradient curves is not anymore well defined.

The only way to correctly account for finite $\rho^* = \rho_s/a$ effects is therefore performing global simulations, which will be discussed in the following chapter. The flux-tube simulations presented here may nonetheless already provide qualitative or semi-quantitative information regarding the stiffness properties of the profiles, although one has to be very careful given the discrepancy between simulations and experimental e^- flux levels. To this end, one may attempt to correct in an *ad-hoc* way the e^- heat fluxes from the local simulations, adjusting them match match the experimental ones, this correction being assigned to neglected finite ρ^* effects. In doing such an exercise, one must be fully aware of its difficulties and limits. The most simple-minded way of accounting for global effects in our results would be to rescale them. We remember that such an approach was used to present the results obtained with the "*simple physics*" model in Ref. [108]. There, the simulated heat fluxes were all normalized such that for the experimental values of R/L_{T_e} the simulated heat fluxes were all of order unity and local slopes could be compared (see Figure 14 in Ref. [108]). Such choice was based on the assumption that finite ρ^* are independent from shape and local value of gradients. We stress the fact that such an approach, and the results it leads to, has to be taken with extreme caution because any rescaling will also inevitably change stiffness. This is particularly relevant at $\rho_{tor} = 0.5$ where there is almost no difference between positive and negative δ_{LCFS} flux-tube results. Thus, assuming a single scaling factor for each radial location, stiffness would appear for each δ_{LCFS} decreasing from core to edge. Moreover, depending on what reference is used to compute the scaling factor, this decrease of stiffness from core to edge will be more or less enhanced. On the other hand, if one rescales each curve independently such as to match simulated and measured fluxes for the experimental gradients (accounting therefore for the factor 2 reduction associated to negative δ at all radial locations), then for negative triangularity the core position ($\rho_{tor} = 0.5$) would appear less stiff than $\rho_{tor} = 0.7$ and almost as stiff as $\rho_{tor} = 0.95$. Some examples of such rescalings of the "*full physics*" simulations are depicted in Figure 5.13, illustrating the different possible results they can lead to and thus how careful one has to be in interpreting them. In particular, in Figure 5.13.a the scaling factors have been computed such has to match simulation results-experimental measurements for the positive δ discharge, therefore they are evaluated at each radial location as $1.3/\langle Q_e \cdot S\rangle_{\exp,\delta>0}$ (1.3 MW is the input heating power of that discharge while $\langle Q_e \cdot S\rangle_{\exp,\delta>0}$ indicates the simulated heat power associated of the experimental value of the gradients). In Figure 5.13.*b* the factors have been computed in order to match the negative δ discharge results, while finally in Figure 5.13.*c* distinct scaling factors for the two discharges have been used.

Therefore the question about profile stiffness still remains open and we cannot draw a clear and definitive conclusion about it. Nevertheless, keeping in mind our two initial hypotheses about the relation between profile stiffness, critical gradients and triangularity, if one looks at Figure 5.11 it appears that the strongest effect exerted by negative triangularity is an increase of the critical gradient. This feature is in fact already visible with the "*simple physics*" model results (Figure 5.9), however is less pronounced and one would also find negative critical gradients for the $\rho_{tor} = 0.95$ case. Considering the "*full physics*" results and linearly extrapolating (dot-dashed lines in Figure 5.11), one finds that the critical temperature gradient is increased by a factor 2 (resp. 3) $\rho_{tor} = 0.7$ (resp. 0.95) going from $\delta_{\text{LCFS}} > 0$ to $\delta_{\text{LCFS}} < 0$. For the $\rho_{tor} = 0.5$ position there is still an upshift when going from positive to negative triangularity, but the relative difference is much smaller ($\sim 50\%$) and the overestimation of fluxes too large to be definitive. Nevertheless these results hint towards an upshift of $R/L_{T_e,crit}$ depending on δ. No significant effect of triangularity on local profile stiffness is found. However for both triangularities stiffness appears to be reduced as one moves towards the plasma edge. This is particularly evident when considering the dependence of the heat fluxes on the density gradient. Figure 5.12 shows that the heat fluxes are very sensitive to small variations of R/L_n at $\rho_{tor} = 0.5$ and 0.7, much less at $\rho_{tor} = 0.95$, where the profiles appear to be non-stiff, in agreement with the linear results shown in Figures 5.4 and 5.5.

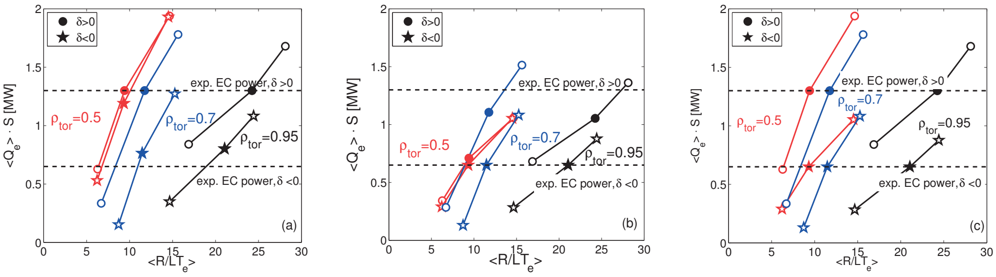

Figure 5.13 : Examples of possible rescalings of the flux-tube results such as to account for finite ρ^* effects in our local simulations. Shown are (*a*) rescaling assuming a scaling factor depending only on ρ_{tor} and computed as $1.3/\langle Q_e \cdot S\rangle_{\exp,\delta>0}$, (*b*) again a simply radially varying scaling factor but this time evaluated as $0.65/\langle Q_e \cdot S\rangle_{\exp,\delta<0}$ and (*c*) scaling factor depending on both ρ_{tor} and δ. Here $\langle Q_e \cdot S\rangle_{\exp}$ indicates the simulated power for the experimental value of the gradients; 1.3 MW (resp. 0.65 MW) is the experimental heating power for the positive (resp. negative) δ discharge. Simulation results from "*full physics*" model.

5.6 Conclusions

Linear and non-linear flux-tube simulations have been performed in order to study (linear and non-linear) critical gradients and profile stiffness in the TCV tokamak and in particular their dependence on radius and triangularity. Experimental temperature and density profiles as well as magnetic geometry have been used, and for the considered discharges TEM and ETG modes have been identified as the dominant instabilities. These modes not only have the largest growth rates at the ion and electron scales respectively but also provide the largest contribution to non-linear fluxes. ETG only provides a non-negligible contribution ($\sim 10\%$ of the measured heat flux) at the plasma edge ($\rho_{tor} = 0.95$).

Two types of non-linear simulations, corresponding to different levels of realism, have been carried out aiming at reproducing the experimental electron heat flux measurements and dependencies. Considering realistic m_D/m_e mass ratio, retaining finite collisionality, impurities and EM effects (without necessarily $B_\|$ fluctuations), was shown to be essential when simulating TCV conditions. Neglecting these effects and assuming $m_D/m_e = 400$, the simulated heat transport level is unrealistically high, overestimating the measurements by a factor ~ 20 in the core region and ~ 8 at the edge. A strong reduction is obtained with the "*full physics*" model. Finite collisionality is found to be responsible for most of the transport reduction, by a factor 2 at the core position. Realistic m_D/m_e leads to another $\sim 40\%$ reduction. The effects of impurities and finite β are of the same order and in opposite directions (C content reduces by $\sim 10\%$, while finite β increases the electrostatic heat flux, the contribution to the flux from electromagnetic fluctuations still being negligibly small).

Based on our local simulations, it appears that the strongest effect exerted by negative triangularity is an increase of the critical gradient while no significant effect of triangularity on local profile stiffness is found. A strong overestimation of the heat flux however remains, and in particular for the core simulations. Global simulations are expected to recover at least part of this discrepancy thanks to finite machine size stabilization. They will be the subject of the next chapter.

6 Global simulations of TCV discharges with positive and negative triangularity

As we have seen in the previous chapter, local simulations are unable to fully reproduce the experimental observations made in TCV, and a possible candidate that can be invoked to explain the observed discrepancies between measurements and flux-tube results are finite ρ^* effects. Such effects are known to potentially lead to a strong turbulence suppression in machines of the size of TCV [114–116].

Before moving to actual TCV simulation results, it is useful to recall certain practical details about global runs, how they are performed and how their results are interpreted. Hence, the first part of this chapter will present some basic considerations regarding global runs. Simulation results addressing the effect of triangularity will be discussed in the second one.

6.1 Gradient vs. flux driven global simulations

One of the main differences between local and global simulations, besides the obvious fact that the latter retain the radial variations of equilibrium profiles which are neglected by the former, is associated to sources and sinks. While flux-tube runs do not require any source term in order to maintain the background temperature and density profiles, which are fixed during the evolution of the system, this is not the case when global simulations are performed. In this case profiles will evolve in time and the corresponding gradients will ultimately relax below their critical values if a proper source is not applied to the system.

As already mentioned in section 3.6, two different options, corresponding to two different ways of handling this issue, are available. The first one, adopted in *gradient-driven* runs, consists in assuming given temperature and density profiles, and adding time-varying sources/sinks, possibly non-zero at any point in the plasma, such as to maintain these profiles (in a time averaged sense) during the evolution of the system. The second, so-called *flux-driven* approach, considers instead a constant imposed localized source and sink and the profiles are left to freely evolve in time under the action of this source/sink

until a quasi-stationary state is reached. From this point of view, flux-tube simulations are intrinsically gradient driven. Whenever one is aiming at reproducing experimental observations of turbulent transport with global simulations, flux-driven runs are a priori the preferable choice because the experimental source term is usually well known, both in its intensity and in its spatial location (e.g. the ECH heating), whereas the experimental profiles, and especially their gradients, are normally characterized by larger error bars. The major drawback however of this kind of simulations is their computational cost, which is particularly significant because the system has to evolve till the profiles settle, and this requires to simulate for a time of the order of the confinement time, scaling as a^2/D where D is the diffusion coefficient and a the minor radius of the device.
Conversely, gradient-driven simulations are normally cheaper than flux-driven, because profiles don't need to evolve significantly. One is actually aiming at maintaining them in a time-average sense, thus one “only” needs to wait for non-linear saturation to occur and then collect enough time statistics. This happens on a much shorter time scale. For this practical reason, gradient driven runs are usually preferred to flux driven ones, even though they are less close to the real physical evolution of a plasma.

The problem with gradient-driven approach is that, because of profile stiffness, a localized variation of input profiles might lead to a large variation of the local turbulence level and associated fluxes, which in turns can impact the entire system. Moreover, by setting the background profiles the source terms become an output of the simulation. Therefore, one must not only verify that the transport level resulting from a given simulation is consistent with what is measured, but also that the sources required to maintain the profiles are meaningful in comparison with the experimental ones. This comparison can be done only a posteriori, and should be made looking at both the intensity and the spatial distribution of all source terms.

6.2 General remarks about setting up a global simulation

Resolution requirements

A first important aspect requiring particular care when setting up a global simulation is defining the simulation grids. The discretization along all phase space directions must be carefully chosen, first of all because it significantly impacts the cost of the run and one therefore wants to make best use of the available computing resources and very often a compromise between the ideal set-up and a feasible one must be made. In particular, convergence studies are particularly expensive, and one normally cannot afford carrying them out as extensively as for local runs.
The most critical choice is in defining the velocity space grids. Currently GENE adopts radially independent velocity grids which are normalized with respect to constant values relative to a given radial reference position x_0. This means that the radial variation of the temperature profile must be accounted for when defining the extent and the

resolution of the velocity grids. Based on convergence studies, in a flux-tube simulation usually one sets $\hat{L}_{v_\parallel} \times \hat{L}_\mu = 3.0 \times 9.0$, adopting $n_{v_\parallel} \times n_\mu$=48 × 8 for ITG dominated regimes and 64 × 16 for TEM cases. In a global run however this would be appropriate only for the radial reference position x_0. The innermost part of the plasma will be characterized by higher temperatures, therefore requiring larger velocities to be properly described, while the outermost part of the plasma, where the temperature is lower, will require more gridpoints to correctly resolve plasma dynamics. Ideally the grid extension should be based on the ratio $(T_{\max}/T(x_0))^{1/2}$, where $T_{\max}$ is the maximum temperature to be simulated, and the number of grid points in $n_{v_\parallel}$ and n_μ on $(T(x_0)/T_{\min})^{1/2}$ and $T(x_0)/T_{\min}$ respectively, assuming that structures in velocity space at the lower end of the temperature profile scale at least linearly with the thermal velocity. This would allow to have at all radial position a same velocity grid as in an equivalent flux-tube simulation. In practice, TCV experimental profiles are often characterized by a ratio $T_{\max}/T_{\min} \simeq 10$ or more, translating typically into $\hat{L}_{v_\parallel} \times \hat{L}_\mu = 4.3 \times 18.0$ and requiring up to $n_{v_\parallel} \times n_\mu = 140 \times 80$ for a collisional TEM dominated case. Compared to a local simulations where 64 × 16 gridpoints are sufficient to properly resolve the plasma dynamics, this translates into global simulations being at least 10 times more expensive than flux-tube ones, even without accounting for further restrictions to the time step due to the reduced CFL limit.

Heat and particle sources

As already mentioned, Krook type sources are the standard choice for carrying out global gradient-driven runs. The typical way one proceeds in defining the relaxation rates is by first carrying out global linear runs and determining the linear spectra. Then, the relaxation rates are chosen as typically a tenth of the maximum linear growth rate, such as to allow some profile relaxation without impacting too much the instability drive [76]. In principle, one should carry out a convergence study to investigate the impact on the resulting transport of a particular choice of relaxation rates, however such studies are normally too expensive to be carried out systematically in practice. The rule of thumb previously presented has proven to be a reasonable choice in most of the cases presented here.

Whenever simulations with fully kinetic electrons are carried out, a particle source might be necessary together with a heat source. Given that experimentally there is no particle source in TCV discharges, corresponding experimental core conditions are assumed to be effectively characterized by a vanishing particle flux. In the simulation this is often not ensured and a particle source is normally required to maintain density profiles, typically with a relaxation rate smaller by a factor of two compared to the one adopted for the heat source. The observed particle source turns out to be larger as one approaches the LCFS ($\rho \gtrsim 0.8$), where also experimentally the interaction of the plasma with the wall can provide a non negligible source term.

Radial buffers and treatment of the magnetic equilibrium for investigating the effect of triangularity

Radial buffer regions are employed in order to smoothly damp the fluctuations as one approaches the boundaries of the simulations domain. In these regions one often also smoothly decreases the gradient profiles to zero, so as to reduce at the same time the turbulent drive.
When setting the extent of these buffer regions, a compromise must be made. Too narrow buffer regions can lead to numerical instabilities, while unnecessarily large ones will significantly impact the computational cost of the run. A typical choice consists in dedicating 10% of the simulation domain to these two boundary regions, but a larger extent might be necessary if the fluctuation level is particularly large.

Correctly handling buffer regions is particularly important when simulating the edge region, as is the case for the simulations investigating the role of triangularity that will be presented in the following. Because δ is largest in magnitude towards the LCFS, one is naturally led to assume that simulating the whole minor radius of the plasma is necessary when aiming at reproducing the stabilizing effect associated to $\delta < 0$. This requires to place the outer buffer region beyond the actual LCFS.
The simplest solution that we have found to this problem is to extrapolate the experimental magnetic geometry outside the plasma boundary, and an effective way to do so consists in assuming constant geometric coefficients beyond $\rho = 1$, taken equal to the ones of the LCFS. This turns out to be necessary when handling shaped plasmas because otherwise even a linear extrapolation can lead to a non physical metric (e.g. $k_\perp^2 = g^{xx}k_x^2+g^{yy}k_y^2+2g^{xy}k_xk_x < 0+$. Clearly this procedure leads to an inconsistent equilibrium. Before applying this strategy to model actual TCV discharges with fully kinetic electrons, we have performed linear and nonlinear tests in order to validate such an approach in a simplified scenario, considering adiabatic electrons and simulating only the outermost fraction of the plasma minor radius. In all the tests we have carried out we have not found any obvious artifact caused by our way of proceeding. In fact, an equilibrium constructed as previously described is an equilibrium where the buffer region is characterized by a metric equivalent to what one would use in order to carry out a flux-tube simulation centered on the LCFS. Therefore, in order to mimic as much as possible a local set-up, a linearized q profile, with magnetic shear equal to s(LCFS) is also assumed.

6.3 Global simulations with TCV experimental profiles

6.3.1 Preliminary runs relative to core conditions

A first attempt to reproduce actual TCV conditions with global simulations has been initially carried out considering only the core plasma. This choice was mainly motivated by the very strong overestimation of the heat fluxes obtained in this region with flux-tube simulations. To develop an understanding of the importance of finite machine size effects, the radial annulus $0.3 \lesssim \rho_{tor} \lesssim 0.7$ has thus been simulated. The grids used for carrying out such simulations are listed in Table 6.1. As already explained, these runs are sensibly more expensive than local simulations, with each simulation requiring approximately 1M CPU-hrs. Therefore, in order to reduce the overall cost, collisions have been neglected. Simulations are run up to $\sim$100 R_0/c_s in order to collect enough statistics in the saturated state, while time averages are taken over the second half of the run.

	n_x	n_{k_y}	n_z	$n_{v_\parallel}$	n_μ	$k_{y,min}$	L_x	$L_{v_\parallel}$	L_μ
positive δ	400	48	32	128	64	0.046 (n =2)	55	4.3	18.0
negative δ	400	48	32	108	46	0.031 (n =1)	50	3.9	15.3

Table 6.1 : Numerical parameters used for carrying out global simulations reproducing the core conditions of TCV ($0.3 \lesssim \rho_{tor} \lesssim 0.7$).

We note that using ρ_{tor} as a radial coordinate causes the temperature profiles to be not exactly the same between the $\delta > 0$ and $\delta < 0$ cases, while they are as a function of ρ_{vol}. Moreover, the minor radius of the plasma a also varies between the discharges, therefore ρ^* turns out to be not the same at a given radial position for the two plasmas. Furthermore, q profiles are not exactly equal, so the radial annulus extent has been varied so as to cover in both plasmas the region $1 < q < 2.1$. The lower limit is fixed so as to avoid the $q = 1$ rational surface, where sawtooth activity might lead to large errors in the determination of the experimental profiles. The upper one is arbitrarily chosen to exclude the edge region. An extra 10% extent of the domain is dedicated to radial buffers at both ends. This is in practice obtained by centering the simulation domain at two different radial locations (ρ_{tor}=0.55 for $\delta < 0$ and ρ_{tor}=0.6 for $\delta > 0$), and using different radial domain widths as detailed in Table 6.1. This implies also different minimal toroidal mode numbers to be retained, smaller in the case of negative triangularity. Similar radial resolutions are used in the two runs, adopting the same number of points to ease the parallelization and setting radial hyper diffusion to `hyp_x`=2. Having a narrower annulus when $\delta < 0$ allows one to use velocity space grids with a smaller extent, while similar resolution has been used in both simulations. Krook relaxation rates have been set to $\gamma_H = 0.2\ c_s/R_0$ and $\gamma_P = 0.1\ c_s/R_0$ for heat and particles respectively .

The results of these first global simulations are illustrated in Figure 6.1, where the radial profile of the electron heat power is shown for both positive and negative triangularity cases. Ion and carbon fluxes are not shown as they are negligible. Compared to the flux- tube results in Figure 5.11, one already observes a significant reduction of the heat transport towards the experimentally measured values, and, contrary to local results, a clear difference between the two triangularities now remains even at the radial positions $\rho_{tor} \sim 0.5$. A discrepancy by approximately a factor of 4-5 for the total power nevertheless remains between simulations and experiments for both shapes.

From the flux-tube runs it is known that finite collisionality can reduce the fluxes by up to a factor of two. Thus these first results appear as a promising first step towards matching

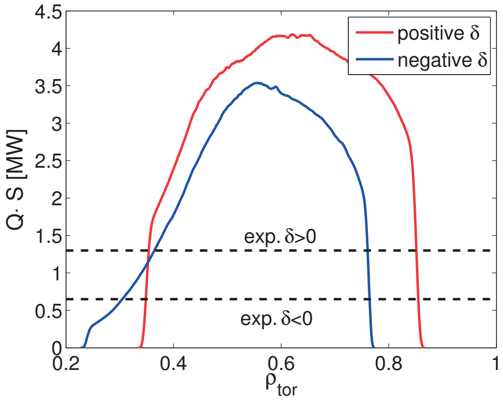

Figure 6.1 : Radial profiles of electron heat power $Q \cdot S$ in MW crossing a given flux surface. Shown in red are the results for positive triangularity while in blue for negative. Simulations are performed retaining carbon impurities but neglecting collisions.

the experimental heat flux levels. As will be shown in the next section, collisions alone are however not sufficient to match simulations and experiments.

6.3.2 Full-radius simulations with realistic profiles

Further global simulations have been carried out covering the plasma minor radius up to the LCFS and placing the buffer outside the actual plasma boundary as described in the introduction. These simulations will be referred in the following as “full-radius” to distinguish them from the “core” ones presented before. Various runs, with different numerical settings, have been carried out without being able to achieve better agreement with experiments as for simulations presented in the previous section.

The same fine resolutions adopted for carrying out the “core” runs described in the previous sections cannot be adopted for carrying out a full-radius simulation because of the resulting computational cost. A simple scaling of the radial and velocity space grids considering the ideally desired extent of a full-radius run is also likely to lead to practical computation limitations because of the total number of grid points involved (this is in fact related to a hardware memory limit that can be avoided by increasing the number of processors used per single simulation, in turn increasing the cost of the run). Furthermore, based on experience, the inclusion of collisions roughly doubles the computational time required per each time step.
A compromise must therefore be made, and we decided to lower as much as possible the resolution in all directions but keeping the highest possible one in the radial direction. This choice is based on previous experience in simulating TCV internal transport barriers [30], where the transport level was found to be reduced when increasing n_x because of better resolved fine structures around MRS.

Given the limited resources available, a first attempt was made considering only two species and retaining collisions. Similar values of hyper diffusion and of Krook relaxation rates have been used as the ones adopted for the core runs. The simulation grids are reported in Table 6.2. The affordable radial resolution is sensibly lower than the one used for the runs described in the previous section, mainly because of the larger radial domain resulting from having placed the radial buffer outside the LCFS. Smaller velocity grids are used but with a higher resolution such as to at least partly resolve the low T tail of the temperature profile. The number of velocity grid points is based on the temperature at $\rho_{tor} = 0.9$, resolving up to the LCFS would require to further increase by at least 30% the number of points. We have verified that such radial resolution is not affecting too much the linear growth rate γ of the global $k_y < 0.8$ modes, which are the ones dominating nonlinear fluxes: with 50% more radial grid points γ is varying by less than 10%.

Few nonlinear runs, with higher resolution but shorter time and thus unfortunately limited statistics ($\sim$30 R_0/c_s), have been carried out in selected cases in order to verify that the numerical setting was not the main cause for the observed discrepancies in the simulated electron heat flux compared to the experimental one.

	n_x	n_{k_y}	n_z	$n_{v_\parallel}$	n_μ	$k_{y,min}$	L_x	$L_{v_\parallel}$	L_μ
positive δ	416	48	32	140	80	0.041 (n =2)	98	4	16
negative δ	384	48	32	140	80	0.048 (n =2)	91	4	16

Table 6.2 : Numerical parameters used for carrying out 2 species collisional full-radius global simulations.

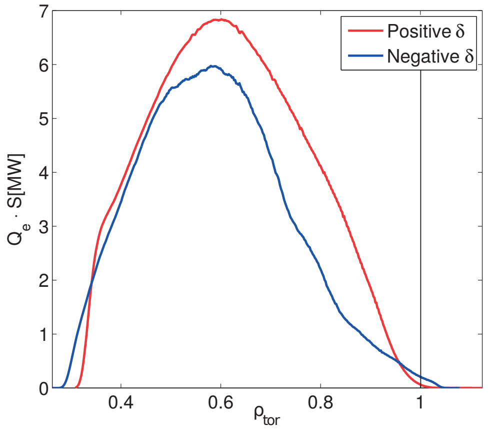

Figure 6.2 : Radial profiles of electron heat power $Q \cdot S$ in MW crossing a given flux surface. Shown in red are the results for positive triangularity while in blue for negative. Compared to Figure 6.1, runs are in this case performed without carbon impurities but retaining collisionality. A vertical line indicates the location of the LCFS.

The resulting electron powers are shown in Figure 6.2 for both plasma shapes. One observes that the exclusion of carbon is not compensated by collisions and the final heat fluxes is actually higher than the ones obtained in the simulations showed in Fig. 6.1. Considering e.g. the position ρ_{tor}=0.6 the heat transport level is higher by approximately 50% than what was obtained when simulating only the core.

Furthermore, the time averaged profile of the heat power shows a very unrealistic radial profile, strongly peaked at $\rho_{tor} = 0.6$ and then rapidly decaying as one moves towards the LCFS. This behaviour is reflected also in the time averaged heat sources (not shown here). A strong injection of heat is required in the core in order to maintain the local background profiles whereas immediately outside $\rho_{tor} = 0.7$ a strong sink is necessary. As a result, at locations $\rho_{tor} \gtrsim 0.9$ the turbulent flux is practically zero, as nearly nothing is radially transported while locally the unstable modes are not retained in the current set-up (one would need to at least double the number of k_y modes so as to have the relevant unstable ones included).

Comparing the two magnetic geometries, a 10-15% difference between the heat transport level is observed in the core ($\rho_{tor} < 0.6$), Q_e being lower when $\delta < 0$. This difference further increases up to a factor 1.5-2 at $\rho_{tor} > 0.7$. Even though these ratios are similar to the ones that were obtained for results in Fig. 6.1, on the one hand they remain smaller than the experimental ones in the innermost position and, on the other hand, the still very high overestimation of heat transport does not allow us to claim anything about the electron heat confinement dependence on δ.

The run relative to negative triangularity, which is the one where the overestimation is largest, has been repeated using the experimental value of Z_{eff} in the collision operator only, while still assuming a single ion species, without obtaining a significant difference. Time averaged fluxes are indeed only lowered by $\sim 10\%$, which is within the uncertainty associated to the time average procedure.

The cost of carrying out the same simulations including three active gyrokinetic species is foreseen to be at least 10 MCPU-hrs per magnetic geometry, a computation that can be done only once. Before carrying out such simulations it is thus necessary to assess the impact of experimental uncertainties in the input profiles. We already know from flux-tube simulations that heat fluxes are particularly sensitive to the density gradient, an observation that is further confirmed by carrying out linear global simulations considering a density profile flattened as much as possible to still agree with the experimental data points and associated error bars.

We have carried out a few preliminary nonlinear simulations assuming heavy electrons (m_e/m_i=400). This approximation has been avoided in all other runs previously discussed because the mass ratio is significantly affecting the transport level, with a reduction by at least a factor of two when going from heavy electrons to realistic deuterium/electron mass ratio. Moreover, part of the difference between positive and negative δ is removed if the real mass ratio is not assumed. Heavy electron runs can nevertheless be used to "quickly" determine whether a variation of the density profile leads to a significant flattening of the simulated heat flux profiles. In our case, we find that lowering R/L_n within the limits of experimental error bars only in the core region (at $\rho_{tor} < 0.6$) shifts the peak of the simulated fluxes towards the LCFS without significantly changing the maximum value. A possible solution is to carry out a simulation allowing the density profiles to relax by not imposing a particle source. In this case the relaxation of the density profile turns out to be large and beyond the experimental uncertainties.

From all our runs, both local and global, the density gradient appears as the most sensitive parameter in determining the actual transport level. Because of profile stiffness, a small localized change of n_e can lead to very different heat fluxes. Reconstructing the actual profile with the help of flux-tube simulations, following e.g. a flux-matching procedure where local gradients are adapted until predictions by local simulations match the experiments, is an option. However, besides being a computationally very expensive exercise, such an approach is likely to lead to an underestimation of the correct gradient profiles because local simulations do not account for finite ρ^* effects. Furthermore, carbon and collisionality appear as necessary ingredients to be retained together in the simulations.
The uncertainty in the original input profiles are particularly large, and it thus appears not justified to invest a large amount of resources modifying by hand the input profiles so as to obtain a better agreement. It is thus desirable to repeat the simulations using experimental input profiles characterized by smaller error bars, which has become available thanks to the upgraded TCV diagnostic systems.
We also note that besides invoking experimental error bars as an explanation for the discrepancy between GENE results and actual flux levels, one can also speculate about the importance of other effects, like plasma rotation, that have been neglected in all simulations discussed so far. The original measured data for TCV shots #28008 and #28014 unfortunately do not allow us to estimate a value of the experimental shearing rate associated to the plasma rotation nor to clearly identify any qualitative plasma rotation dependence on δ.

A repetition of the original discharges, such as to better diagnose profiles, is foreseen during the experimental TCV campaign in the second half of 2016. Quite extensive experimental scans (of e.g. shape, current, power, density) have nonetheless already been carried out in previous experimental sessions. We have thus decided to consider a new set of input parameters corresponding to a different discharge, discussed in the next session.

6.4 Beyond the original parameter set

Not having recent experimental data of discharges with same temperature and density profiles as shots # 28008 and 28014, we focus here on a triangularity scan, where the shape of the LCFS was modified during the discharge, going from negative to positive δ_{LCFS}, while attempting to maintaining all other parameters unchanged. The plasma magnetic geometries, together with the profiles of safety factor, elongation and triangularity are shown in Figure 6.4.

To help the reader and avoid confusion, we will refer in the following to this new discharge as the "*new*" parameter set, to distinguish it from the "*original*" one considered up to now.

This discharge was carried out at constant power, therefore temperature and density profiles are different between the two shapes, as shown in Figure 6.5. One obtains a better confinement when $\delta < 0$, in form of a higher core pressure. In Figure 6.3 we plot the experimental power balance, and as for the "original" discharges one indeed observes a better electron energy confinement at all radial locations from $\rho_{tor} = 0.5$ to the LCFS. We nevertheless remark that the relative improvement in confinement (dot-dashed line) seems to increase with ρ_{tor}, at least in the innermost part of the plasma minor radius.

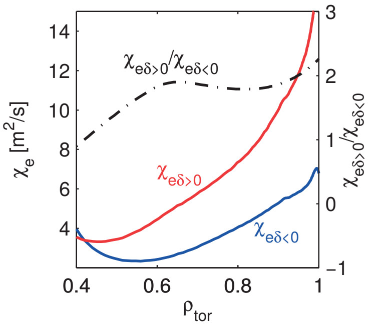

Figure 6.3 : Electron heat diffusivities χ_e in m^2/s computed from the experimental power balance. In red the diffusivity obtained in the TCV discharge #49541 when $\delta > 0$ and in blue when $\delta < 0$. The ratio positive/negative is indicated with a black dot-dashed line.

We note that there is a significant difference in the density profiles, with higher edge density n_{LCFS} when $\delta < 0$, whereas the density gradient ∇n_e is $\sim 30\%$ smaller for $0.85 < \rho_{tor} < 1$ and comparable for $0.5 < \rho_{tor} < 0.8$ (see Fig. 6.5(f)). Similar electron temperatures are measured at the LCFS, with a larger gradient for the $\delta < 0$ case. Finally, for positive triangularity the ion profiles are characterized by a larger value of T_i and of the associated gradient (by at least a factor of two) at all radial locations where it has been measured. As a result, when looking at normalized logarithmic gradients, one finds that R/L_{T_e} and R/L_{T_i} are larger for the negative triangularity shape at $\rho_{tor} \gtrsim 0.7$. For $\rho_{tor} \lesssim 0.7$, the electron temperature gradient inverts its behaviour (smaller for $\delta < 0$), while the ion ones are the same for the two shapes. Finally R/L_n is larger at all radial locations larger for the $\delta > 0$ case.

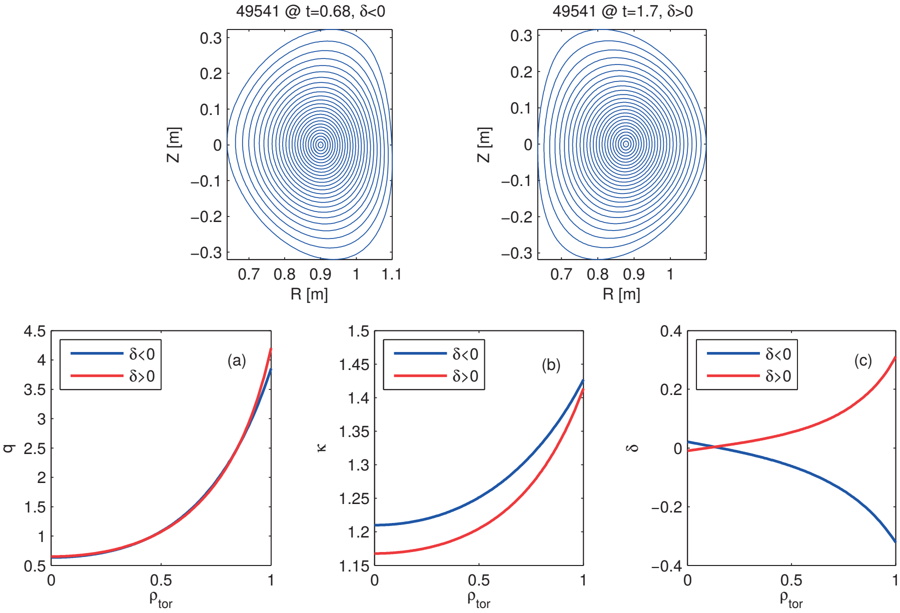

Figure 6.4 : Radial profiles, as a function of ρ_{tor} of (a) safety factor q, (b) elongation κ and (c) triangularity δ for TCV discharge #49541 at t=0.68 s (blue curves), corresponding to negative δ_{LCFS}, and t=1.5 s (red curves) for positive δ_{LCFS}. The two plasma equilibria are shown in the first row.

6.4.1 Local results

Before embarking into global simulations, a preliminary analysis has been carried out with flux-tube simulations. All the runs described in the following, unless differently specified, are carried out considering only one ion species and electrons. Collisions, as well as electromagnetic effects, are retained.

We first carried out a series of linear local simulations at different radial locations. ETG modes are expected to be unstable, however they will not be resolved in the corresponding non linear runs. Thus linear spectra have been resolved only at the ion scales, i.e. considering modes up to $k_y\rho_s \sim 2$. For this analysis we selected four locations, ρ_{tor} =0.5, 0.6, 0.75 and 0.85. The corresponding plasma parameters are listed in Table 6.3, where one notes, as expected, that negligible differences are found between values of safety factor and magnetic shear, while, as already discussed, different gradients characterize each shape.

The obtained growth rates and real frequencies are plotted in Figure 6.6, in blue for negative triangularity and in red for positive. We also considered a mixed situation, that is the negative δ magnetic equilibrium with temperature and density gradients measured with the positive δ (between the discharges the profiles are assumed to be equivalent as a function of ρ_{vol}, as shown in [13]). They are represented with green stars in Figure 6.6.

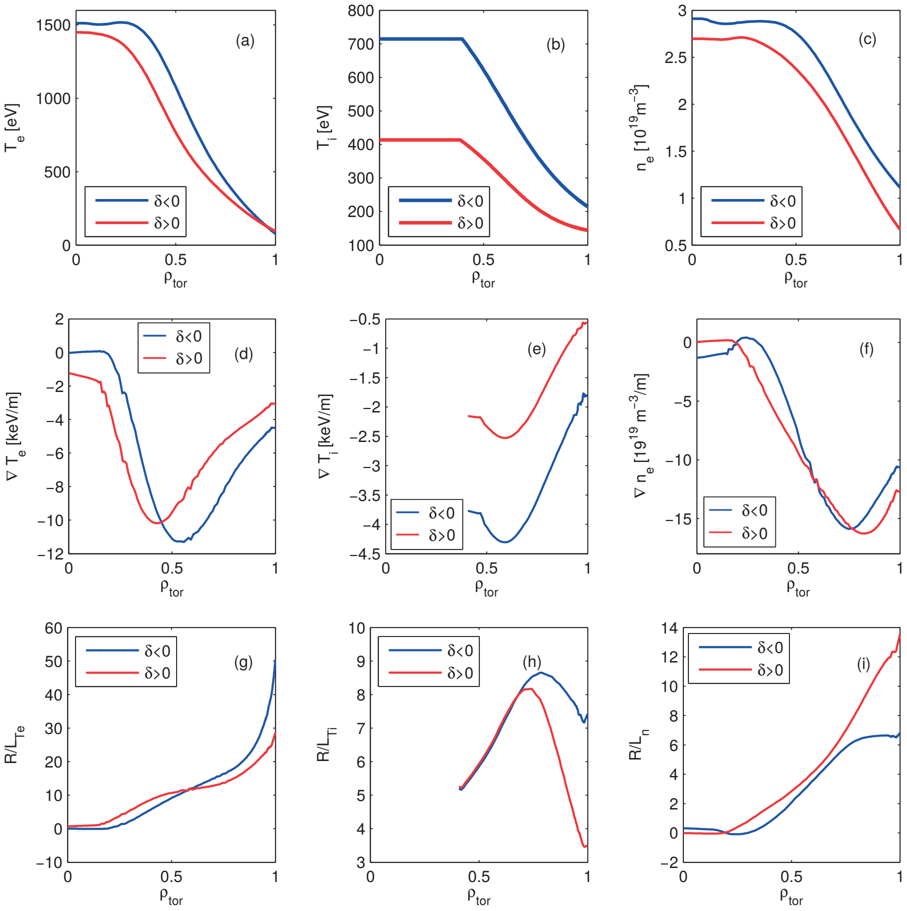

Figure 6.5 : Radial profiles of (a) electron temperature T_e, (b) ion temperature T_i and (c) electron density n_e. Note that in (b) a constant T_i is assumed where no CXS measurements are available. This region will not be considered for simulations. The corresponding gradients are shown in subplots $(d-f)$, whereas the normalized logarithmic gradients $R/L_{T,n}$ in $(g-i)$. Blue curves correspond to profiles measured with negative δ_{LCFS}, red curves with positive.

A coexistence of ITGs and TEMs modes is found at ρ_{tor}=0.5 and 0.65, regardless of the sign of triangularity and plasma profiles. Further out, TEM are instead dominating over ITG for all the modes we have inspected. For the two innermost positions we also observe that when assuming the experimental temperature and density gradients, the lowest k_y modes, $k_y\rho_s = 0.2$ and 0.4, are characterized by higher growth rates when $\delta < 0$ (γ is twice as large for $k_y\rho_s$=0.2) while the maximum growth rate is always smaller when $\delta < 0$. At ρ_{tor}=0.75 and 0.85 growth rates for $k_y\rho_s < 1$ are instead very similar between the two shapes. Finally, for all positions we note a different behaviour of the high k_y modes, which are characterized by much larger growth rates when $\delta < 0$. When the same profiles are assumed, the growth rates of the $\delta < 0$ shape are reduced, becoming smaller than the corresponding $\delta > 0$ counterpart.

	ρ_{tor}=0.5	ρ_{tor}=0.6	ρ_{tor}=0.75	ρ_{tor}=0.85
q	1.08 (**1.07**)	1.34 (**1.32**)	1.93 (**1.90**)	2.52 (**2.52**)
$\hat{s}$	1.01 (**0.97**)	1.38 (**1.34**)	1.94 (**1.98**)	2.31 (**2.52**)
T_i/T_e	0.58 (**0.43**)	0.66 (**0.56**)	0.85 (**0.63**)	1.10 (**0.77**)
R/L_n	2.10 (**2.84**)	3.97(**4.24**)	6.20 (**7.26**)	6.78 (**10.12**)
R/L_{T_e}	8.29 (**9.58**)	10.60 (**9.51**)	13.37 (**10.82**)	17.15 (**14.13**)
R/L_{T_i}	4.83 (**4.73**)	6.11 (**6.25**)	7.13 (**6.42**)	7.02 (**5.25**)
$\nu_{ei}[c_s/R]$	0.18 (**0.30**)	0.30 (**0.50**)	0.73 (**0.99**)	1.53(**1.65**)
β_e	5.73(**3.54**)$\times 10^{-3}$	3.81(**2.29**)$\times 10^{-3}$	1.64(**1.04**)$\times 10^{-3}$	0.81(**0.35**)$\times 10^{-3}$

Table 6.3 : Parameters characterizing the TCV discharge #49541 at the different radial locations assumed for carrying out gyrokinetic simulations. In plain text are listed the values associated to negative triangularity while in parenthesis and in bold the ones associated to positive δ

Nonlinear results

A series of flux-tube nonlinear simulations have been carried assuming plasma parameters at the positions ρ_{tor}=0.6 and 0.75. For all these runs a grid composed of $n_{k_x} \times n_{k_y} \times n_z \times n_{v_\parallel} \times n_\mu$=256 × 64 × 32 × 64 × 16 grid points has been used. The minimum k_y has in all cases been adapted so as to correspond to the toroidal mode number $n = 2$, while the radial domain has been chosen to have $L_x \sim 140\rho_s$.

The time traces of the simulated heat fluxes, in normalized units, are shown in Figure 6.7, separately for ions and electrons. Values are averaged over the simulation volume. One observes that at ρ_{tor}=0.6 the heat flux is equally carried by ions and electrons, which is compatible with the mixed ITG/TEM nature found in linear runs. At $\rho_{tor} = 0.75$ the heat transport is dominated by the electron channel, consistently with the dominant TEM instability found in linear simulations. Comparing the results obtained when assuming experimental gradients, i.e. red to blue curves in Fig. 6.7, one observes that while at $\rho_{tor} = 0.75$ the normalized transport level is similar between the two magnetic geometries in both its absolute value and in the ion to electron ratio, at $\rho_{tor} = 0.6$ a clearly higher flux is carried by both electrons and ions in the negative triangularity case. One should also remember that the values of the reference temperature and density used for normalization are different between the two discharges, therefore the differences between positive and negative δ fluxes are further amplified when comparing the corresponding quantities in physical units, e.g. MW (see Fig.6.8).
In agreement with what was described in the previous chapter, we observe that when one assumes for the $\delta < 0$ case the same profiles as for positive δ (green to red curves), then a lower heat transport is found for the negative triangularity shape, with a difference with the positive counterpart that increases when going towards the LCFS, i.e. when δ gets larger.

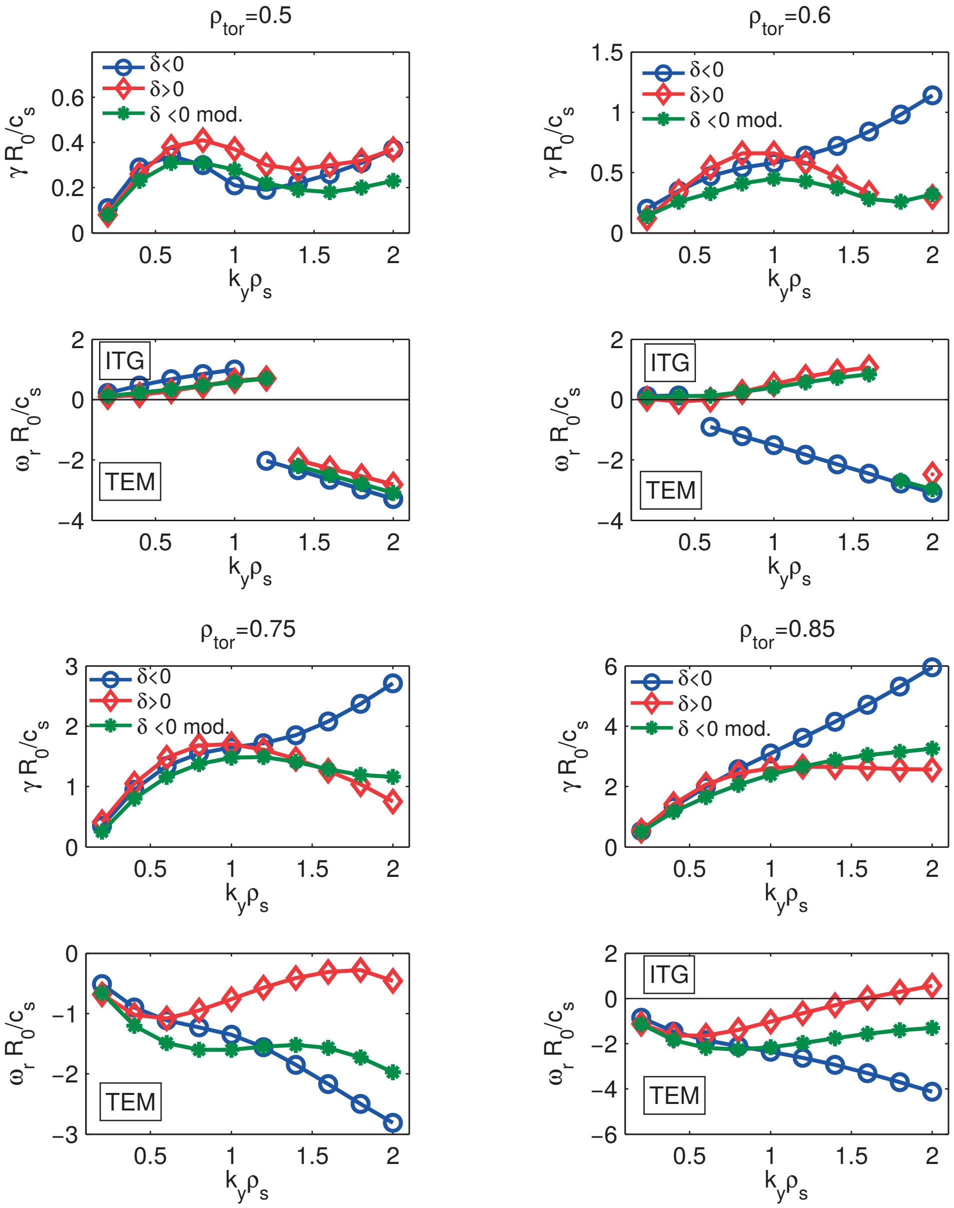

Figure 6.6 : Linear growth rates γ and real frequencies ω_r in units of c_s/R_0, as a function of the binormal wave vector $k_y\rho_s$. Shown are the results obtained, at different radial locations, considering negative δ experimental conditions (blue curves), positive δ ones (red curves) and a mixed set-up where the magnetic geometry of the negative triangularity is used with the positive δ profiles (green curves). Note also that each curve is normalized using the local value of the sound speed and Larmor radius, different for each radial position and for each of the three scenarios.

The time averaged heat fluxes are compared to the experimental power balance in Figure 6.8. The latter is computed based on experimental measurements and accounts for both the ECH heating (∼ 0.46 MW for this particular discharge) and the Ohmic power

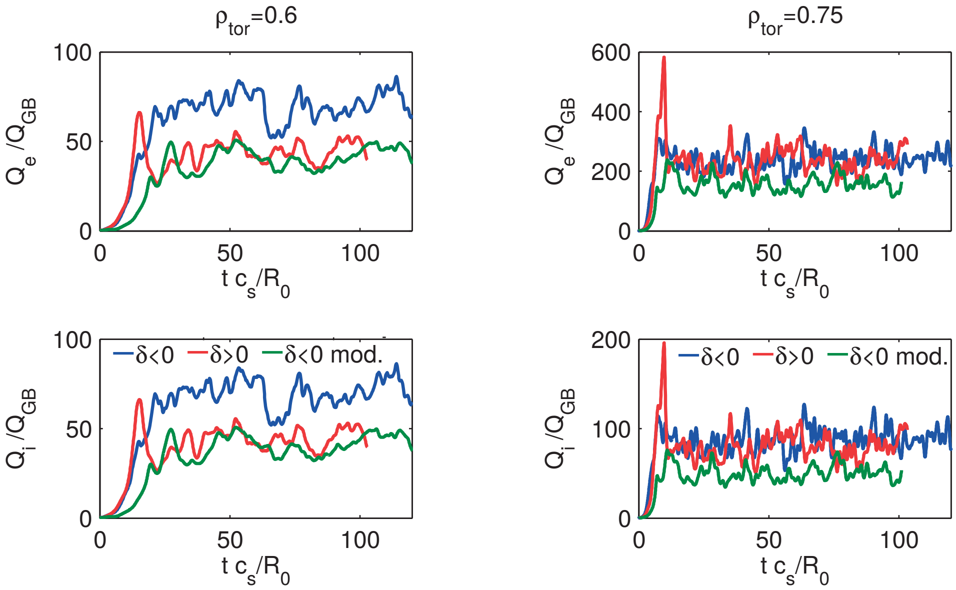

Figure 6.7 : Time traces of the simulated heat ion and electron fluxes in Gyro-Bohm units, $Q_{\mathrm{GB}} = n_e T_e c_s (\rho_s/R_0)^2$ as a function of position (ρ_{tor}=0.6 on the left and ρ_{tor} =0.75 on the right) and plasma parameters. Blue curves indicate results obtained assuming TCV parameters corresponding to negative triangularity while red to positive δ. Green curves indicate runs carried out with the magnetic geometry of negative triangularity and profiles of positive δ.

(varying with shape from $\sim$ 220 kW for the $\delta < 0$ case to $\sim$ 180 kW when $\delta > 0$). Equipartition power and variation of plasma energy are accounted for, even though they are negligible in magnitude compared to the previous two terms.

Considering first the electron heat flux Q_e, one observes that the simulations carried out for the $\delta < 0$ case are significantly overestimating the experimental transport levels compared to the ones associated to $\delta > 0$. When considering the positive triangularity conditions, we obtain that at ρ_{tor}=0.6 the predicted electron heat flux is approximately 10% lower than what measured, while 15% higher at ρ_{tor}=0.75. Such differences are compatible with the uncertainty in the input profiles and in the time averages of our results. Furthermore, we have neglected carbon impurities, whose inclusion further lowers the transport level.

From the simulations carried out assuming plasma parameters associated to the negative triangularity conditions, one observes instead a clear overestimation of the heat flux through the electron channel, which is larger by a factor of 5 (resp. 4) at $\rho_{tor} = 0.6$ (resp. $\rho_{tor} = 0.75$).

An overall overestimation of fluxes is evident when inspecting the simulated ion heat fluxes Q_i, which are found in all cases to largely exceed the experimental ones, by at least a factor of ten. As already pointed out before, when considering $\delta < 0$ at $\rho_{tor} = 0.6$, Q_i is actually larger than Q_e (the ion heat flux is in this case more than 60 times larger

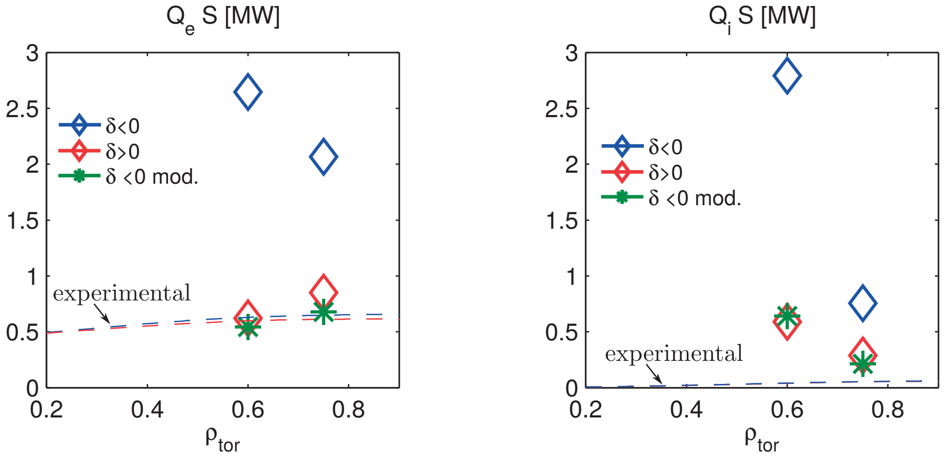

Figure 6.8 : Time averaged heat power, carried by electrons Q_e (left), and by ions, Q_i, (right) graph, expressed in MW. The results obtained when assuming the negative δ experimental TCV conditions are shown with blue diamonds, while with red the positive δ. Green stars indicate mixed parameters. The experimental power balance is shown with dashed lines, following the same color coding.

than the experimental one), leading to a non-physically large transport level.

6.4.2 First global simulations

Global nonlinear simulations have been carried out considering the new profiles and geometries. The same numerical set-up as local simulations has been used in order to carry out also global simulations, which are therefore fully electromagnetic collisional runs without impurities. The real electron to ion mass ratio is assumed. In order to reduce the cost of the runs, the extrapolation of the equilibrium outside the LCFS is avoided, and simulations cover the radial extent $0.45 < \rho_{tor} < 1$, the the last 10% devoted to buffer regions. In these regions we also smoothly reduce the experimental gradients down to zero.

	n_x	n_{k_y}	n_z	$n_{v_\parallel}$	n_μ	$k_{y,min}$	L_x/ρ_s	$L_{v_\parallel}$	L_μ
negative δ	512	64	32	110	60	0.019 (n =1)	71	4.14	18
positive δ	512	48	32	110	60	0.032 (n =2)	81	4.14	18

Table 6.4 : Numerical parameters used for carrying out 2 species collisional full-radius global simulations with the “new” parameter set.

The grids adopted for carrying out such runs are reported in Table 6.4. The negative δ case has been carried out considering the maximum currently affordable resolutions, that is assuming the full toroidal domain in the binormal direction and a radial resolution Δx corresponding to $\sim 1/7\rho_s$. These settings have been relaxed in the run simulating the $\delta > 0$ case, which has been performed retaining only half toroidal domain in the binormal direction and with lower the radial resolution to save CPU resources.

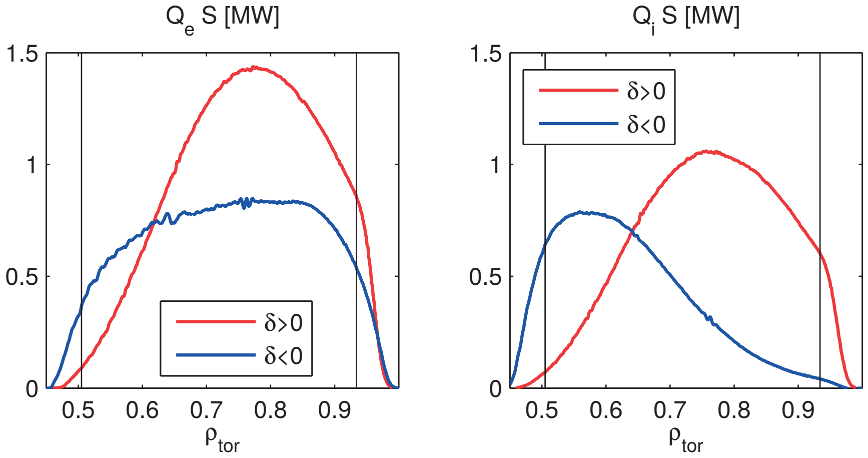

Figure 6.9 : Electron (on the left) and ion (on the right) power crossing a flux surface as a function of the radial position. Shown in red the results obtained assuming the experimental conditions of $\delta > 0$ and in blue for $\delta < 0$. Vertical lines indicate the position of the buffers.

At the time of writing, limited statistics have been acquired for the runs ($\sim 50\ R_0/c_s$). Longer simulations should be performed, but given that non-linear saturation has already occurred, we plot in Fig 6.9 the resulting heat power profiles. Global effects appear in this case particularly strong, especially for the negative δ case, where a reduction of Q_e by a factor of five is found at both $\rho_{tor} = 0.6$ and 0.75 as compared to the flux-tube results. As a result, electron heat flux profiles obtained appear to be already in very good agreement with the experimental one, both in its absolute vale and in the radial dependence. The positive triangularity case instead appears to be less affected by finite ρ^* stabilization, with global results essentially reproducing the same electron heat flux as the local one. A weaker reduction of the transport is found also in the ion channel. How much of this difference between the two shapes is due to the different value of $k_{y.min}$ is currently under investigation.

We once again remark that only limited statistics have been acquired so far and impurities, which with in flux-tube simulations are found to be strongly stabilizing both channels of transport (see next section), have been neglected, so one cannot exclude this partial result as partly coincidental. We also point out that the total heat transport $Q_i + Q_e$ remains higher than the experimental one by at least a factor of two for the negative δ and three for the positive δ case.

6.4.3 Further remarks about the effects of carbon impurities and plasma rotation

All the simulations described in the previous section have been carried out neglecting impurities mainly for having the same set-up between local and global simulations. We however have already pointed out, based on both simulations and experimental evidence, that carbon plays a significant role in stabilizing turbulence.

As was already noted in Ref. [43], negative triangularity plasmas are normally characterized by a larger value of $Z_{\rm eff}$ compared to positive δ discharges, because of the different interaction with the wall. Furthermore, the effect of increasing $Z_{\rm eff}$ is found to be stronger when $\delta < 0$ [13]. A shape dependent carbon concentration can thus help in furthermore reducing the transport level predicted by simulations towards experimentally measured values.

In the following we will further discuss the strong effect played by carbon, with the help of numerical simulations carried out considering TCV parameters of the "new"triangularity scan. One could have used different plasma parameters (temperature and density gradients as well as magnetic geometries), like e.g. the "original" one used for the local stiffness study presented in Chapter 5. However, being the "new" set derived from an experimentally better diagnosed discharge, we prefer this latest choice. At the same time, rotation measurements are available in this case, so they will be discussed as well.

We recall that two different experimental ways of measuring the C content, and consequently $Z_{\rm eff}$, are available. One can determine the carbon concentration directly from Charge eXchange Recombination Spectroscopy (CXRS), and, neglecting all other impurities, compute main ion and impurity content as a function of radius based on quasi-neutrality. Alternatively, one can evaluate a radially constant $Z_{\rm eff}$ such as to obtain a plasma resistivity that matches the experimental one. Typically the second method leads to an higher value of $Z_{\rm eff}$ because other elements, not diagnosed by the CXRS system, are present in the plasma. Using the measurement based on resistivity one might thus be overestimating the carbon content of the discharge. We furthermore remark that assuming CXRS values allows to use different values of density gradients for each plasma species, while a radially constant $Z_{\rm eff}$ constrains R/L_n to be the same for all species.

For the case we are looking at in this section, the value of $Z_{\rm eff}$ measured with CXRS is $\sim$1.85 for the positive δ and 2.35 for the negative δ case (these values are based on an radial averages over $0.4 < \rho_{tor} < 1$), while the estimate based on plasma resistivity leads to $Z_{\rm eff}$ respectively 3.46 and 3.53. The origin of such a big experimental discrepancy remains unclear.

Lacking a clear experimental measurement, the "correct" value of carbon concentration to be retained in numerical simulation can be assessed only through dedicated runs. As was done in e.g. Ref. [32], one can investigate the zero particle flux point, which can provide a further physical constraint to the possible values assumed by the different plasma parameters. This is a somewhat long and tedious exercise, which we leave for future investigations. We have assessed the impact of carbon by assuming the most favourable condition in lowering the heat flux, that is the highest $Z_{\rm eff}$, i.e. 3.46 (resp. 3.53) for positive (resp. negative) δ. This latter consideration is based on linear local growth rates, reduced when increasing the carbon content.

We have thus repeated all nonlinear runs retaining carbon as a third gyrokinetic species,

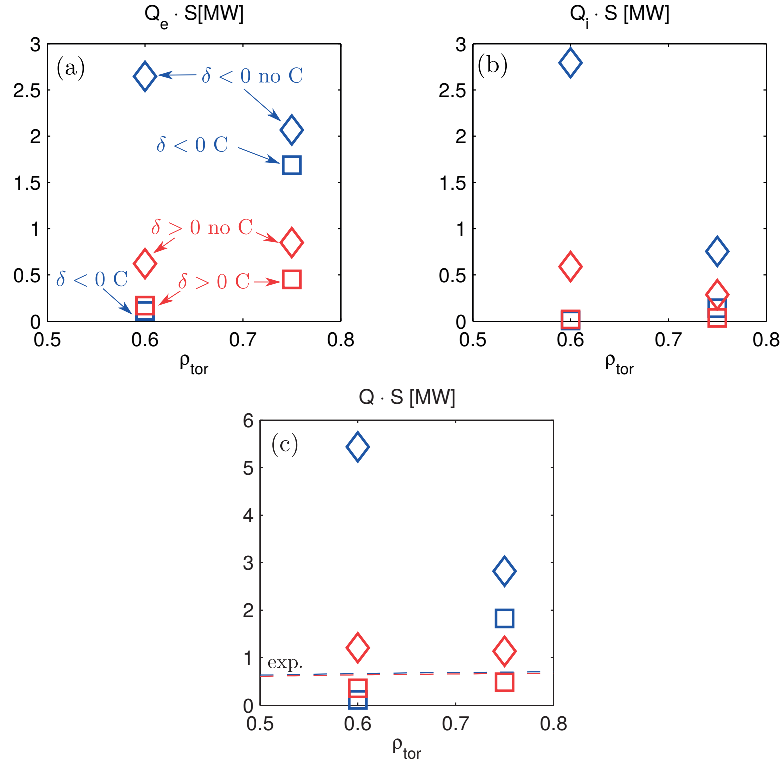

Figure 6.10 : Heat power as a function of the radial location for different plasma edge triangularities obtained from local simulations carried out with and without carbon impurities. Shown are (a) the electron heat flux Q_e, (b) the ion Q_i and (c) the total Q. With diamonds shown are the results obtained neglecting carbon while with squares retaining a C concentration matching the value of Z_{eff} measured based on plasma resistivity, i.e. 3.46 (resp. 3.53) for positive (resp. negative) δ. Blue points refer to negative triangularity of the LCFS while red positive δ. For clarity the simulated data points are labelled only in subplot (a), the same coding is used in all subplots.

obtaining a very large reduction of the total heat flux, and in particular of the ion one, as can be seen from Figure 6.10. This stabilization is particularly strong at ρ_{tor}=0.6, where in fact the profiles become less unstable and the simulated total flux is below the experimental transport level (see Fig. 6.10(c)). This latter observation is consistent with Phase Contrast Imaging measurements that detect only a very weak turbulence level at such radial location.

The total simulated heat power is now found to be lower than the experimental one for all conditions with the exception of $\delta < 0$ at $\rho_{tor} = 0.75$, where an overestimation, by approximately a factor of two, remains.

The strong stabilization induced by C is consistent with the behaviour of linear growth rates, as shown in Figure 6.11 for the position $\rho_{tor} = 0.6$. Including carbon, low k_y ITG modes that strongly contribute to nonlinear fluxes, are stabilized and TEMs, with a smaller growth rate, become the most unstable ones for both shapes. The ITG branch found in the positive δ case at $k_y\rho_s \sim 1$ is also stabilized. Finally, for both triangularities we find a stabilization of the high k_y ETG modes which are replaced by a short-wave ITG branch when impurities are included. Such modes however do not contribute much to nonlinear fluxes.

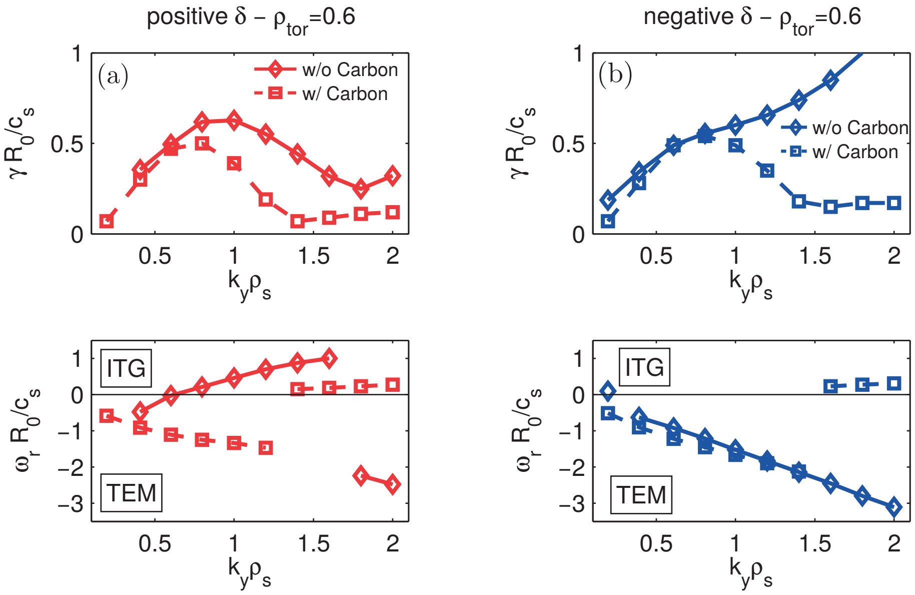

Figure 6.11 : Growth rates γ and real frequencies ω_r in units of R_0/c_s for the most unstable mode as a function of the binormal wave vector $k_y\rho_s$. Shown with diamonds and solid lines the results obtained without including carbon, while with squares and dashed lines the values obtained when impurities are included. Results valid for simulations at $\rho_{tor} = 0.6$ considering (a) positive and (b) negative δ.

Compared to the local simulations described in chapter 5, besides a 10% higher value of $\hat{s}$, the main difference between plasma parameters is in fact collisionality. Because of the lower electron temperature and at the same time higher density, ν_{ei} turns out to be the same value (in normalized units) as the one used for the stiffness study when carbon is neglected (compare Tables 4.3 and 6.3). Including impurities is thus sensibly increasing ν_{ei}, lowering the fluxes and allowing to match with the experimental ones much more closely than what obtained before.

Investigating the sensitivity of these local results with respect to carbon content and collisionality is naturally the next step to be undertaken, given both the extremely high sensitivity of the simulated turbulent fluxes with respect to the impurity content and the large experimental uncertainty.

Nonetheless, regarding the importance of global effects, we note that the value of $\rho^* = \rho_s/a$ is quite similar between the conditions assumed for the "original" runs, and the "new" discharge, and therefore similar global effects are expected. At $\rho_{tor} = 0.6$ we find $\rho^* \sim 1/95$ (resp. $\rho^* \sim 1/110$) for the "original" (resp. "new") scenario. At

$\rho_{tor} = 0.75$ instead we have $\rho^* \sim 1/130$ vs. $\rho^* \sim 1/135$. Those value represent an average between positive and negative triangularity shapes, as with the "new" profiles, because of the lower electron temperature, ρ^* is lower for the $\delta > 0$ case, while in the "original" discharge minor differences were due only to geometric effects. Based on the results discussed in this section it thus appears that one need to invoke less strong finite machine size effects in order to reproduce TCV transport level for the "new" discharge. In thus appears that the overestimation obtained when assuming the "original" parameter set is at least to be partly attributed to large uncertainty in the input profiles, as also local simulations too strongly overestimate the transport even if carbon is included with a large concentration.

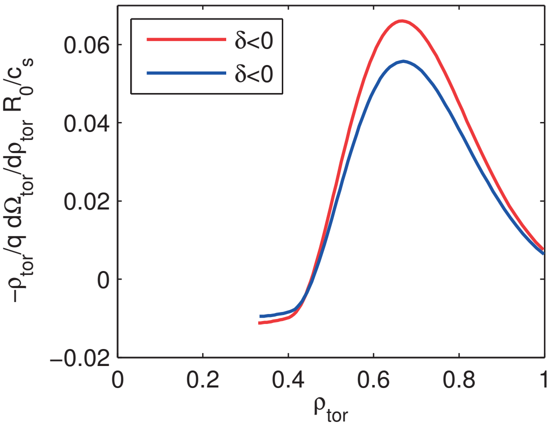

Figure 6.12 : Radial profiles of the toroidal angular velocity shearing rate ω_{tor}, see Eq. (6.1), measured with CXRS for (red) positive and (blue) negative triangularity.

Finally, using this new parameter set we were also able to measure the effect of rotation on turbulence, an analysis that was not possible using the "original" parameters because of lack of experimental data. In the local approximation, GENE implements background flows by shifting in time the Fourier k_x modes, see Ref. [30] for more details. Using the experimentally measured value of toroidal angular velocity Ω_{tor} as well as it shearing rate

$$\omega_{\mathrm{tor}} = -\frac{\rho_{tor}}{q}\frac{\mathrm{d}\Omega_{\mathrm{tor}}}{\mathrm{d}\rho_{tor}}\frac{R_0}{c_s}, \tag{6.1}$$

which is depicted in Figure 6.12, we do observe only minor variations of the heat flux, slightly larger at $\rho_{tor} = 0.6$ where including rotation lowers the fluxes by $\sim 10\%$ compared to $\rho_{tor} = 0.7$ where it has an almost negligible effect. In all cases the variation is much weaker than the one observed when carbon is included.

6.5 Conclusions

In this chapter we have discussed global simulations carried out with the aim of reproducing the experimental confinement improvement associated with negative triangularity. Because of the limited computational resources available it has not been possible to perform simulations that retain at the same time carbon and finite collisionality, which are both expected to be crucial in order to match the experimental transport level.

For the plasma conditions used in the previous chapter to model profile stiffness, global effects are found in terms of a reduction of the heat transport in the innermost locations, and a more radially uniform difference between the heat fluxes for the two plasma shapes. A large overestimation, up to a factor of at least six remains in the core. Moreover, the simulated profile of transport appears to be unrealistic, strongly peaked in the core and rapidly decreasing towards the LCFS, while one would expect it to be roughly constant as a function of radius, as it is experimentally observed.
While one can still speculate that a run carried out with carbon and collisionality could significantly lower the simulated transport level to values more closely matching the experimental ones, such a computationally expensive simulation should be performed only when the uncertainties in the input profiles are minimized and cannot explain the discrepancy in the local results.
The experimental error bars in the measured profiles are large for the case we have examined, and a reduction of the density gradient in the core region is found to help reducing the transport (a density gradient driven TEM is the most unstable mode associated in our case). At the same time the original data are affected also by large uncertainty in the carbon content measurements, which can similarly strongly reduce the heat fluxes.

In order to understand whether a more recent and better diagnosed experimental discharge can more easily allow to match simulations and measurements, we have initiated investigating an experimental δ scan carried out at constant power. The parameters, e.g. n_e and T_e, are sensibly different and as a result one is, at least in the plasma core, in a mixed ITG-TEM regime. In this case a much better agreement is obtained already by flux-tube simulations, which are found to reproduce the experimental transport level within a factor of two when impurities are retained. The local values of ρ^* are not significantly different from the ones that characterize the first set of runs, therefore one would expect similar global effects.
Global simulations have been initiated (neglecting C to reduce their cost) and with this new parameter set strong global effects are observed, in the form of a very large reduction of transport, especially in the negative δ case. For this geometry, the simulated electron heat flux is already in good agreement with the experimental one. The total heat flux remains however higher in comparison with the experiments, mainly because of a large overestimation of the transport through the ion channel. Based on local results, this contribution is expected to be strongly suppressed if impurities are retained.

It thus appears that most of the discrepancy between simulations, both local and global, carried out with the original parameter set and the corresponding and experimental measurements is due to the uncertainty in the input profiles. In particular in our case a too large density gradient. Local simulations are able to reproduce TCV conditions already with a good agreement, and one must thus be very careful in not overestimating the importance of finite machine size stabilization attributing to ρ^* effects that are in fact due to incorrect profile inputs. Global effects are nonetheless present, and should be retained and measured. A meaningful next step is thus to carry out global simulations with three species (deuterium, carbon, electrons) including collisions for the “new” triangularity experimental scan which is better diagnosed than the “original” discharges.

We find the dynamics of low k_y modes, the ones contributing more strongly to transport, to be very sensitive to carbon concentration. Different turbulent regimes, and associated fluxes mainly through the ion channel, are observed when C is not included in the runs. This is thus another very important element to be addressed, also because the carbon concentration can experimentally be δ dependent, and with an effect that depends on shape. We remind that in the “original” simulations set up, Z_{eff} was taken as 3.2 for both shapes, which is the highest possible value (taken from resistivity estimates, as the CXS system was at the time not sufficiently accurate). Thus, one must also verify that this concentration is not too high and that an even larger modification of input profiles of the “original” parameters is necessary.

We finally remark that all these observations are also related to the fact that we have carried out gradient-driven simulations, which constrain the temperature profile to a prescribed background. Ideally, one would want to carry out more realistic flux-driven runs, which are however out of practical reach for the currently available computational resources.

7 Study of GAM dynamics in TCV relevant conditions

Observations of axisymmetric oscillations in the frequency range of the Geodesic Acoustic Mode have been reported by various authors in different machines, see [55] and references therein. While it is not certain that all these observations are true GAMs, in the following we shall refer them as "GAMs" for the sake of simplicity. Thanks to both the very flexible set-up of the diagnostic system and the versatility of the machine in obtaining plasmas with different shapes, which is one of the known parameters affecting the mode frequency [57], the GAM has also been extensively investigated in TCV [55, 62, 117, 118].

In particular, the density fluctuation component of the GAM has been measured thanks to the Tangential Phase Contrast Imaging (T-PCI) system [43, 55], studying both the frequency, wavelength and the spatial localization of the mode. For typical TCV conditions the GAM appears as a *radially coherent*, i.e. an oscillation at a constant frequency f_{GAM} over a large fraction of the plasma minor radius [62], contrary to the predicted dependency of f_{GAM} on the local sound speed provided by the local linear description of zonal flows (see section 2.7). This latter condition, referred to in the following as *dispersive* mode, has been observed only during an edge safety factor ramp-up [117]. Note that analytic theory predicts the existence of GAM eigenmodes at frequency $f_{\mathrm{GAM}}^{\mathrm{global}}$ and with a finite radial extent, when the temperature is inhomogeneous [119, 120]. In this case, the mode is predicted to propagate in the low temperature region i.e. in the region where $f_{\mathrm{GAM}}^{\mathrm{global}} > f_{\mathrm{GAM}}^{\mathrm{local}}$. We prefer not to use this nomenclature here because for the TCV cases studied here, the observed global GAM is found, in both experiments and simulations, to propagate at frequency much lower than the local one. Moreover, as it will be discussed in the following, in our simulations oscillations at the same frequency can be found also in the profiles of heat and particle fluxes, suggesting a coupling between GAM oscillations and avalanches [121], and making non trivial the distinction between them.

In all experimental cases, the amplitude of the GAM oscillation is observed to increase towards the LCFS, in agreement with the linear mode damping being proportional to $\exp(-q^2)$. Plasma shaping is experimentally found to affect the GAM. As predicted by analytic theory and simulations [57, 122], the elongation κ reduces the frequency of the mode and lowers the amplitude of the density fluctuation component. A similar role is observed to be played by negative δ. Furthermore, the magnetic fluctuation associated to the GAM has been characterized [62], and a dominant $m = 2$ poloidal component observed.

Numerical simulations, both local and global, have been performed in order to model some of the experimental TCV conditions where the GAM has been observed. The obtained results will be discussed in this chapter, which is organized as follows. First, we will present the simulations relative to the TCV discharge #46068, a density ramp-up where the GAM was observed disappearing in the PCI spectra at increasing density and experimentally interpreted as a result of the increased broadband turbulence. Local GENE simulations qualitatively agree with the observed behaviour and predict similar trends of f_{GAM} with respect to the background density. The nonlinear simulated frequency, which similarly to the experiments is found significantly lower than predictions based on linear GAM dynamics, is however higher than measured. The dependency of this frequency with plasma parameters has been investigated and possible explanations of this observed discrepancy will be discussed.
Note that the local approximation does not allow to address either the global nature of the mode or any possible privileged direction of propagation. These aspects have therefore been addressed with dedicated global runs, presented in the last part of the chapter. The observation of the safety factor q dependency will also be partly addressed.

7.1 Analysis of an experimental TCV density ramp-up

7.1.1 TCV discharge #46068

The TCV plasma #46068 is a density ramp-up carried out during an Ohmic discharge, with the aim of investigating, among others, the effect of increasing collisionality on GAMs and, generally, on broadband turbulence. Density fluctuations have thus been experimentally measured using the PCI system. An effort was made to keep the shape of the LCFS fixed, while the density increased by a factor of ~ 6 before the plasma disrupted. During the discharge evolution the diagnostic beam was maintained tangential to the magnetic surface at the location $\rho_\psi = 0.8$. Here ρ_ψ indicates a radial coordinate based on the normalized poloidal flux, $\rho_\psi = \sqrt{\psi/\psi_{\mathrm{LCFS}}}$, which approximately corresponds to $\rho_{tor} = 0.66$. The time trace of the line-integrated electron density (measured with a Far InfraRed interferometer) is shown in Figure 7.1, together with an example of the plasma magnetic geometry (evaluated at t=0.3 s).
The GAM was detected during the first part of the discharge, when the plasma was kept at low density, at a frequency of approximately $\sim$ 27 kHz. Then, starting from t=0.7 s the GAM peak disappeared in the broadband turbulence background, see Figure 7.14 and Ref. [117]. Bicoherence analysis hinted to the GAM drive not being simply proportional to the turbulence intensity. We also note that during this discharge a quasi-

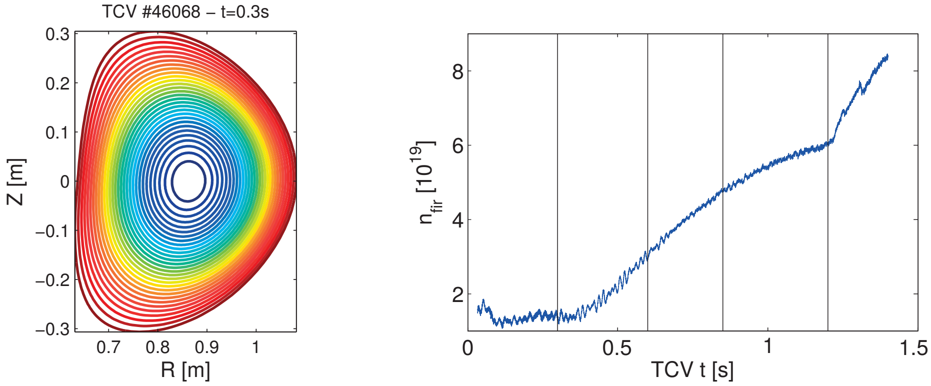

Figure 7.1 : On the left, flux-surface contours showing the magnetic geometry of the TCV discharge being analyzed. On the right, line-integrated electron density (measured with the TCV Far InfraRed interferometer diagnostic system) as a function of the discharge time. Vertical lines indicate the instants considered for carrying out simulations (t=0.3 s, t=0.6 s, t=0.85 s and t=1.2 s.

coherent mode (a mode localized in k space but broad in frequency) was observed at intermediate densities, which however will not be addressed here. In order to investigate, and potentially partly reproduce, the experimental observations, we have carried out a series of flux-tube simulations at fixed radial position (corresponding to the experimental location of the T-PCI diagnostic laser beam, $\rho_\psi = 0.8$) considering plasma parameters representative of TCV conditions at different times. Note that the radial coordinate used to carry out the simulations is ρ_{tor}, which varies in time as reported in Table 7.1. We choose in particular the following four time instants: t=0.3 s, t=0.6 s, t=0.85 s and t=1.2 s. The first one is representative of a low density plasma where, as will be shown, TEM modes constitute the dominant instability at the ion scale. For all times later than t=0.7 s, ITG modes are found to be dominant. The parameters at t=0.6 s are therefore representative of an intermediate transition condition, while the ones at t=0.85 s represent an ITG dominated situation. The last time chosen, t=1.2 s, is close to the experimental plasma disruption, so the parameters (in particular gradients and magnetic geometry) are affected by a significant error bar. Nonetheless, given the striking complete disappearance of the GAM peak from the PCI spectra at this late time of the discharge, it appears as an interesting situation to be investigated.

Naturally, temperature and density profiles of all species evolve in time, as depicted in Figure 7.2. In particular, electron temperature is decreasing in time while the ion one, as well as R/L_{T_i}, is increasing.
In order to be as close as possible to realistic TCV conditions, we decided to vary all parameters from one simulation to another according to the actual measurements, at the price of not being able to easily isolate the effect of individual terms. The actual plasma parameters adopted for carrying out the runs are detailed in Table 7.1 we have reported

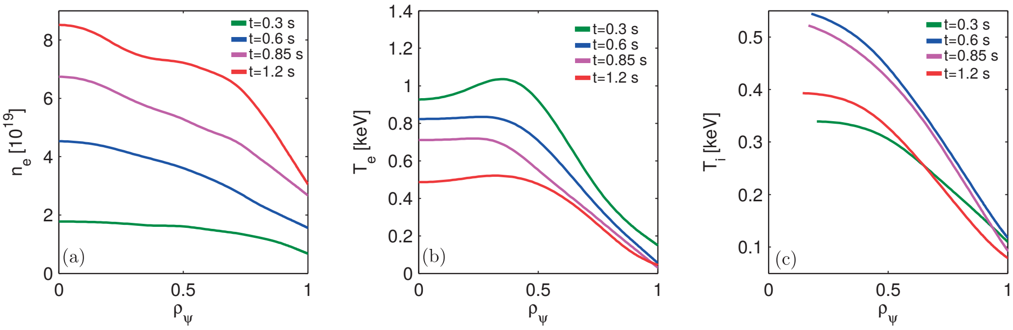

Figure 7.2 : Radial profiles, as a function of ρ_ψ of (a) electron density n_e, (b) electron temperature and (c) ion temperature T_i relative to the TCV discharge 46068. Shown in green are the values measured at t=0.3 s, in blue at t=0.6, in magenta at t=0.85 s and in red at t=1.2 s. The same color coding will be used in all plots to distinguish the different time instants during the discharge.

the value of the effective collisionality [123]

$$\nu^* = \frac{4}{\sqrt{3}\pi}\frac{q}{\epsilon^{3/2}}\frac{n_i}{n_e}\nu_{ei}\frac{R_0}{v_{\mathrm{th},e}} \tag{7.1}$$

instead of ν_{ei}, to provide a value independent of T_e, which varies in time.

7.1.2 Local linear analysis

Mode frequency and growth rate

In order to investigate the type of underlying microinstabilites at play at the four selected time instants, a series of linear simulations has been carried out considering k_y modes up to the electron scale. These simulations have been performed considering the experimental magnetic geometries reconstructed with CHEASE. All runs consider three fully gyrokinetic species: the main deuterium ion species, electrons and carbon as minority impurity with a concentration matching the measured Z_{eff}. Electromagnetic fluctuations, even though they turn out not to be the dominant for the cases considered here, have been accounted for assuming the experimental value of β. Finally, the experimental value of collisionality ν^* has been assumed. All the simulations performed at the ion scale ($k_y\rho_s \leq 10$) have been carried out considering a grid with $n_{k_x} \times n_z \times n_{v_\parallel} \times n_\mu = 48 \times 32 \times 64 \times 16$, with $\hat{L}_\parallel \times \hat{L}_\mu = 3 \times 9$. The stability of modes at the electron scale ($k_y\rho_s \geq 10$), given that they are typically more ballooned, has been investigated using the same numerical grids except in the radial direction, for which only $n_{k_x} = 32$ modes were sufficient.

The results obtained are summarized in Figure 7.3, where real frequencies and growth rates are shown as a function of the wave number k_y. One indeed observes at the ion

	t=0.3s	t=0.6s	t=0.85s	t=1.2s
ρ_{tor}	0.68	0.66	0.66	0.63
q	1.98	1.85	1.84	1.53
$\hat{s}$	1.25	1.36	1.36	1.52
T_i/T_e	0.53	0.87	0.90	0.84
R/L_n	3.91	5.05	4.17	4.85
R/L_{T_e}	10.70	11.70	11.40	13.09
R/L_{T_i}	5.61	7.21	7.89	7.90
n_e $[10^{19} 1/m^3]$	1.23	2.38	3.98	5.63
$T_e[eV]$	370	288	238	204
ν^*	0.32	0.64	1.33	1.35
β_e	0.89×10^{-3}	0.13×10^{-2}	0.18×10^{-2}	0.22×10^{-2}
Z_{eff}	2.59	1.48	1.33	1.38

Table 7.1 : Parameters characterizing the TCV discharge #46068 at the various times considered for carrying out gyrokinetic simulations. All values are referred to the radial location $\rho_\psi = 0.8$; the corresponding values of ρ_{tor} are listed as well.

scale a transition from TEM (modes possessing a negative real frequency in Fig. 7.3 (*a*)) to a ITG (positive frequency) dominated regime when the density is increased. More in detail, at the beginning of the discharge (t=0.3 s) TEMs are the dominant instability for all $k_y\rho_s \sim 1$ modes analyzed, while at later times (t$\geq$ 0.85 s) all dominant ion scale modes are ITGs. Considering the parameters of the intermediate time t$\sim$ 0.6 s, TEM and ITG coexist, with the latter being the most unstable at $k_y\rho_s > 0.5$. We also note that there is a continuous transition from TEM to ITG without any frequency jump, with the former branch continuously connected to the latter.

We remark that at the electron scale ETG modes are unstable in all cases considered for $k_y\rho_s \sim 10$, with a maximum growth rate that increases despite the increasing collisionality. This latter result is in agreement with the increasing electron temperature gradient in time.

In order to address the sensitivity of these findings with respect to the radial location assumed as the center of the flux-tube, we performed a radial scan centering the simulation domain (and therefore considering also the actual local experimental plasma parameters) at seven equally spaced radial positions $0.5 \leq \rho_{tor} \leq 0.8$. Given that ETG modes will not be taken into account in the following nonlinear simulations, only wave numbers at the ion scale were considered. The results are depicted in Figure 7.4. The same analysis has been repeated also assuming zero collisionality ($\nu^* = 0$), as shown in Fig. 7.5.

From Figure 7.4 one sees that, at the beginning of the discharge, ITG modes are already unstable, but only in the core ($\rho_{tor} \leq 0.55$) and over a narrow range of k_y modes. Then, for all the other simulated instants they gradually become the dominant instability at $k_y\rho_s \leq 1$. Only at t=0.6 s (Figure 7.4 (*b*) one observes a true coexistence of ITG with TEM modes, with the latter being the most unstable at the lower end of the k_y spectrum

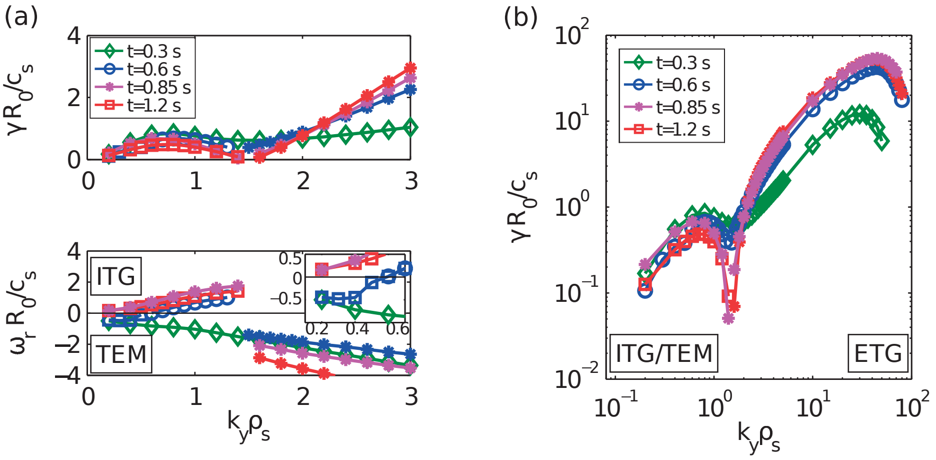

Figure 7.3 : Growth rate γ and real frequencies ω_r in units of R_0/c_s of the most unstable mode as a function of the wave number $k_y\rho_s$. Results have been obtained considering the TCV discharge #46068, using the magnetic equilibrium and plasma parameters measured at respectively t=0.3 s (green diamonds), t=0.6 s (blue circles), t=0.85 s (magenta stars) and t=1.2 s (red squares). In order to illustrate the continuous TEM-ITG transition found at $k_y\rho_s < 0.5$ for the parameters at t=0.6 s, a zoom on the low k_y part of the spectra is shown. The results obtained at the ion scale ($k_y\rho_s \sim 1$) are shown in lin-lin scale in (a), whereas growth rates are also plotted log-log scale in (b) such as to illustrate the ETG contribution ($k_y\rho_s \sim 10$). All simulations are performed centering the flux-tube at ρ_ψ=0.8.

and for $\rho_{tor} \lesssim 0.7$. Finally, one observes that edge modes at high k_y become more and more unstable at later instants of the discharge.

A comparison with the results of the same analysis carried out neglecting collisionality, see Fig. 7.5, reveals that ITG modes are the dominant instability in a major fraction of the plasma only at t=0.85 s. A small ITG dominated region is found also in the simulations carried out with the parameters associated to t=1.2 s. However it is much more narrow in both radial and k_y extent. Based on these results, for each of the times that we are considering, even if radial variations exist, the type of turbulence appears not to be particularly sensitive to the radial location, therefore validating the specific radial location used for flux-tube simulations.

Between the four instants considered, collisionality is significantly changing, by at least a factor of eight (see Table 7.1), and experimentally it is assumed as the most relevant varying factor. Gradients, however, do change as well, potentially inducing a turbulent regime transition. In order to assess the influence of ν^* on the obtained results, for each time instant we have artificially varied the collisionality while keeping fixed all the other parameters. For each time, linear runs have thus been performed for the four values of ν^* tabulated in Table 7.1. The corresponding results are summarized in Figure 7.6.

The only case in which an increase of collisionality appears to be able to induce a regime transition is when assuming the plasma equilibrium and gradients of t=0.3 s (first graph

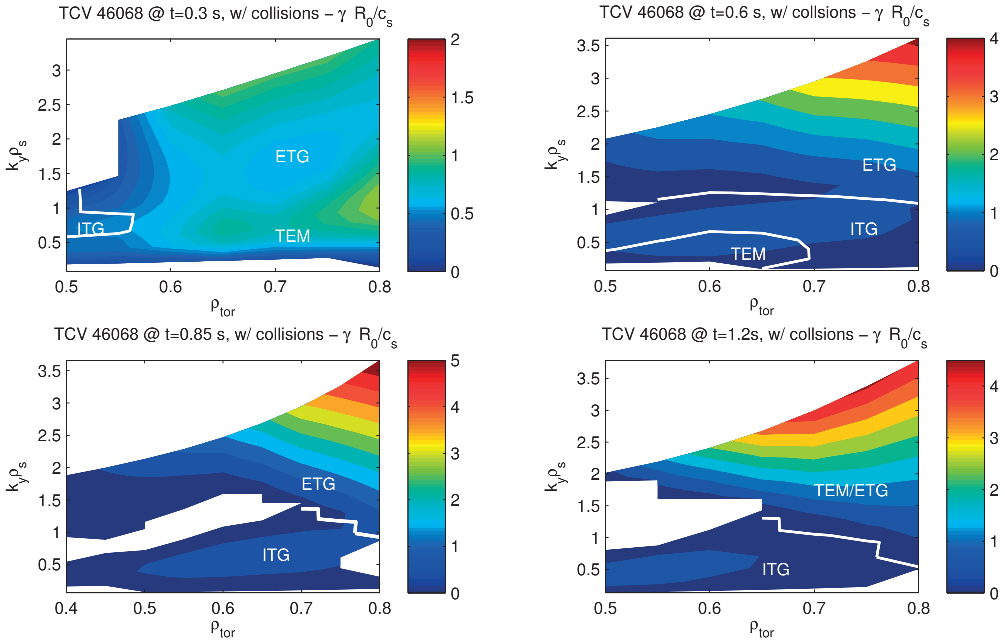

TCV 46068 @ t=0.3 s, w/ collisions – γ R_0/c_s

TCV 46068 @ t=0.6 s, w/ collisions – γ R_0/c_s

TCV 46068 @ t=0.85 s, w/ collisions – γ R_0/c_s

TCV 46068 @ t=1.2s, w/ collisions – γ R_0/c_s

Figure 7.4 : Growth rate γ in units of c_s/R_0 as a function of the radial location ρ_{tor} and the wave number $k_y\rho_s$. Results are normalized with respect to sound speed (and Larmor radius) evaluated at the radial location where non-linear flux-tube simulation have been performed, *i.e.* the same normalizations as adopted in Fig. 7.3. The white line indicates a zero frequency contour, where ITG to TEM transition happens.

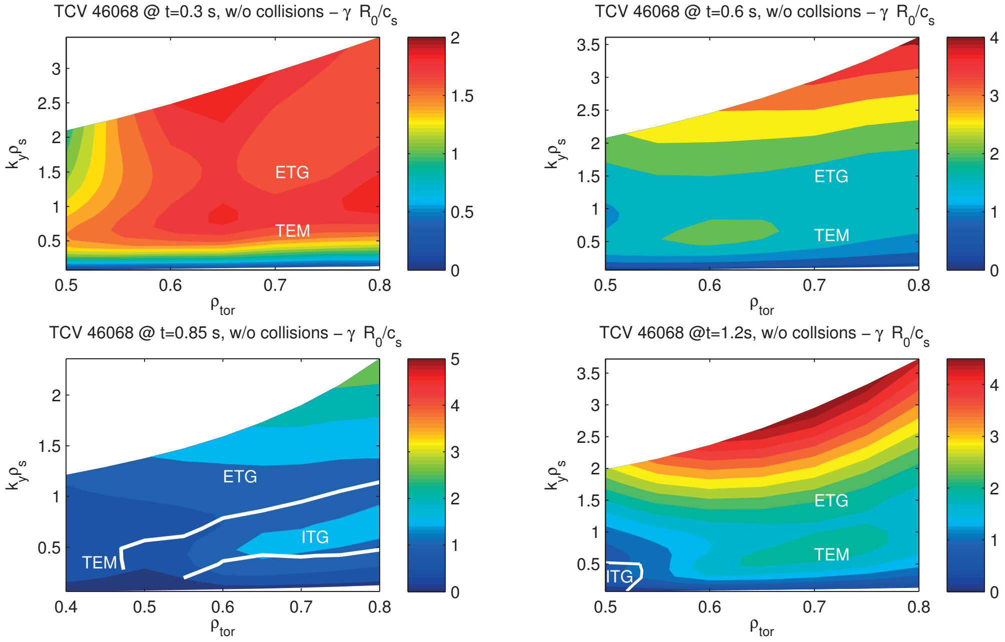

TCV 46068 @ t=0.3 s, w/o collisions – γ R_0/c_s

TCV 46068 @ t=0.6 s, w/o collsions – γ R_0/c_s

TCV 46068 @ t=0.85 s, w/o collisions – γ R_0/c_s

TCV 46068 @t=1.2s, w/o collisions – γ R_0/c_s

Figure 7.5 : Same as Figure 7.4 but showing results obtained neglecting collisions. Note that the same color coding has been used with respect to Fig. 7.4 such as to illustrate the stabilizing effect of collisions, especially on TEMs.

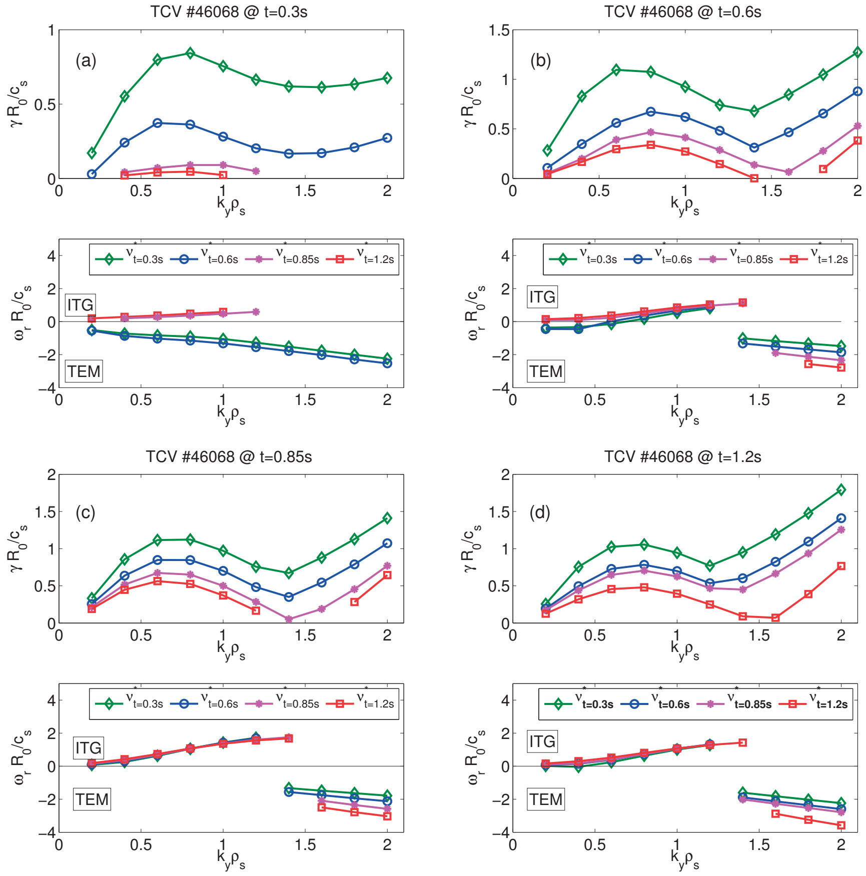

Figure 7.6 : Collisionality scan. Growth rates γ and real frequencies ω_r in units of R_0/c_s of the most unstable mode as a function of the wave number $k_y\rho_s$ and for different values of collisionality ν^*. Magnetic geometry, as well as temperature and density gradients, have been kept fixed and correspond to the experimental values at (a) t=0.3 s, (b) t=0.6 s, (c) t=0.85 s and (d) and t=1.2 s and $\rho_\psi = 0.8$. Only the collisionality ν^* instead has been varied among the experimental values at the four time instants.

in Figure 7.6). In this case the most unstable mode at $k_y\rho_s < 1$ remains a TEM except when considering the two highest values of ν^*, where a transition to ITG is observed. The associated increase of density and reduction of temperature correspond to respectively a five and eight fold increase in the ion to electron collisionality in comparison to the experimental one, therefore beyond the experimental uncertainty on the value of ν_c. For all the other cases an increase of collisionality alone is not sufficient to induce a change in the turbulent regime. Comparing also with Figures 7.4 and 7.5, one can therefore conclude that collisionality induces a significant stabilization of the linear growth rates in all cases, but is not the main cause for regime transitions. In particular, when going from the plasma parameters of t=0.3 s to the ones associated to t=0.6 s, the increase in collisionality is not necessary to induce a transition from TEM to mixed TEM/ITG regime, which is in fact associated to a variation of the different turbulent drives, R/L_T,

R/L_n and T_e/T_i. We nevertheless remark that collisionality is playing a strong stabilizing role on all modes, reducing the growth rates up to $\sim 50\%$, and therefore it is expected to be an essential effect to be retained in nonlinear simulations in order to aim at matching the experimental transport level.

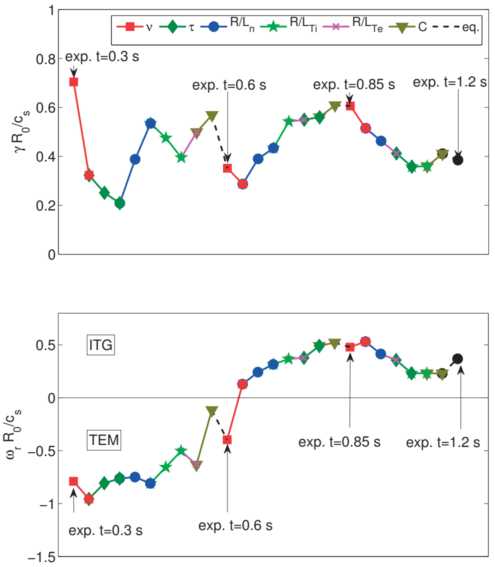

Figure 7.7 : Variation of growth rate γ and real frequency ω_r for fixed $k_y\rho_s = 0.5$ continuously changing all plasma parameters from the experimental values measured at t=0.3 s to the ones of t=1.2 s. The legend indicates the parameter being changed at each step: red squares collisionality ν^*, green diamonds temperature ratio τ, blue circles density gradient R/L_n, green stars ion temperature gradient R/L_{T_i}, magenta crosses electron temperature gradient R/L_{T_e} and gold triangles carbon content. Finally, dashed lines indicate a variation of the magnetic geometry. The actual experimental points are indicated with arrows.

At last, given that all plasma parameters change among the different instants of the discharge, identifying which one is the most relevant is not an obvious exercise. In order to investigate this aspect, we have continuously changed in turn all the plasma parameters between the four different experimental sets, from the first at t=0.3 s to the last one at t=1.2 s. Hence collisionality, density and ion and electron temperature gradients, ion to electron temperature ratio, carbon content and magnetic geometry have been varied following the experimental variations. Naturally there is no privileged order to follow when performing this kind of analysis, and different choices can actually lead to different results (i.e. different paths between two experimental points in Figure 7.7). We have therefore varied the plasma parameters in order of their relative variation, starting from the most important one. Furthermore, the magnetic equilibrium has been changed at once and always after having modified all other quantities. The results obtained for

$k_y\rho_s = 0.5$ mode, *i.e.* the most unstable linearly and non-linearly, are shown in Figure 7.7. Going from the parameters of t=0.3 s to the ones of t=0.6 s, a strong stabilization, by $\simeq 50\%$ is observed as a result of the increased collisionality. Similarly, the growth rate is decreased by another factor of two because of the increased ion temperature. Then, the increase of both density and electron temperature gradient further destabilize the TEM mode while the increase of the ion temperature gradient is reducing the growth rate and strongly increasing the mode frequency towards positive values. The most unstable mode associated to $k_y\rho_s$=0.5 becomes an ITG only when all parameters of t=0.6 s are assumed together with the collisionality of t=0.85 s, which is larger by a factor of two with respect to the experimental one. Then, all changes towards the actual plasma parameters of t=0.85 s further destabilize the ITG. Conversely, moving towards the ones of t=1.2 s all variation contribute to a stabilization of the ITG, with the exception of the increase of carbon content. We remark that these observations are valid only for the particular mode number that we have chosen. Other values of $k_y\rho_s$ might produce different trends.

GAM frequency estimate via Rosenbluth-Hinton test

In order to estimate the frequency of the GAM, the Rosenbluth-Hinton (RH) test has been performed considering the magnetic equilibria associated to the four time instants under investigation. This exercise provides a reference linear frequency to be compared with analytic estimates ans then with nonlinear results.

The RH test is carried out in the adiabatic electron regime, considering the experimental content of carbon. All simulations have been performed evolving in time an initial zonal perturbation associated to the $k_x\rho_s = 0.02$ mode. A numerical grid composed of $n_z \times n_{v_\parallel} \times n_\mu$=$64 \times 512 \times 64$ points covering a domain in velocity space $\hat{L}_{v_\parallel} \times \hat{L}_\mu = 4 \times 16$ has been used. No numerical hyperdiffusion has been used, which is the reason for the increased resolution also in the parallel direction and in velocity space compared with all other linear runs previously discussed. The time traces of the normalized flux-surface-average electrostatic potential are shown in Figure 7.8, together with the obtained values of GAM frequency, damping and residual potential amplitude $\langle\phi(\infty)\rangle/\langle\phi(0)\rangle$.

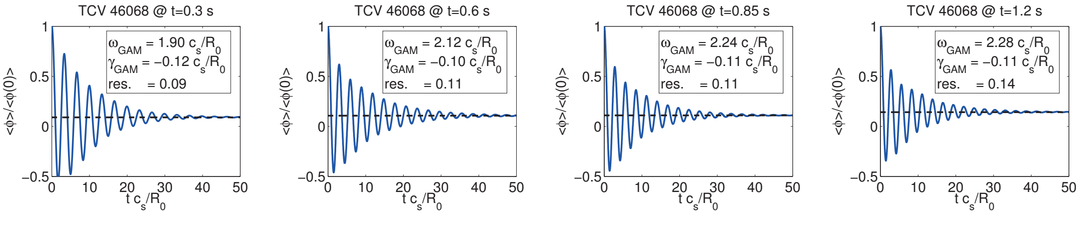

Figure 7.8 : From left to right, results of the Rosenbluth-Hinton test performed to measure the GAM frequency ω_{GAM}. The value obtained for each time is shown for each subplot in units of c_s/R_0 together with the simulated GAM damping γ_{GAM} and the residual potential.

The GAM frequency, in normalized units, appears to increase by $\sim 20\%$ from the lowest density case to the highest one, essentially because of the variation of q. The damping instead remains approximately constant. It is to be noted that all frequencies have been normalized to the actual value of the sound speed, which is changing between the different runs because of the variation of the electron temperature (reduced by $\sim 45\%$ when going from t=0.3 s to t=1.2 s, see Table 7.1). The corresponding values of GAM frequency $f_{\text{GAM}} = \omega/2\pi$ in physical units are reported in Table 7.2, together with the analytic estimates provided in Refs. [56, 57].

	f_{GENE} [kHz]	f_{Sugama}[kHz]	f_{Gao} [kHz]
t=0.3 s	45.37	48.95	40.59
t=0.6 s	45.06	51.93	48.54
t=0.85 s	43.28	49.67	47.99
t=1.2 s	40.83	44.65	42.77

Table 7.2 : Simulated frequency $F_{\text{GAM}} = \omega_{\text{Gao}}/2\pi$ of the GAM expressed in kHz. For comparison the analytic estimates f_{Sugama} and f_{Gao} given respectively in Refs. [56] and [57] are tabulated as well.

Given that the reduction of the sound speed is stronger than the increase of the normalized GAM frequency, the GAM frequency *decreases* with increasing density. We also note that simulation results do agree reasonably well already with the analytic prediction from Sugama *et al.* [56], which is valid for circular plasmas only. The simulated frequency turns out to be always 10-15% lower than theoretical estimate, a difference that is reduced when the effect of elongation is accounted for, as e.g. by Gao *et al.* in Ref. [57].
A the same time, one observes that the residual level increases with increasing density, mainly because of the decrease of the safety factor.

7.1.3 Local nonlinear results

Transport level

Nonlinear simulations have been performed with the aim of reproducing the experimentally measured transport as well as the density and temperature fluctuation level and the GAM physics. All simulations have been carried considering a simulation grid composed of $n_{k_x} \times n_{k_y} \times n_z \times n_{v_\parallel} \times n_\mu = 512 \times 64 \times 32 \times 64 \times 16$ points. While the grids in velocity space have the same extent as the ones used for the linear simulations, $\hat{L}_{v_\parallel} \times \hat{L}_\mu = 4 \times 16$, the perpendicular size of the simulation domain in configuration space varies between the different runs, as detailed in Table 7.3. This reflects a different value of the minimum wave number $k_{y,min}$ retained in each run, which has been adapted such as to have it corresponding to a given toroidal mode number n_{min} according to the relation (4.3). The different value of the electron temperature, and consequently the corresponding Larmor radius, causes $k_{y,min}$ to be different for each run. This choice is not expected to affect simulation results, but simply ease the post-processing of the data.

	$k_{y,min}\rho_s$	n_{min}	$k_{y,max}\rho_s$	L_y/ρ_s	L_x/ρ_s
t=0.3 s	0.060	3	3.80	104	119
t=0.6 s	0.050	3	3.10	126	132
t=0.85 s	0.045	3	2.85	139	114
t=1.2 s	0.059	5	3.71	107	134

Table 7.3 : Input parameters defining the size of the simulation box in configuration space used for nonlinear runs.

All simulations have been carried out with the same physical model as the one used for carrying out linear runs, i.e. fully electromagnetic, collisional runs including carbon impurities. All runs are limited to the ion scale. Therefore, in order to avoid any nonphysical pile-up in the turbulent spectra due to unresolved short scale modes, hyperdiffusion in both x and y directions has been used, setting $\texttt{hyp}_x = \texttt{hyp}_y = 0.2$. A particularly high resolution was used in the radial direction where, because of the kinetic response of the electrons, one is expecting fine radial structures to appear around low order mode rational surfaces. Such structures, as already discussed, if not properly resolved can lead to a significant overestimation of the transport level [106]. We have verified the convergence of our simulations with respect to the number of radial grid points by comparing the results obtained with $n_{k_x} = 256$ to the ones obtained with $n_{k_x} = 512$. No significant difference was observed between the transport level (any variation found was within the error bars associated to time averaging, estimated at 10-15%), justifying our current set-up.

For a given resolution, increasing the collisionality increases the cost of a run because of the smaller time step required for numerical stability. All simulations have been run typically up to t$\sim 150R_0/c_s$ in order to ensure enough time statistics. Given the sensibly higher cost, less statistics (up to $t \sim 90R_0/c_s$) have been acquired for the at highest density case at t=1.2 s. The corresponding time traces of the electrostatic turbulent heat fluxes are shown in Figure 7.9 (the electromagnetic contribution to the heat fluxes is smaller by approximately two orders of magnitude).

One observes, as expected, that the regime transition is reflected by a significant change in the transport level, mainly in the ion channel. Comparing the results relative to the instant t=0.3 s to the ones of 0.6 s, the TEM to ITG transition, one finds a slight reduction ($\sim -10\%$) of the transport in the electron channel but a strong increase, by a factor of six, in the ion one (blue to green curves in Figure 7.9 (a) and (b)). Then, when considering the parameters relative to t=0.85 s (magenta curves, pure ITG regime) both ion and electron fluxes further increase, actually becoming comparable. Finally, for the highest density at t=1.2 s, a strong suppression of turbulence is observed and consequently fluxes reduce as well.

For the sake of completeness, the time traces of the heat flux carried by carbon are shown as well, even though these fluxes are clearly negligible in magnitude in comparison with the ion and electron ones.

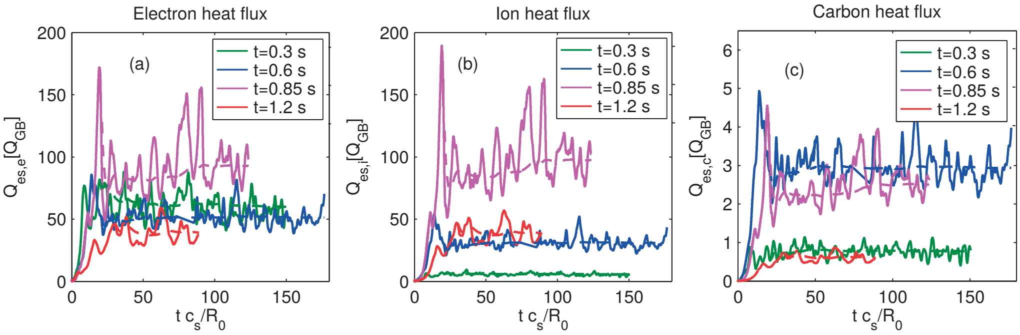

Figure 7.9 : Time traces of the electrostatic heat flux Q_{es} in GyroBhom units as a function of time, obtained from nonlinear simulations corresponding to different time instants in the TCV discharge #46068. All normalizations are with respect to the actual sound speed, different in each simulation due to changes in plasma parameters. Shown are the electrostatic heat fluxes of (a) electrons, (b) main deuterium ions and (c) carbon. Dashed lines indicate running averaged values started at t=20 R_0/c_s.

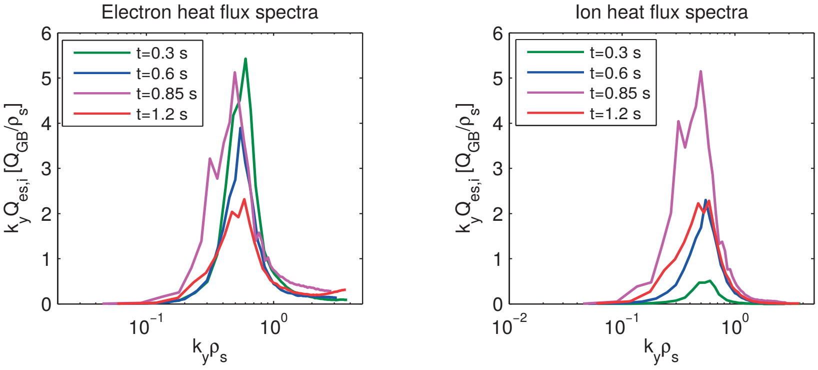

Figure 7.10 : k_y-spectra of the (a) electron and (b) ion heat fluxes. Shown are the time averaged values over the same time window as indicated in Fig. 7.9.

The k_y spectra of electron and ion heat fluxes are depicted in Figure 7.10. Looking at the electron ones, Fig. 7.10 (a), one sees that the flux increase when going from t=0.6 s to t=0.85 s is associated to a larger contribution coming from the low k_y part of the spectra ($k_y \lesssim 0.4$). These are also the modes that are then mostly stabilized when further increasing the density. As for the ion spectra, the variation from t=0.3 s to 0.6 s is accompanied by a uniform increase by approximately the same factor at all k_y. Then, similarly to the electron channel, further changes are essentially due to a strong destabilization of low k_y modes.

In order to compare the simulated transport level with the experimental one, a power balance analysis of the discharge has been carried out so as to identify the electron and ion experimental fluxes. They are estimated according to the following relations:

$$Q_e(\rho_{tor}) = P_{\rm Ohm} + P_{\rm equi} - \frac{\rm dW_e}{\rm dt},$$

$$Q_i(\rho_{tor}) = -P_{\text{equi}} - \frac{\mathrm{dW_i}}{\mathrm{dt}}.$$

Here, Q_e (resp. Q_i) indicate the total electron (resp. ion) power crossing a given flux surface, while P_{Ohm} is the Ohmic power generated within the volume enclosed by the flux surface $\rho = \rho_{tor}$. P_{equi} is the equipartition power and, finally, $\mathrm{dW_{e,i}/dt}$ indicates the variation of electron and ion species energy. Given that the plasma density is increasing in time, $\mathrm{dW_{e,i}/dt}$ is in general not negligible, even though the power balance remains dominated by the Ohmic heating contribution. All the required fluxes are estimated based on experimental measurements. The results obtained are listed in Table 7.4, together with GENE predictions. One observes an astonishingly good agreement between simulations and experimental transport level, somewhat surprising especially in comparison with the results obtained for the triangularity scan presented in the previous chapters. For t=0.3 s and t=0.6 s, the difference is within the error bars, while at t=0.85 s and t=1.2 s, a significant discrepancy is found, with GENE over-predicting both fluxes in the first case and under predicting the total transport in the second one. For the highest density case, bearing in mind also the larger uncertainty of the input parameters, the total transport appears compatible with the GENE predictions, which however shows a different distribution of fluxes between ion and electron channels. When instead considering the parameters of t=0.85 s, the transport level is higher by at least a factor of two for the electrons and by nearly a factor of four for the ions in comparison with that predicted by the experimental power balance estimates. We note that the main difference in the input parameters for this specific simulation in comparison to the other flux-tube runs is a lower density gradient, see Tab 7.1. One can speculate that an increase of R/L_n, as suggested also by the experimental time trend of this parameter, lowers the ion flux by reducing the ITG drive, bringing simulation results even closer to experimental values. Preliminary simulations with a 10% increase of R/L_n show indeed a 30% reduction of the heat fluxes, in both ion and electron channels.

	t=0.3 s			t=0.6 s			t=0.85 s			t=1.2 s		
	Q_e	Q_i	Q_{tot}	Q_e	Q_i	Q_{tot}	Q_e	Q_i	Q_{tot}	Q_e	Q_i	Q_{tot}
Exp. [kW]	223	20	243	135	60	195	156	83	239	40	280	320
GENE [kW]	189	18	196	152	90	240	290	304	594	117	116	233

Table 7.4 : Comparison between the heat fluxes obtained from the experimental power balance and GENE simulations. Q_{tot} indicates the total heat flux, summed over all species.

This set of simulations seems to indicate that flux-tube simulations are in fact suited to reproduce quite closely the transport levels in TCV for these specific conditions, without needing to invoke finite machine size effects and global simulations. We remember however that in all these simulations we have neglected ETG contributions which appear to be strongly unstable and whose contribution should be quantified with at least electron scale simulations, and perhaps multi-scale simulations. Furthermore, the biggest ρ^* value corresponding to the parameters in our simulation is $\rho^* \sim 1/145$, somewhat smaller than the typical TCV core conditions ($\rho^* \sim 1/80$), but still not negligible [116]. Global effects can nonetheless be significant once again, and once more their true relevance can be quantified only with actual global simulations.

$\mathbf{E} \times \mathbf{B}$ velocity and non-linear GAM estimates

In order to characterize the GAM activity in the nonlinear simulations, and also compare simulations with experimental observations, we studied the radial and time dependence of the flux-surface-averaged $\mathbf{E} \times \mathbf{B}$ velocity. In Figure 7.11, the $v_{\mathbf{E}\times\mathbf{B}}$ profiles obtained from nonlinear runs corresponding to the different TCV conditions along the density scan are plotted and analyzed. We limit the analysis of each run to its nonlinear, saturated phase.

We first note that for all the TCV conditions being modeled here, a criss-crossing pattern of both inwards and outwards propagating oscillations of $v_{\mathbf{E}\times\mathbf{B}}$ is observed. One can already speculate the absence of a preferred radial direction of propagation as a consequence of the periodic boundary conditions applied in local runs.

The radial wave vector and the frequency of these oscillations have been identified evaluating respectively the frequency-wavenumber spectrum

$$f(\omega, k) = \left| \int f(x,t) \mathrm{e}^{\mathrm{i}\omega t} \mathrm{e}^{\mathrm{i}k_x x} \mathrm{d}t \mathrm{d}x \right|, \tag{7.2}$$

and the (temporal) power spectral density

$$S(\omega, x) = \left| \int f(x,t) \mathrm{e}^{\mathrm{i}\omega t} \mathrm{d}t \right|^2 . \tag{7.3}$$

While the former quantity has been computed over the entire simulation time trace and over the full radial domain, the latter, which is used to measure any nonlinear frequency ω_{NL} in the simulations, has been evaluated using Welch's estimate. The simulated signal is thus divided into sections of length 10 t_{GAM}, where t_{GAM} is the GAM period estimated from the linear RH results, and to each of them an Hamming window is applied. The Fourier transform is then carried out followed by an average between the results obtained in the different intervals. We prefer this method because even if at first glance one can identify by eye a dominant frequency, the Fourier spectra typically show many harmonics contributing and therefore some averaging, also to compensate the limited statistics, must be made in order to identify any dominant frequency.

The spectrum defined in (7.2) is used to determine the k_x of these GAM oscillations. Once the frequency ω_{NL} is identified, the value of k_x is then taken as the wave vector associated to the maximum Fourier amplitude at $\omega = \omega_{\mathrm{NL}}$.

The specific values obtained for each simulation are reported in the respective plots of Fig. 7.11, where in the last column we also show the space-time autocorrelation function.

This quantity exhibits patterns typical of a standing wave, a feature that is mostly evident in the results obtained for the parameters of t=0.3 s, see Fig. 7.11(a), compared to results relative to later instants. For each run we have evaluated, fitting by hand on these auto-correlation plots, the corresponding group velocity, which is reported in each corresponding Figure.

Regarding the frequency of $\mathbf{E}\times\mathbf{B}$ oscillations, one observes that ω_{NL} is always lower, by at least $\sim 30\%$, than the linear estimates provided by the RH test. At the same time, the dominant k_x mode appears to be little affected by variation of plasma parameters, and remains $\sim \pm 0.3\rho_s^{-1}$ for all the cases considered here. A significant difference is however noted in the dispersion relation. From the simulation results relative to the low density experimental conditions to the ones representative of high density, one clearly observes an increased contribution from low ω - low k_x components. While at t=0.3 s, a single clear peak in both frequency and wave vector can be seen in the Fourier decomposition (which we note is very similar to the one discussed in [124]), this is not anymore the case for the conditions of t=0.85 s, where all modes up to $k_x\rho_s \sim 2$ are strongly excited. For the highest density case (bottom line of Fig. 7.11) it appears that the major contribution is originated from near zero frequency modes. A dispersion relation of the form $\omega = v_g k_x$ provides the best fit of our results. The group velocity v_g is evaluated from the autocorrelation functions, and in agreement with Ref. [125], it increases with the frequency.

We also note that the fine scale radial modulation associated to lowest order mode rational surfaces can be observed in the autocorrelation plots. The amplitude of this modulation is increasing with increasing experimental background density, making it mostly evident in the lower right plot of Fig. 7.11. This radial modulation should not be confused with the one associated to the GAM radial wave vector k_x previously discussed which one observes in e.g. the power spectra plots.

When looking at the time-averaged profiles of e.g. $v_{\mathbf{E}\times\mathbf{B}}$ one observes, as expected, that there is modulation around lowest rational surfaces, which is related to periodic boundary conditions. We recall that for a given k_y mode, the radial modes $2\pi\hat{s}k_x$ are coupled by the parallel boundary condition, in turn defining the radial width of the simulation domain $L_x = n_{\mathrm{exc}}/\hat{s}k_y = n_{\mathrm{exc}}2\pi/k_{x,min}$, with n_{exc} an integer, see also section 3.2. Another modulation, at a somewhat smaller radial wave vector, the GAM k_x, is observed. This is responsible for the structures that one observes at finite frequency in the power spectra plots. To further clarify this point, we plot in Figure 7.12 the $\mathbf{E}\times\mathbf{B}$ velocity and its shearing rate $\omega_{\mathbf{E}\times\mathbf{B}}$, together with their time averaged values. We show the results obtained for the TCV parameters at t=0.3 s, as the GAM pattern is most regular in this case. Lowest order rational surfaces can be identified by the characteristic radial modulation and further pointed out with red dashed lines. As the shearing rate is an higher order radial derivative, these structures are further highlighted when looking at $\omega_{\mathbf{E}\times\mathbf{B}}$ in comparison to $v_{\mathbf{E}\times\mathbf{B}}$.

In figure 7.13 we furthermore analyze the $\mathbf{E}\times\mathbf{B}$ velocity by computing its radial Fourier

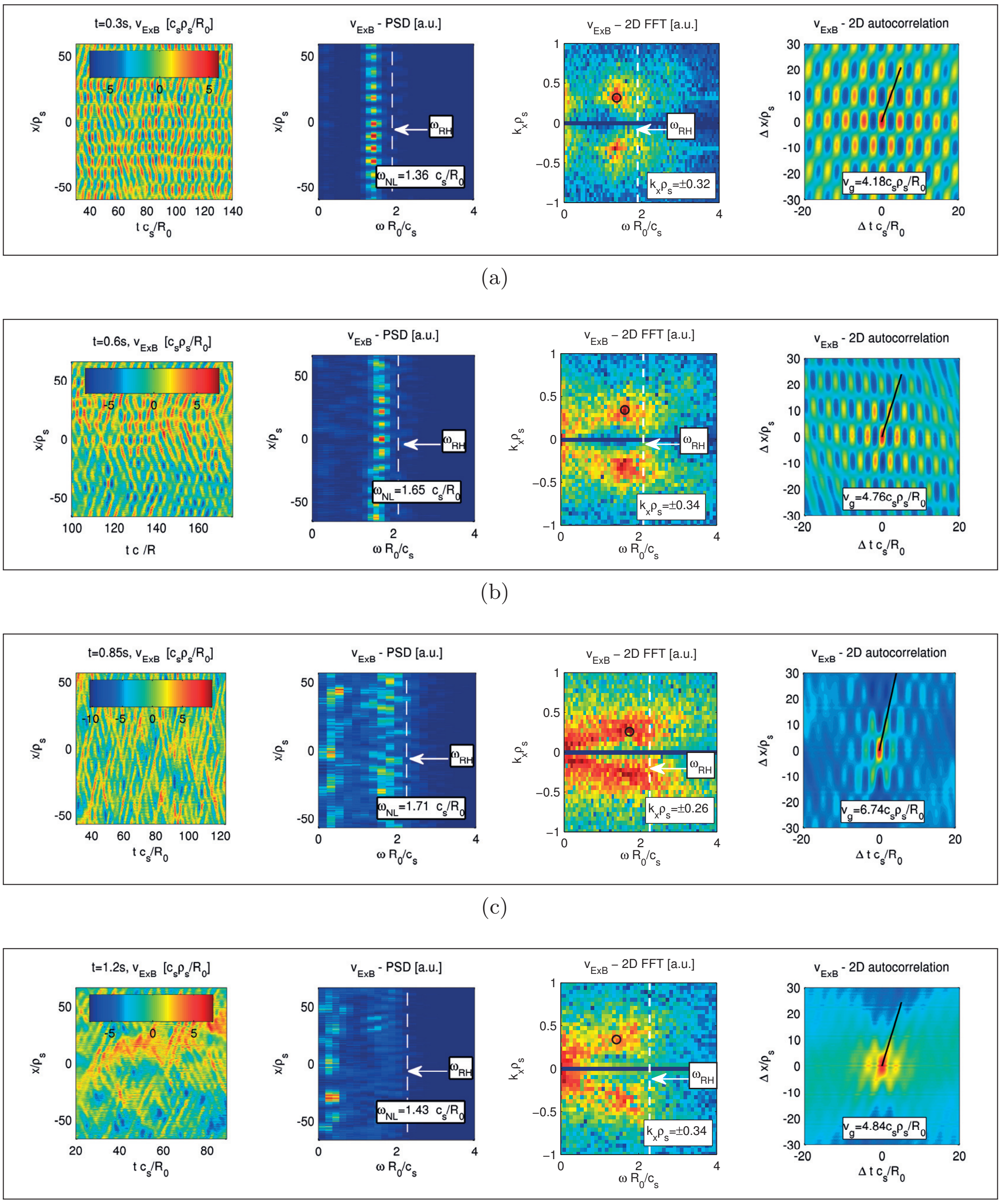

(a)

(b)

(c)

(d)

Figure 7.11 : For each row, from left to right shown are the radial and time evolution of $v_{\mathbf{E}\times\mathbf{B}}$, the corresponding Power Spectral Density (PSD) defined in (7.3), the frequency-wavenumber spectrum (see Eq. (7.2)) and the space-time autocorrelation. The white dashed lines in both PSD and spectra plots indicate the GAM frequency $\omega_{\rm RH}$ estimated via the Rosenbluth-Hinton test, while the black circles in the Fourier spectra identifies the dominant$(\omega_{|rmNL}, k)$ associated to the GAM Simulation parameters are taken from TCV data at (*a*) t=0.3 s, (*b*) t=0.6 s, (*c*) t=0.85 s and (*d*) t=1.2s.

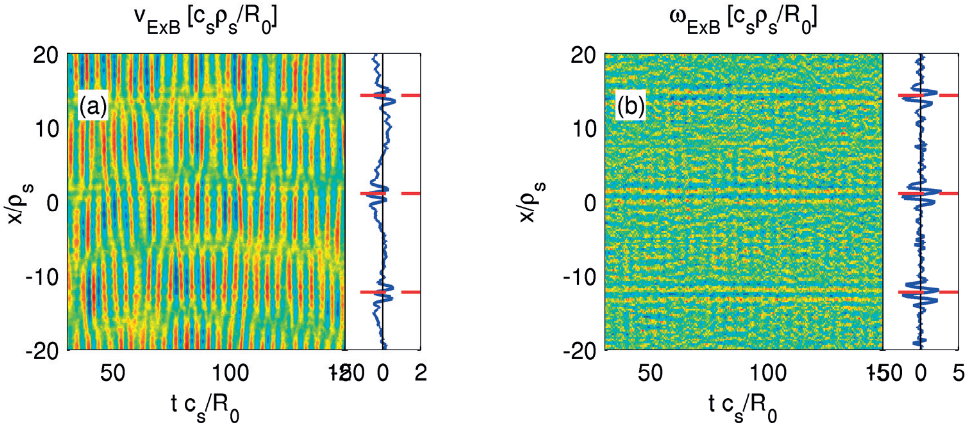

Figure 7.12 : Radial and temporal profiles of (*a*) $\mathbf{E}\times\mathbf{B}$ velocity and (*b*) the corresponding shearing rate $\omega_{\mathbf{E}\times\mathbf{B}}$. Time averaged values are depicted in blue while the location of lowest order mode rational surfaces is indicated with red dashed lines. Simulations obtained using the conditions of t=0.3 s.

decomposition

$$v_{\mathbf{E}\times\mathbf{B}}(x,t)=\sum_{k_x}\hat{v}_{\mathbf{E}\times\mathbf{B}}(k_x,t)\mathrm{e}^{\mathrm{i}k_x x}. \tag{7.4}$$

The top panel shows the time-averaged $v_{\mathbf{E}\times\mathbf{B}}$ as a function of the entire radial flux-tube domain to better show the low k_x modulation, while the lower one depicts in the amplitude of the Fourier radial harmonics $|\hat{v}_{\mathbf{E}\times\mathbf{B}}|$. In blue the results obtained decomposing the time average velocity, while in magenta the GAM oscillation. The latter has been obtained using a narrow band-pass filter centered around ω_{NL}. The multiples of $k_{x,min}=\hat{s}k_{y,min}$ are reported with black lines. One notes that, for both the time-averaged and the GAM component, the maximum amplitude is associated to the GAM radial wave vector, which is smaller than $k_{x,min}$. Harmonics multiple of $k_{x,min}$ are contributing only to the time averaged velocity (with further higher $k_{x,min}$ harmonics not shown here and responsible of the fine scale radial modulation observed in the the top plot of Fig. 7.13). We also note that the maximum contribution to the time averaged $v_{\mathbf{E}\times\mathbf{B}}$ is due to a wave vector larger than the GAM one, as was also visible in the Fourier spectra of Figure 7.11.

The numerically simulated $\mathbf{E}\times\mathbf{B}$ velocity can be compared to experimental PCI measurements looking at the frequency and the intensity of the GAM peak. Some care however must be taken, given that one is not comparing exactly the same quantity and some features in the corresponding spectra can be different. In particular, a mixture of radial and poloidal modes contribute to the PCI spectra [126] while only the $n=0$ is selected in evaluating $v_{\mathbf{E}\times\mathbf{B}}$ in the simulations. The power spectral densities are depicted in Figure 7.14. In both experiments and simulations one observes that the GAM peak becomes less evident when experimentally the density is increased, while its frequency is

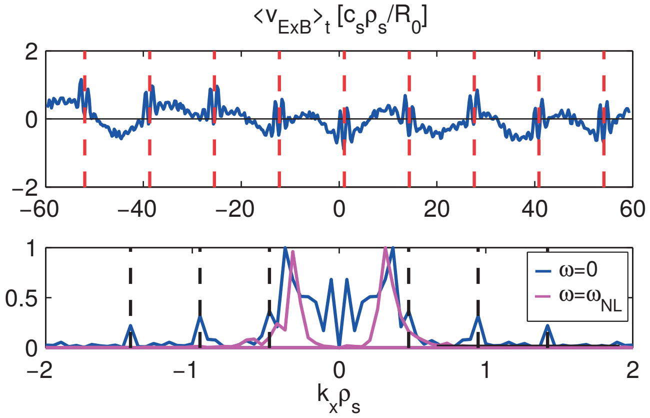

Figure 7.13 : Radial profile of $v_{\mathbf{E}\times\mathbf{B}}$. The top graph shows the velocity time averaged over the nonlinear phase of the simulation. The location of lowest order mode rational surfaces is indicated with red dashed lines (in this case $n_{\rm exc} = 9$ was used, translating into a nine fold repetition of $L_{x,min}$ in defining the flux-tube radial domain extent). The lower plot shows the amplitudes, in arbitrary units, of the radial Fourier harmonics computed according to Eq. 7.4. The blue curve is the time averaged $v_{\mathbf{E}\times\mathbf{B}}$ while the magenta curve refers to the GAM component, obtained with a narrow band-pass filter around $\omega_{\rm NL}$. Vertical black dashed lines point out the multiples of $k_{x,min} = \hat{s}k_{y,min}$.

little affected. However, while in the simulations the peak amplitude seems to diminish, in the experiments it appears that the GAM contribution is covered by the broadband turbulence. A detailed comparison of the dominant frequency $f_{\rm GAM}$ is presented in Fig. 7.15 and discussed later on. Here we simply note that for the highest experimental density no peak is detected measured with the PCI, while in the simulation the intensity is indeed weak but one can still distinguish a corresponding frequency peak in the spectra. Moreover, in the experiment a strong contribution is observed at the $f \sim 70$ kHz (the quasi coherent mode) for the intermediate times (t=0.6 s and t=0.85 s), which is not found in the corresponding simulated $\mathbf{E}\times\mathbf{B}$. We remark also that in the simulations one can identify broader GAM peaks than in the corresponding measurements. This is however related to the choice of evaluating the spectra looking at $v_{\mathbf{E}\times\mathbf{B}}$; repeating the same analysis on the shearing rate $\omega_{\mathbf{E}\times\mathbf{B}} = {\rm d}v_{\mathbf{E}\times\mathbf{B}}/{\rm dx}$ leads to narrower peaks. One can also analyze the flux-surface-averaged electron density fluctuation, as this fluctuation is very close to what experimentally measured with the T-PCI. In this case a similar picture to the one obtained when looking at $v_{\mathbf{E}\times\mathbf{B}}$ is found.

GENE simulated frequencies are compared to experimental measurements in Figure 7.15. The values are also listed in Table 7.5, with the exception of t=1.2 s where experimentally one does not observe any GAM peak in the PCI spectra. In order to account for the experimental errors associated to profiles determination, we add to the numerical prediction an error bar based on the uncertainty of the T_e measurement (due

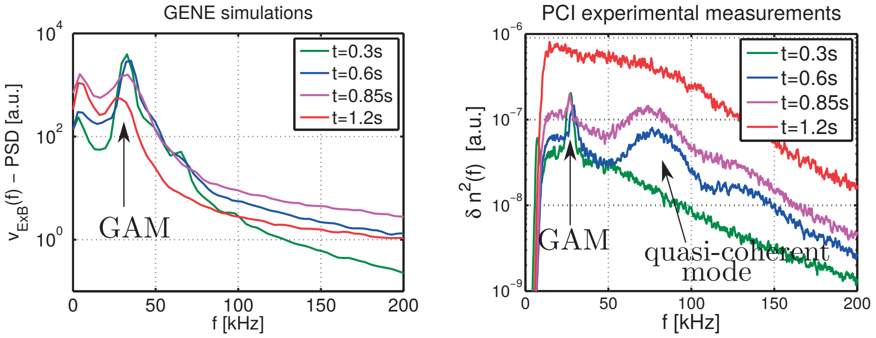

Figure 7.14 : On the left, simulated power spectra densities of $v_{\mathbf{E}\times\mathbf{B}}$ radially averaged over the simulation domain. On the right, the power spectra of the density fluctuations experimentally measured with PCI technique.

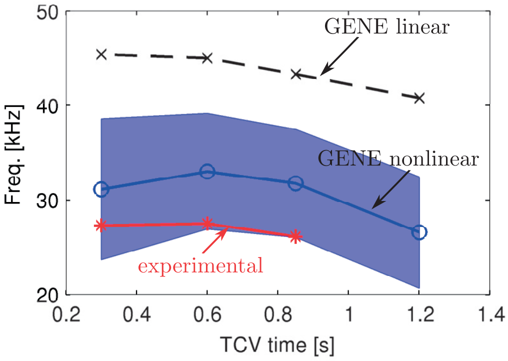

Figure 7.15 : Frequency of $\mathbf{E} \times \mathbf{B}$ oscillations in kHz (blue circles)compared to experimentally measured GAM (red stars). A shaded area has been added to the simulation results in order to account for the error bars of T_e measurement. The estimates obtained from linear RH tests are shown for reference in black. The actual results are also listed in table 7.5.

to the fitting of Thomson scattering data) when converting from GENE normalized quantities to physical units. GENE runs provide a frequency which is always higher than the one experimentally measured, by 15% to 20% ($\sim 5-8$ kHz). This difference lies however within the just mentioned error bars. Naturally, simulations should be repeated accounting for this uncertainty which would affect the results by further increasing the plasma collisionality for lower temperatures, i.e. lower end of error bars, as well as the uncertainty on all other input parameters, as they might sensibly affect the turbulence level. Based on theoretical predictions [61], one can also speculate about a relation between ω_{NL} and the turbulent level. Given that one expects further transport reduction from finite machine size stabilization, this effect may as well further contribute to a better agreement between simulations and measurements. Finally, we remark that these GAM oscillations are in fact characteristic not only of the $\mathbf{E} \times \mathbf{B}$ velocity, but they appear as a common feature of all fluxes and fluctuations. As an illustrative example, we plot in

	0.3 s	0.6 s	0.85 s	1.2 s
ω_{NL} $[c_s/R_0]$	1.36	1.65	1.71	1.43
f_{GENE} [kHz]	31.1	33.0	31.7	26.5
f_{exp} [kHz]	27.3	27.5	27.1	-

Table 7.5 : Simulated GAM frequencies ω_{NL} in units of c_s/R_0, as well as $f_{\mathrm{GENE}} = \omega_{\mathrm{NL}}/2\pi$ in kHz. Experimentally measured values are also listed.

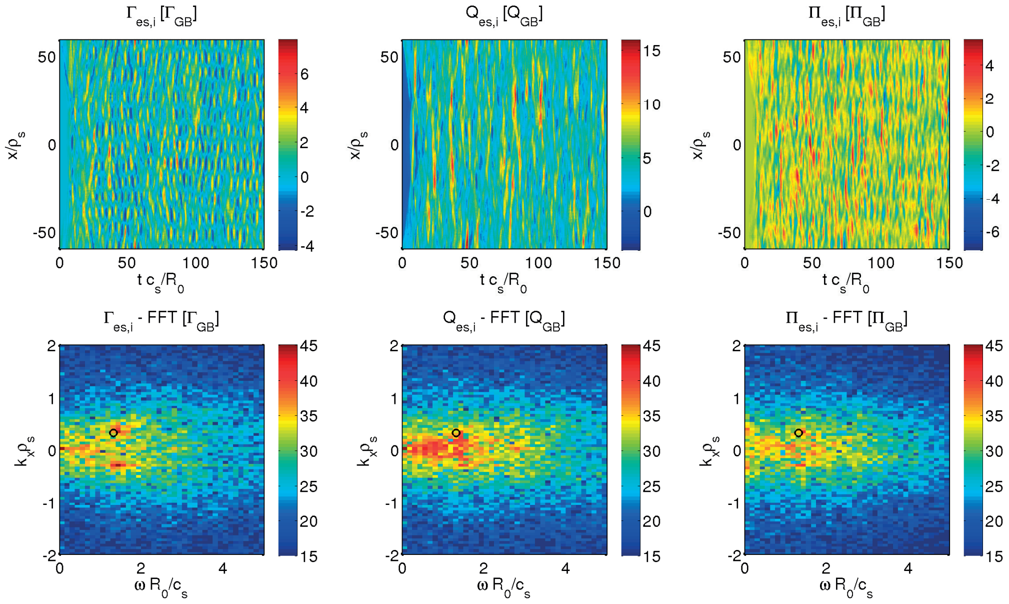

Figure 7.16 : From left to right, ion particle Γ_{es}, heat Q_{es} and momentum Π_{es} fluxes, in Gyro-Bohm units (simulation parameters are relative to t=0.3 s). Top line shows the fluxes as a function of space and time, while in the bottom line are depicted (in log. color scale) the corresponding Fourier amplitudes (estimated over time interval [50-150] c_s/R_0. The black circle indicates the point at $(k_x, \omega_{\mathrm{NL}})$ estimated from $v_{\mathbf{E}\times\mathbf{B}}$ analysis.

the first column of Figure 7.16 the ion particle flux $\Gamma_{es,i}$ together with its power spectral density, evaluated from the simulation relative to t=0.3 s. A crisscrossing pattern is once again observed, with frequency and radial wave vectors very similar to the ones observed in the corresponding $\mathbf{E} \times \mathbf{B}$ flow. Similar avalanche-like structures are found in heat and momentum fluxes as well, also shown for completeness in Figure 7.16. The particle flux is characterized by the most regular pattern. Less regular structures corresponding to broader spectra, with contribution from a larger subset of frequencies and wave vectors, characterizes both $Q_{es,i}$ and $\Pi_{es,i}$.

We have shown the results relative to t=0.3 s because this is the case where, in analogy to the $\mathbf{E} \times \mathbf{B}$ flow behaviour, structures appear mostly regular. Similar observations can nevertheless be made analyzing all the other simulations, which do show equivalent features. Moreover, ions are the species where one can more easily isolate regular patterns, but they are also found in electron and carbon fluxes.

Temperature and density fluctuations

Temperature and density fluctuations, the former separating between the parallel and perpendicular components to the magnetic field, have been analyzed looking at the time evolution of their volume averaged counterpart δA, where A stands for any of the aforementioned quantities, defined as

$$\delta A = \sqrt{\langle |\delta A|^2 \rangle_{\mathrm{V}}}, \tag{7.5}$$

with V indicating the flux-tube volume. Considering first density fluctuation δn, as a result of quasi-neutrality and carbon being present with a minor concentration, the electron and ion fluctuations are very similar, both in amplitude and in the trends observed when changing parameters. Therefore, simulated fluctuations relative to electrons are shown in Figure 7.17. The amplitude first increases with increasing background density, by roughly a factor of two from the simulation relative to t=0.3 s to the one of t=0.85 s. Then a significant drop, by 70% is found at the highest density. The carbon density fluctuation (not shown here) is instead less affected by the variation of the background parameter. With the exception of the results relative to t=0.3 s where $\delta n_c/n_c \sim 3\%$, it remains in all other cases $\sim 6\%$, that is larger by at least a factor of two in comparison to both main plasma species.

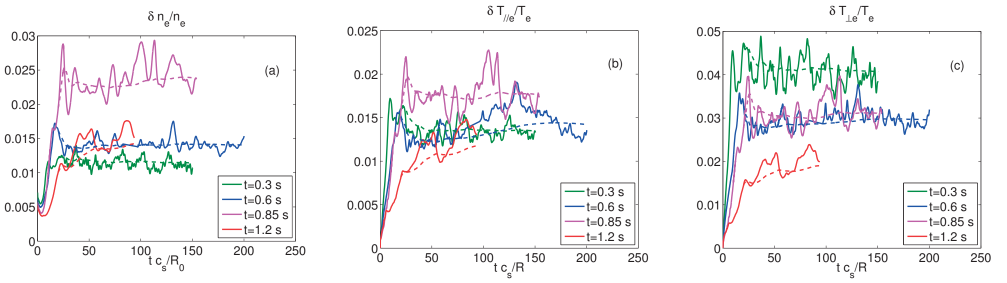

Figure 7.17 : Time traces of the relative fluctuation amplitude of (*a*) electron density $\delta n_e/n_e$, (*b*) electron parallel temperature $\delta T_{\parallel,e}/T_e$ and (*c*) electron perpendicular temperature $\delta T_{\perp,e}/T_e$.

Temperature fluctuations exhibit different trends and amplitudes between the different species. For main ions and carbon, $\delta T_{\parallel}/T$ and $\delta T_{\perp}/T$ are increasing with increasing density and then drop for the parameters of t=1.2 s. The same is observed for $\delta T_{\parallel,e}/T_e$, as shown in Figure 7.17 (*b*). For electrons however, $\delta T_{\perp}/T$ is, with the exception of the results obtained for t=0.85 s, decreasing with increasing density. This is consistent with a transition from a TEM to an ITG regime. Unfortunately, there are no available ECE measurements to compare these observations with experimental data.

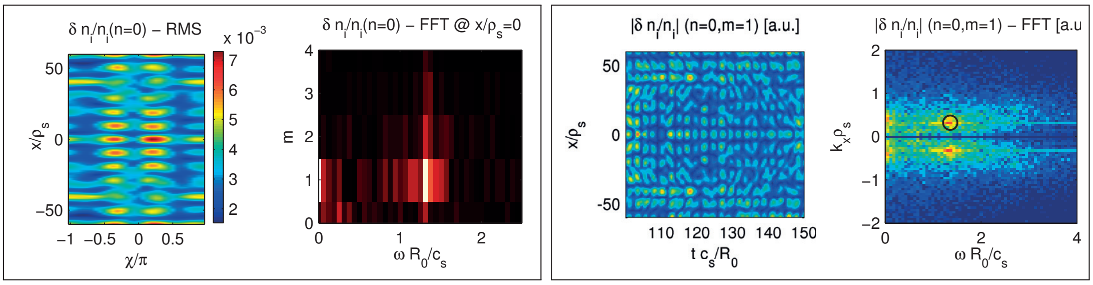

Figure 7.18 : Analysis of the $n = 0$ zonal component of the ion density fluctuation $\delta n_i/n_i$. The left panel shows the RMS value computed over the saturated state of the simulation as a function of the radial position x and the poloidal angle χ, and the amplitude of the time-poloidal Fourier transform (evaluated at x=0). The right panel depicts the time and radial evolution of the poloidal Fourier $m = 1$ component and the corresponding k_x, ω spectra. The black circle in the last plot indicates the dominant $(k_x, \omega_{\rm NL})$ obtained from the analysis of $v_{\mathbf{E}\times\mathbf{B}}$. Results from the simulation relative to t=0.3 s.

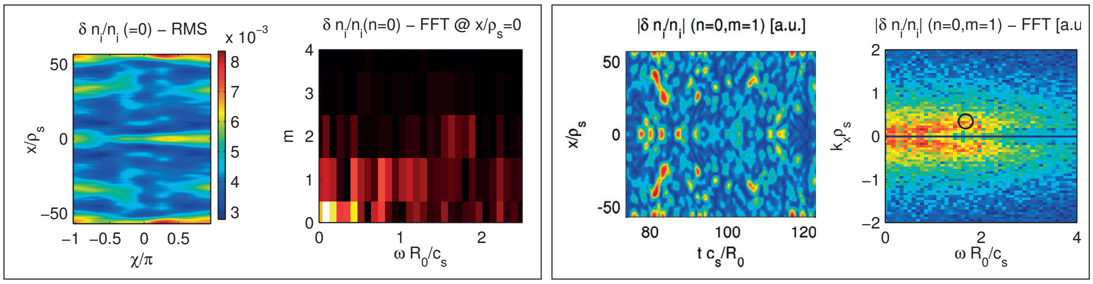

Figure 7.19 : Same as Figure 7.18 but showing the results obtained when simulating TCV conditions at t=0.85 s.

In order to investigate the poloidal structure of the density fluctuation associated to the toroidal mode $n = 0$, we look at the space and time dependence of δn_i. We will show and discuss only the results obtained from the simulation with TCV parameters of t=0.3 s and t=0.85 s. The density fluctuations strongly reflect the patterns observed in the $\mathbf{E} \times \mathbf{B}$ profiles. Therefore, the simulation relative to the first instant is the one where the standing wave character is most evident and, as will be shown, one can clearly identify a dominant $m = 1$ contribution at the frequency $\omega = \omega_{\rm NL}$. Similarly, from the simulation at t=0.85 s one still identifies a dominant component at $m = 1$, but broader in frequency. The run representative of t=0.6 s shows an intermediate behaviour, while too limited statistics have been acquired for correctly analyzing the t=1.2 s case.

The results of the analysis are shown in Figure 7.18 for the run relative to t=0.3 s and in Fig. 7.19 for t=0.85 s. In both cases, we first compute the Root Mean Square (RMS) average of $\delta n_i(k_y = 0)$ over the steady state of the simulation. While in the case relative to t=0.3 s one can already guess a dominant $m = 1$ structure, the simulation relative to t=0.85 s appears to be characterized by a more complex dependency on m. This is further confirmed when looking at the amplitude of the Fourier decomposition in time and poloidal angle χ (the second plot in the first panel of Figs. 7.18 and 7.19). We consider in this case only the position x/ρ_s=0. We remark that this is not a special position and one can carry out the same analysis at other radial locations obtaining similar results. The dominant $n = 0, m = 1$ GAM density component is then plotted as a function of time and radial position, and the amplitude of the corresponding $k_x - \omega$ Fourier modes are shown in the rightmost plots of Figures 7.18 and 7.19. As already anticipated, the dispersion relation of density fluctuations closely resembles the $v_{\mathbf{E}\times\mathbf{B}}$ one, and becomes broader in frequency when the experimental density is increased. This is reflected by the radial profile of δn, which shows a much more complex pattern at t=0.85s compared to the one relative to t=0.3s, which shows strong standing wave like features.

The same analysis can be repeated considering the temperature fluctuation, obtaining similar spatial and temporal dependencies.

7.1.4 Local adiabatic electron results for ITG dominated regimes

Transport level

Given that for the plasmas at t=0.6 s, 0.85 s and 1.2 s linear and nonlinear spectra are dominated by ITG modes, it makes sense to compare the previously obtained results with numerical predictions based on pure ion temperature gradient (adiabatic electrons) simulations. This kind of runs are expected not to be sufficiently accurate for reproducing the transport level measured in TCV, given that they do not capture the dynamics of electrons that can influence the ITG branch both via coupling with the sub-dominant TEM and the smaller scale ETG modes. Nevertheless, the computational requirement of these runs is reduced by a significant factor in comparison to the simulations presented in section 7.1.3, therefore allowing to more easily scan plasma parameters and investigate any trend or dependence of ω_{NL}.

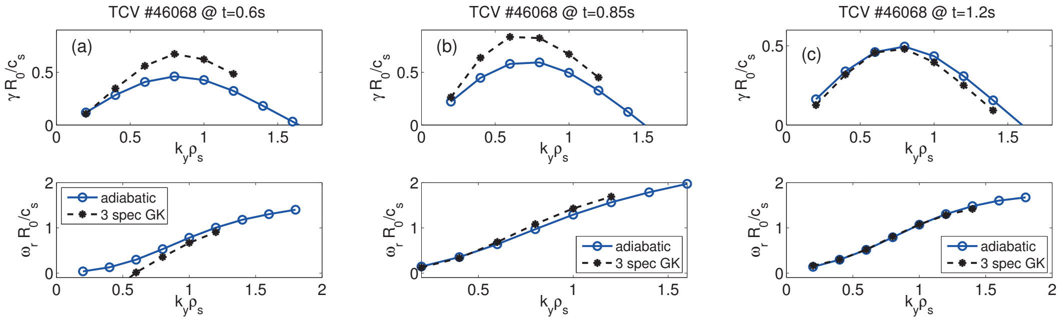

Figure 7.20 : Adiabatic electron runs (blue curves). Growth rate and frequency of the most unstable mode for a k_y scan. Plasma parameters assumed from (*a*) t=0.6 s, (*b*) t=0.85 s and (*c*) t=1.2 s. For comparison the results with fully gyrokinetic ions and electrons are reported as well with black dashed lines.

Linear k_y-spectra are shown in Figure 7.20, where they are compared with the ITG branch obtained from simulations performed with three gyrokinetic species. Assuming adiabatic electrons leads to a $\sim 20\%$ reduction of the growth rates for all cases with the exception of t=1.2 s, where the adiabatic electrons results are essentially the same as the fully gyrokinetic ones. Similarly to the results discussed in the previous paragraphs, the parameters at t=0.85 s are the ones that lead to the highest growth rates.

Nonlinear simulations have been performed considering the same value of $k_{y,min}$ as reported in Table 7.3 and adopting grids composed by $n_{k_x} \times n_{k_y} \times n_z \times n_{v_\parallel} \times n_\mu = 256 \times 32 \times 32 \times 48 \times 8$ points. Given that carbon was found to weakly affect the linear growth rates, it has been neglected, further reducing the cost of the runs. For the sake of completeness, a nonlinear simulation has also been carried out for the parameters of t=0.3 s, even though experimentally this is a TEM dominated case. The time traces of the ion heat flux and the corresponding spectra are shown in Figure 7.21. When varying the plasma parameters reproducing the different TCV conditions, one observes trends very similar to ones obtained when carrying out runs with fully gyrokinetic electrons and carbon: the heat flux first increases (from the parameters of t=0.3 s to 0.85 s) and then decreases (from 0.85 s to 1.2 s). Again this difference is mainly due to a different contribution from the low k_y modes. In all cases adiabatic electron runs provide a lower ion heat flux, by approximately a factor of two, than the one obtained when carrying out simulations with fully gyrokinetic electrons.

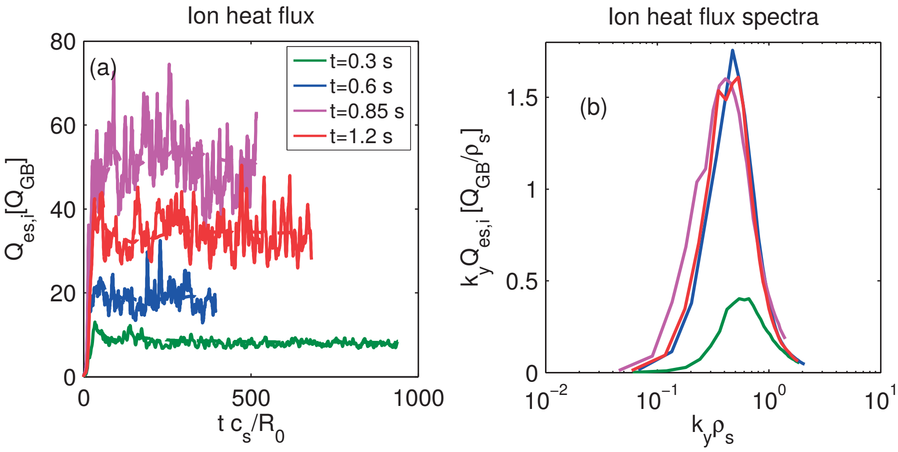

Figure 7.21 : Adiabatic electron simulations results: (*a*) time traces of the ion heat flux and (*b*) corresponding ky spectra. Shown are the results for t=0.3 s (green), t=0.6 s (blue), 0.85 s (magenta) and t=1.2 s (red).

$\mathbf{E} \times \mathbf{B}$ velocity

The very same analysis of the $\mathbf{E} \times \mathbf{B}$ velocity has been repeated for this new set of runs. Compared to the kinetic electrons results, we observe in all simulations a different behavior in the initial (linear) phase of the simulations. Non-propagating oscillations with a damped amplitude develop from the initial perturbation. Then, when the system enters in the nonlinear quasi-stationary saturated regime, the typical crisscrossing pattern of inward and outward propagating perturbations is recovered. The oscillations of the linear phase of the simulations are characterized by a frequency and a damping which, within less than 5%, are the same as the ones estimated by the linear RH test, a difference that can be explained by the reduced statistics available from the linear phase of nonlinear simulations. Then, in the saturated state the frequency of $\mathbf{E}\times\mathbf{B}$ oscillations diminishes, by approximately $\sim 35\%$. The detailed analysis of both the linear and nonlinear phases of all runs is reported in Figs. 7.22 and 7.23. Once again very regular patterns are recovered, with a frequency ω_{NL} and a group velocity v_g that increase when the parameters are varied from t=0.3 to 1.2 s. In order to further illustrate the frequency downshift between the linear and nonlinear phases of the simulation, we have computed a wavelet decomposition (using Morlet continuous wavelet transform [127]) of the $\mathbf{E}\times\mathbf{B}$ flow profiles obtained for the simulation at t=0.6 s and 0.85 s. The x-averaged results are shown in Figure 7.24.

The frequency of the $\mathbf{E}\times\mathbf{B}$ oscillations are summarized in Fig. 7.25, where the results of linear RH tests, as well as nonlinear adiabatic and fully kinetic runs are compared. One observes an astonishing regular downshift, by approximately $\sim 40\%$ between linear and nonlinear adiabatic runs, for all plasma parameters considered. Fully kinetic electron runs provide a sightly higher frequency, which also seems to follow the trend predicted by the linear simulations even though the downshift factor is in this case somewhat more dependent on the simulation parameters. The fully kinetic simulation relative to t=1.2 s appears as an exception, as the frequency measured in the nonlinear runs is the same regardless from the simulation model. The limited statistics acquired doesn't allow to clearly exclude this as being a coincidence.

Nevertheless, we note that the difference between kinetic and adiabatic simulations results appears to be related to the linear growth rates: kinetic runs are always more unstable(and thus provide a higher frequency) than adiabatic, with the exception of t=1.2 s, see Fig. 7.20.

Based on the previously discussed flux-tube results, few questions remain open and need further investigation to be clarified. First, the regular oscillations that are found in the $\mathbf{E}\times\mathbf{B}$ velocity profiles are observed also in the heat and particle flux profiles. GAM oscillations at a frequency ω_{NL} are associated to the $n=0$ mode and consequently do not contribute to radial fluxes. The structures observed in the flux profiles are instead interpreted as large-scale bursts or avalanches (see e.g. Ref. [121]). There therefore seems to be a coupling between the GAM and these avalanche events, and simulation results can be interpreted as transport bursts possessing GAM-like features.

A second question is associated to the frequency of these avalanche-like events. The observed trends seem to indicate a dependence on the turbulence level, with a downshift of ω_{NL} in comparison to the linear GAM frequency, observed in both fully kinetic and adiabatic runs, which is reduced at increasing turbulence (both in term of flux and

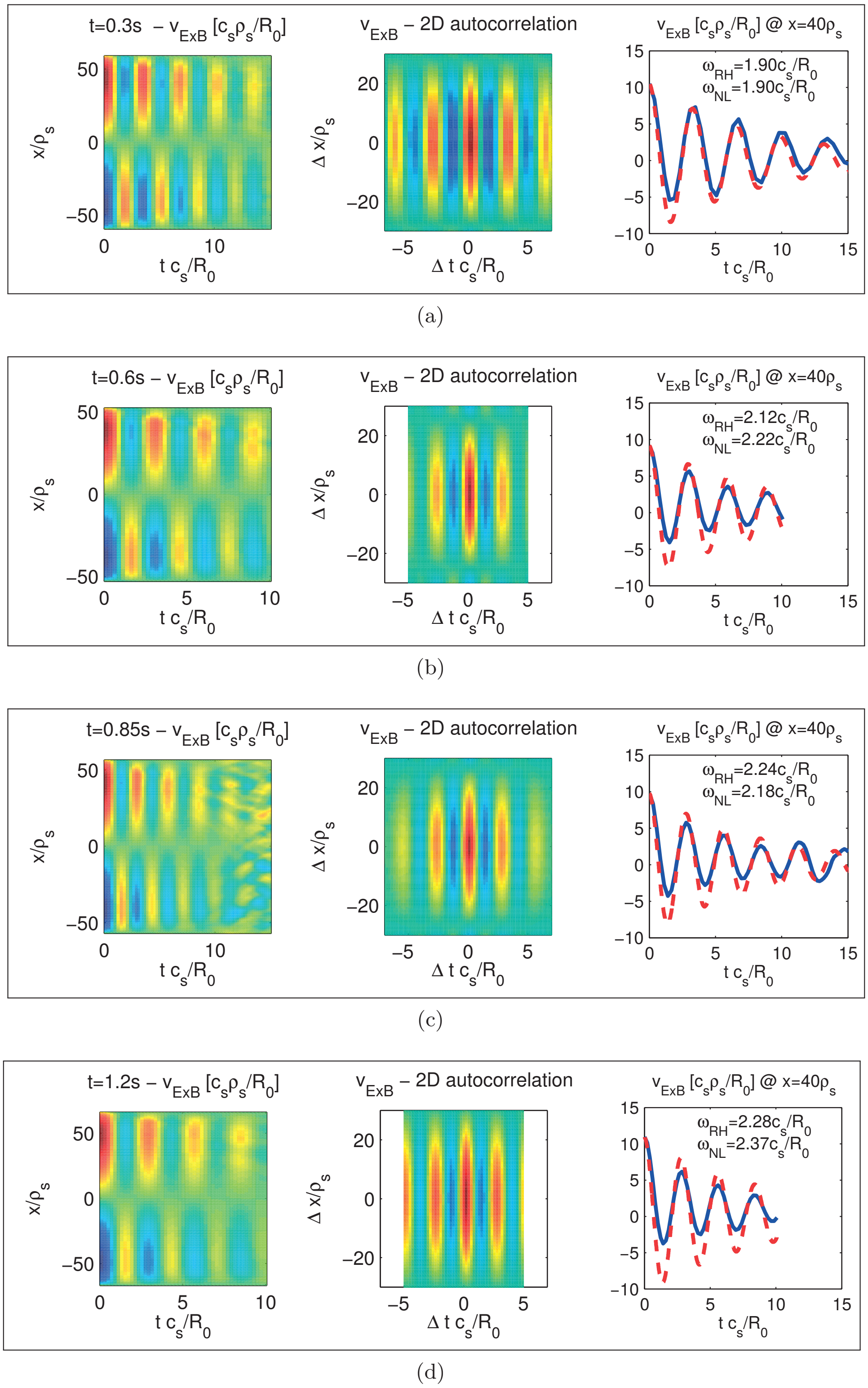

Figure 7.22 : From left to right, shown are the $x-t$ evolution of $v_{\mathbf{E}\times\mathbf{B}}$ over the linear phase of each run, its 2D autocorrelation and the time trace at $x=40\rho_s$. The red dashed lines in the rightmost plots indicate a damped oscillation of the form $\cos(\omega_{\mathrm{RH}}t)\exp(-\gamma_{\mathrm{RH}}t)$ where ω_{RH} and γ_{RH} are the values obtained from RH test. Simulation parameters are assumed from TCV data at (*a*) t=0.3 s, (*b*) t=0.6 s, (*c*) t=0.85 s and (*d*) t=1.2s.

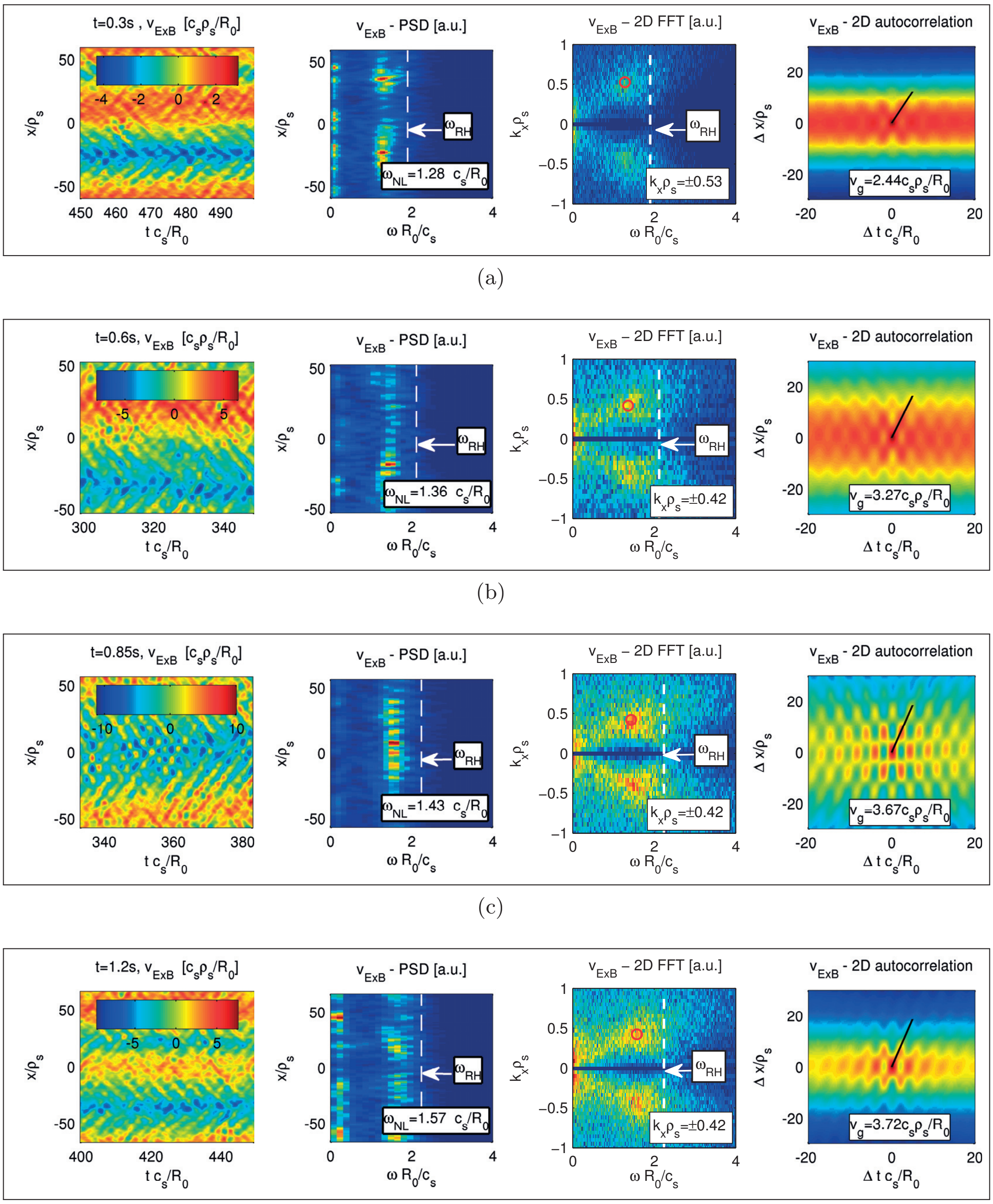

(a)

(b)

(c)

(d)

Figure 7.23 : Same as Fig. 7.11 but showing the results obtained with adiabatic electrons simulations.

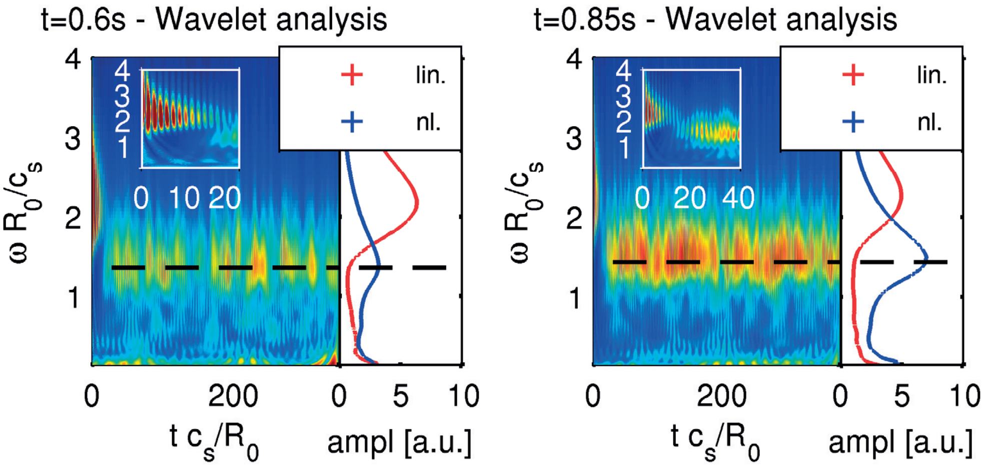

Figure 7.24 : Wavelet decomposition (using Morlet continuous wavelet transform) of the $\mathbf{E} \times \mathbf{B}$ velocity profiles. From left to right, results relative to t=0.6 s and t=0.85 s. For each simulation the x-averaged amplitude is shown as a function of frequency and time, with a zoom on the initial (linear) phase. Time averaged values are shown in red (resp. blue) for the linear (resp. nonlinear) phase. The nonlinear frequency ω_{NL} is indicated with a dashed black line.

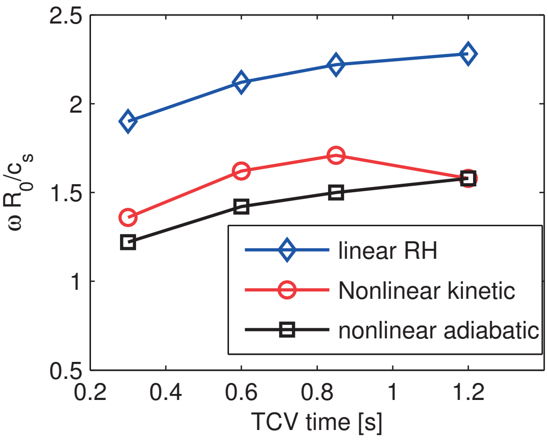

Figure 7.25 : Comparison between frequency of the $\mathbf{E} \times \mathbf{B}$ obtained from GENE simulations. Shown are in blue the predicted values based on linear Rosenbluth-Hinton test, in red the ones obtained in the nonlinear phase of simulations with fully kinetic electrons and in black with adiabatic electron model.

fluctuation levels). However, what sets the magnitude of the observed downshift, or, in other words, what is the minimum frequency that one can observe, remains unclear. Similarly, whether, provided a sufficiently strong turbulence, it is possible to recover oscillations at the linear or at even higher values of ω.

Finally, neither any preferred direction of propagation nor any finite radial extent of the GAM can be addressed within the local limit, as radially periodic boundary conditions are applied. The existence of a preferred direction of propagation even in flux-tube simulations is suggested in Ref. [128], provided that the flux-surface of interest is up-down asymmetric. In our case the plasma is slightly tilted, see Fig. 7.1, nevertheless the effective asymmetry at the radial location considered is weak and not sufficient to introduce a preferential direction of propagation.

This last points can be addressed with global simulations, which will be discussed in the following.

7.2 Global simulations of TCV discharge #45353 with a radially coherent GAM

7.2.1 Motivation

TCV discharge #45353 is a limited plasma where the GAM was observed as a global mode at constant frequency throughout a significant fraction of the minor radius (see Fig. 7.26). For a detailed description of the experimental set-up we refer to Refs. [55]

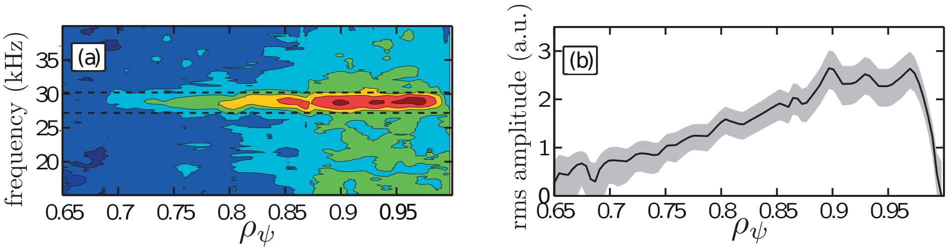

Figure 7.26 : Experimental characterization of the GAM in TCV discharge #45353. Shown are (a) the auto power spectrum of the electron density fluctuation measured with the Phase Contrast Imaging and (b) the RMS amplitude. Adapted from Ref. [62].

and [62]. A first attempt of modeling this discharge with gyrokinetic simulations was already carried out using ORB5 in Ref. [38], where a relatively good agreement between the frequency and spatial localization of the mode was recovered. Reproducing the same discharge with the GENE code therefore appears as a very valuable exercise, not only to investigate the GAM properties in TCV relevant conditions, but also to compare with the results obtained with ORB5.

The original ORB5 simulation considered the experimental magnetic geometry and the measured electron density and temperature profiles. No ion temperature measurements are available for this plasma, therefore a fixed ratio $T_e/T_i = 3.75$ was assumed at all radial locations. Similarly, impurities were neglected as there is no measurement allowing to determine their concentration. This simulation set-up was also kept for performing the GENE runs. The simulation in Ref. [38] was carried out assuming a hybrid model for describing electron dynamics and neglecting collisions. These approximations will be relaxed and their effect investigated by comparing hybrid results with a fully gyrokinetic description.[1] We will also show that collisionality plays an important role on the transport level, and appears also to affect GAM dynamics. In particular, even if the dominant radially global nature of the mode and its frequency appear not to be modified by including collisions, other continuum-like frequencies, i.e. following the linear local GAM dispersion relation, appear to get more excited when collisions are included. Finally, we remark that the original ORB5 run was carried out with artificially heavy electrons, $m_i/m_e = 200$. Here, unless differently specified, we will use the true mass ratio $m_i/m_e = 3670$. All the simulations presented are gradient-driven.

The magnetic geometry and the plasma radial profiles are depicted in Figures 7.27 and 7.28, where the radial extent of the annulus $0.25 < \rho_{vol} < 0.85$ considered for carrying out GENE simulations is indicated with vertical black lines. Going furthermore inside towards the magnetic axis is not of interest as the GAM is measured only in the outer part of the plasma. Conversely, extending the domain of the simulation towards the LCFS is naturally of high interest because the GAM amplitude is experimentally observed to be stronger at the plasma edge (see Fig. 7.26). Nonetheless, in order to limit the computational cost of the run, at least initially, we limit the outer boundary of the simulation domain to $\rho_{vol} = 0.85$. This last choice will be relaxed in section 7.2.5, where GENE and ORB5 results are finally compared.

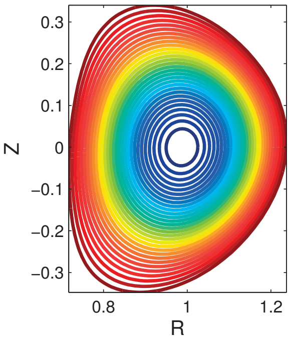

Figure 7.27 : Constant contours of the poloidal magnetic flux function ψ/ψ(LCFS) for the TCV discharge #45353.

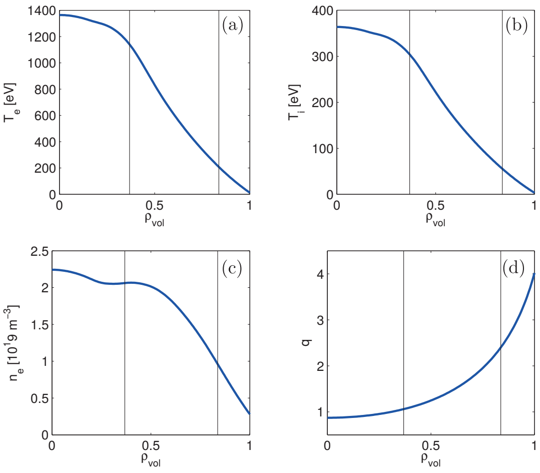

Figure 7.28 : Radial profiles, as a function of ρ_{vol}, of (a) electron temperature T_e, (b) ion temperature T_i, (c) electron density n_e and (d) safety factor q. Vertical lines indicate the extension of the radial annulus considered for non-linear global simulations.

The nature of the underlying micro-instabilities has first been investigated with global linear simulations, carried out with both hybrid and fully kinetic electron models. The results are shown in Figure 7.29, where growth rates and frequencies are plotted against wave numbers $k_y\rho_s$. Both models agree on a mixed ITG-TEM regime, with TEM modes being the most unstable at $k_y\rho_s < 2$, while ITGs are found dominant at medium wave numbers ($2 < k_y\rho_s < 3$). At even higher k_y, a different behaviour is observed between hybrid and fully kinetic electrons results. Using hybrid electrons one finds a contribution from ITG modes up to at least $k_y\rho_s \sim 4.5$, while a fully kinetic description shows that ITG modes are rapidly overcome by ETGs. These latter modes have not been resolved since they require a particularly high radial resolution. Furthermore, they are not retained in nonlinear simulations, which will be limited to the ion scales. For the sake of completeness, we have carried out a scan at all scales with the local version of GENE employing a fully kinetic description. The results are shown in the plot on the right of Figure 7.29, where in agreement with the global code results, a transition to ETG is observed at short wavelength.

---

[1] For simplicity, in the following we will refer to the results obtained with the full gyrokinetic response of electrons simply as fully kinetic.

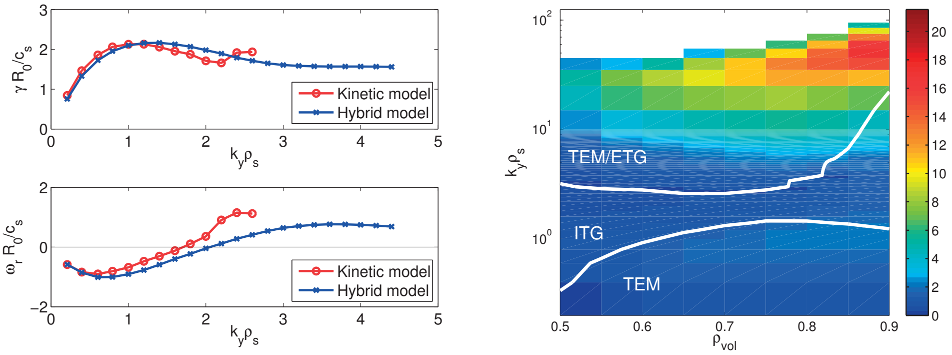

Figure 7.29 : Growth rates γ and real frequencies ω_r (in units of c_s/R_0) as a function of $k_y\rho_s$. Shown on the left are results obtained with global simulations using for the electron dynamics a fully gyrokinetic (red) and a hybrid electron model (blue). On the right, the growth rates obtained with the local version of GENE varying the position of the flux tube. In this latter case c_s is evaluated at ρ_{vol}=0.65, in order to have the same normalization as the the global code results. Furthermore, white lines indicate the transition from positive (ITG modes) to negative frequency (TEM/ETG modes).

7.2.2 Nonlinear simulations

As already mentioned, nonlinear simulations have been performed considering both a hybrid and a fully kinetic model in order to describe electron dynamics.

The two models require different radial resolutions to converge the heat transport. In both cases we have carried out a "*low resolution*" and a "*high resolution*" run, the former considering 128 radial grid points and the latter 416, for a simulation domain $L_x = 65\rho_s$. While for the hybrid model one can use the lower resolution, providing reasonably converged fluxes, for a fully kinetic description the "*high resolution*" set-up is necessary. Incidentally, we note that the maximum time step is not significantly affected by the choice of the electron model. The hybrid one is therefore cheaper essentially thanks to the possibility of using a lower radial resolution (thus a lower number of total grids points), reducing the actual CPU time per time step required by the computation.

All simulations have been performed considering a half torus in the toroidal direction. We have verified that the results are not significantly modified if the full toroidal domain is considered. Fluxes are reduced by ~ 10%, which is within the error bars of time-averaged values. Therefore, 64 k_y modes have been used to represent the binormal direction, ranging between $k_y\rho_{s,min}$=0.049 and $k_y\rho_{s,max} = 3.1$. The parallel direction z has been discretized with 48 grid points, while the velocity space with $n_{v_\parallel} \times n_\mu = 96 \times 48$ points (for grids covering $0 < \hat{L}_{v_\parallel} < 18$ and $-4.2 < \hat{L}_\mu < 4.2$). A reduced value of magnetic pressure, corresponding to $\beta = 10^{-4}$, has been used for the fully kinetic run, to avoid any destabilization of kinetic ballooning modes. All reference quantities used for normalizations are taken at $\rho_{vol} = 0.65$.

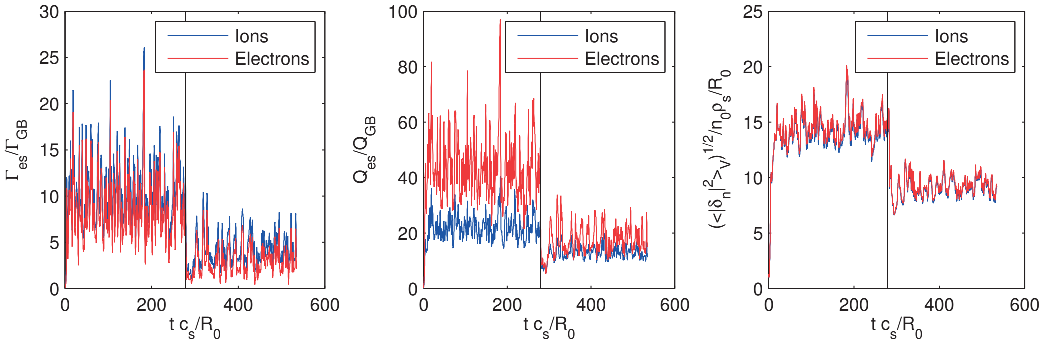

Figure 7.30 : From left to right: Shown are the time traces of heat flux Q, particle flux Γ and density fluctuations δn for both ions and electrons. Results obtained with "*high resolution*" hybrid electrons simulations. The vertical black line at t $\sim 280 R_0/c_s$ indicates the moment where collisions are switched on.

Considering both the hybrid and the fully kinetic model, collisions play a major role in stabilizing the turbulence, and therefore must be retained in the simulations. If neglected, fluxes, as well as fluctuations, are unrealistically too high. As an illustrative example, in Figure 7.30 we plot the time traces of the heat and particle fluxes and of the density fluctuations obtained from the "*high resolution*" hybrid simulation. All the aforementioned quantities are averaged over the entire simulation volume. Collisions have been turned on at $t \sim 280\ R_0/c_s$ (indicated with a vertical line in the corresponding plots). One observes a very strong effect on all turbulent quantities: a reduction by a factor of four is found for the electron heat flux and by approximately a factor of two for the ion one. Furthermore, the ion and electron heat fluxes become comparable when collisionality is retained, hinting towards a strong stabilization of TEMs modes. Similarly, all fluctuations are strongly reduced when collisions are switched on. Equivalent results can be obtained when looking at the fully kinetic simulations, and regardless of the radial resolution adopted. We note that ion and electron particles are identical as a result of the quasi-neutrality and that impurities are not considered.

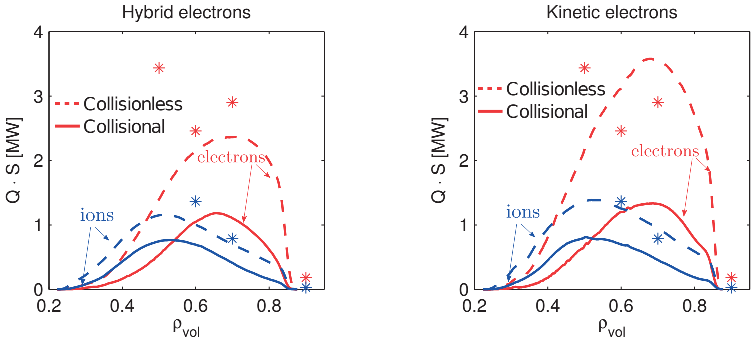

Figure 7.31 : Heat power in MW crossing a given flux surface. Results obtained with global gradient driven simulations, considering (left) hybrid and (right) kinetic electrons. Dashed lines from runs without collisions, while full lines show predictions based on collisional simulations. Ion fluxes are indicated in blue while electron ones ion red. Stars indicate collisional local results, carried out with kinetic electron model, obtained centering the flux-tube at ρ_{vol}=0.5, 0.6, 0.7 and 0.9 (the ion heat flux obtained with local simulations at $\rho_{vol} = 0.5$ is not shown as it falls outside the vertical axis). The color coding is the same for local and global results.

We remark that even when retaining finite collisionality, the simulated heat transport, and in particular the ion heat flux, is sensibly higher compared to the experimental one. The total heat power crossing a flux-surface is shown for both ions and electrons in Figure 7.31. Even without carrying out a detailed power balance analysis, we are considering an Ohmic discharge, whose total power leaving the LCFS is $\sim$ 500 kW. Simulations predict a total heat flux (ion and electron contributions) which is larger by at least a factor of three at all radial locations, with an increasing difference approaching the LCFS. This discrepancy can at least be partially attributed to having assumed a radially constant temperature ratio between ions and electrons. This choice causes, especially in the core, a very large ion temperature gradient for a moderate density gradient (e.g., $R/L_{T_i} \sim 7$ and $R/L_n \sim 1.5$ for $\rho_{vol} = 0.5$) that strongly destabilizes ITG modes, leading to unrealistic fluxes. This picture is confirmed by a series of flux-tube simulations carried out at different radial locations (see Appendix D for more details) that predict an nonphysically large heat flux in the core ($Q_i \sim 4.4$ MW and $Q_e \sim 3.4$ MW for electrons) while seem to approach realistic values only towards the plasma edge. Furthermore, one has neglected carbon in all these runs, which usually has a strongly stabilizing effect for TEM modes, thus lowering the electron heat flux.

7.2.3 GAM frequency characterization

In Figure 7.32 we plot the space-time evolution of the $\mathbf{E}\times\mathbf{B}$ shearing rate $\omega_{\mathbf{E}\times\mathbf{B}} = dv_{\mathbf{E}\times\mathbf{B}}/dx$. Being a higher order radial derivative compared to $v_{\mathbf{E}\times\mathbf{B}}$, it further highlights the short scale radial modulation around low order rational surfaces that in particular distinguish fully kinetic and hybrid simulations.

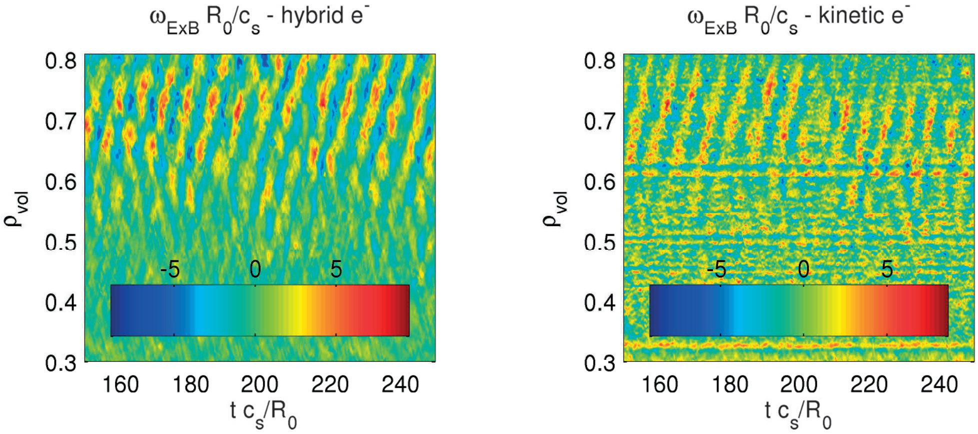

Figure 7.32 : Shearing rate $\omega_{\mathbf{E}\times\mathbf{B}}$ in units of c_s/R_0 obtained from collisionless simulations and adopting a hybrid (left) and a fully kinetic (right) model for describing electron dynamics. The same color coding has been used for the two figures. Radial buffer regions have already been excluded from the plots.

One observes that the two simulation models provide a similar picture of mainly outwards propagating avalanche-like structures over the outer part of the simulation domain ($0.6 \lesssim \rho_{vol} \lesssim 0.8$). A clear difference however appears between the two simulations in the form of a much stronger radial fragmentation in case of the fully kinetic electron simulation compared to the hybrid one. This difference is due to the fully kinetic response of passing electrons around low order mode rational surfaces. A fine scale modulation of the temperature and density profiles develops around these surfaces when kinetic electrons are retained. This in turns influences the flux-surface averaged component of the electrostatic potential and the associated $\mathbf{E}\times\mathbf{B}$ shearing rate. This is furthermore illustrated in Figure 7.33, where time-averaged values of the shearing rate, as well as temperature and density gradient profiles are plotted. As expected, one observes at the positions of low order mode rational surfaces (depicted with vertical dashed lines) a flattening of both R/L_n and R/L_{T_e} (stronger for the latter quantity), while the shearing rate at these same points goes through zero, very similar to what described for local simulations in Ref. [106]. We remark that the amplitude and extent of these fine scale structures are affected by the radial resolution adopted.

The effect of collisions has been investigated considering both electron models. The time traces of the obtained $\omega_{\mathbf{E}\times\mathbf{B}}$ are depicted in Figure 7.34. Regardless of the electron model,

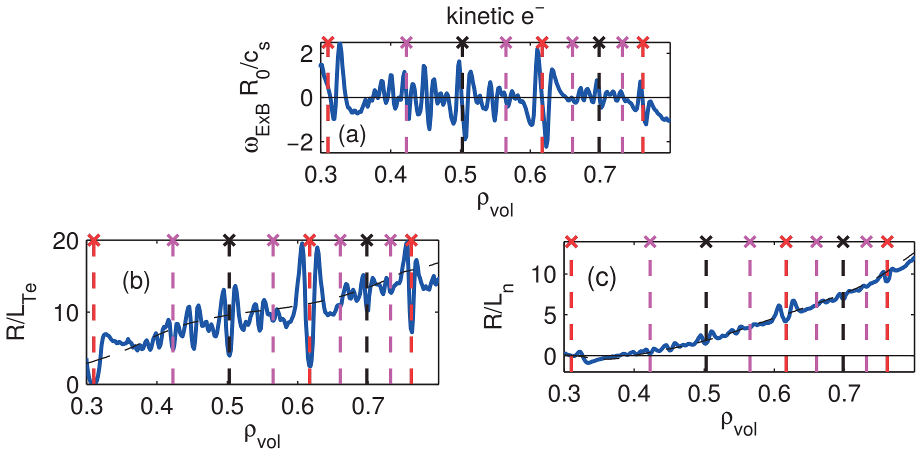

Figure 7.33 : From top to bottom, (*a*) the time-averaged shearing rate $\omega_{\mathbf{E}\times\mathbf{B}}$ in units of c_s/R_0, (*b*) the normalized logarithmic temperature gradient R/L_{T_e} and (*c*) the normalized logarithmic electron density gradient R/L_n, plotted as a function of the radial position. The location of rational surfaces has been indicated with vertical dashed lines, in red the ones associated to the lowest considered toroidal mode number $n = 2$, in black n=4 and in magenta for n=6. Results obtained with the "*high resolution*" fully kinetic run.

collisions are found to influence the GAM and in particular its direction of propagation. The dominant outwards propagation that was clearly visible in Fig. 7.32 is now replaced by a more complex pattern of both outwards and inwards propagating avalanches. In fact we note that the inwards propagation was already present in the collisionless results, however it was less evident.

The frequency of the GAM has been determined in a similar way as described in section 7.1.3. Results obtained with the two electron models have been analyzed separately, considering both the collisionless and the collisional interval of each simulation. The results are depicted in Figure 7.35 (resp. 7.36) for the collisionless (resp. collisional) part of each run. Note that for each plot the same color coding has been used for hybrid and fully kinetic results. furthermore, the lowest spectral components have been filtered out to highlight the global GAM. In each plot, we also present the results obtained with local nonlinear flux-tube simulations (magenta diamonds), the local GENE linear prediction obtained with the Rosenbluth Hinton test (red dot-dashed lines) and the analytic prediction provided in Ref. [57] (green dashed lines).

Comparing the hybrid to the fully kinetic results, one first notes that the stronger fragmentation observed in the fully kinetic radial profiles of the shearing rate, is also found in the frequency spectra. This is particularly evident in Figure 7.36. In all cases, one can identify a dominant GAM frequency $\sim$ 32 kHz, however the simulated mode appears to be less coherent and with a narrower radial extent than what is experimentally observed, see Fig. 7.26. Furthermore, contribution from other frequencies, both lower

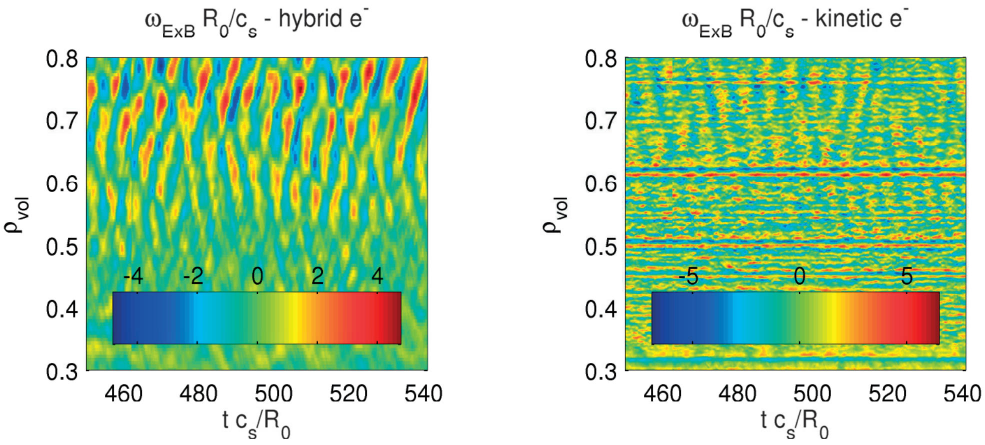

Figure 7.34 : Same as Figure 7.32 but showing results obtained retaining collisions.

and higher than the leading one, and following the radial profiles of the sound speed, are non negligible. we therefore believe that we are simulating a GAM with a prominent global nature, but nonetheless not as coherent and “radially global” as in the experiments. Some of this discrepancy might be attributed to the fact that our simulation domain is limited to $\rho_{vol} = 0.85$, but also the artificially constant temperature ratio T_e/T_i cannot be excluded as part of the explanation.
As we will show later on, further extending the radial domain of the simulation enhances the radial extension of the dominant GAM frequency component, see e.g. Figure 7.40, while the other peaks appear less affected. A much more coherent and global mode is also obtained when simulating a better experimentally diagnosed discharge, reproducing a GAM oscillation with an amplitude that increases up to the last radial point retained, see e.g. Fig. 7.43 in section 7.3 and Appendix C.

Nonetheless, both electron models agree in describing a dominant frequency of the GAM at approximately 32 kHz, which is already in good agreement with the experimentally measured value of 28 kHz.
This picture and the mode frequency is not dramatically affected by the inclusion of collisions. One can nonetheless point out that, besides the already mentioned effect on direction of propagation, collisions are found to affect the relative amplitudes of GAMs at different frequencies.

7.2.4 GAM fluctuations

A basic investigation of the density, temperature and magnetic fluctuations associated with the GAM has been carried out analyzing the results of both hybrid and fully kinetic runs. In the following, for simplicity, we will address only the results obtained with the fully kinetic simulation, as, besides being the most accurate modeling possible,

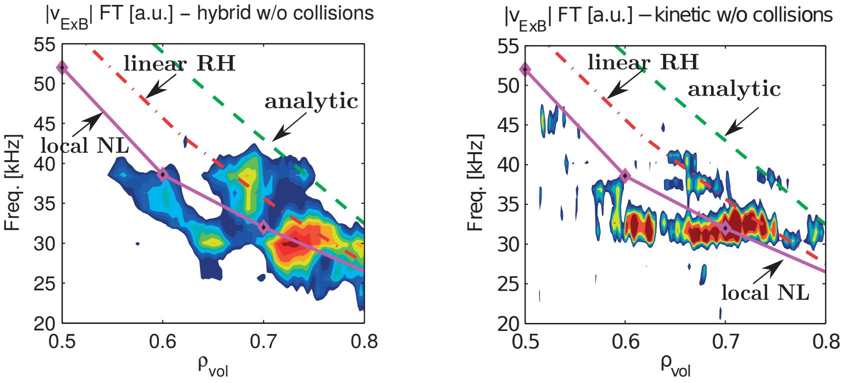

Figure 7.35 : Amplitudes, in arbitrary units, of the time Fourier transform of the $\mathbf{E} \times \mathbf{B}$ velocity as a function of the radial position and the mode frequency. On the left results obtained with hybrid electrons model while on the right with the fully kinetic one. Collisions are neglected. The green dashed line indicates the analytic prediction given in Ref. [57], the dot-dash red one the results obtained with local Rosenbluth-Hinton test while the magenta diamonds the results obtained with local fully kinetic flux-tube simulations.

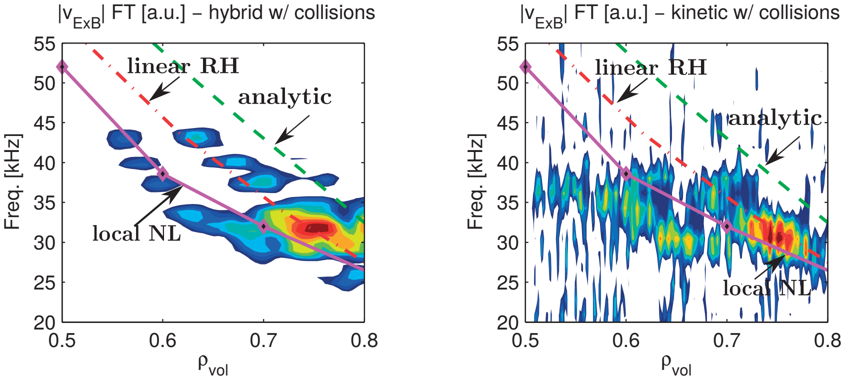

Figure 7.36 : Same as Figure 7.35 but showing results obtained analyzing the interval of the simulation where collisions are retained.

it also provides electromagnetic fluctuations related to $\delta A_{\parallel}$. Concerning density and temperature fluctuations δn and δT, hybrid and kinetic electrons provide quantitatively similar results, which agree between each other regarding both the dominant Fourier poloidal harmonics and the RMS amplitudes.

In all cases we have analyzed, we observe that the amplitude of δn_e (as well as δT_e) increase from the core to the edge. As a purely illustrative example, we plot in Figure 7.37 a snapshot of the electron density fluctuation field evaluated at the end of simulations with respectively hybrid and fully kinetic electron models, showing very similar amplitudes.

Similarly to the analysis of the flux-tube runs, the poloidal structure of e.g. density fluctuation associated to the GAM has been obtained studying, the $k_y = 0$ mode contribution. The most important difference is that in this case each radial location is

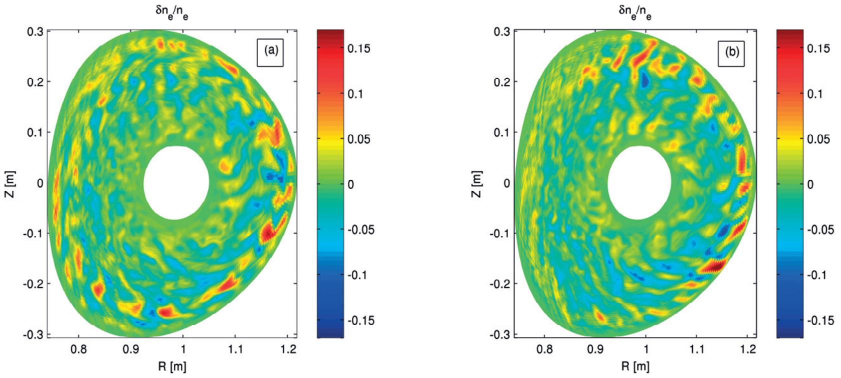

Figure 7.37 : Snapshots of the electron density fluctuation, taken at the end of each simulation, obtained assuming (*a*) a hybrid and (*b*) a kinetic electron model.

characterized by a different value of the electron temperature (and consequently sound speed), therefore some care must be taken when computing x-averaged values, as only narrow radial annuli should be considered.

In Figure 7.38, we plot the amplitudes of the Fourier transform in both time and poloidal angle of the electron density fluctuation associated to $k_y = 0$, radially averaged over $0.7 < \rho_{vol} < 0.75$ (i.e. the region of the maximum GAM amplitude from the $\mathbf{E} \times \mathbf{B}$ velocity analysis, see Figs. 7.35 and 7.35). As expected, a dominant $m = 1$ component at 32 kHz (the GAM frequency) is found, accompanied by $m = 2$ sidebands, which, thanks to the local RH analysis, which shows similar relative amplitudes of poloidal Fourier modes (see Fig D.5), we attribute to the actual plasma magnetic geometry. The same analysis can be repeated at different radial locations, obtaining for each point a dominant $m = 1$ component at a frequency that follows the local sound speed (lower moving towards LCFS). The amplitude reaches a maximum at $\rho_{vol} = 0.75$, in agreement with the behaviour of $v_{\mathbf{E}\times\mathbf{B}}$. Other poloidal harmonics, in particular $m = 2$ and $m = 3$ are excited moving towards the LCFS, once again as a result of the actual plasma shape, in particular increasing δ. For completeness, we have also looked at the radial extension of components at different frequencies (obtained filtering the simulated signal using a narrow band pass filter). As expected, we observe the largest radial excitation at the frequency of 32 kHz, covering approximately $0.65 < \rho_{vol} < 0.77$.

We have repeated the same analysis looking at temperature and $\delta A_{\|}$ fluctuations. For the former, global results appear to indicate, in contrast to local results and analytic predictions, a dominant $m = 0$ component even at finite frequency, accompanied by lower amplitude m=1 and m=2 sidebands. The origin of this poloidally uniform component is currently under investigation. Concerning $\delta A_{\|}$, having carried out the simulations with a reduced value of β doesn't allow to clearly identify neither a dominant frequency nor the poloidal harmonics, as the simulated signal is too weak.

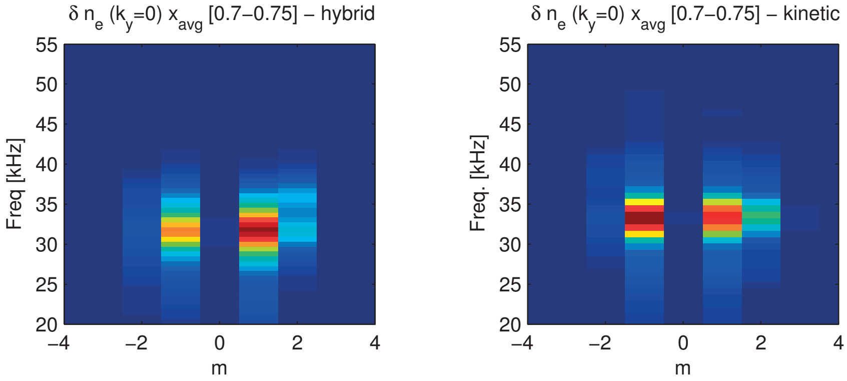

Figure 7.38 : Amplitudes of the Fourier transform in both time and poloidal angle of the electron density fluctuation associate to the $k_y = 0$ mode. Amplitudes are averaged over $0.7 < \rho_{vol} < 0.75$. A GAM peak is visible around 32 kHz and dominated by the $m = \pm 1$ poloidal Fourier component. Results obtained (on the left) with hybrid and (on the right) with fully kinetic electrons. Collisional simulations.

7.2.5 Comparison with ORB5 results

The results that we have discussed so far appear only to be qualitatively similar to what was originally obtained and discussed in Refs. [38, 55, 62]. For reference, we have reproduced in Figure 7.39 the simulated shearing rate and its time-Fourier analysis from Ref. [55]. The most evident difference is a much more uniform avalanche pattern observed in ORB5 compared to the GENE results (see Figs. 7.32 and 7.34). Very clean striations appear in the **E** × **B** shearing rate plots function of radius and time, which are characterized by a dominant frequency f (see Fig. 7.39(b)). While the value of f obtained in ORB, 32 kHz, is identical to the dominant GAM frequency estimated from GENE results, the mode appears much more global radially than in the GENE simulations reproduced and discussed in the previous sections.

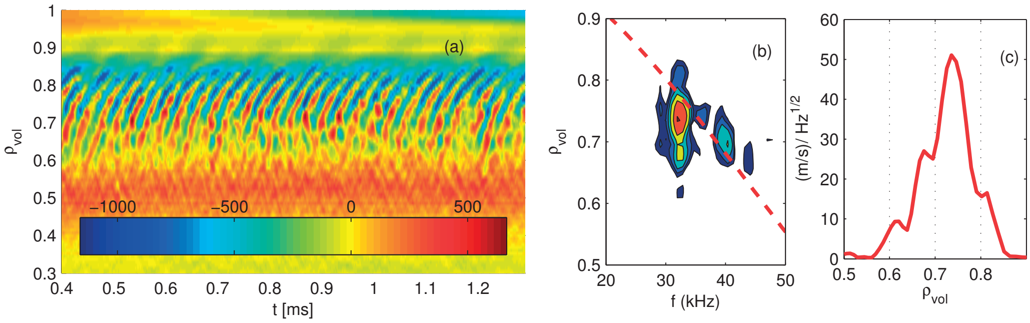

Figure 7.39 : Original ORB5 simulation performed in [38]. Shown are (a) the **E** × **B** shearing rate as a function of radius and time, (b) the power spectral density (dB scale, step 3 dB) of the **E** × **B** velocity and (c) a cut of the plot in (b) at 32 kHz. The red dashed line indicates $\sqrt{2}c_s/(2\pi R_0)$. Note the different radial extents between graphs (a) and (b, c). Reproduced from [55].

We recall that the simulation of Ref. [38] was performed in the collisionless electrostatic regime, assuming a hybrid electron model, the latter with artificially heavy mass (m_i/m_e=200). Furthermore, the run was carried out considering the long wavelength approximation in the field solver. All these approximations allowed to adopt a much coarser radial grid, 128 grid points covering the full minor radius, compared to what we used (with this choice one has $\delta\rho_i = 0.63$ at the surface $\psi/\psi_{\mathrm{LCFS}} = 0.6$ in ORB5 while the "*high resolution*" GENE set-up corresponds to $\delta\rho_i = 0.16$). Finally, in the ORB5 simulation a different radial domain was considered as well, with temperature and density profiles inspired by the experimental ones but with gradients smoothly reduced to zero beyond $\rho_{vol} = 0.8$, such as to avoid instabilities developing in the edge region that would require an increase of the resolution. The absence of a sufficiently strong drive to destabilize microturbulence can also be seen in Figure 7.39(a), where the shearing rate rapidly goes to zero for $\rho_{vol} > 0.8$.

In order to understand how much these different settings affect the results, we have carried out one GENE run with a numerical set-up as close as possible to the original ORB5 one. We therefore simulate the radial annulus $0.15 < \rho_{vol} < 1$, discretized with 128 points, using the last 10% at both ends as buffer regions. The slightly larger number of radial grid points per Larmor radius in the GENE run compensates for the different choice of the radial coordinate between the two codes. Given that already in Ref. [38] there was no claim that the ORB5 simulation results reproduced the experimental turbulent state for $\rho_{vol} > 0.8$, given that the measured temperature and density profiles were artificially modified and an artificial shielding of the electric field furthermore applied at the plasma edge, the same velocity grids as the one used for the previous GENE runs have been used without more accurately resolving the edge region. We remark that, thanks to these approximations, the simulation is computationally much lighter, requiring, in comparison to the hybrid run described in section 7.2.2, a third of the computational resources to achieve the same time statistics.

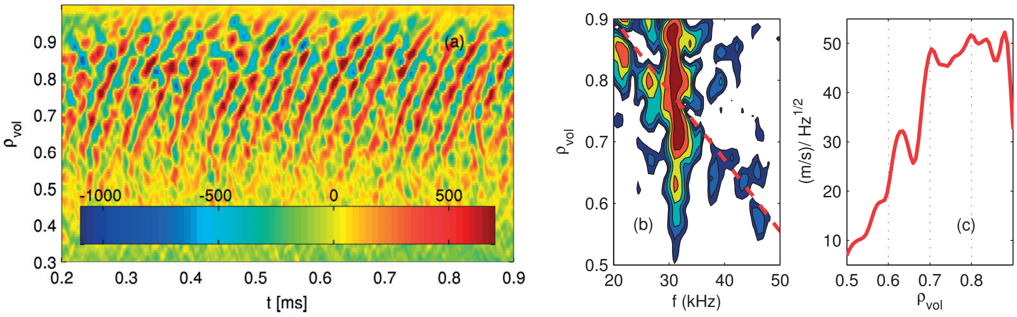

Figure 7.40 : Same quantities and same color coding as Fig. 7.39. In this case shown are results obtained with GENE using the same physical model and numerical set-up as ORB5.

The shearing rate analysis of this new run is reported in Figure 7.40, where we have plotted the results using the same color coding as in Fig. 7.39. We note that thanks to

the simplified numerical set-up, the $\mathbf{E} \times \mathbf{B}$ fluctuations present a more radially coherent character, extending up to $\rho_{vol} = 0.9$ (the mode is damped further out by the radial buffer). The dominant frequency is ~ 31 kHz, in agreement with ORB5 estimates as well as our other GENE simulations. We remark that GENE results, compared to ORB5, still present a stronger contribution from other frequencies (radially localized following the local sound speed profile) than the dominant one. The low part of the spectrum, $f < 32$ kHz related to edge fluctuations, appears affected by the different treatment between the two codes of the boundary region. At higher frequencies, corresponding to oscillations located radially more inside in the plasma and thus at locations where the boundary conditions are expected not to affect simulation results, GENE output indicates contributions from a broader range of frequencies compared to ORB5, which finds only a clear contribution at $\sim$38 kHz. This result is in agreement with the previously presented GENE runs.
Furthermore, GENE appears to predict a more mixed outwards-inwards direction of fluctuation propagation, compared to an almost exclusively outwards propagation in ORB5. This is also reflected by a stronger radial short scale modulation of the $\mathbf{E} \times \mathbf{B}$ avalanches. Part of this difference seems to be related to the long wavelength approximation originally adopted in the ORB5 field solver, which, once relaxed, appears to lead to a stronger modulation of e.g. the shearing rate, i.e. qualitatively closer to what is observed in GENE [129].

Comparing all GENE simulations carried out modeling TCV discharge #45353, we conclude that a global oscillation at approximately 32 kHz is found, in agreement with the experiments. However, this frequency is $15 - 20\%$ higher than what is experimentally measured with T-PCI. Moreover, in the simulations one observes contributions from other frequencies that are not detected experimentally. Explanations of these discrepancies can be found in the approximations adopted for carrying out such runs: impurities have been neglected and an artificially constant electron to ion temperature ratio has been assumed, the latter leading in particular to a non-physically large transport level.
The dominant frequency of the $\mathbf{E} \times \mathbf{B}$ flow appears as a quite robust parameter, not significantly affected by the details of the simulation model (e.g. hybrid vs. fully kinetic electrons), while the radial extent of the mode is more susceptible to the numerical set-up. Collisionless runs carried out with artificially heavy electrons allow to determine the leading GAM frequency with a reduced computational cost, and in this limit a reasonably good agreement between GENE and ORB results was recovered. Nonetheless, considering true electron to ion mass ratio and collisions is desirable as these parameters are found to affect the mode properties, and consequently the turbulence level.
We finally remark that one has to be extremely careful when analyzing the results obtained from any code. The limited time statistics acquired lead to particularly important uncertainties on the frequencies. One thus has to make sure that the way simulation data is post-processed does not artificially highlight some specific features of the results.

7.3 Radially coherent vs. dispersive GAM regimes

As already mentioned in the introduction of this chapter, the GAM is normally measured in TCV as a radially coherent oscillation, in contrast with other machines where it appears to be more radially localized and to possess a frequency that follows more closely the local sound speed (typically a staircase profile is observed, rather than a continuous dependence of f_{GAM} on radius) [130]. The only experimental TCV condition in which the mode was observed to possess a more local nature than usual, was during a q_{95} ramp. Here q_{95} is the safety factor at 95% of the plasma minor radius. In this case, the mode appeared as less coherent and with a dispersive frequency when q_{95} was increased beyond ~ 6, see Figure 7.41 and Ref. [131]. Incidentally, we note that this appears in contrast with what observed in ASDEX [132], where the eigenmode GAM was observed in diverted discharges and the dispersive in limited ones. In general, the conditions under which the regime transition happens are not yet understood and still under active investigation, both experimentally and theoretically.

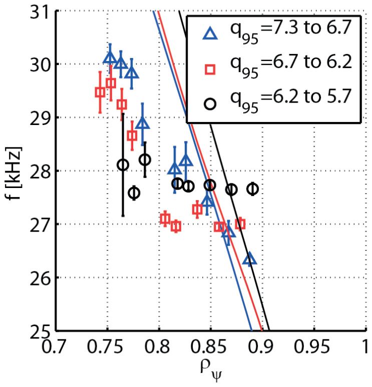

Figure 7.41 : Measured frequency of the GAM oscillations obtained from the electron density fluctuations using the PCI diagnostic system. When increasing the edge safety factor q_{95}, one observes a transition from a radially coherent mode, i.e. a constant frequency over a significant fraction of the plasma minor radius (black circles), to a dispersive regime where the frequency varies with the radial location (blue triangles). From Ref. [117].

In order to address the TCV observations, we have carried out two global simulations assuming the experimental conditions corresponding to a radially coherent and a dispersive GAM[2]. Contrary to the simulations discussed in the previous section, the discharges considered here have ion profiles measured with the Charge eXchange Spectroscopy system (CXS), which will therefore be used. At the same time, in order to limit the cost of these runs, the hybrid electrons model is used and, furthermore, artificially heavy

---

[2] The global GAM considered here is different from the one presented in section 7.2 in order to have exactly the same numerical set-up for comparing the coherent and dispersive GAM cases. Furthermore, the discharge we consider in this section was experimentally better diagnosed and, as it will be shown, the GAM appears in this case much more radially "global" than the case previously discussed.

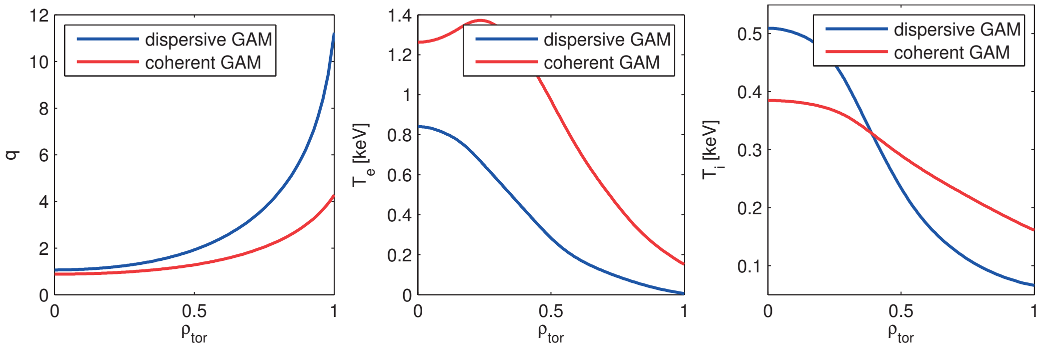

Figure 7.42 : Measured profiles of safety factor, electron and ion temperature for the dispersive and coherent GAM. The two TCV discharges are respectively #49032 at t=0.6 s and #45886 at t=1.1 s.

electrons (m_i/m_e=400) are assumed. This choice is mainly motivated by the different electron temperature profiles observed in the two scenarios, making the dispersive mode scenario computationally very expensive to be simulated with real mass ratio electrons. Even though there is no experimental evidence of a relation between T_e and the radial localization of the GAM (only a scaling of the mode frequency with $T_e^{1/2}$, see e.g. Ref. [55], has been shown, as expected from GAM theory), we note that the dispersive mode is measured in conjunction with a significantly lower electron temperature profile (see also Fig. 7.42). This translates in a lower ρ^* compared to the global case ($\rho_s/a = 1/294$ vs. $\rho_s/a = 1/122$ measured at $\rho_{tor} = 0.7$). In order to have the same radial resolution (in both cases we simulate the outer half of the plasma, $0.4 < \rho_{tor} < 1$, with a 10% buffer region at both ends of the computational domain), a higher number of n_x points is required for the dispersive mode case, which is unfortunately also combined with larger velocity space grids, required because of larger radial temperature variation. The grids used are reported in Table 7.6. Finally, we also remark that the electron density is quite different in the two cases, higher for the local GAM, increasing in turn plasma collisionality and further reducing the maximum numerical time step.

	n_x	n_y	n_z	$n_{v_\parallel}$	n_μ	$\hat{L}_x$	n_{min}	$\hat{L}_{v_\parallel}$	$\hat{L}_\mu$
coherent	240	32	48	110	48	68	2	18.0	4.14
dispersive	480	32	48	136	78	146	2	20.1	4.47

Table 7.6 : Resolutions used for the global simulations investigating the coherent vs. dispersive GAM.

Based on all the previous considerations, we already point out that this investigation should be considered as preliminary and exploratory, essentially addressing the possibility of a transition to a local GAM because of the higher q (or lower ρ^*) rather than a proper attempt to reproduce the experimental microturbulence level. This latter task, based on all the results already discussed, can be accomplished only thanks to a more realistic simulation model, featuring kinetic electrons with real mass ratio. Given the actual plasma profiles for the local GAM scenario, requiring as mentioned previously high numerical resolution, this is an extremely challenging effort, which is left for future investigation.

The usual time evolution of the radial profiles of the $\mathbf{E} \times \mathbf{B}$ velocity obtained from our simulations are plotted in Figures 7.43(a) and 7.44(a), for respectively coherent and dispersive GAM conditions. Because of the much shorter (collisional) time step, limited statistic have been collected for the run corresponding to the latter experimental conditions. In both cases, we have carried out a first part of the simulation without collisions, which are then switched on in order to measure their effect on zonal flows. In the plots, the instant where they have been activated is indicated with a vertical line. Moreover, in Figs. 7.43(b) and 7.44(b) we plot the amplitude of the corresponding time Fourier transforms, evaluated over the collisional part of the runs.

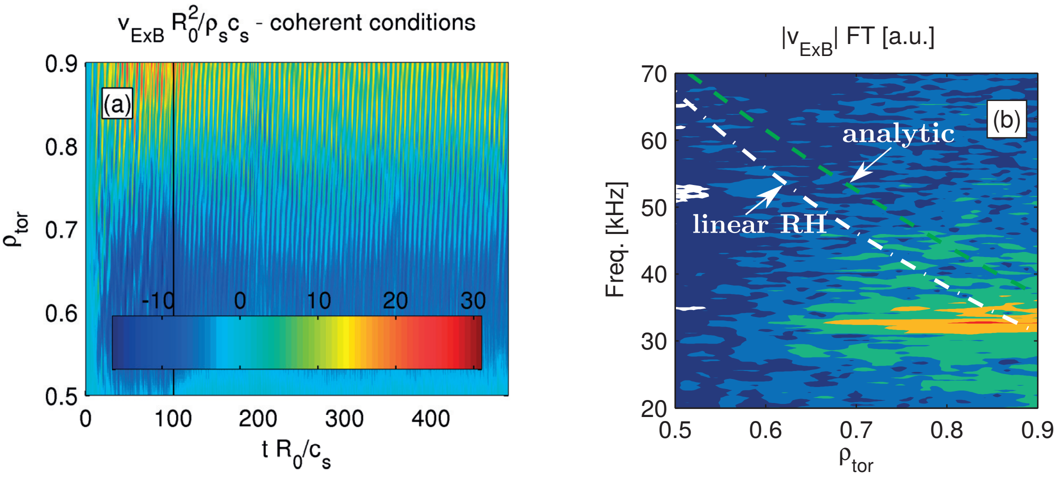

Figure 7.43 : (a) $\mathbf{E} \times \mathbf{B}$ velocity as a function of time and radius for the coherent GAM conditions (TCV #45886), and (b) amplitude of the Fourier transform in time evaluated over the collisional interval of the run. The green dashed line indicates the local theoretical GAM frequency according to Gao *et al.* [57], while the dot-dashed white one corresponds to the local frequency estimated via a series of local Rosenbluth-Hinton tests.

Looking at Figures 7.43 and 7.44, one observes a clear difference between the results of the two simulations, which, in agreement with the experimentally observed behaviour, show once a radially coherent and once a dispersive GAM. Indeed, in correspondence with the coherent conditions, we obtain in Fig. 7.43 a very clear single frequency oscillation over a large fraction of the minor radius, with an amplitude increasing when approaching the LCFS. This oscillation is at about 31 kHz (see Appendix C for more details) while experimentally the GAM is measured at $\sim$ 28 kHz. This difference, which is already within the experimental and simulation error bars, can also be reduced if one were to include carbon impurity, which are known to reduce the GAM frequency [133]. We note that the frequency that we obtain from the simulation is closely matching the one obtained with the Rosenbluth-Hinton test carried out at the $\rho_{tor} = 0.9$, i.e. the outermost position before the radial buffer (see dot-dash line in Figure 7.43(b)). This appears more as a coincidence rather than a numerical effect of the buffer region itself.

When instead the TCV conditions of the dispersive mode are simulated, we obtain a GAM frequency that is following the local RH prediction, with each point being a source of an oscillation that propagates radially only for a short extent. This is reflected by the band of frequencies visible in Fig. 7.44(b), which closely follow the local prediction obtained with the RH test.

The differences between the two discharges are however significant and not limited to the safety factor profile. In both cases, based on the relative amplitudes of the heat fluxes ($Q_e \gg Q_i$), we infer from the nonlinear results a TEM dominated regime. However, besides the obvious differences between the magnetic geometries, the origin of different GAM regimes can potentially be attributed to the different temperature and density, as well as the corresponding gradient profiles, which obviously affect the local turbulence level.

In order to rule out at least the effect of the different q profile, we have thus carried out another run where the two experimental conditions are mixed. We assume the temperature and density profiles corresponding to the coherent GAM while the magnetic geometry of the dispersive case. A complete investigation would require to carry out a run also with the other combination. It has not yet been done for lack of CPU resources and the high computational cost foreseen for such a run. The results obtained are presented in Figure 7.45, where one clearly observes a global mode at a frequency of ~31 kHz, very similar to what is shown in Figure 7.43. In this case the GAM appears to be even more global than what obtained assuming the experimental conditions for the global GAM, with oscillations covering the region $0.6 < \rho_{tor} < 0.9$, even though less statistics have

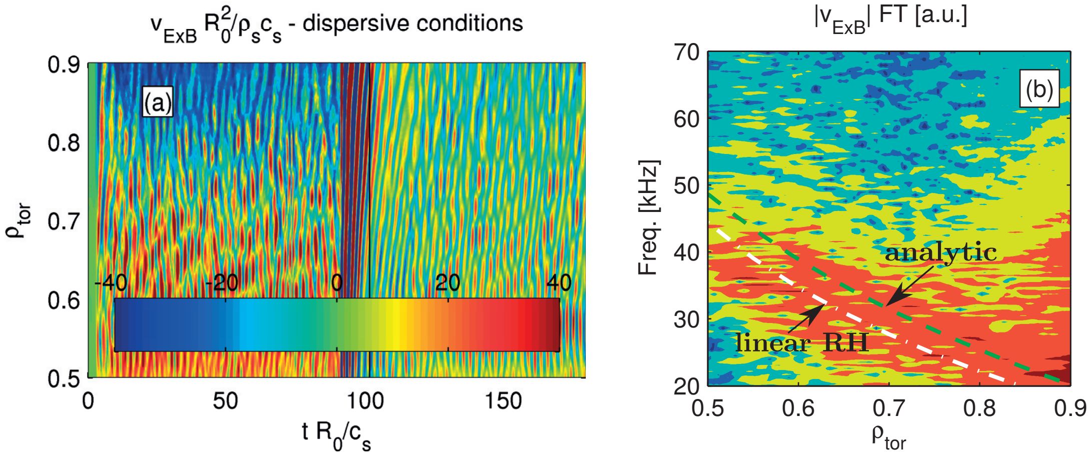

Figure 7.44 : Same as Figure 7.43 but showing the results obtained modeling the dispersive TCV experimental conditions (TCV #49032).

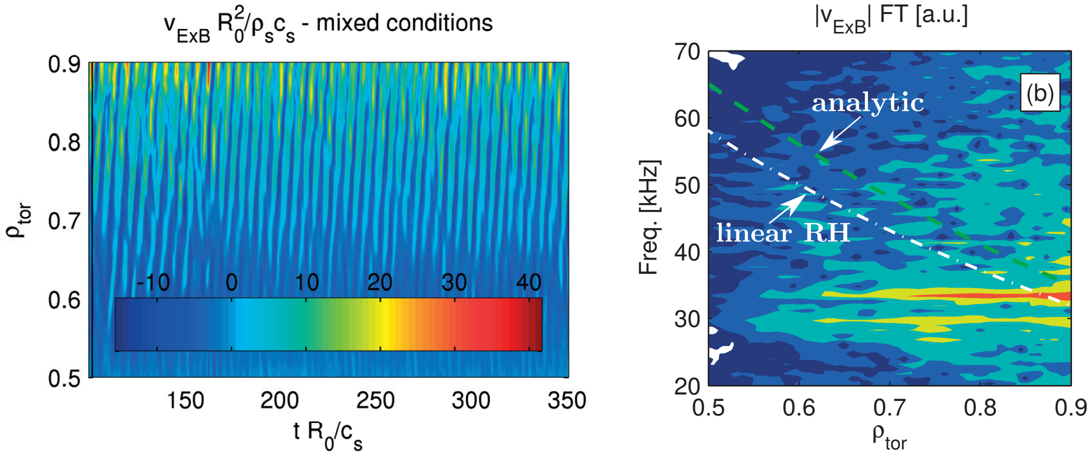

Figure 7.45 : Same as Figure 7.43 but showing the results obtained mixing experimental TCV conditions: temperature and density profiles of the radially coherent GAM with magnetic geometry of the dispersive GAM.

been acquired. Based on this result, we conclude that simply varying the safety factor is not sufficient to induce a regime transition from radially coherent to dispersive GAM.

7.4 Conclusions

In this chapter we have presented several efforts of investigating GAM dynamics in TCV relevant conditions and reproducing some of the many experimental observations that have been reported. To this aim, we have carried out local and global simulations, using different simulation models, in particular to develop an understanding of what physical effects must be retained in order to reproduce the mode as it is observed in the experiments.

We have first investigated with flux-tube simulations the behaviour of the GAM during an experimental density ramp-up. Local runs reproduce a behaviour qualitatively and quantitatively similar to what is experimentally observed. The intensity of the GAM decreases with increasing density, while its frequency is little affected. Changes in the turbulent regime are observed, from a TEM to an ITG dominated, which are mainly caused by the variation of background plasma profiles. The simulated transport level is within the error bars of the experimental one. We remark that the results obtained are very sensitive to the input gradients, as minor changes within the experimental uncertainties of the input parameters lead to significant variations of the transport level.

The local analysis, even though it appears to properly reproduce the experimental turbulence level in this case, is however unable to simulate the preferred direction of propagation of the GAMs, as experimentally observed. Similarly, if such modes posses a global structure, this cannot be represented in the flux-tube limit. We have therefore investigated an experimental radially coherent GAM discharge with the global version of GENE. Different numerical models have been used, and both hybrid and fully kinetic electrons qualitatively reproduce the frequency and the spatial location of the GAMs. Simulations appear however to reproduce a more continuum-like mode than what is experimentally observed, with other frequencies excited at different radial locations. This discrepancy is understood as a consequence of both the simulation set-up and the approximations considered when prescribing the input plasma profiles. An agreement with previous ORB5 simulations is recovered when the same numerical set-up is used.

Finally, we have investigated the different GAM regimes observed in TCV as a function of the safety factor profiles. Our simulations succeeded in reproducing the "*radially coherent*" as well as the "*dispersive*" GAM when the corresponding experimental conditions (magnetic geometry together with temperature and density profiles) are assumed. We have showed that the sole variation of the safety factor profile is insufficient to induce a regime transition, which instead appears to be more associated to the actual plasma profiles. We can only speculate that the main responsible for the different regimes is ρ^*, which is larger, by approximately a factor of two, for the coherent conditions compared to the dispersive ones. Stronger finite machine size effects can thus be expected in the first case compared to the latter. A simple way to investigate this hypothesis is by carrying out a ρ^* scan, and measure in the different cases the mode frequency. We have initiated such a study in the collisionless regime. The results obtained so far are however insufficient to confirm or disprove our hypothesis and it appears necessary to further pursue the investigation including also the effect of collisionality.

Furthermore, we have carried out all our runs considering a simplified model for describing the plasma, i.e. assuming hybrid heavy electrons. We have nonetheless obtained a good agreement with the experimentally measured frequency. It is however desirable to repeat at least the two simulations corresponding to the experimental coherent and dispersive GAM, assuming more realistic fully kinetic electrons and with real mass ratios. This, on the one hand will allow one to confirm our results with the most accurate modeling possible, on the other hand, it will allow to carry out a more detailed comparison with experiments looking also at density, temperature and electromagnetic fluctuations. Finally, truly one to one comparisons should be done with the help of synthetic diagnostics. This new set of runs is expected to be computationally very expensive, not only due to the high required resolutions but also because long statistics are necessary to accurately measure the GAM frequency in the simulations. A more detailed review of the existing TCV database, identifying possible discharges with flatter temperature profiles so as to reduce the cost of the discretization of velocity space, it is thus desirable, especially for the dispersive mode case which is currently too expensive to be simulated.

In principle, carbon impurities should also be retained, as they can lead to a lower frequency and therefore further improve the agreement between simulation and experiments. Including a third species is however expensive from a computational point of view, and will probably only lead to a minor variation of the mode frequency.

8 Conclusions

8.1 Summary

In this work we have extensively used the Eulerian gyrokinetic code GENE, in both its local and global versions, in order to model TCV relevant conditions and study the resulting microturbulent state, which is in turn responsible for most of the macroscopic transport phenomena experimentally observed.

For the sake of completeness, a description of microinstabilities and the gyrokinetic model have been recalled, together with some details about the actual implementation of the gyrokinetic equations in GENE.

In view of using GENE with the TCV experimental magnetic geometry, series of benchmarks have been developed in order to verify the interface of the code with the MHD equilibrium solver CHEASE. Various tests have been successfully carried out in the linear local limit, where GENE has been successfully compared to the flux-tube codes GKW and GS2, looking at growth rates and frequencies of the most unstable modes at both ion and electron scales, at the effect of a finite ballooning angle and at linear dynamics of zonal flows as described by the standard Rosenbluth-Hinton test. In all cases an excellent agreement has been recovered. Elongation of the plasma cross-section appears as the shaping parameter inducing the strongest effects for the geometries that we have considered, stabilizing the linear growth rates and increasing the ZF residual level. These benchmarks have been generalized to global codes, in an effort currently involving GENE and the Lagrangian δf, PIC code ORB5. A good agreement has already been found when comparing linear growth rates, and similarly for nonlinear fluxes. The GENE code has then been applied to investigate some of the experimental observations reported in the TCV tokamak, which are summarized in the following.

One of the most interesting and not yet fully understood observations made on TCV L-mode discharges is the strong beneficial effect played by negative triangularity of the LCFS, which, compared to standard positive triangularity shapes, is found to uniformly reduce the electron heat transport level by approximately a factor of two at all radial locations in the outer half of the plasma minor radius. Experimentally, half the heating power is required in order to maintain the same electron temperature and density profiles, which is interpreted as a better electron energy confinement. While one can speculate that the origin of this confinement improvement is related to the TEM stabilizing effect played by negative triangularity, how this shaping parameter, which has a finite radial penetration depth, can uniformly influence all the outer half of the plasma remains unclear. Local simulations indeed provide a beneficial effect for $\delta < 0$, which is a function of the radial position ρ, compatible with the experimental results only for $\rho \gtrsim 0.7$ where triangularity is large, while negligible in the core at $\rho \simeq 0.5$. The hypothesis of a shape-dependent profile stiffness, suggested by a recent analysis of a large database of TCV discharges and potentially explaining the confinement improvement as being a consequence of a less stiff edge when $\delta < 0$, was investigated with the help of flux-tube simulations. Based on these numerical results, TCV profiles appear to be very stiff with respect to the density gradient, less with respect to the electron temperature gradient. Even when using the most accurate numerical model possible, a large overestimation, by at least a factor of five, remains when comparing locally-simulated and measured heat fluxes in the TCV core, while a better agreement is observed moving towards the LCFS. The overestimation of fluxes in fact prevents us from drawing firm conclusions about an eventual profile stiffness dependence on δ and one has to be very careful not to over-interpret simulation results by applying ad-hoc re-scaling factors to mimic global effects.

Finite machine size stabilization, the so-called finite ρ^* effects, with $\rho^* = \rho_s/a$, is expected to play a major role in typical TCV conditions ($\rho^* \sim 1/80$) and the only way to correctly account for such effects is by carrying out global simulations. These runs are particularly expensive and, due to limited available computational resources, it has not been possible to carry them out retaining at the same time impurities and collisions, which are both expected to play a major stabilizing role. We have developed a strategy to carry out "full-radius" simulations, where buffer regions required for numerical stability are placed outside the actual LCFS, so as to be able to include the region where δ is largest in the main simulation domain. Compared to local runs, results obtained with global simulations carried out including collisions but neglecting carbon show some global effects, in the form of a reduction of the maximum heat flux and a more radially uniform difference between positive and negative δ shapes, which is now observed also at core locations. Nevertheless, the simulated difference remains smaller than the observed factor of two, and a heat transport overestimation remains, larger for the $\delta < 0$ case. Moreover, the simulated radial transport profile appears unrealistic as it is strongly peaked in the core, while, based on the experiments, one would expect a much more radially uniform transport level. Even though one has neglected carbon, this result appears to be mainly the consequence of having used for the simulations a density profile providing a too large gradient in the core, which in turn generates very strong turbulence and large heat fluxes. This reflects also the limitation of carrying out gradient-driven runs in comparison to the more realistic, but computationally too expensive, flux-driven runs. Varying the profiles "manually" in order to attempt to lower the turbulent drive in the core is a non trivial exercise, given that from our preliminary results it appears that all profiles would need to be adjusted and the overall computational effort would be too large. We have therefore started modeling a more recent and experimentally better diagnosed discharge. In this case, one is aiming at reproducing an experimental δ scan, carried out at constant heating power, resulting in different profiles depending on the shape (a larger pedestal is observed when $\delta < 0$). Once again, in order to limit the computational effort, carbon has been initially neglected. In this case, a much better agreement between simulations and experiments is nevertheless recovered. Already with flux-tube simulations, the overestimation of the transport level appears to be smaller and very strong global effects are observed, with the heat flux being compatible with the experimental one within a factor of two. We also note a large ion heat flux, in both local and global simulations, which, based on flux-tube simulations, is expected to be reduced to a negligible level when carbon is included.

Another very interesting series of observations has been made on TCV regarding GAM dynamics. This mode, which can play a significant role in the self regulation of turbulence, is normally observed as radially coherent, i.e. an oscillation of e.g. electron density fluctuations at a constant frequency over a large fraction of the plasma minor radius ($\rho \gtrsim 0.6$), contrary to analytic linear predictions of the mode frequency being proportional to the local sound speed. Various parameter scans have been experimentally performed in order to better understand this behaviour and the only condition in which the mode was observed to possess a radially dispersive nature was when the edge safety factor was significantly increased.

We have first investigated, using the flux-tube version of the code, an experimental density ramp-up for which the GAM was observed to disappear at increasing density as a result of a larger broadband turbulence overcoming the GAM peak in the Phase Contrast Imaging (PCI) spectra. When looking at the transport level for this specific discharge, local GENE results appear to be already in a very good agreement with the experiments, without invoking the need of strong global effects. This is understood as a consequence of having analyzed a position ($\rho_\psi = 0.8$) in the outer region of the plasma minor radius for which the local value of $\rho*$ is somewhat smaller than typical core conditions. Moreover, strong ETG contributions have been neglected, and they should be quantified with at least electron scale runs. We have analyzed the GAM dynamics by inspecting the $\mathbf{E} \times \mathbf{B}$ velocity as a function of radius and time. Typical criss-crossing patterns are found, without a preferred direction of propagation, an observation that we relate to having carried out local simulations that adopt radially periodic boundary conditions. The frequency of this oscillations (~ 31 kHz) is slightly higher than the experimental one (~ 28 kHz). Nonetheless, if one accounts for the uncertainty in the experimental input profiles by simply adding an error bar to the conversion from code normalized quantities to physical units, simulation results appear to be compatible with experiments. We observe oscillations at the same frequency as the GAMs in the profiles of heat and particle fluxes. There therefore seems to be a coupling between GAM oscillations, which

are associated to the $n = 0$ mode and consequently do not contribute to radial fluxes, and transport avalanches, requiring further investigations.
Given that local simulations cannot reproduce any preferred direction of propagation nor determine a finite radial extent of the mode, we have also carried out global GENE simulations addressing these aspects. We have first performed simulations, with different numerical models, investigating a discharge that was already studied with ORB5 runs. Our global simulations, assuming both hybrid and fully kinetic electrons, qualitatively reproduce the experimental frequency and the spatial location of the GAMs. However, numerical results present a more continuum-like mode than experimentally observed, i.e. with different frequencies excited at different radial locations. The structure of the GAM and the mode frequency are not dramatically affected by the inclusion of collisions. Nonetheless, in addition to a reduction of the turbulence level, retaining collisions is found to affect the relative amplitudes of GAMs at different frequencies and give rise to a more complex pattern of inward and outward propagation. These discrepancies are understood as a consequence of both the simulation set-up and the approximations considered when prescribing the input plasma profiles. An agreement with previous ORB5 simulations is recovered when the same numerical set-up is used.
Finally, we have investigated the different GAM regimes observed in TCV as a function of the safety factor profiles. To reduce the cost of the computational effort, which is particularly high, we have adopted the hybrid electron model assuming a mass ratio $m_e/m_i = 1/400$. Our simulations succeeded in reproducing the coherent as well as the dispersive GAM when the corresponding experimental conditions (magnetic geometry together with temperature and density profiles) are assumed. We have shown that the sole variation of the safety factor profile is insufficient to induce a regime transition, which instead appears to be associated with the actual plasma temperature and density profiles.

8.2 Outlook

The experimental transport levels experimentally observed with positive and negative δ_{LCFS} has not yet been fully reproduced with simulations. The new experimental discharge that we have started to investigate appears as a better suited case than the original one reported in Ref. [13], thanks to much better diagnosed plasma profiles. It is thus desirable to first pursue the two species simulations we have started by acquiring better statistics (at least simulating up to $100R_0/c_s$ is required) and then repeat the two simulations including at the same time three species (deuterium, carbon and electrons) and finite collisionality. This will provide the most realistic description of microturbulence in a TCV plasma. The understanding of the beneficial effect of $\delta < 0$ is naturally easier if the electron profiles are the same. The numerical effort of a global simulation is huge and, based on out experience, it is reasonable to carry out such runs only if the uncertainties in all measured profiles are as small as possible, rather than account for experimental

error bars performing parameter scans. To this end, flux-tube simulations provide a very valuable tool, as they are significantly less expensive and, even though global effects are expected to play a significant role, a too large overestimation of transport levels with these local runs should be interpreted as a sign of unrealistic values of input gradients.
The investigation of GAM dynamics should be further pursued by carrying out a collisional ρ^* scaling in order to assess the relevance of global effects and their impact on the experimentally observed global nature of the GAM. This study can be carried out considering a simplified model (hybrid heavy electrons) in order to limit the computational effort which would otherwise render this approach unpractical. The experimental radially coherent and dispersive GAM TCV conditions that we have already simulated in this work should nonetheless be repeated assuming fully kinetic electrons and, if possible, carbon. This will provide the most accurate modeling of actual TCV conditions and allow a true one-to-one comparison between simulations and PCI spectra, thanks to synthetic diagnostics already implemented as a post-processing tool.
The density ramp-up that we have described in section 7.1 should also be further investigated. In particular, the quasi-coherent mode that we have not addressed here should be analyzed first by carrying out a series of nonlinear local simulations at different radial locations, given that experimentally the signal from this mode is stronger moving towards the LCFS. The impact of experimental uncertainties is another element that needs to be addressed. Moreover, even if in this particular case the flux-tube approach appears to provide already a very good agreement between simulation and experiments, simulating at least some of the experimental conditions with global runs, appears valuable to provide further insight on GAM dynamics.
Finally, ETG modes have been neglected in almost all runs even though linearly they are found unstable. Carrying out global multi-scale simulations is computationally extremely expensive, and it appears almost impossible with the current CPU resources to foresee a global run with multiple kinetic species and collisions, including contributions from the ion down to the electron scale. It is nevertheless desirable to carry out a few local multi-scale simulations, which are still very CPU intensive, but feasible in practice. In this case one should assume edge-like conditions, where the local ρ^* is smaller and therefore finite machine size effects can be expected to be less relevant.
At last, we have carried out only gradient driven simulations, as flux-driven ones are too expensive especially when kinetic electrons are considered. A few runs of this kind can nonetheless be made assuming adiabatic electrons and addressing some basic properties, such as the global nature of the GAM and its relation to avalanches.

A crucial next step of gyrokinetic simulations, which will require a huge effort also in code development, is towards simulating the plasma edge. Even if in this work we have not explicitly addressed issues, like e.g. the L-H transition or the ELM suppression, that are crucial open questions intrinsically associated to the plasma boundary, it already appears evident that a correct description of the plasma edge is of vital importance. Correctly reproducing the effect of shaping or the GAM dynamics is strongly related to a proper description of the edge, where also prescribing the most realistic possible boundary conditions is desirable and necessary.

The strong gradients and large fluctuation amplitudes of the edge region ultimately lead to a breakdown of the standard δf gyrokinetic ordering. Therefore, an extension of GENE towards a full-f description is necessary. Furthermore, more realistic sheath boundary conditions should be implemented in order to be able to deal with open field lines.

While all these improvements are associated to the physical model implemented in the code, a successful extension of GENE will necessarily rely also on further improvements of the algorithms and numerical techniques, allowing for a reduction of the computational effort and, at the same time, an optimal usage of the future supercomputers.

A The GKW code

A.1 GKW coordinate system

The GKW code [95] employs a field aligned coordinate system (r, ζ, s) similar to the (x, y, z) system considered in GENE. The r coordinate corresponds to the geometric minor radius $r = (R_{max} - R_{min})/2$, while ζ is equivalent to the y coordinate in GENE defined in Eq. (3.2) within a scaling factor $2\pi C_y$:

$$\zeta = \frac{1}{2\pi}\left[q\left(\bar{\psi}\right)\chi - \varphi\right] = \frac{1}{2\pi C_y} y, \tag{A.1}$$

Similar to Eq. (3.3), the magnetic field can thus be written as

$$\mathbf{B} = F\left(\bar{\psi}\right)\nabla\varphi + \nabla\varphi \times \nabla\bar{\psi} = 2\pi\frac{d\bar{\psi}}{dr}\nabla r \times \nabla\zeta, \tag{A.2}$$

Comparing Eq. (3.3) to (A.2) one notes that the definitions for the poloidal magnetic fluxes ψ and $\bar{\psi}$ considered in GENE and GKW respectively differ by a factor 2π, $\bar{\psi}=\psi/2\pi$. In general, caution must be taken regarding the different definitions and orientations of the coordinates considered in various codes for representing the magnetic field. A detailed description of this issue is given in Ref. [134], together with practical indications for conversion between different choices characterized by a so-called COCOS value.

The “parallel” coordinate s considered in GKW is however different from the straight field line angle poloidal angle χ in GENE. The s coordinate is in fact one of the Hamada coordinates $\left(\bar{\psi}, s, \gamma\right)$, defined as $s = s\left(\bar{\psi}, \theta\right)$, $\gamma = \gamma\left(\bar{\psi}, \theta, \varphi\right)$, and such that the corresponding contravariant component of the magnetic field

$$B^s = \mathbf{B} \cdot \nabla s \qquad B^\gamma = \mathbf{B} \cdot \nabla\gamma \tag{A.3}$$

are flux functions, i.e. $B^\gamma = B^\gamma\left(\bar{\psi}\right)$, $B^s = B^s\left(\bar{\psi}\right)$.
From these conditions one can derive

$$s\left(\bar{\psi},\theta\right) = \int_0^\theta \frac{d\theta'}{\mathbf{B}\cdot\nabla\theta'} \bigg/ \oint \frac{d\theta'}{\mathbf{B}\cdot\nabla\theta'}\,, \tag{A.4}$$

$$\gamma\left(\bar{\psi},\theta,\varphi\right) = \frac{\varphi}{2\pi} + g(\theta,r) \tag{A.5}$$

and

$$B^s\left(\bar{\psi}\right) = \left[\oint \frac{d\theta'}{\mathbf{B}\cdot\nabla\theta'}\right]^{-1}, \tag{A.6}$$

$$B^\gamma\left(\bar{\psi}\right) = \frac{F}{2\pi}\langle\frac{1}{R^2}\rangle, \tag{A.7}$$

with

$$g\left(\bar{\psi},\theta\right) = \frac{F\left(\bar{\psi}\right)}{2\pi}\int_0^\theta \frac{d\theta'}{\mathbf{B}\cdot\nabla\theta'}\left[\langle\frac{1}{R^2}\rangle - \frac{1}{R^2}\right]. \tag{A.8}$$

Here $\langle\cdot\rangle$ stands for the flux surface average defined by (2.108), which can in fact also be rewritten as

$$\langle\mathcal{A}\rangle = \oint ds\mathcal{A} = \frac{\oint d\theta' \frac{\mathcal{A}}{\mathbf{B}\cdot\nabla\theta'}}{\oint \frac{d\theta'}{\mathbf{B}\cdot\nabla\theta'}} \tag{A.9}$$

for a quantity $\mathcal{A} \neq \mathcal{A}\left(\bar{\psi}\right)$. One notes that the safety factor can be expressed as

$$q\left(\bar{\psi}\right) = \frac{B^\gamma\left(\bar{\psi}\right)}{B^s\left(\bar{\psi}\right)} = \frac{F}{2\pi}\oint \frac{1}{R^2}\frac{d\theta}{\mathbf{B}\cdot\nabla\theta}. \tag{A.10}$$

One can also show that the ζ coordinate defined in Eq. (A.1) can be written as

$$\zeta = q\left(\bar{\psi}\right)s - \gamma, \tag{A.11}$$

from which one derives the relation between s and χ

$$\chi = 2\pi\left[s - \frac{g}{q\left(\bar{\psi}\right)}\right]. \tag{A.12}$$

As in the flux-tube version of GENE, any fluctuating field quantity $A(r,\zeta,s)$ is Fourier transformed with respect to r and ζ. The corresponding Fourier representation therefore reads

$$A(r,\zeta,s) = e^{\mathrm{i}k_\zeta\zeta}\sum_{k_r}\hat{A}_{k_r}(s)e^{\mathrm{i}k_r r} \sim e^{-\mathrm{i}n\varphi}, \tag{A.13}$$

yielding together with Eq. (A.1)

$$n = \frac{k_\zeta}{2\pi}. \tag{A.14}$$

2π-periodicity with respect to χ in $(\bar{\psi},\chi,\varphi)$ coordinates translates in (r,ζ,s) coordinates to the pseudo-periodic condition with respect to s:

$$A(r,\zeta,s+1) = A(r,\zeta - q(r),s) \tag{A.15}$$

For a given k_ζ mode, this condition leads to coupling between the set of considered k_r modes, $k_r = \delta k_r + p\Delta k_r$ with $\Delta k_r = k_\zeta dq/dr$, so that Eq. (A.13) becomes, after having furthermore linearized the safety factor

$$\begin{aligned} A(r,\zeta,s) &= e^{\mathrm{i}k_\zeta\zeta}e^{\mathrm{i}\delta k_r r}\sum_{p=-\infty}^{+\infty}\hat{A}_{\delta k_r + p\Delta k_r}(s)e^{\mathrm{i}p\Delta k_r r},\\ \hat{A}_{\delta k_r+p\Delta k_r}(s+1) &= \hat{A}_{\delta k_r+(p+1)\Delta k_r}(s). \end{aligned} \tag{A.16}$$

It is to be noted that when specifying the input parameters, $k_\theta|_{\mathrm{GKW}}$ is given instead of k_ζ itself. The value of k_ζ is then determined from $k_\theta|_{\mathrm{GKW}} = \sqrt{g^{\zeta\zeta}k_\zeta^2}$ evaluated at the outer midplane ($s=0$), $g^{\zeta\zeta} = \nabla\zeta\cdot\nabla\zeta$ being the diagonal metric tensor related to ζ. In a similar way, the value of k_r is specified via $k_R = \sqrt{g^{rr}k_r^2}$.
In the same way as one derived Eq. (4.8) from (4.7), one can express the ballooning representation given in (4.8) in terms of GKW-specific variables:

$$\begin{aligned} A(r,\zeta,s) &= e^{\mathrm{i}k_\zeta\zeta}\sum_{p=-\infty}^{+\infty}\hat{\mathcal{A}}(\chi+p2\pi)e^{\mathrm{i}\frac{k_\zeta}{2\pi}\frac{dq}{dr}\left(r+\frac{r_0}{\hat{s}}\right)(p2\pi-\chi_0)}\\ &= e^{\mathrm{i}k_\zeta\zeta}e^{-\mathrm{i}\frac{k_\zeta\frac{dq}{dr}\chi_0}{2\pi}}\sum_{p=-\infty}^{+\infty}\hat{\mathcal{A}}(\chi+p2\pi)e^{\mathrm{i}p\Delta k_r r\frac{dq}{dr}}, \end{aligned} \tag{A.17}$$

having again shifted the radial coordinate $r + r_0/\hat{s} \to r$. Comparing Eq. (A.17) to Eq. (A.16) one can identify

$$\begin{cases} \chi_0 = -2\pi\dfrac{\delta k_r}{k_\zeta\frac{dq}{dr}}\\ \hat{\mathcal{A}}(\chi+p2\pi) = \hat{A}_{\delta k_r+p\Delta k_r}(s). \end{cases} \tag{A.18}$$

A.2 Normalization

As in the GENE code, all quantities are normalized to be order unity and again species-dependent normalization factors are adopted for the velocity space. The specific choices are however different, and are discussed here. In the GKW code, reference mass m_{ref}, density n_{ref}, temperature T_{ref} and major radius R_{ref} are defined, and the user is free to choose their value. When interfacing with the CHEASE code, $R_{\mathrm{ref}} = R_{geom}(LCFS)$ it is assumed and the reference value of the magnetic field B_{ref} is evaluated at the same location. These quantities are related via the definition of the reference thermal velocity $v_{\mathrm{th,ref}}$

$$v_{\mathrm{th,ref}} = \sqrt{\frac{2T_{\mathrm{ref}}}{m_{\mathrm{ref}}}} \tag{A.19}$$

and used to compute the reference gyroradius $\rho_{\mathrm{ref}} = v_{\mathrm{th,ref}}/\Omega_{\mathrm{ref}}$. These reference values are then used to compute for each species a dimensionless mass $\tilde{m}$, thermal velocity $\tilde{v}$, density $\tilde{n}$ and temperature $\tilde{T}$

$$\tilde{m} = \frac{m}{m_{\mathrm{ref}}}, \qquad \tilde{v} = \frac{v_{\mathrm{th}}}{v_{\mathrm{th,ref}}}, \qquad \tilde{n} = \frac{n}{n_{\mathrm{ref}}}, \qquad \tilde{T} = \frac{T}{T_{\mathrm{ref}}}.$$

With these choices, the GKW phase space coordinates are all normalized according to

$$r = \tilde{r} R_{\mathrm{ref}}, \qquad \zeta = \tilde{\zeta}, \qquad s = \tilde{s}$$

$$v_{\parallel,j} = \tilde{v}_{\parallel} v_{\mathrm{th,j}}, \qquad \mu = \tilde{\mu}\, \frac{m v_{\mathrm{th,j}}^2}{B_{\mathrm{ref}}}, \qquad t = \tilde{t}\, \frac{R_{\mathrm{ref}}}{v_{\mathrm{th,ref}}},$$

where $v_{\mathrm{th,j}}$ is the thermal velocity of the $j-$species as defined in Eq.(A.19).
We explicitly remark the different definition of the reference velocity with respect to what is done in the GENE code, which is responsible, within a factor $\sqrt{2}$, for a different normalization of the microscopic scales quantities as well as of time. On the other hand, the normalized velocity space variables are the same. Furthermore, the normalization of the radial direction with respect to the macroscopic length R_{ref} causes a factor $\bar{\rho} = \rho_{\mathrm{ref}}/R_{\mathrm{ref}}$ to explicitly appear in the normalized equivalent of the Fourier representation given in e.g. Eq. (A.13) which then reads

$$\tilde{A}(\tilde{r}, \tilde{\zeta}, \tilde{s}) = e^{\frac{\mathrm{i}\tilde{k}_\zeta \tilde{\zeta}}{\bar{\rho}}} \sum_{\tilde{k}_r} \hat{\tilde{A}}_{\tilde{k}_r}(\tilde{s}) e^{\frac{\mathrm{i}\tilde{k}_r \tilde{r}}{\bar{\rho}}}. \tag{A.20}$$

B The GS2 code

B.1 GS2 coordinate system

The GS2 code [96] employs a Clebsch formulation to express the magnetic field as

$$\mathbf{B} = \nabla\alpha \times \nabla\psi, \tag{B.1}$$

where ψ is the poloidal flux function, defined as in the GENE code. The function $\alpha = \alpha(\psi, \theta, \varphi)$ is determined by comparing Eq. (B.1) to the equivalent representation $\mathbf{B} = F(\psi)\nabla\varphi + \nabla\varphi \times \nabla\psi$ as

$$\alpha = \varphi - q\chi \tag{B.2}$$

The GS2 field-aligned coordinate system (X, Y, θ) is directly based on the function α defined in Eq. (B.2). In particular it is assumed for the radial direction X

$$X = \frac{q_s}{r_0 B_a}\psi, \tag{B.3}$$

while for the binormal Y coordinate

$$Y = \frac{d\psi}{dr}\frac{\alpha}{B_a}, \tag{B.4}$$

where B_a is the toroidal magnetic field measured at the geometric center of the flux surface of interest: $B_a = F(R_{geom})/R_{geom}$. We point out that in the GS2 code, the geometric poloidal angle θ is used to parametrize a field line, therefore defining a "parallel" direction equivalent to the z coordinate in GENE or the s direction in GKW. Also the binormal direction Y is again equivalent, within a sign and different scaling factors, to both the y coordinate defined in Eq. (3.2) for the GENE code and the ζ coordinate defined in Eq. (A.1) for the GKW code:

$$y = -C_y B_a \frac{dr}{d\psi} Y, \tag{B.5}$$

and

$$\zeta = -\frac{B_a}{2\pi}\frac{dr}{d\psi} Y, \tag{B.6}$$

As for the GENE and GKW codes, fluctuating field quantities $A(X, Y, \theta)$ are Fourier transformed with respect to both the radial and binormal directions. The corresponding Fourier representation in GS2 variables therefore reads

$$A(X, Y, \theta) = e^{\mathrm{i}k_Y Y} \sum_{k_X} \hat{A}_{k_X}(\theta) e^{\mathrm{i}k_X X} \sim e^{\mathrm{i}n\varphi} \tag{B.7}$$

where we note the different sign appearing in the eikonal with respect to the ones in GENE and GKW representations given in equations (3.8) and (A.13) respectively, yielding together with Eq.(B.4)

$$n = \frac{1}{B_a}\frac{d\psi}{dr} k_Y. \tag{B.8}$$

The set of radial k_X modes, $k_X = \delta k_X + p\Delta k_X$, with $\Delta k_X = 2\pi\hat{s}k_Y$, are again coupled as a consequence of 2π-periodicity with respect to χ in (ψ, χ, φ) coordinates Equation (B.7), after linearizing the safety factor, can thus be rewritten as

$$\begin{gathered} A(X, Y, \theta) = e^{\mathrm{i}k_Y Y} e^{\mathrm{i}\delta k_X X} \sum_{p=-\infty}^{+\infty} \hat{A}_{\delta k_X + p\Delta k_X}(\theta) e^{\mathrm{i}p\Delta k_X X}, \\ \hat{A}_{\delta k_X + p\Delta k_X}(\theta + 2\pi) = \hat{A}_{\delta k_X + (p+1)\Delta k_X}(\theta). \end{gathered} \tag{B.9}$$

Proceeding as already explained in section4.1.3 for the GENE code, one derives the ballooning representation given in Eq. (4.8) in terms of GS2-specific variables:

$$\begin{aligned} A(X, Y, \theta) &= e^{\mathrm{i}k_Y Y} \sum_{p=-\infty}^{+\infty} \hat{\mathcal{A}}(\chi + p2\pi) e^{\mathrm{i}k_Y \hat{s}\left(X + \frac{X_0}{\hat{s}}\right)(p2\pi - \chi_0)} \\ &= e^{\mathrm{i}k_Y Y} e^{-\mathrm{i}k_Y \hat{s}\chi_0 X} \sum_{p=-\infty}^{+\infty} \hat{\mathcal{A}}(\chi + p2\pi) e^{\mathrm{i}p\Delta k_X X}. \end{aligned} \tag{B.10}$$

having once again shifted the radial coordinate $X + X_0/\hat{s} \to X$. Comparing Eq. (B.10) to Eq. (B.9) one finds:

$$\begin{cases} \chi_0 = -2\pi \dfrac{\delta k_X}{k_Y \hat{s}} \\ \hat{\mathcal{A}}(\chi + p2\pi) = \hat{A}_{\delta k_X + p\Delta k_X}(\theta). \end{cases} \tag{B.11}$$

B.2 Normalization

In the GS2 code, one chooses a reference value for temperature, density and mass, respectively T_{ref}, n_{ref} and m_{ref}, while the reference thermal velocity $v_{\mathrm{th,ref}}$ is defined as $v_{\mathrm{th,ref}} = \sqrt{2T_{\mathrm{ref}}/m_{\mathrm{ref}}}$. These values are used to compute the reference Larmor radius and frequency ρ_{ref} and Ω_{ref}, where we note that the magnetic field B_{ref} is in this case defined as the toroidal field at the location of geometric center of the flux surface of interest, $B_{\mathrm{ref}} = B_a$. All the macroscopic lengths are normalized to the minor radius a. In the same way as in the GENE and GKW codes, the velocity space variables are species-dependent normalized.

Therefore, the GS2 coordinate system can be written as

$$X = \tilde{X}\rho_{\mathrm{ref}}, \qquad Y = \tilde{Y}\rho_{\mathrm{ref}}, \qquad \theta = \tilde{\theta},$$

$$\mathcal{E} = \tilde{\mathcal{E}}T_j, \qquad \lambda = \tilde{\lambda}B_{\mathrm{ref}}, \qquad t = \tilde{t}\,\frac{v_{\mathrm{th,ref}}}{a}$$

We note that with the aforementioned choices, the reference Larmor radius is the same as in the GKW code, while a factor $\sqrt{2}$ remains compared to the GENE code. However time and gradients of equilibrium quantities, because of the different choice of the macroscopic reference length, are normalized to a different value with respect to both GENE and GKW.

C Development of synthetic diagnostics for T-PCI and C-ECE systems

C.1 A Matlab post-processing graphic tool

A post-processing graphical interface written in IDL is already available together with GENE. During this work a similar tool has been developed in Matlab.

The enormous amount of information contained in the distribution function evolved by GENE is typically reduced by the code itself taking the relevant velocity moments which are then saved, together with the electromagnetic fields, at a rate which is user-defined. Usually this is done every few hundreds time steps, such as to avoid the creation of too big output files maintaining at the same time a sufficiently high temporal resolution. These files contain, for each the species, the four dimensional space-time evolution of fluctuations, such as δT or δn. Normally, a further post processing of such information is required, in order e.g. to compute the corresponding fluxes, the k-spectra or simply evaluate averages and obtain quantities that can be directly compared with experimental observables. Having a user friendly interface which allows to easily evaluate and visualize such quantities is naturally of great help when one has to analyze and interprete the results of a simulation.

In order to allow also non IDL users to profit of such a tool, a Matlab equivalent of the existing one has been created. It consists of a graphical interface which allows the user to specify the simulation he is interested in analyzing and then various diagnostics are made available such as to obtain the most common quantities of interest. The tool has been built modularly, such as to easily allow the introduction of any new diagnostic. Similarly to the IDL one, the diagnostics are divided in groups according to their functionality (e.g. analysis of local simulations, or of global runs or parameter scans). Differently to what is currently done in IDL, we have introduced another layer of data saving. For each required time step every diagnostic saves its own output in a specific file, such that for a subsequent analysis it does not need to be recomputed but can simply be read.

C.2 Synthetic diagnostics

Thanks to the experience gained in developing the Matlab GUI, a user interface has been written also for T-PCI and C-ECE synthetic diagnostics. We recall that the Phase Contrast Imaging measures a line integrated electron density fluctuation along a laser beam [43]. Here Tangential refers to the specific geometry adopted in TCV, where the laser beam crosses the plasma with a certain inclination. This allows to localize the measurement where the beam is tangent to the magnetic field, therefore obtaining a high radially resolution [55]. The C-ECE instead, collects the Electron Cyclotron Emission, and through correlation analysis allows to determine the electron temperature.

A first preliminary version of synthetic diagnostics, valid only for flux-tube simulations carried out considering circular concentric flux surfaces, was developed in [135]. During this thesis this tool has been rewritten and generalized such as to be able to handle any magnetic geometry, for both local and global version of the code. The mappings between a position in cylindrical coordinates (R, Z) and flux-surface coordinates (ψ, χ) are provided by the CHEASE code.

The synthetic diagnostics is build as a post-processing tool and relies on the integration of fluctuating fields on diagnostic volumes reproducing the experimental ones. This choice allows more flexibility in investigating the effect of e.g. the diagnostic spatial position, compared to a direct implementation of the synthetic diagnostic directly in GENE, at the price of handling large files as a higher sampling rate can be required to reproduce the experimental acquisition rates.

Both the PCI and the ECE synthetic diagnostic are based on the integration of either density or temperature fluctuation on a diagnostic volume which matches the experimental one, such as to reproduce the experimental cut offs. In both cases, diagnostic volumes need to be properly placed in the plasma. For the T-PCI, the spatial localization is provided by the point at which the laser beam is tangent on a magnetic field line, around which the density fluctuations are integrated (the integration length is left as a input parameter). For the ECE one instead looks at a given flux-surface and integrates the temperature fluctuation over a volume whose size is at the moment an input parameter. The implementation of a ray tracing code, such as to properly reconstruct the emission volume [136] is foreseen for the future.

Once synthetic signals have been collected, they can be analyzed using the very same procedure as done in the experiments, even though the synthetic acquisition time is normally much shorter than in reality, thus extreme care must be used when temporal averages need to be computed.

As an example, we apply the PCI synthetic diagnostic to the simulation of the TCV discharge #45886 described in section 7.3. We use the same geometry as in the experimental measurements, considering all channels as acquiring. In the actual experimental set up, only a part of the acquisition detector is functional (16 channels out of 30). Therefore, a more sophisticated analysis must be used accounting for the non uniform spatial sampling when evaluating the k numbers. We avoid such complication here also because it would further impact the already limited time statistics.

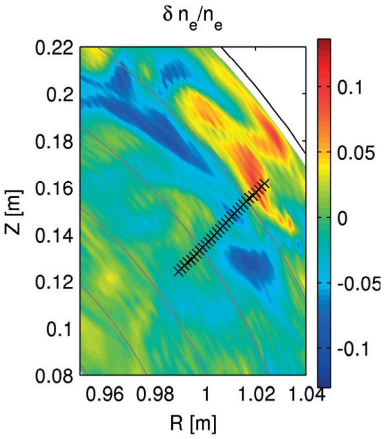

Figure C.1 : Location of the PCI tangency points, indicated with a black cross, projected on a poloidal plane. A snapshot of the electron density fluctuation δn_e is shown in the background.

The specific location of the PCI tangency points for this discharge is shown in Fig. C.1 where they are projected on the poloidal plane of the middle channel, together with a snapshot of the electron density fluctuation. The synthetic signals, already spatially integrated are show in Figure C.2 together with the corresponding spectral amplitudes as a function of frequency and k vector (here k is measured on the detector). One observes a dominant component at 32 kHz radially propagating outwards with $k \sim 2$ cm^{-1} (negative k according to our conventions). The simulated amplitudes can be remapped on their radial location, as shown in Figure C.3, which shows a very good agreement with the experimental corresponding, given in Figure 7.26.

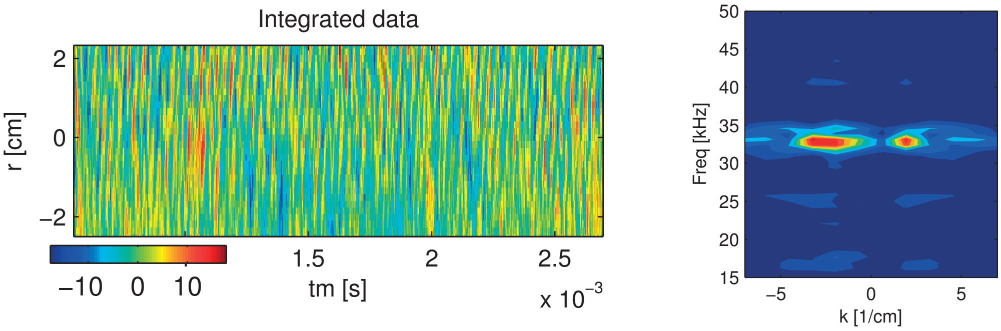

Figure C.2 : Simulated signals from PCI diagnostic as a function of time and corresponding 2D spectral amplitudes.

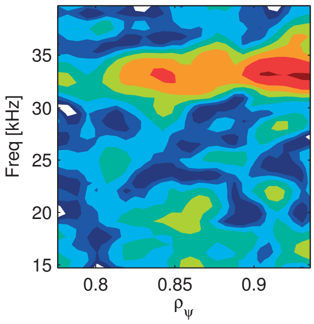

Figure C.3 : Fourier amplitudes of the PCI signals remapped on their radial location ρ_ψ. To be compared with Figure 7.26

D Local simulations for the TCV discharge #45353

A series of local simulations, centered at ρ_{vol}=0.5, 0.6, 0.7 and 0.9, have been performed considering the experimental TCV discharge #45353 already presented in chapter 7. Aim of this exercise was to investigate the GAM properties with less expensive local runs and help interpreting the results obtained with global simulations. Even though the frequency and the radial localization of the GAM turn out to be different than the one predicted with global runs, and the local code is in fact reproducing oscillations at a frequency proportional to the local sound speed, density and magnetic fluctuations appear to posses the same poloidal structure as the one observed in global simulations. Based on this consideration we have therefore also carried out an extensive series of linear Rosenbluth-Hinton tests such as to investigate, other than the dependency of the GAM frequency on radial location, the effect of the experimental TCV magnetic geometry on δn, δT and $\delta A_{\|}$.

	ρ_{vol}=0.5	ρ_{vol}=0.6	ρ_{vol}=0.7	ρ_{vol}=0.9
q	1.25	1.45	1.76	2.84
$\hat{s}$	0.71	1.02	1.42	2.64
R/L_n	1.78	4.6	7.64	20.85
R/L_T	9.56	10.89	13.42	32.90
$\nu_{ei}[c_s/R]$	0.23	0.36	0.62	3.02
β_e	0.33×10^{-2}	0.2×10^{-2}	0.13×10^{-2}	0.17×10^{-3}

Table D.1 : Experimental plasma parameters characterizing the three radial locations considered for flux-tube simulations.

All runs have been performed considering the experimental magnetic geometry as well as the measured temperature and density profiles. Electromagnetic fluctuations and collisions have been retained. The fundamental local plasma parameters are summarized in Table D.1. Simulations grids have been adapted for each run such as to ensure a sufficiently large domain in the perpendicular direction, e.g. $\hat{L}_x \times \hat{L}_y \sim 150 \times 200$. A

typical grid uses $n_{k_x} \times n_{k_y} \times n_z \times n_{v_\parallel} \times n_\mu = 256 \times 64 \times 48 \times 64 \times 16$ points.

D.1 GAM frequency from nonlinear simulations

The frequency of the GAM has been again evaluated by analysis the time evolution of the $\mathbf{E} \times \mathbf{B}$ velocity. The results are shown in Figure D.1.

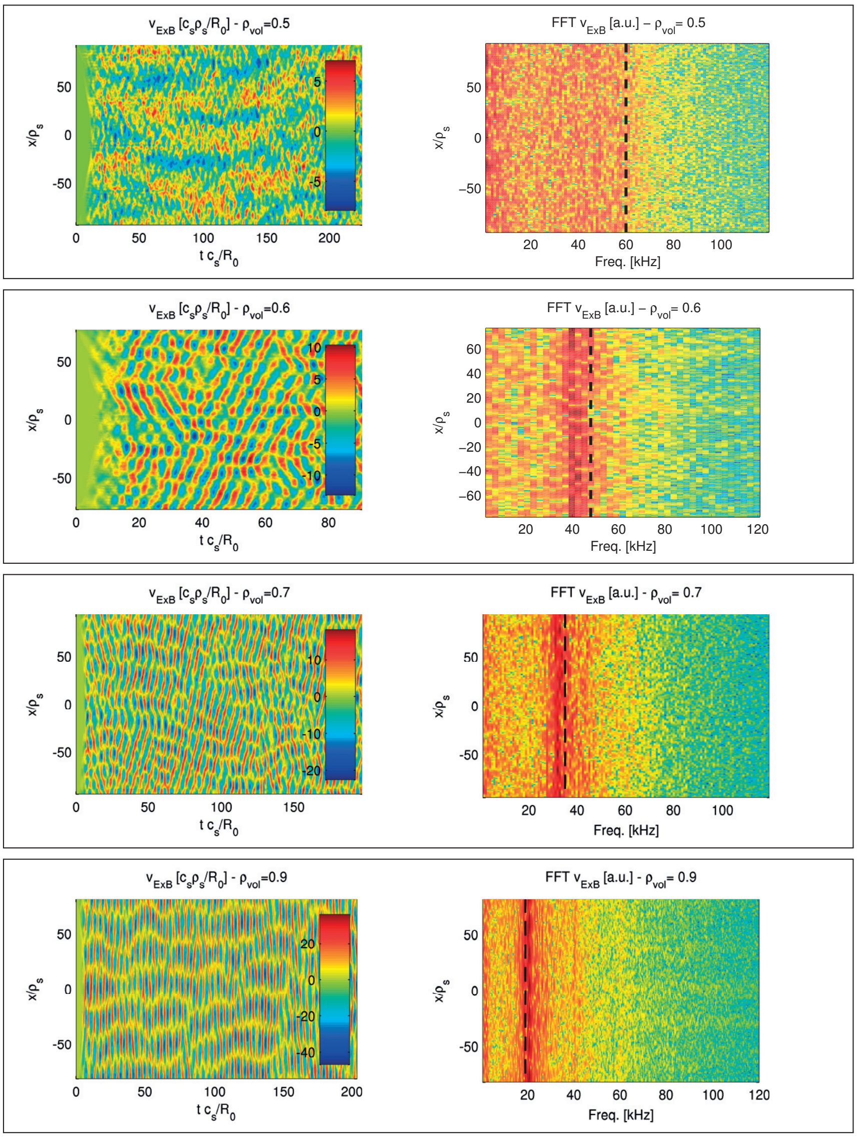

Figure D.1 : On the left, radial and temporal evolution of $\mathbf{E} \times \mathbf{B}$ velocity profiles and, on the right, the corresponding Fourier amplitudes (in log. color scale) evaluated over the stationary state of the runs. Vertical black lines indicate the RH linear frequency. From top to bottom results relative to ρ_{vol} =0.5, 0.6, 0.7 and 0.9.

We note that in this case one finds GAM oscillations for all cases, with the exception of the innermost position where a non-coherent pattern develops in the turbulent state for which it is quite hard to identify a dominant frequency. A very weak peak is found at ~ 52 kHz which was then used for the plots in section 7.2. In all simulations the GAM frequency is lower than what obtained from the linear Rosenbluth Hinton test, with a difference that increases moving towards the magnetic axis.

D.2 GAM density and magnetic component

In order to investigate the poloidal structure of any fluctuation associated to the GAM, we pick up the component associated to the $k_y = 0$ mode. This already selects the zonal $(n = 0)$ contribution, whose poloidal structure can then be studied by further Fourier decomposing along the poloidal angle χ. The obtained amplitudes are then averaged over the radial direction. The results for the electron density fluctuation are shown in Figure D.2 for the four different radial locations analyzed.

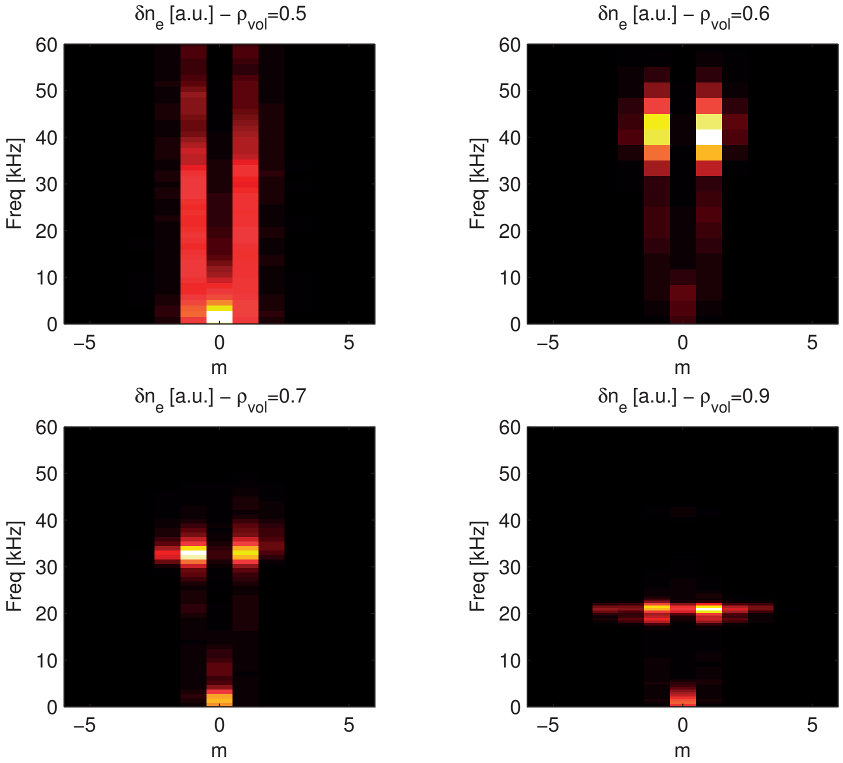

Figure D.2 : For each row, amplitude as a function of poloidal harmonics m and frequency in kHz of the electron density fluctuation associated to the $k_y = 0$ mode. The values have been averaged over the radial direction. From left to right results relative to ρ_{vol}=0.5, 0.6, 0.7 and 0.9.

In all cases, one observes a contribution from zero frequency modes (stationary zonal flows) and a GAM contribution at finite f_{GAM}. The latter, in agreement with the

previously described behaviour of the $\mathbf{E} \times \mathbf{B}$ velocity, is not clearly seen in the core ($\rho_{vol} = 0.5$), where however a broad $m = 1$ contribution from all modes having a frequency below the linear GAM one (~ 52 kHz at this position) is found.
As expected, at ρ_{vol} =0.6, 0.7 and 0.9 the GAM density fluctuation is dominated by $m = \pm 1$ poloidal harmonics. A narrow band pass filter around the GAM frequency has been applied to $\delta n_e(t)$ in order to isolate any the sidebands that are already visible in Fig. D.2. We find a contribution from $m = \pm 2$ at $\rho_{vol} = 0.7$ and $m = \pm 2, \pm 3$ at $\rho_{vol} = 0.9$. These latter contributions, thanks also to the Rosenbluth-Hinton tests described in the next section, are interpreted as a consequence of the actual plasma shape. In particular, triangularity is associated to $m = 3$ contributions.

The same analysis has been repeated analyzing $\delta A_\parallel$. In this case the analysis is more delicate, as fluctuations are dominated at all radii by the near zero frequency, $m = \pm 1$ component. One can nevertheless isolate in the two intermediate positions ρ_{vol}=0.6 and 0.7 a finite frequency contribution, constituted mainly by $m = \pm 1$ and ± 2. The $m = \pm 1$ poloidal harmonic is especially evident at ρ_{vol}=0.6, i.e. at the location where β is the largest value for which one still observes clear GAM oscillations in the nonlinear fluctuations. At ρ_{vol}=0.9 one observes also contributions from the $m = \pm 3$ poloidal harmonics. Again those components are understood as due to the actual magnetic geometry, as discussed in the next section.

D.3 Rosenbluth-Hinton tests investigating shaping effects

A number of Rosenbluth-Hinton tests have been carried out employing the same set-up as the one described in section 4.1.4. In this case however we have carried out all simulations assuming non adiabatic electrons and retaining electromagnetic fluctuations. Because of the light electrons, the recurrence problem cannot be avoided by increasing recurrence time with higher resolution in velocity space (for the required resolution simulations would rapidly become too expensive). Some numerical hyperdiffusion must instead be used. We have thus carried out all runs assuming $\texttt{hyp}_\texttt{v} = 0.5$, which is sufficient to allow carrying out simulations on grids with $n_z \times n_{v_\parallel} \times n_\mu = 64 \times 128 \times 48$ points. This value has to be lowered when the damping is weak i.e. when looking at circular geometries as otherwise it will impact the residual level.
In order to investigate the dependency of the GAM on shaping parameters, we have again made use of the Miller parametrization given in Eqs. eqs. (4.1) and (4.2) such as to easily vary each shaping parameter from the experimental situation to the circular case. This analysis has been performed limited to the flux-surfaces $\rho_{vol} = 0.7$ and $\rho_{vol} = 0.9$, whose shaping parameters are listed in Table D.2. They have been subsequently varied according to their magnitude, and we have verified that changing the order with which they are modified is not changing the results obtained.

	ϵ	ζ	δ	κ	$r\frac{\partial\zeta}{\partial r}$	$\frac{r}{\sqrt{1-\delta^2}}\frac{\partial\delta}{\partial r}$	$\frac{r}{\kappa}\frac{\partial\delta}{\partial r}$	dR/dr	dZ/dr
$\rho_{vol}=0.7$	0.20	3.310^{-3}	0.15	1.20	0.023	0.31	0.16	-0.049	-0.035
$\rho_{vol}=0.9$	0.25	1.810^{-2}	0.26	1.27	0.17	0.96	0.43	-0.066	-0.081

Table D.2 : Coefficients describing the flux surfaces $\rho_{vol}=0.7$ and 0.9 of TCV discharge #45353 computed according to the parametrization provided in Eqs. (4.1) and (4.2).

GAM frequency and damping

We discuss here how the linear frequency of the GAM varies with plasma shaping. The corresponding results are depicted in Figures D.4 and D.4. One notes that the trends associated to a variation of a certain shaping parameter are the same for the two positions being considered. Considering the GAM frequency ω_{GAM} and the mode growth rate γ_{GAM}, we observe that the Miller equilibrium exhibits a $\sim 10\%$ larger ω_{GAM} compared to the original TCV equilibrium, which therefore depends mainly on the up-down asymmetry of the experimental flux surfaces. The frequency further increase

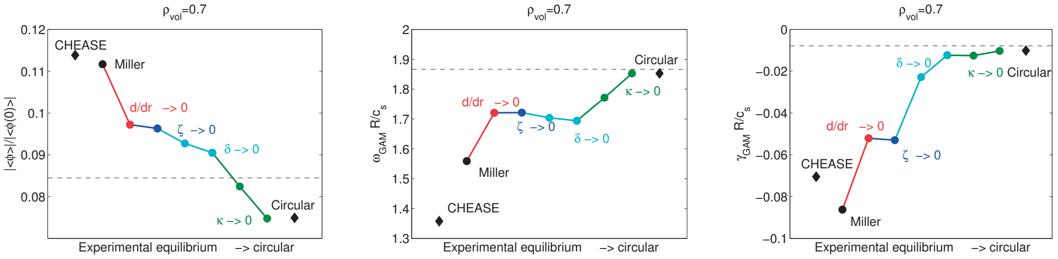

Figure D.3 : Dependence of the residual potential, GAM frequency and damping on shaping parameters. From the flux surface of interest, starting from its Miller parametrization (computed according to Eqs.(4.1) and (4.2)) the shaping parameters are relaxed down to a circular plasma. For comparison the value obtained with CHEASE and circular model are shown as well, while dashed lines indicate the Rosenbluth-Hinton residual level [101], and the analytic GAM estimate of Sugama [56].

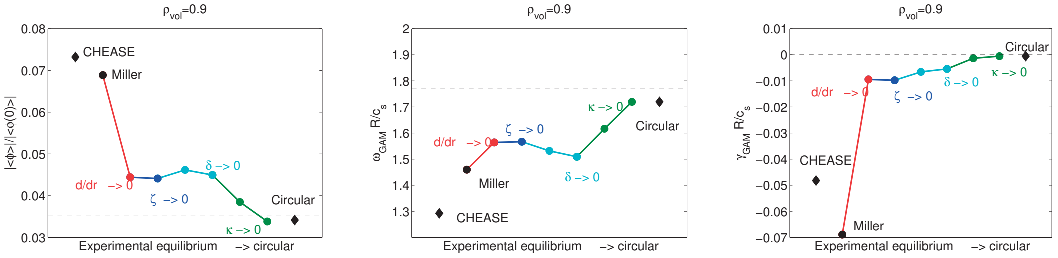

Figure D.4 : Same as Figure D.3, but showing the results for ρ_{vol}=0.9.

when the radial dependencies of the shaping coefficients, as well as Shafranov shift, are dropped. At the same time, the damping is found to be larger in the Miller equivalent equilibria compared to the CHEASE ones, and strongly reduced when radially constant shaping coefficients are assumed. We note that for all the CHEASE equilibria and their Miller counterpart the damping is significantly large and a strong initial transient is found, which makes the evaluation of $\gamma_{\rm GAM}$ non trivial. In agreement with the results presented in Section 4.1.4, a reduction of elongation κ increases both frequency and damping of the mode. From this set of runs, contrary to the one carried out for the geometry benchmarks, one can more clearly identify the role played by triangularity, whose reduction is causes the GAM frequency to diminish and the growth rate to increase. Finally, we remark a strong decrease of the residual potential is always found when triangularity elongation are reduced.

Density component

The previously described strategy of continuously relaxing the shaping parameters allows also to study the evolution of the poloidal structure of the GAM density fluctuation. We accomplish this exercise by analyzing the simulated density fluctuation over the first part of the time trace (typically up to $t \sim 30R_0/c_s$). We then decompose the density fluctuation in Fourier series in time

$$\delta n(\chi, t) = \sum_{\omega} \hat{\delta} n_{\omega}(\chi) e^{\mathrm{i}\omega t},$$

and investigate the poloidal structure of $\hat{\delta}_{\omega_{\rm GAM}}$, where $\hat{\delta}_{\omega_{\rm GAM}}$is the component at the GAM frequency. Thanks to carefully choice of the time window over which this is applied, we avoid the need of filtering the signal in time to remove possible spurious harmonics due to the initial transient phase.

In Figure D.5 the amplitudes of the poloidal harmonics, defined according to

$$\hat{\delta}_{\omega_{\rm GAM}}(\chi) = \sum_{m} \hat{\hat{\delta}}_{\omega_{{\rm GAM},m}} e^{\mathrm{i}m\chi} \tag{D.1}$$

are plotted as a function of the poloidal mode number m. For clarity we show only the results obtained with *i*) the Miller parametrization of the actual TCV flux-surfaces, *ii*) elongated and triangular equivalent, *iii*) only elongated and *iv*) circular flux surfaces. One observes, as expected from the linear GAM theory, that the leading therm is the $m = 1$ component. Higher harmonics, and in particular m=2 as predicted in Ref. [60], have already a non zero contribution even in the circular case. The introduction of a finite triangularity is found to strongly enhances them.

The very same analysis can be repeated looking at the GAM temperature fluctuation, and thus the pressure perturbation, which show the same poloidal structure.

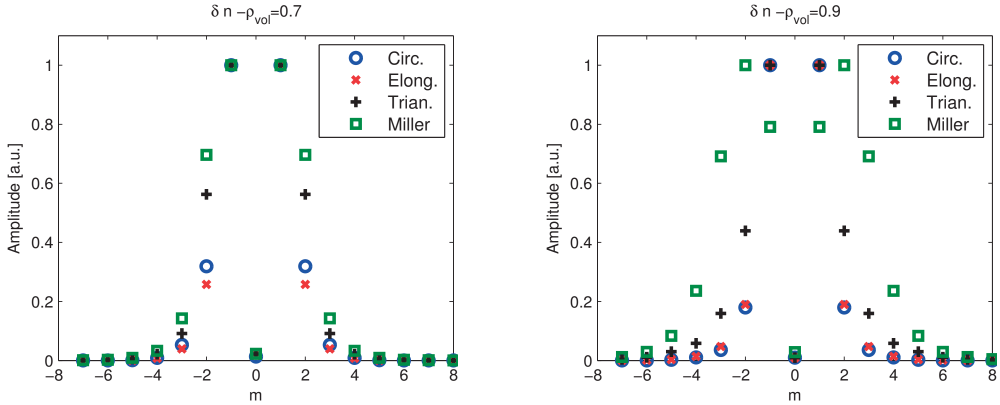

Figure D.5 : Fourier decomposition in poloidal harmonics of δn_{GAM} fluctuations. Shown are the results obtained with the Rosenbluth-Hinton test varying the shape of the flux-surface. Starting from the Miller parametrization of TCV surfaces ρ_{vol}=0.7 (green squares on the left graph) and 0.9 (on the right), the shape is then relaxed to maintaining only finite triangularity and elongation (black plus), then elongation only (red crosses) and finally circular flux surfaces (blue circles).

Magnetic component

Similarly to the δn, we have investigated also at $\delta A_{||}$ and $\delta B_{||}$ fluctuations. The results of our analysis are plotted in Figures D.6 and D.7 (showing respectively $\delta A_{||}$ and $\delta B_{||}$). The leading term is in all cases m=2 (we note that because of the lower value of β the simulations relative to $\rho_{vol} = 0.9$ show a smaller amplitude of the electromagnetic fluctuations, but the effect of magnetic geometry is expected to be somewhat stronger in comparison to ρ_{vol}=0.7). As predicted in e.g. Ref. [60], when plasma shaping is introduced, a richer number of harmonics contribute to electromagnetic fluctuations. In particular, we observe that triangularity δ is strongly destabilizing m=1 and m=3 harmonics of $\delta A_{||}$ (mainly m=1 of $\delta B_{||}$), which are even furthermore contributing (together with higher m terms) when the full Miller parametrization (or, equivalently, the actual TCV experimental equilibria, not shown here) is used. Elongation instead appears to play only a minor role.

We remark that even when the plasma shape is simplified to flux-surfaces with circular cross section, a strong m=1 component is always observed in both $\delta A_{||}$ and $\delta B_{||}$ fluctuations. It turns out that the origin of this harmonic is to be found in finite aspect ratio effects. Reducing ϵ by two orders of magnitude indeed results in a dominant m=2 component, as the analytically predicted.

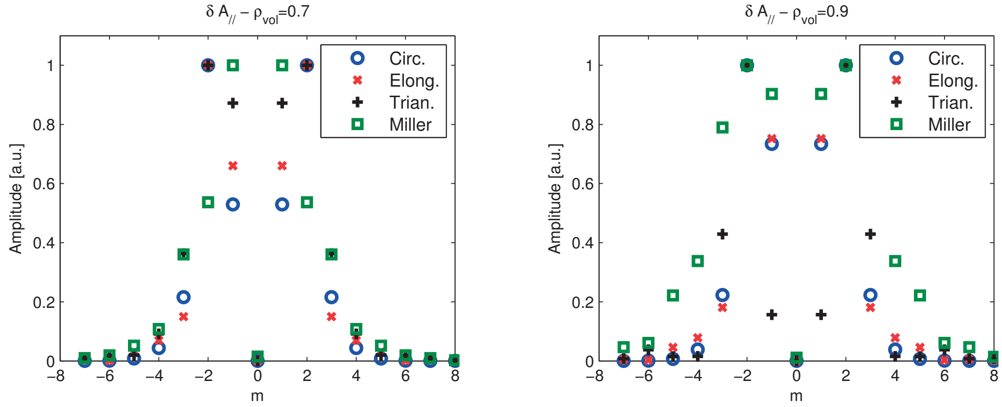

Figure D.6 : Fourier decomposition in poloidal harmonics of $\delta A_{\|}$ fluctuations. Shown are the results obtained with the Rosenbluth-Hinton test varying the shape of the flux-surface. Starting from the Miller parametrization of TCV surfaces ρ_{vol}=0.7 (green squares on the left graph) and 0.9 (on the right), the shape is then relaxed to maintaining only finite triangularity and elongation (black plus), then elongation only (red crosses) and finally circular flux surfaces (blue circles).

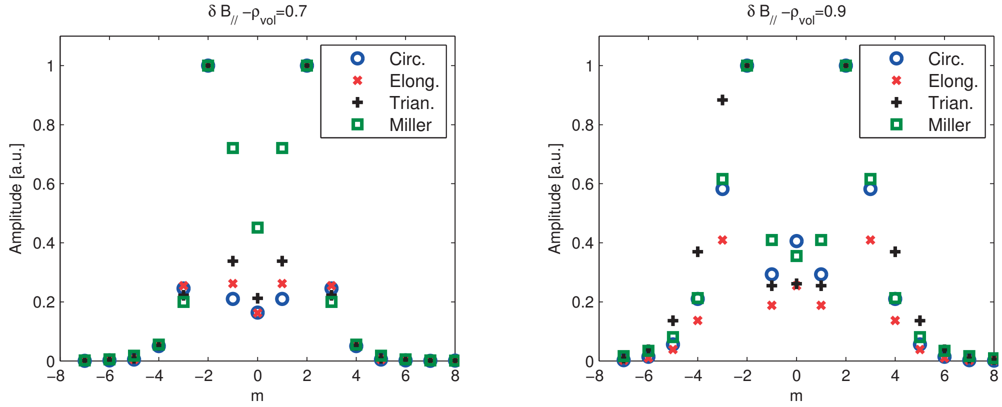

Figure D.7 : Same as Figure D.6 but showing the results for $\delta B_{\|}$.

Bibliography

[1] R. Atkinson and F. Houtermans, Z. für Physik **54**, 656 (1929).

[2] K. Krane, *Introductory nucelar physics* (Wiley, NewYork, 1987).

[3] J. Wesson, *Tokamaks* (Oxford University Press, Oxford, 2004).

[4] T. Northrop, *The adiabatic motion of charged particles* (Interscience Publishers, Inc., London, 1963).

[5] J. Freidberg, *Plasma physics and Fusion Energy* (Cambridge University Press., Cambridge, 2007).

[6] "Iter - the way to a new energy," www.iter.org.

[7] J. Nührenberg, Plasma Physics and Controlled Fusion **52**, 124003 (2010).

[8] P. Helander, C. D. Beidler, T. M. Bird, M. Drevlak, Y. Feng, R. Hatzky, F. Jenko, R. Kleiber, J. H. E. Proll, Y. Turkin, and P. Xanthopoulos, Plasma Physics and Controlled Fusion **54**, 124009 (2012).

[9] F. L. Hinton and R. D. Hazeltine, Rev. Mod. Phys. **48**, 239 (1976).

[10] P. Helander and D. Sigmar, *Collisional transport in Magnetized Plasmas* (Cambridge University Press, Cambridge, 2002).

[11] X. Garbet, Y. Idomura, L. Villard, and T. Watanabe, Nuclear Fusion **50**, 043002 (2010).

[12] F. Jenko, W. Dorland, M. Kotschenreuther, and B. N. Rogers, Physics of Plasmas **7**, 1904 (2000).

[13] Y. Camenen, A. Pochelon, R. Behn, A. Bottino, A. Bortolon, S. Coda, A. Karpushov, O. Sauter, G. Zhuang, and the TCV team, Nuclear Fusion **47**, 510 (2007).

[14] W. D'haeseleer, W. Hitchon, C. J.D., and J. Shohet, *Flux coordinates and magnetic field structure* (Springer-Verlag, Berlin, 1991).

[15] V. Shafranov, Reviews of Plasma Physics **2** (1966).

[16] A. M. Dimits, G. Bateman, M. A. Beer, B. I. Cohen, W. Dorland, G. W. Hammett, C. Kim, J. E. Kinsey, M. Kotschenreuther, A. H. Kritz, L. L. Lao, J. Mandrekas, W. M. Nevins, S. E. Parker, A. J. Redd, D. E. Shumaker, R. Sydora, and J. Weiland, Physics of Plasmas **7**, 969 (2000).

[17] J. P. Graves, Plasma Physics and Controlled Fusion **55**, 074009 (2013).

[18] J. Graves, "Plasma instabilities," Doctoral School Lectures (2014).

[19] A. J. Wootton, B. A. Carreras, H. Matsumoto, K. McGuire, W. A. Peebles, C. P. Ritz, P. W. Terry, and S. J. Zweben, Physics of Fluids B **2**, 2879 (1990).

[20] E. Mazzucato, Phys. Rev. Lett. **48**, 1828 (1982).

[21] R. J. Fonck, G. Cosby, R. D. Durst, S. F. Paul, N. Bretz, S. Scott, E. Synakowski, and G. Taylor, Phys. Rev. Lett. **70**, 3736 (1993).

[22] W. Horton, Rev. Mod. Phys. **71**, 735 (1999).

[23] E. A. Frieman and L. Chen, Physics of Fluids **25**, 502 (1982).

[24] R. G. Littlejohn, Journal of Plasma Physics **29**, 111 (1983).

[25] A. J. Brizard and T. S. Hahm, Rev. Mod. Phys. **79**, 421 (2007).

[26] H. Goldstein, *Classical mechanics* (Addison-Wesley, London, 2001).

[27] T. S. Hahm, Physics of Fluids **31**, 2670 (1988).

[28] T. S. Hahm, W. W. Lee, and A. Brizard, Physics of Fluids **31**, 1940 (1988).

[29] T. Dannert, *Gyrokinetische simulation von plasmaturbulenz mit gefangenen teilchen und elektromagnetischen effeckten*, Ph.D. thesis, Technische Universität München (2005).

[30] D. Told, *Gyrokinetic microturbulence in transport barriers*, Ph.D. thesis, Universität Ulm (2012).

[31] P. Angelino, A. Bottino, R. Hatzky, S. Jolliet, O. Sauter, T. M. Tran, and L. Villard, Physics of Plasmas **13**, 052304 (2006).

[32] X. Lapillone, *Local and global eulerian gyrokinetic simulations of microturbulence in realistic geometry with applications to the TCV tokamak*, Ph.D. thesis, EPFL Lausanne (2010).

[33] F. Merz, *Gyrokinetic simulations of multimode plasma turbulence*, Ph.D. thesis, Universität Münster (2008).

[34] M. Beer, *Gyrofluid Models of Turbulent Transport in Tokamaks*, Ph.D. thesis, Princeton University (1994).

[35] H. Doerk, *Gyrokinetic simulations of microtearing turbulence*, Ph.D. thesis, Universität Ulm (2012).

[36] S. Brunner, "Review of the landau collision operator and (approximate) linearized forms for numerical implementation," .

[37] W. Horton, D. Choi, and W. Tang, Physics of Fluids **24** (1981).

[38] T. Vernay, *Collisions in global gyrokinetic simualtions of tokamak plasmas using the Delta-f Particle-In-Cell approach: neoclassical physics and turbulent transport*, Ph.D. thesis, EPFL Lausanne (2013).

[39] S. Brunner, "Waves and instabilities in inhomogenous plasmas," Doctoral School Lectures (2014).

[40] F. Jenko and W. Dorland, Phys. Rev. Lett. **89**, 225001 (2002).

[41] B. Kadomtsev and O. Pogutse, Zh.Eksp.Teor.Fiz. **51** (1966).

[42] S. Brunner, *Global approach to the spectral problem of microinstabilities in tokamak plasmas using a gyrokietic model*, Ph.D. thesis, EPFL Lausanne (1997).

[43] A. Marinoni, *Plasma fluctuation studies in the TCV tokamak: modeling of shapign effects and advanced diagnostic developement*, Ph.D. thesis, EPFL Lausanne (2009).

[44] D. Pfefferlé, W. A. Cooper, J. P. Graves, and C. Misev, Computer Physics Communications **185** (2014).

[45] H. Doerk, F. Jenko, M. J. Pueschel, and D. R. Hatch, Phys. Rev. Lett. **106**, 155003 (2011).

[46] M. J. Püschel, *Electromagnetic effects in gyrokinetic simulations of plasma turbulence*, Ph.D. thesis, Universität Münster (2009).

[47] C. Bourdelle, X. Garbet, R. Singh, and L. Schmitz, Plasma Physics and Controlled Fusion **54**, 115003 (2012).

[48] M. Barnes, F. I. Parra, E. G. Highcock, A. A. Schekochihin, S. C. Cowley, and C. M. Roach, Phys. Rev. Lett. **106**, 175004 (2011).

[49] P. H. Diamond, S.-I. Itoh, K. Itoh, and T. S. Hahm, Plasma Physics and Controlled Fusion **47**, R35 (2005).

[50] K. Itoh, S.-I. Itoh, P. H. Diamond, T. S. Hahm, A. Fujisawa, G. R. Tynan, M. Yagi, and Y. Nagashima, Physics of Plasmas **13**, 055502 (2006).

[51] Z. Lin, T. S. Hahm, W. W. Lee, W. M. Tang, and R. B. White, Science **281**, 1835 (1998).

[52] J. Lang, S. E. Parker, and Y. Chen, Physics of Plasmas **15**, 055907 (2008).

[53] F. Merz and F. Jenko, Phys. Rev. Lett. **100**, 035005 (2008).

[54] N. Winsor, J. L. Johnson, and J. M. Dawson, Physics of Fluids **11** (1968).

[55] K. DeMeijere, *An experimental study of plasma fluctuations in the TCV and TEXTOR tokamaks*, Ph.D. thesis, EPFL Lausanne (2013).

[56] H. Sugama and T.-H. Watanabe, Journal of Plasma Physics **72**, 825 (2006).

[57] Z. Gao, Physics of Plasmas **17**, 092503 (2010).

[58] K. Itoh, S.-I. Itoh, P. H. Diamond, A. Fujisawa, M. Yagi, T. Watari, Y. Nagashima, and A. Fukuyama, Plasma and Fusion Research **1**, 037 (2006).

[59] H. Berk, C. Boswell, D. Borba, A. Figueiredo, T. Johnson, M. Nave, S. Pinches, S. Sharapov, and J. E. contributors, Nuclear Fusion **46**, S888 (2006).

[60] C. Wahlbergh and J. P. Graves, submitted to Plasma Physics and Controlled Fusion (2016).

[61] F. Zonca and L. Chen, EPL (Europhysics Letters) **83**, 35001 (2008).

[62] C. A. de Meijere, S. Coda, Z. Huang, L. Vermare, T. Vernay, V. Vuille, S. Brunner, J. Dominski, P. Hennequin, A. Krämer-Flecken, G. Merlo, L. Porte, and L. Villard, Plasma Physics and Controlled Fusion **56** (2014).

[63] C. Wahlberg, Plasma Physics and Controlled Fusion **51**, 085006 (2009).

[64] T. Görler, *Multiscale effects in plasma microturbulence*, Ph.D. thesis, Universität Ulm (2009).

[65] T. Görler, X. Lapillonne, S. Brunner, T. Dannert, F. Jenko, F. Merz, and D. Told, Journal of Computational Physics **230**, 7053 (2011).

[66] "The gene code," (), http://genecode.org.

[67] P. Xanthopoulos and F. Jenko, Physics of Plasmas **13** (2006).

[68] A. Arakawa, Journal of Computational Physics **1**, 119 (1966).

[69] V. Hernandez, J. E. Roman, and V. Vidal, ACM Trans. Math. Software **31**, 351 (2005).

[70] X. Lapillonne, S. Brunner, T. Dannert, S. Jolliet, A. Marinoni, L. Villard, T. Görler, F. Jenko, and F. Merz, Physics of Plasmas **16**, 032308 (2009).

[71] H. Lütjens, A. Bondeson, and O. Sauter, Computer Physics Communications **97**, 219 (1996).

[72] L. L. Lao, H. S. John, R. D. Stambaugh, A. G. Kellman, and W. Pfeiffer, Nucl. Fusion **25**, 1611 (1985).

[73] P. Xanthopoulos, W. A. Cooper, F. Jenko, Y. Turkin, A. Runov, and J. Geiger, Physics of Plasmas **16**, 082303 (2009).

[74] R. L. Miller, M. S. Chu, J. M. Greene, Y. R. Lin-Liu, and R. E. Waltz, Physics of Plasmas **5**, 973 (1998).

[75] M. Pueschel, T. Dannert, and F. Jenko, Computer Physics Communications **181**, 1428 (2010).

[76] B. F. McMillan, S. Jolliet, T. M. Tran, L. Villard, A. Bottino, and P. Angelino, Physics of Plasmas **15**, 052308 (2008).

[77] M. Oberparleiter, *Interaction between the neoclassical equilibrium and microturbulence in gyrokinetic simualtions*, Ph.D. thesis, Universität Ulm (2015).

[78] Y. Sarazin, V. Grandgirard, J. Abiteboul, S. Allfrey, X. Garbet, P. Ghendrih, G. Latu, A. Strugarek, and G. Dif-Pradalier, Nuclear Fusion **50** (2010).

[79] Y. Chen, S. E. Parker, W. Wan, and R. Bravenec, Physics of Plasmas **20** (2013).

[80] X. Lapillonne, B. F. McMillan, T. Görler, S. Brunner, T. Dannert, F. Jenko, F. Merz, and L. Villard, Physics of Plasmas **17**, 112321 (2010).

[81] G. L. Falchetto, B. D. Scott, P. Angelino, A. Bottino, T. Dannert, V. Grandgirard, S. Janhunen, F. Jenko, S. Jolliet, A. Kendl, B. F. McMillan, V. Naulin, A. H. Nielsen, M. Ottaviani, A. G. Peeters, M. J. Pueschel, D. Reiser, T. T. Ribeiro, and M. Romanelli, Plasma Physics and Controlled Fusion **50**, 124015 (2008).

[82] R. V. Bravenec, J. Candy, M. Barnes, and C. Holland, Physics of Plasmas **18**, 122505 (2011).

[83] R. V. Bravenec, Y. Chen, J. Candy, W. Wan, and S. Parker, Physics of Plasmas **20**, 104506 (2013).

[84] T. Görler, A. E. White, D. Told, F. Jenko, C. Holland, and T. L. Rhodes, Physics of Plasmas **21**, 122307 (2014).

[85] D. R. Mikkelsen, M. Nunami, T.-H. Watanabe, H. Sugama, and K. Tanaka, Physics of Plasmas **21**, 112305 (2014).

[86] S. Satake, Y. Idomura, H. Sugama, and T.-H. Watanabe, Computer Physics Communications **181**, 1069 (2010).

[87] G. Merlo, O. Sauter, S. Brunner, A. Burckel, Y. Camenen, F. J. Casson, W. Dorland, E. Fable, T. Görler, F. Jenko, A. G. Peeters, D. Told, and L. Villard, Physics of Plasmas **23**, 032104 (2016).

[88] J. Dominski, to be submitted (2016).

[89] A. Burckel, O. Sauter, C. Angioni, J. Candy, E. Fable, and X. Lapillonne, Journal of Physics: Conference Series **260**, 012006 (2010).

[90] A. Marinoni, S. Brunner, Y. Camenen, S. Coda, J. P. Graves, X. Lapillonne, A. Pochelon, O. Sauter, and L. Villard, Plasma Physics and Controlled Fusion **51**, 055016 (2009).

[91] J. Candy, Plasma Physics and Controlled Fusion **51**, 105009 (2009).

[92] M. Kammerer, F. Merz, and F. Jenko, Physics of Plasmas **15**, 052102 (2008).

[93] F. Merz, C. Kowitz, E. Romero, J. Roman, and F. Jenko, Computer Physics Communications **183**, 922 (2012).

[94] J. E. Roman, M. Kammerer, F. Merz, and F. Jenko, Parallel Computing **36**, 339 (2010), parallel Matrix Algorithms and Applications.

[95] A. Peeters, Y. Camenen, F. Casson, W. Hornsby, A. Snodin, D. Strintzi, and G. Szepesi, Computer Physics Communications **180**, 2650 (2009).

[96] M. Kotschenreuther, G. Rewoldt, and W. Tang, Computer Physics Communications **88**, 128 (1995).

[97] J. Connor, R. J. Hastie, and J. Taylor, Physical Review Letters **40** (1978).

[98] R. Singh, S. Brunner, R. Ganesh, and F. Jenko, Physics of Plasmas **21**, 032115 (2014).

[99] Y. Camenen, Y. Idomura, S. Jolliet, and A. Peeters, Nuclear Fusion **51**, 073039 (2011).

[100] P. Migliano, Y. Camenen, F. J. Casson, W. A. Hornsby, and A. G. Peeters, Physics of Plasmas **20**, 022101 (2013).

[101] M. N. Rosenbluth and F. L. Hinton, Phys. Rev. Lett. **80**, 724 (1998).

[102] J. Candy and R. E. Waltz, Physics of Plasmas **13**, 032310 (2006).

[103] Y. Xiao, P. J. Catto, and W. Dorland, Physics of Plasmas **14**, 055910 (2007).

[104] D. Zhou and Y. W., Physics of Plasmas **18**, 052505 (2011).

[105] L. Villard, A. Bottino, O. Sauter, and J. Vaclavik, Physics of Plasmas **9**, 2684 (2002).

[106] J. Dominski, S. Brunner, T. Görler, F. Jenko, D. Told, and L. Villard, Physics of Plasmas **22**, 062303 (2015).

[107] "Benchmark for gyrokinetic codes with kinetic electrons and mhd equilibrium," (), http://crpp.epfl.ch/benchmark.

[108] O. Sauter, S. Brunner, D. Kim, G. Merlo, R. Behn, Y. Camenen, S. Coda, B. P. Duval, L. Federspiel, T. P. Goodman, A. Karpushov, A. Merle, and T. Team, Physics of Plasmas **21**, 055906 (2014).

[109] G. Merlo, S. Brunner, O. Sauter, Y. Camenen, T. Görler, F. Jenko, A. Marinoni, D. Told, and L. Villard, Plasma Physics and Controlled Fusion **57**, 054010 (2015).

[110] F. Hofmann, J. B. Lister, W. Anton, S. Barry, R. Behn, S. Bernel, G. Besson, F. Buhlmann, R. Chavan, M. Corboz, M. J. Dutch, B. P. Duval, D. Fasel, A. Favre, S. Franke, A. Heym, A. Hirt, C. Hollenstein, P. Isoz, B. Joye, X. Llobet, J. C. Magnin, B. Marletaz, P. Marmillod, Y. Martin, J. M. Mayor, J. M. Moret, C. Nieswand, P. J. Paris, A. Perez, Z. A. Pietrzyk, R. A. Pitts, A. Pochelon, R. Rage, O. Sauter, G. Tonetti, M. Q. Tran, F. Troyon, D. J. Ward, and H. Weisen, Plasma Physics and Controlled Fusion **36**, B277 (1994).

[111] Y. Camenen, A. Pochelon, A. Bottino, S. Coda, F. Ryter, O. Sauter, R. Behn, T. P. Goodman, M. A. Henderson, A. Karpushov, L. Porte, and G. Zhuang, Plasma Physics and Controlled Fusion **47**, 1971 (2005).

[112] P. Angelino, X. Garbet, L. Villard, A. Bottino, S. Jolliet, P. Ghendrih, V. Grandgirard, B. F. McMillan, Y. Sarazin, G. Dif-Pradalier, and T. M. Tran, Phys. Rev. Lett. **102**, 195002 (2009).

[113] L. Villard, B. F. McMillan, O. Sauter, F. Hariri, J. Dominski, G. Merlo, S. Brunner, and T. M. Tran, Journal of Physics: Conference Series **561** (2014).

[114] Z. Lin, S. Ethier, T. S. Hahm, and W. M. Tang, Phys. Rev. Lett. **88**, 195004 (2002).

[115] J. Candy, R. E. Waltz, and W. Dorland, Physics of Plasmas **11** (2004).

[116] B. F. McMillan, X. Lapillonne, S. Brunner, L. Villard, S. Jolliet, A. Bottino, T. Görler, and F. Jenko, Phys. Rev. Lett. **105**, 155001 (2010).

[117] Z. Huang, S. Coda, G. Merlo, C. de Meijere, J. Graves, S. Brunner, M. Fontana, L. Porte, L. Vermare, L. Villard, C. Wahlberg, J. Dominski, P. Hennequin, and A. Krämer-Flecken, in *EFTSOMP* (2015).

[118] S. Coda, Z. Huang, G. Merlo, L. Porte, S. Brunner, M. Fontana, and L. Villard, in *US-EU Joint Transport Task Force Workshop* (2011).

[119] K. ITOH, S.-I. ITOH, P. H. DIAMOND, A. FUJISAWA, M. YAGI, T. WATARI, Y. NAGASHIMA, and A. FUKUYAMA, Plasma and Fusion Research **1**, 037 (2006).

[120] Z. Gao, K. Itoh, H. Sanuki, and J. Q. Dong, Physics of Plasmas **15**, 072511 (2008).

[121] B. F. McMillan, S. Jolliet, T. M. Tran, L. Villard, A. Bottino, and P. Angelino, Physics of Plasmas **16**, 022310 (2009).

[122] P. Angelino, X. Garbet, L. Villard, A. Bottino, S. Jolliet, P. Ghendrih, V. Grandgirard, B. F. McMillan, Y. Sarazin, G. Dif-Pradalier, and T. M. Tran, Physics of Plasmas **15**, 062306 (2008).

[123] H. Doerk, "The gene collisionality," .

[124] R. Hager, *Radial propagation of geodesic acoustic modes*, Ph.D. thesis, Technische Universität München (2011).

[125] R. Hager and K. Hallatschek, Phys. Rev. Lett. **108**, 035004 (2012).

[126] Z. Huang, private communication.

[127] A. Teolis, *Computational signal processing with wavelets* (Springer, 1998).

[128] R. Hager and K. Hallatschek, Physics of Plasmas **17**, 032112 (2010).

[129] J. Dominski, private communication.

[130] A. Storelli, L. Vermare, P. Hennequin, Ö. D. Gürcan, G. Dif-Pradalier, Y. Sarazin, X. Garbet, T. Görler, R. Singh, P. Morel, V. Grandgirard, P. Ghendrih, and T. S. team, Physics of Plasmas **22** (2015).

[131] Z. Huang, S. Coda, and C. de Meijere, in *57th Annual Meeting of the APS Division of Plasma Physics* (2015).

[132] P. Simon, G. D. Conway, A. Biancalani, T. Happel, P. Manz, D. Prisiazhniuk, U. Stroth, and the ASDEX Upgrade Team, in *EFTSOMP* (2015).

[133] W. Guo, S. Wang, and J. Li, Physics of Plasmas **17** (2010).

[134] O. Sauter and S. Y. Medvedev, Computer Physics Communications **184** (2013).

[135] F. Margairaz, *Synthetic Diagnostics of CECE and PCI based on non-linear gyrokinetic flux-tube simulation relevant to the TCV Tokamak*, Master's thesis, EPFL Lausanne (2012).

[136] V. Vuille, *Spectral and spatial analysis of micro-turbulence by correlation ECE radiometry on the tokamak TCV*, Master's thesis, EPFL Lausanne (2012).

Acknowledgements

First of all, I would like to thank my supervisors, Stephan Brunner and Laurent Villard. They gave me the unique possibility of working on a subject which is extremely intriguing and exciting. I don't know how many times I went to Stephan's office asking questions and I always found an immediate and clear answer, no matter what the question was about. Thanks for all the help, for having always supported and encouraged me, even when simulations were far from making any sense. I am very thankful also to Laurent, with whom I interacted less, but who always had the right remarks and comments to improve and direct the work. Being a teaching assistant for Physique Numerique was also extremely useful in understanding physics and how to explain simple things I give for granted.

I'm very thankful to Frank Jenko and his group, Tobias Görler, Hauke Doerk and Daniel Told, for the many useful discussions about my work and for being always available and supportive whenever I had any problem with the code. Cannot forget the great time I spent when visiting Garching. Danke!

A big thanks to Xavier Garbet, Tobias Görler and Stefano Coda, as well as to Stephan and Laurent, for having examined this thesis and, besides making it readable, helping in making it much better.

I then have to deeply thank all the clusters that (almost always) gracefully allowed me to carry out the runs I did, keeping me company during many weekends: HPCFF, HELIOS, Bellatrix, Deneb, Lemanicus, Rosa, PizDaint and PizDora.
For similar reasons I have to thank also Minh, for the help in solving the issues with PPB110 and never complaining about me using up all resources available (for this I should probably thank also all CRPP-theory people).

I'm grateful to Olivier Sauter, for all the useful scientific discussions and meetings, and for having explained me CHEASE. I shall not remember the chance I was given to go to Japan.

Thanks to Stefano Coda, for having started the fluctuation meetings creating a stimulating group where I had the chance to discuss my work and try to really understand what is

measured in TCV, getting also ideas for my runs.

Thanks to Edith and Roxane for the help with administrative stuff, and in particular thanks to Thushi for always kindly reminding me, every month, that I had forgotten to do the time sheets.

Of course these four years would not have been so easy and funny without some of the people I have met at CRPP, in particular Claudio and Federico. The number of coffees and beers (probably more beers) we shared I think is countless, as well as the number of girls we looked at and never talked to. In spite of the runaway girl effect, I really had a great time with you.
A special thanks to Emmanuel. We shared the office for few months only but definitely it has been the best office time ever, even though it was when I had to write the thesis. I'm also grateful to Jérémy and Stéphane, for the all the Aperos and coffee breaks. Thanks to Fabio, for Rabadan and Scareglia above all.
It was also great to have fun and interact with all the PhD students Christoph, Himank, Jonathan, Julien, Matteo, Paola, Pedro, Rogerio, Zhouji and all the others. The same is true for the not-anymore-PhDs Antoine and Umar.

Thanks to Greta, for the many chats we had about life and recipes. The same, without the recipes part, to Andrea Usel. It was great to meet you again in Lausanne and see that you have finally moved over PLD. There is still room for improving on football. Thanks to Laura, who has definitely been quite relevant in all this. Merci à Carole, who taught me most of the French I know.

Finally, my family. Whatever I am and whatever I managed to do I owe to them. I had the privilege to do what I wanted, being always fully supported and motivated. Grazie.

Gabriele Merlo
Ch. Porchat 4
1004 Lausanne
Switzerland

Born in Como, Italy
August 29, 1986
Italian

Phone : +41 21 693 1935
+41 76 742 3183
E-mail : `gabriele.merlo@epfl.ch`

Education

March 2012-present	Ph.D Candidate in plasma physics **Swiss Plasma Center (SPC-EPFL)**, Lausanne, Switzerland Provisional thesis title: "*Flux-tube and global grid-based gyrokinetic simulations of plasma microturbulence and comparisons with experimental TCV measurements*" Thesis directors: Prof. L. Villard, Dr. S. Brunner
December 2010	Master Degree *cum laude* in Nuclear Engineering **Politecnico di Milano**, Milan, Italy Thesis: "*Development of nanostructured Rhodium films for fabrication of diagnostic mirrors in nuclear fusion systems*" (italian) Advisor: Dr. M. Passoni
July 2008	Bachelor Degree *cum laude* in Energy Engineering **Politecnico di Milano**, Milan, Italy Thesis: "*Pulsed neutron sources*" (italian) Advisor: Prof. A. Cesana
June 2005	**Liceo scientitifico "G. Terragni"**, Olgiate C., Italy

Publications

First author

G. Merlo, O. Sauter, S. Brunner, et al. "*Linear multispecies gyrokinetic flux tube benchmarks in shaped tokamak plasmas*", Physics of Plasmas **23**, 3 (2016)

G. Merlo, S. Brunner, O. Sauter, et al. "*Investigating profile stiffness and critical gradients in shaped TCV discharges using local gyrokinetic simulations of turbulent transport*", Plasma Physics and Controlled Fusion **57** 5 (2015)

Co-author

C.A. de Meijere, S. Coda, Z. Huang, et al. "*Complete multi-field characterization of the geodesic acoustic mode in the TCV tokamak*" Plasma Physics and Controlled Fusion **56** 7 (2014)

L. Villard, B.F. McMillan, O. Sauter, et al. "*Turbulence and zonal flow structures in the core and L-mode pedestal of tokamak plasmas* Journal of Physics Conference Series **561** (2014)

O. Sauter, S. Brunner, D. Kim, et al., "*On the non-stiffness of edge transport in L-mode tokamak plasmas*", Physics of Plasmas **21** 5 (2014)

D. Dellasega, G. Merlo, C. Conti, et al., "*Nanostructured and amorphous-like tungsten films grown by pulsed laser deposition* Journal of Applied Physics **112** 8 (2012)

Conference contributions

"*Global gyrokinetic simulations of TCV plasmas*", 57th Annual Meeting of the American Physical Society, Division of Plasma Physic. Savannah, USA, November 2015

"*Global gyrokinetic benchmarks of shaped Tokamak plasmas in ITG regime*", NumKin Workshop, Garching, Germany, October 2015

"*Gyrokinetic simulations of turbulent transport in TCV plasmas with positive and negative triangularity*", IAEA Technical Meeting on Steady State operation, Nara, Japan, May 2015

"*Linear and non-linear global gyrokinetic benchmarks of shaped tokamak plasmas*", NumKin Workshop, Garching, Germany October 2014

"*Investigating the role of profile stiffness on turbulent transport in shaped TCV discharges using gyrokinetic simulations*", Joint Varenna-Lausanne International Workshop on Theory of Fusion Plasmas, Varenna, Italy, September 2014

"*Gyrokinetic turbulence simulations of plasma shaping and profile resilience effects in the TCV tokamak*", Swiss Physical Society Annual Meeting, Freibourg, Switzerland, June 2014

"*Gyrokinetic simulations of shaping effects on turbulent transport*", 15th European Fusion Theory Conference, Oxford, UK, September 2013

Extra-curricula experience

Mobility Trip: Max-Planck Institut für Plasmaphysik, Garching (2012)

Teaching assistant: Physique Numérique I/II, Swiss institute of Technology (EPFL) 2012-2015

Languages

Italian: mother tongue
English: advanced knowledge
French: basic knowledge

Computer skills

Scientific software : Matlab, Mathematica, HDF5, LaTex
Programming language : Fortran, C++, MPI, Bash

Awards

Gold medal for best graduated student, Politecnico di Milano, 2010

Gold medal for best graduated student, Politecnico di Milano, 2008